



**MONASH** University

**Precipitation pathways in Al-Cu-(In-Sb)/Ge alloys**

Yong Zhang

A Thesis Submitted for the Degree of Doctor of philosophy  
at Monash University (2019)

Department of Materials Science and Engineering  
Monash University  
January 2019



## **Copyright notice**

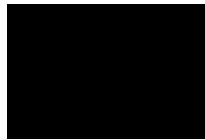
© Yong Zhang 2018.

I certify that I have made all reasonable efforts to secure copyright permissions for third-party content included in this thesis and have not knowingly added copyright content to my work without the owner's permission.

## **Declaration**

This thesis contains no material which has been accepted for the award of any other degree or diploma at any university or equivalent institution and that, to the best of my knowledge and belief, this thesis contains no material previously published or written by another person, except where due reference is made in the text of the thesis. I independently carried out all the research presented in the thesis.

Signature: ...



Print Name: ...Yong Zhang...

Date: ...24 January 2019.....

# Acknowledgements

I would like to express my sincere thanks to my supervisors, A/Prof. Laure Bourgeois and A/Prof. Nikhil V. Medhekar, for their invaluable guidance. I am also grateful to members of our research group for their ideas and help. I thank Zezhong Zhang and Dr Kelvin Chen for their useful discussion and thank Dr Yuefeng Yin, Dr Runhong Huang, Mahdi Javadi and Jodie Yuwono for their help on computer simulations. Furthermore, I acknowledge Prof. Nick Birbilis, Mr Sam Gao and Dr Jiehua Li (University of Leoben, Austria) for their inputs on alloy preparation.

I acknowledge the financial support from Monash University and the access to the facilities in the Monash Centre for Electron Microscopy (MCEM). The kind and professional staff from MCEM trained me how to use these facilities. Great thanks to Dr Russell King, Mr Renji Pan, Dr Emily Chen and Dr Tim Williams. I also acknowledge the access to the high-performance computer named Monash Campus Cluster, Raijin and Magnus.

Finally, thanks to my family for their unwavering support through these years. Especially, I would express my sincere thanks to Ms Yue Liu, who has given me so much help and support.



# Abstract

Understanding phase transformations at the atomic level is of great importance for microstructure and property control in materials. Since nanoparticles (generally called precipitates in aged alloys) that nucleate in solid solutions are the dominant strengthening constituent of most wrought Al alloys, understanding and manipulation of the size and morphology of these precipitates are critical to the design of high-strength Al alloys. However, despite many decades of studies on this subject, many outstanding questions remain regarding the nucleation of precipitates in Al alloys, and in particular: what is the composition and structure of a nucleus, and what is the role of vacancies in nucleation? Addressing these two questions should benefit both the aluminium industry and the fundamentals of nucleation theory.

Microalloying is one of the main practical methods for changing the formation process of precipitates in Al alloys. Here the effects of InSb additions and Ge additions in an Al-1.7at.%Cu alloy, a textbook model of precipitation hardening, are investigated by combining high-resolution scanning transmission electron microscopy and density functional theory calculations. Both InSb and Ge additions are found to promote precipitation in the Al-Cu alloy. It is shown that the microalloying additions operate in two distinct ways.

The first one involves precipitating InSb particles or Ge particles first, which subsequently act as heterogeneous nucleation sites for  $\theta'$ , the dominant Cu-rich precipitate phase in the Al-Cu binary alloy. More than 90% of  $\theta'$  precipitates nucleate heterogeneously from InSb particles in an Al-1.7Cu-0.025In-0.025Sb (at.%) alloy aged at 200 °C, while less than 20% of  $\theta'$  precipitates nucleate heterogeneously from Ge particles in an Al-1.7Cu-0.78Ge alloy aged at 200 °C. Experiments and atomic-scale calculations strongly suggest that tight enough binding between the microalloying solute atoms and vacancies is the key prerequisite for the mechanism to operate, which is influenced by ageing temperature, solute-vacancy binding energy and solute-vacancy cluster size.

The second role of the additions is (trapping and) releasing excess vacancies and increasing the diffusivity of Cu in the Al matrix. This mechanism is hypothesized to be operative when the binding between the microalloying elements and vacancies is not strong enough at a given ageing temperature. Two unexpected Cu-rich phases, H and  $\eta^*$ , were observed and were suggested to arise from the increased diffusivity of Cu under certain circumstances. The two

phases have similar atomic structure and composition ( $\sim\text{Al}_1\text{Cu}_1$ ) and are structurally related to the bulk equilibrium phases. In addition, the two phases are found to form before  $\theta'$  and proposed to be the precursors for  $\theta'$  formation.

This work highlights the complexity of non-equilibrium solid-state precipitation in even "simple" model aluminium alloys and how this complexity is related to the presence of excess vacancies.

# Table of contents

<b>Acknowledgements .....</b>	<b>III</b>
<b>Abstract.....</b>	<b>V</b>
<b>Table of contents .....</b>	<b>VII</b>
<b>List of Figures.....</b>	<b>XI</b>
<b>List of Tables .....</b>	<b>XXI</b>
<b>Chapter 1 .....</b>	<b>1</b>
<b>Introduction.....</b>	<b>1</b>
<b>Chapter 2 .....</b>	<b>4</b>
<b>Literature review .....</b>	<b>4</b>
<b>2.1 Precipitation in Al-Cu alloys .....</b>	<b>4</b>
2.1.1 Al-Cu binary system .....	4
2.1.2 Trace solute additions enhancing precipitation .....	8
2.1.3 Solute additions changing precipitate phase .....	12
<b>2.2 Roles of lattice defects in precipitation.....</b>	<b>17</b>
2.2.1 Vacancies .....	17
2.2.2 Dislocations .....	22
2.2.3 2D defects .....	27
<b>2.3 Effects of processing parameters on precipitation .....</b>	<b>28</b>
2.3.1 Ageing temperature and time.....	28
2.3.2 Cold working before artificial ageing .....	30
2.3.3 Phase selection depending on processing parameters.....	32
<b>2.4 Ways to optimise mechanical properties by tuning precipitation .....</b>	<b>33</b>
2.4.1 Grain refinement.....	33
2.4.2 Lowering lattice misfit.....	34
<b>2.5 Open questions and outline of the research.....</b>	<b>36</b>
<b>Chapter 3 .....</b>	<b>39</b>
<b>Experimental and computational methodologies.....</b>	<b>39</b>
<b>3.1 Alloy preparation and heat treatment protocols.....</b>	<b>39</b>
<b>3.2 Hardness measurement.....</b>	<b>40</b>

<b>3.3 Transmission electron microscopy .....</b>	<b>41</b>
<b>3.4 First-principles calculations .....</b>	<b>43</b>
3.4.1 Density functional theory.....	44
3.4.2 Parameters in DFT calculations.....	45
3.4.3 Formation energy and interfacial energy calculations .....	46
<b>3.5 Thermodynamic database for the Al-Cu binary alloy .....</b>	<b>49</b>
<b>Chapter 4 .....</b>	<b>50</b>
<b>Two precipitation sequences in an Al-1.7at.%Cu-0.025at.%In-0.025at.%Sb alloy ..</b>	<b>50</b>
<b>4.1 Hardness response.....</b>	<b>51</b>
<b>4.2 Microstructures at different ageing conditions .....</b>	<b>52</b>
4.2.1 Without natural ageing or interrupted quenching .....	52
4.2.2 With natural ageing or interrupted quenching .....	59
<b>4.3 DFT calculations of solute-vacancy binding energies .....</b>	<b>61</b>
<b>4.4 A rationale for the two different precipitation sequences: the critical role of vacancies .....</b>	<b>62</b>
<b>4.5 Possible segregation of In and Sb solutes at the <math>\theta'</math>/Al semi-coherent interface.....</b>	<b>67</b>
<b>4.6 Interfacial structure between an InSb particle and a <math>\theta'</math> precipitate .....</b>	<b>69</b>
<b>4.7 Conclusions .....</b>	<b>70</b>
<b>Chapter 5 .....</b>	<b>71</b>
<b>Multiple precipitation mechanisms of Cu-rich precipitates in an Al-1.7at.%Cu-0.78at.%Ge alloy.....</b>	<b>71</b>
<b>5.1 Hardness response.....</b>	<b>72</b>
<b>5.2 Main precipitate phases and their crystallography at different ageing temperatures</b>	<b>73</b>
5.2.1 200 °C ageing .....	73
5.2.1 160 °C ageing .....	80
5.2.3 250 °C ageing .....	81
<b>5.3 Nucleation mechanism of <math>\theta'</math> type I without the attachment of a Ge crystal: the critical role of vacancies.....</b>	<b>82</b>
<b>5.4 Heterogeneous nucleation of <math>\theta'</math> (type I, II, IV and V) on Ge particles .....</b>	<b>85</b>
<b>5.5 Two nucleation mechanisms of <math>\theta'</math> type III .....</b>	<b>87</b>
5.5.1 The H phase located at the $\theta'$ type III/Al coherent interface.....	88
5.5.2 Crystal structure and formation energy of the H phase .....	90
5.5.3 Low interfacial energy of the H/Al coherent interface .....	93
5.5.4 Long and thin $\theta'$ type III precipitates nucleating inside H phase precipitates .....	97
5.5.5 Short and thick $\theta'$ type III precipitates nucleating heterogeneously on Ge particles ....	98
<b>5.6 Possible formation mechanism of <math>\Omega</math> precipitates .....</b>	<b>99</b>

5.7 Possible Ge segregation at the semi-coherent $\theta'$ type I/Al interface.....	100
5.8 Conclusions .....	102
<b>Chapter 6 .....</b>	<b>104</b>
<b>An unexpected phase (<math>\eta^*</math>) preceding <math>\theta'</math> in Al-Cu alloys with abundant vacancies .</b>	<b>104</b>
6.1 $\eta^*$ in the Al-Cu-In-Sb alloy and its crystal structure.....	105
6.1.1 Isolated $\eta^*$ precipitates .....	105
6.1.2 $\eta^*$ segment at the semi-coherent $\theta'$ /Al interface .....	112
6.1.3 $\eta^*$ precipitates embedded in $\theta'$ precipitates .....	113
6.2 $\eta^*$ in the Al-Cu-Ge alloy and its crystal structure .....	115
6.3 Phase transformations at the $\eta^*$ decorated $\theta'$ /Al semi-coherent interface .....	117
6.3.1 Proposed growth (lengthening) mechanism of $\theta'$ at the $\eta^*$ decorated $\theta'$ /Al semi-coherent interface.....	117
6.3.2 Proposed growth (lengthening) mechanism of $\eta^*$ at the $\eta^*$ decorated $\theta'$ /Al semi-coherent interface.....	120
6.4 Discussion: thermodynamic analysis of $\theta'$ and $\eta^*$ .....	122
6.4.1 Driving force of nucleation from DFT calculations and a thermodynamic database. 123	
6.4.2 Interfacial energies of the $\eta^*$ /Al and $\theta'$ /Al interfaces: the first energy cost of nucleation .....	127
6.4.3 Strain energy: the second energy cost of nucleation.....	129
6.5 Discussion: kinetic analysis of the phase selection between $\theta'$ and $\eta^*$ .....	131
6.5.1 Role of vacancies on the formation of $\theta'$ and $\eta^*$ at the $\eta^*$ decorated $\theta'$ /Al semi-coherent interface.....	131
6.5.2 Roles of vacancies on the phase selection between $\eta^*$ and $\theta'$ .....	133
6.5.3 Role of vacancies on $\eta^*$ thickening .....	135
6.6 Strong similarities between $\eta^*$ and H.....	137
6.7 $\eta^*$ /H precipitates being the precursors of $\theta'$ precipitates.....	138
6.7 Conclusions .....	139
<b>Chapter 7 .....</b>	<b>141</b>
<b>Conclusions and future work.....</b>	<b>141</b>
7.1 Conclusions .....	141
7.1.1 Two precipitation sequences correlated with excess vacancies in Al-Cu-In-Sb .....	141
7.1.2 Multiple precipitation mechanisms of Cu-rich precipitates in Al-Cu-Ge.....	142
7.1.3 An unexpected phase ( $\eta^*$ ) preceding $\theta'$ in Al-Cu alloys with abundant vacancies ....	143
7.1.4 More remarks: comparing the two kinds of microalloying additions.....	144
7.2 Recommendations for future work.....	144
<b>Publications and conference presentations.....</b>	<b>147</b>

<b>References.....</b>	<b>148</b>
<b>Appendix 1.....</b>	<b>159</b>
<b>Atomic models used in Chapter 5.....</b>	<b>159</b>
<b>Appendix 2.....</b>	<b>162</b>
<b>Atomic models used in Chapter 6.....</b>	<b>162</b>
<b>Appendix 3.....</b>	<b>167</b>
<b>CIF files for the newly-reported Cu-rich precipitates.....</b>	<b>167</b>
<b>Appendix 4.....</b>	<b>173</b>
<b>Rare <math>\eta^*</math>-decorated semi-coherent <math>\theta'/Al</math> interface observed in the Al-Cu-Ge alloy .</b>	<b>173</b>

# List of Figures

Fig. 2.1 Crystal structures and schematic morphologies of $\theta''$ , $\theta'$ and $\theta$ precipitates in Al–Cu (filled circles are Cu atoms, open circles are Al atoms). Reproduced with permission from [22].	5
Fig. 2.2 Experimental HAADF-STEM images with overlaid atomic models and simulated images for the bulk and GP-zone-like interfacial structure of the $\theta'/\text{Al}$ interface. Reproduced with permission from [27].	7
Fig. 2.3 Complex at the semi-coherent $\theta'/\text{Al}$ interface. (a) Interfacial energies, (b) and (c) HAADF-STEM images of the diffuse interface. Reproduced with permission from [28].	8
Fig. 2.4 Dislocation densities in (a) Al-1.7at.% Cu electropolished at -20 °C after quenching, (b) Al-1.7at.% Cu-0.02at.% Cd electropolished at -20 °C after quenching, (c) Al-1.7at.% Cu electropolished at 70 °C, (d), Al-1.7at.% Cu-0.02at.% Cd electropolished at 70 °C. Reproduced with permission from [38].	9
Fig. 2.5 APT and annular dark field STEM (ADF-STEM) observations showing Sn particles at the semi-coherent $\theta'/\text{Al}$ interface. Green particles are Sn particles, and orange particles are $\theta'$ precipitates. Reproduced with permission from [40, 46].	11
Fig. 2.6 Aluminium-rich corner of the Al–Cu–Mg phase diagram indicating the present phases after long term ageing at 190 °C. Reproduced with permission from [54].	12
Fig. 2.7 Hardness curves for Al–1.1Cu–xMg (where x=0, 0.2, 0.5, 0.75, 1.0, 1.7 at.%) aged at 150 °C. Reproduced with permission from [55].	13
Fig. 2.8 Bright field transmission electron micrographs and corresponding selected area electron diffraction patterns (the top row), showing the evolution of microstructure in the ternary Al-1.7Cu-0.3Mg (at.%) alloy aged at 180 °C for (a)15 s; (b) 30 s; (c) 120 s; (d) 720 s; (e) 9000 s. The electron beam is parallel to $\langle 001 \rangle_{\text{Al}}$ . Reproduced with permission from [55].	13
Fig. 2.9 HAADF-STEM images showing the interfacial structures and corresponding atomic models for $\Omega$ precipitates with different thicknesses in an Al-Cu-Mg-Ag alloy. Reproduced with permission from [63].	15
Fig. 2.10 Bright field transmission electron micrographs and corresponding selected area electron diffraction patterns (the top row), showing the evolution of microstructure in a	

quaternary Al-Cu-Mg-Ag alloy aged at 180 °C for (a) 15 s; (b) 30 s; (c) 120 s; (d) 720 s, and (e) 9000s. The electron beam is near $\langle 001 \rangle_{Al}$ . Reproduced with permission from [14].	15
.....	
Fig. 2.11 Atomic-resolution HAADF-STEM images of embedded $T_1$ precipitates, (a) and (b) are images along the $\langle 110 \rangle_{Al}$ and $\langle 112 \rangle_{Al}$ orientations, respectively. Reproduced with permission from [67].	16
Fig. 2.12 Equilibrium vacancy concentration from first-principles calculations (LDA and GGA quasiharmonic calculations) are plotted in comparison with experimental data. Reproduced with permission from [57]. The references in the figure are from the original paper.	18
Fig. 2.13 Five frequency model illustration for the case of an fcc system with a dilute impurity concentration. The arrows indicate the direction of the vacancy jump and the numbers $n$ stand for the $n$ th nearest neighbouring site to the impurity. Reproduced with permission from [84].	20
Fig. 2.14 Evolution of hardness during room temperature storage and artificial ageing after quenching for the Al-Mg-Si alloy AA6061 with and without Sn additions. Reproduced with permission from [26].	21
Fig. 2.15 Bright field STEM images and APT reconstructions showing the segregation of Mn atoms along dislocations in a Fe-Mn alloy. Reproduced with permission from [94].	23
Fig. 2.16 Si diffusion along dislocations in an Al-Si alloy and the diffusion coefficients of Si for diffusion along dislocations and diffusion in the Al matrix. Reproduced with permission from [97]. The references in the figure are from the original paper.	24
Fig. 2.17 HAADF-STEM images show the growth of a $\theta'$ precipitate accompanied by a moving dislocation in an Al-Cu alloy. The white line feature is a dislocation. Reproduced with permission from [99].	24
Fig. 2.18 Concentrations of Al, Cu, Mg, Si, and Zn as a function of distance from the coherent (left) and semi-coherent (right) $\theta'/Al$ interfaces after ageing at 463 K for 8 h in an Al-Si-Cu-Mg alloy. Reproduced with permission from [101].	25
Fig. 2.19 DFT calculated segregation energies of 34 elements at the semi-coherent and coherent $\theta'/Al$ interfaces. A negative value means energetically favourable segregation. Reproduced with permission from [102].	25
Fig. 2.20 HAADF-STEM images showing the possible segregation of Sn atoms at the semi-coherent $\theta'/Al$ interface (leftmost, the red circles may indicate the Sn segregation) and the formation of Sn particles (bright big particles in a-d) at the same place in an Al-Cu-Sn alloy. Reproduced with permission from [40].	26

Fig. 2.21 Three boundaries with misorientations of 4° (AB), 6° (BC) and 9.5° (AC) in an Al-4Cu alloy after 2 h ageing at 240 °C. Boundaries AB and BC contain $\theta'$ precipitates, boundary AC contains $\theta$ precipitates. Reproduced with permission from [109].	27
Fig. 2.22 Precipitate free zone in an Al-Zn-Mg alloy aged 3 h at 180 °C. Reproduced with permission from [112]. The region free of dark particles (precipitates) is a precipitate free zone.	28
Fig. 2.23 Diffusion coefficient of Cu in the Al matrix from DFT calculations and experiments. Reproduced with permission from [84]. The references in the figure are from the original paper.	29
Fig. 2.24 Bright-field TEM images and SAED patterns of an Al-1.7 at% Cu alloy aged at 100 °C for 24 h, (a) without deformation, (b) with eight passes of ECAP. Reproduced with permission from [121].	31
Fig. 2.25 TEM images of 2024 alloy aged for (a) 180 min and (b) 720 min after 70% strain deformation. Reproduced with permission from [56].	32
Fig. 2.26 Typical tensile engineering stress-strain curves of 2024 Al alloy under different processing conditions, (i) solid solution treatment (SST) at 493 °C; (ii) SST + aging at 160 °C for 10 h; (iii) SST + cold rolling (CR); (iv) SST + CR + aging at 160 °C for 13 h; (v) SST + CR + aging at 100 °C for 100 h. Reproduced with permission from [123].	34
Fig. 2.27 High density of precipitates in alloys due to a low misfit at the precipitate/matrix interface. (a) $Al_3(Sc_{1-x}Zr_x)$ in an Al-Sc-Zr alloy and (b) Ni(Al,Fe) in a steel. Reproduced with permission from [129, 130].	35
Fig. 2.28 (a) Presence of Cu at the $\beta''$ /Al interface in an Al-Mg-Si alloy [133] and (b) enhanced nucleation frequency of $\beta''$ precipitates in an Al-Mg-Si alloy with Cu additions. Reproduced with permission from [134].	36
Fig. 3.1 Schematic of imaging a specimen using a HAADF detector and a BF detector in a STEM. The blue region and line indicate electron trajectory.	41
Fig. 3.2 Cohesive energy of FCC Al (a), FCC Cu (b), $\theta'$ ( $Al_2Cu$ , in c) and $\eta^*$ ( $Al_1Cu_1$ , in d) relative to $M \times M \times M$ ( $M \times M \times N$ for $\theta'$ and $M \times L \times O$ for $\eta^*$ ) k points. The k points labelled by arrows guarantee an energy convergence better than 0.001 eV/atom.	46
Fig. 3.3 Atomic models of the coherent $\theta'$ /Al interface and the calculated interfacial energies. (a) Atomic models with equivalent or non-equivalent interfaces (normal unit cell of $\theta'$ and a modified cell of $\theta'$ are highlighted by black and red rectangles, respectively), (b) plotting of $E_f/N$ vs $1/N$ .	48

Fig. 3.4 Calculated Al-Cu phase diagram showing precipitates, in comparison with experimental results. Reproduced with permission from [20]. The references in the figure are from the original paper. ....	49
Fig. 4.1 Hardness curves for the Al-Cu alloy and the Al-Cu-In-Sb alloy aged at different temperatures. ....	51
Fig. 4.2 HAADF-STEM images of the alloys and summary of precipitate types and length distribution. (a) the quaternary alloy aged 6 h at 160 °C, (b) the quaternary alloy aged 2 h at 200 °C, (c) the quaternary alloy aged 30 min at 250 °C, (d) the binary alloy aged 2 h at 200 °C, (e) comparison of Cu-rich phases between the binary and quaternary alloys aged 2 h at 200 °C, (f) length distribution for the quaternary alloy at the peak hardness condition. The insets in (a)-(d) are images of typical Cu-rich precipitates. ....	53
Fig. 4.3 HAADF-STEM images of the quaternary alloys aged at 200 °C for different times. (a) 2 min, the inset is an InSb particle truncated only at two faces, (b) 10 min, (c) 10 min, (d) 10 min. ....	54
Fig. 4.4 EDS elemental mappings of the quaternary alloy aged for 30 min at 200 °C. The corresponding HAADF-STEM image is at the top left corner. ....	55
Fig. 4.5 STEM images of the quaternary alloy aged at 250 °C for 2 min. (a) low magnification BF image, (b) and (c) HAADF images, the arrows indicating InSb particles, the inset in (c) showing an InSb particle attaching to a face-on $\theta'$ precipitate. ....	55
Fig. 4.6 (a) nano diffraction patterns of a $\sim 5$ nm InSb particle together with the Al matrix in the quaternary alloy aged for 2 h at 200 °C (B in insets means incident beam), (b) selected area electron diffraction patterns of a $\sim 50$ nm InSb particle together with the Al matrix in the quaternary alloy aged for 30 days at 300 °C, the inset shows the TEM image of the particle, (c) schematics of the measured crystal structure and the corresponding simulated diffraction patterns (left, $\langle 001 \rangle$ , right, $\langle 011 \rangle$ ), (d) schematics of InSb bulk stable crystal structure and the corresponding simulated diffraction patterns (left, B along $\langle 001 \rangle$ , right, B along $\langle 011 \rangle$ ). ....	56
Fig. 4.7 HAADF-STEM images of the quaternary alloys aged at 250 °C for different times after 10 days natural ageing. (a) and (b) 20 min, (c) 1 h. The white circles indicate InSb particles on the broad surface (the coherent interface with the Al matrix) of a $\theta'$ precipitate. ....	60
Fig. 4.8 STEM images of the quaternary alloy aged at 200 °C for different times after interrupted quenching; (a) HAADF image for 10 min aged alloy, (b) and (c) HAADF images for 20 min aged alloy, (c) low magnification BF image for 2 h aged alloy. The	

white and black arrows indicate InSb particles at the semi-coherent and coherent interface of $\theta'$ , respectively.....	60
Fig. 4.9 Binding energies between solute atoms and a vacancy calculated from DFT. The inset shows the schematic configurations of solute atoms around a vacancy and the number in parentheses is the size of the supercell. ....	61
Fig. 4.10 Schematic of nucleation sequence and strategy to change the nucleation sequence using different heat treatments. V indicates a vacancy. ....	66
Fig. 4.11 HAADF-STEM images showing projected morphology $\theta'$ precipitates in the Al-Cu-In-Sb alloy aged for 30 min at 200 °C. The pink circle highlights a $\theta'$ precipitate with a circular shape. The white arrow indicates a squared $\theta'$ precipitate. ....	67
Fig. 4.12 HAADF-STEM images showing possible In and Sb segregation at the semi-coherent $\theta'$ /Al interface in the aged Al-Cu-In-Sb alloy, (a) and (c) 30 min at 200 °C, (b) and (d) 60min at 160 °C. (a) and (b) exhibit the typical $\theta'$ /Al semi-coherent interface that also occurs in Al-Cu binary alloys [28]. (c) and (d) display different interfacial structures with arrows highlighting possible In and Sb segregation.....	68
Fig. 4.13 HAADF-STEM images show the interface between an InSb particle and a $\theta'$ precipitate in the Al-Cu-In-Sb alloy aged for 60 min at 160 °C (a) and 15 min at 200 °C (b). The insets are low magnification images of precipitates.....	69
Fig. 5.1 Hardness curves for the Al-Cu-Ge, Al-Cu-In-Sb and Al-Cu alloys aged at 200 °C (a) and 200 °C after cold rolling (b).....	72
Fig. 5.2 Hardness curves for the Al-Cu-Ge, Al-Cu-In-Sb and Al-Cu alloys aged at 160 °C (a) and 250 °C (b).....	73
Fig. 5.3 HAADF-STEM images of the Al-Cu-Ge alloy aged 2 min at 200 °C. Low- brightness regions (expected to be Cu-rich particles based on image contrast) always decorate Ge particles, but half of $\theta'$ precipitates are free of Ge particles. The insets in (b) are integrated intensity in the green rectangle and the light blue rectangle. ....	74
Fig. 5.4 HAADF-STEM images of the Al-Cu-Ge alloy aged 10 min at 200 °C. Ge particles are always decorated with Cu-rich particles, but more than half of $\theta'$ precipitates are free of Ge particles. The blue lines and orange lines are parallel with $\{111\}_{\text{Ge}}$ and $\{011\}_{\theta'}$ , respectively.....	75
Fig. 5.5 HAADF-STEM images of the Al-Cu-Ge alloy aged 2 h at 200 °C showing $\theta'$ type I, $\theta'$ type II and $\theta'$ type III precipitates. (c) is an enlargement of the red rectangle in (a) and shows $\theta'$ type III, (e) is an enlargement of the red rectangle in (d) and shows $\theta'$ type II. (f)	

shows  $\theta'$  type II from another zone axis. The atomic model of  $\theta'$  is overlapped in the insets. The blue lines and orange lines are parallel with  $\{111\}_{\text{Ge}}$  and  $\{011\}_{\theta'}$ , respectively..... 76

Fig. 5.6 HAADF-STEM images of  $\theta'$  type IV (a) and type V (b) precipitates in the Al-Cu-Ge alloy aged 2 h at 200 °C viewed along  $\langle 011 \rangle_{\text{Al}}$ . The blue lines and orange lines are parallel with  $\{111\}_{\text{Ge}}$  and  $\{011\}_{\theta'}$ , respectively. .... 78

Fig. 5.7 HAADF-STEM images of  $\Omega$  precipitates in the Al-Cu-Ge alloy aged 2 h at 200 °C. The precipitates in red rectangles (a) and (c) are zoomed in and shown in (b) and (d), respectively. The overlaid atomic model of  $\Omega$  is bigger than one unit cell..... 79

Fig. 5.8 HAADF-STEM images of Ge particles, GP zones and  $\theta'$  precipitates in the Al-Cu-Ge alloy aged for 2 h at 160 °C. .... 81

Fig. 5.9 HAADF-STEM images of  $\theta'$  (type I, II and III) precipitates and Ge particles in the Al-Cu-Ge alloy aged for 2 min at 250 °C. (b)  $\theta'$  type II and (c)  $\theta'$  type III..... 81

Fig. 5.10 HAADF-STEM images of  $\theta'$  type I (a), type IV (b) and type V (c) precipitates in the Al-Cu-Ge alloy aged 15 min at 250 °C. The blue and yellow lines are parallel with  $\{111\}_{\text{Ge}}$  and  $\{011\}_{\theta'}$ , respectively. .... 82

Fig. 5.11 HAADF-STEM images of the Al-Cu-Ge alloy without (a) and with 10-day natural ageing before aged at 200 °C (b). Natural ageing hardly changes the fraction of Cu-rich precipitates decorated with a Ge particle..... 83

Fig. 5.12 Binding energies between solute Ge atoms and a vacancy calculated from DFT. The inset shows the schematic configurations of solute atoms around a vacancy and the number in parentheses is the size of the supercell..... 84

Fig. 5.13 Atomic model for the well-matching Ge/ $\theta'$  interface and DFT calculated interfacial energy. (a-d) atomic model of the interface (e) DFT calculated interfacial energy. The red rectangles indicate distortion at the left interface relative to the right one in the green rectangle. The orange and grey lines indicate the crystal planes of  $\theta'$  and Ge crystals, respectively..... 85

Fig. 5.14 HAADF-STEM images of the  $\theta'$ /Ge interface in the Al-Cu-Ge aged for 2 h at 200 °C. The orange lines and grey lines are parallel with the  $\{011\}_{\theta'}$  and  $\{111\}_{\text{Ge}}$  planes, respectively. The two planes are not always parallel but also form different angles. The DFT relaxed atomic model in Fig. 5.13 is overlapped as the inset in (a)..... 86

Fig. 5.15 HAADF-STEM images of the interfacial structure of  $\theta'$  type III precipitates in the Al-Cu-Ge alloy aged at 200 °C for 2 h. (a) a thick  $\theta'$  type III precipitate, (b) an independent H phase precipitate. The atomic models of the H phase and the  $\theta'$  phase are overlapped with the HAADF images. The red rectangles mark the structurally common part between

- the independent H phase precipitate and the special structure at the  $\theta'$ /Al interface, and the black rectangle highlights the difference between them. .... 88
- Fig. 5.16 HAADF-STEM images of (a) an independent H phase precipitate and (b) a thick  $\theta'$  type III precipitate covered by the H phase in the Al-Cu-Ge alloy aged at 200 °C for 1 h. The atomic models for the H phase and the  $\theta'$  phase are overlapped onto the HAADF images. The red rectangles mark the structurally common part between the H phase precipitate and the structure at the  $\theta'$ /Al interface. .... 89
- Fig. 5.17 EDS elemental mappings of (a) an independent H phase precipitate and (b) a  $\theta'$  type III precipitate in the Al-Cu-Ge alloy aged 2 h at 200 °C. The incident electron beam was near  $\langle 001 \rangle_{\text{Al}}$  zone axis (deviation  $< 2^\circ$ ). .... 90
- Fig. 5.18 Atomic models of the H/Al interface and the H phase. (a) and (b) are the atomic models of the interface viewed along  $[100]_{\text{Al}}$  and  $[011]_{\text{Al}}$ , respectively. (c) a unit cell of the H phase and the corresponding lattice parameters. The structure in red rectangles is observed at the  $\theta'$  type III/Al coherent interface, while the structure in black rectangles is not observed at the  $\theta'$  type III/Al coherent interface. CIF file for the H phase is given in Appendix 3. .... 91
- Fig. 5.19 Transformation energy from (an H phase precipitate and the Al matrix) to (a  $\theta'$  type I precipitate and the Al matrix). (a) 4.5 unit cell thick  $\theta'$ , (b) 1.5 unit cell thick  $\theta'$ . The blue spheres are Al atoms and orange ones are Cu atoms. The single blue atom after + is an Al atom, and its energy is the ground state energy in the FCC lattice. The supercells and Al atoms are multiplied (indicated by  $\times$ ) by different times to make sure the numbers of Al and Cu atoms are the same on the left and right sides of the black arrows. .... 92
- Fig. 5.20 Possible atomic models of the direct interface between the Al matrix and a  $\theta'$  type III precipitate. (a) the first possible atomic model, (b) the second possible atomic model. . 94
- Fig. 5.21 DFT calculated interfacial energies of four different interfacial models. The coherent H/Al interface has the lowest interfacial energy. N is the number of atoms in a supercell and  $E_f$  is the formation energies of the supercell (supercells are shown in Appendix 1). 95
- Fig. 5.22 Atomic model of a thick  $\theta'$  type III precipitate covered by the H phase viewed from  $[100]_{\text{Al}}$  and  $[110]_{\text{Al}}$ , (b) comparison between the relaxed atomic model and the HAADF-STEM image (The viewing direction is  $[100]_{\theta'}/[100]_{\text{Al}}$ ). .... 96
- Fig. 5.23 Transformation energies for (a) the transformation from an embedded H phase precipitate to a thick  $\theta'$  type III precipitate covered by the H phase and (b) the transformation from an embedded thick  $\theta'$  type III precipitate covered by the H phase to an embedded 4.5 unit cell thick  $\theta'$  type I precipitate. The blue spheres are Al atoms and orange ones are Cu atoms. The single blue atom before + is an Al atom, and its energy is

the ground state energy in the FCC lattice. The supercells and Al atoms are multiplied (indicated by $\times$ ) by different times to make sure the numbers of Al and Cu atoms are the same on the left and right sides of the black arrows.....	96
Fig. 5.24 Long and thin $\theta'$ type III precipitates in the Al-Cu-Ge alloy aged for 1 h (a) and 2 h (b) at 200 °C. These precipitates are free of a big Ge particle.....	97
Fig. 5.25 Short and thick $\theta'$ type III precipitates nucleating heterogeneously on Ge particles in the Al-Cu-Ge alloy aged for 15 min (a) and 1 h (b) and 2 h (c) at 200 °C. The inset in (c) is the enlargement of the area in the small red rectangle and the superimposed Ge/ $\theta'$ interfacial atomic model. Circles highlight the regions free of the interfacial H phase coverage. The viewing direction is $[100]_{\theta'}/[100]_{Al}$ .....	99
Fig. 5.26 HAADF-STEM images of the semi-coherent $\theta'$ type I/Al interface in the Al-Cu-Ge alloy aged for 1 h at 200 °C. Arrows highlight extra atomic columns that have never been observed in Al-Cu alloys. ....	100
Fig. 5.27 HAADF-STEM images showing the rounding of $\theta'$ precipitates (type I) in the Al-Cu-Ge alloy aged for 2 h at 200 °C. EDS elemental mapping of the area in the yellow square is shown as the inset in (a). The $\theta'$ precipitate in the red rectangle is the common morphology of $\theta'$ precipitates in Al-Cu binary alloys at the peak aged condition. ....	101
Fig. 6.1 HAADF-STEM images displaying one unexpected Cu-rich precipitate in the Al-Cu-In-Sb alloy aged 20 min at 200 °C. The unexpected Cu-rich phase precipitates are rare and not uniformly distributed.....	105
Fig. 6.2 HAADF-STEM images of the $\eta^*$ phase precipitates with two orientations in the Al-Cu-In-Sb alloy aged for 15 min at 200 °C. The inset between (a) and (b) is the atomic model of perfect $\eta_2$ , and the superimposed atomic model on Cu-rich precipitates is $\eta_2$ with a defect (the red rectangles highlight the defect).....	106
Fig. 6.3 The equilibrium Al-Cu phase diagram and the unit cells of $\theta'$ (metastable phase) and $\eta_2$ viewed along $[010]_{\theta'/\eta_2}$ . Reproduced with permission from [156]. ....	107
Fig. 6.4 HAADF-STEM images of $\eta^*$ precipitates in the Al-Cu-In-Sb alloy aged for 1 h at 160 °C. The inserted atomic models were relaxed by DFT calculations. Low magnification images of the $\eta^*$ precipitates are also shown as insets.....	108
Fig. 6.5 HAADF-STEM images of $\eta^*$ precipitates in the Al-Cu-In-Sb aged for 1 h at 160 °C and 10 min at 250 °C. DFT relaxed atomic model of $\eta_2$ are also overlapped. A defect is located at the top surface of these $\eta^*$ precipitates. ....	110
Fig. 6.6 HAADF-STEM images of $\eta^*$ precipitates with the third kind of defect in the Al-Cu-In-Sb alloy aged for 20 min at 200 °C. Two atomic models of the precipitates are	

- superimposed on the HAADF images. The red rectangles indicate the defect part, and the yellow ones highlight a segment of  $\eta^*$ . Model A and Model B have the same structural feature as the HAADF-STEM images, but only Model B matches the positions of atomic columns in HAADF-STEM images. .... 111
- Fig. 6.7 HAADF-STEM images displaying a  $\eta^*$  segment (half unit cell in size along  $[100]_{\eta^*}$ ) at the semi-coherent  $\theta'/\text{Al}$  interface in the Al-Cu-In-Sb alloy aged for 15 min (a-c) or 30 min (d) at 200 °C. (a) and (c) show  $\eta^*$  precipitates, and (b) and (d) show  $\theta'$  precipitates. .... 112
- Fig. 6.8 HAADF-STEM images showing  $\eta^*$  precipitates embedded in or attached to  $\theta'$  precipitates in the Al-Cu-In-Sb alloy. (a), (b), (d) and (e) aged for 1 h at 160 °C, (c) 15 min at 200 °C, (f) 10 min at 200 °C. The green rectangles highlight the 2D structural feature of  $\eta^*$  ..... 114
- Fig. 6.9 HAADF-STEM images of  $\eta^*$  precipitates in the Al-Cu-Ge alloy aged 1 h at 200 °C.  $\eta^*$  precipitates show the same crystal structure as that observed in the Al-Cu-In-Sb alloy. .... 115
- Fig. 6.10 HAADF-STEM images of thick  $\eta^*$  precipitates with a defect in the Al-Cu-Ge alloy aged 1 h at 200 °C. The insets are DFT relaxed atom models overlaid on HAADF-STEM images. .... 116
- Fig. 6.11 HAADF-STEM images showing the semi-coherent  $\eta^*/\text{Al}$  interface in the Al-Cu-Ge alloy aged 2 h at 200 °C. The interfacial structure is different from the  $\theta'/\text{Al}$  semi-coherent interface in the same alloy. .... 117
- Fig. 6.12 HAADF-STEM images (a-d) and atomic model (e) depicting the growth of  $\theta'$  at the  $\eta^*$  decorated semi-coherent  $\theta'/\text{Al}$  interface in the Al-Cu-In-Sb alloy. (a-c) show the growth intermediate (aged 1 h at 160 °C), (d) shows the typical interface before/after the growth intermediate (aged 30 min at 200 °C). Atoms with two tones are located at  $(x, y, 0.5)$  and others are at  $(x, y, 0.0)$ . Cu columns in green circles remain intact during the growth process; atomic columns in yellow squares are expected to be filled by Cu atoms from the Al matrix; Cu atoms in the red circles are expected to diffuse into the yellow circles. The black arrows indicate the possible movement directions of Cu atoms. Each atomic column in (e) is filled by only Al or Cu atoms before and after the transformation. .... 118
- Fig. 6.13 (a) HAADF-STEM images indicating the growth of  $\eta^*$  at the  $\eta^*$  decorated semi-coherent  $\theta'/\text{Al}$  interface from  $t$  ( $t$  is time) to  $t+a$  ( $0 < a < k$ ), (b) atomic model depicting the growth mechanism of  $\eta^*$  at the semi-coherent  $\theta'/\text{Al}$  interface from  $t$  (the atomic model at  $t$  is the same as that in Fig. 6.12 for easy comparison) to  $t+a$ . Atomic columns in yellow

- squares are expected to be filled by Cu atoms from the Al matrix. The black arrows indicate the possible movement directions of Cu atoms. .... 121
- Fig. 6.14 DFT calculated transformation energy from an embedded  $\eta^*$  precipitate in the Al matrix to an embedded  $\theta'$  precipitate in the Al matrix with different thicknesses. (a) 1.5 unit-cell  $\theta'$ , (b) 4.5 unit-cell  $\theta'$ . The blue spheres are Al atoms and orange ones are Cu atoms. The single blue atom is an Al atom, and its energy is the ground state energy in the FCC lattice. The supercells and Al atoms are multiplied (indicated by  $\times$ ) by different times to make sure the numbers of Al and Cu atoms are the same on the left and right sides of the black arrows. .... 125
- Fig.6.15 (a) Gibbs free energies for  $\theta''$ ,  $\theta'$  and  $\eta_2$  phases and chemical potentials for Al and Cu atoms in the Al-1.7at.%Cu solid solution. (b) free energy change for the formation of  $\theta''$ ,  $\theta'$  and  $\eta_2$  phases from the Al-1.7at.%Cu solid solution. The  $\eta_2$  phase has a higher driving force of nucleation than  $\theta'$ . .... 126
- Fig. 6.16 Interfacial energies of  $\eta^*/\text{Al}$  and  $\theta'/\text{Al}$  interfaces calculated using DFT calculations.  $E_f$  is the formation energy of a supercell and N is the total number of Cu and Al atoms in the supercells. A  $\eta^*$  precipitate has a lower interfacial energy compared with that of a  $\theta'$  precipitate without  $\eta^*$  decoration.  $\eta^*$  decoration at the semi-coherent  $\theta'/\text{Al}$  interface lowers the semi-coherent interfacial energy of a  $\theta'$  precipitate. The atomic models of different interfaces are shown in Appendix 2..... 128
- Fig. 6.17 HAADF-STEM images and atomic models showing the misfits between precipitates and the Al matrix. (a) and (b) are  $\theta'$  precipitates in the Al-Cu-In-Sb alloy aged for 30 min at 200 °C, (c) is a  $\eta^*$  precipitate in the Al-Cu-In-Sb alloy aged for 1 h at 160 °C. The red, yellow and green lines indicate the atomic planes for Al,  $\theta'$  and  $\eta^*$ , respectively..... 129
- Fig. 6.18 DFT calculated vacancy formation energies at different positions near the  $\eta^*$ -decorated  $\theta'/\text{Al}$  semi-coherent interface. (a) schematic of the stacking change and the five possible positions for vacancy formation, (b) vacancy formation energies at different positions. Vacancy formation energy is lower near the interface than far away from the interface. .... 132
- Fig. 6.19 Atomic models for the thickening process of a  $\eta^*$  precipitate. The formation energies of the four supercells are also shown at the bottom. (a) and (b) are model A and B in Fig. 6.6. Atoms with two tones are located at (x, y, 0.5) and others are at (x, y, 0.0). Red squares indicate the energetically preferred positions of vacancies, and green arrows indicate the possible motion directions of Cu atoms from (b) to (c). .... 136
- Fig. 6.20 DFT-relaxed atomic models for (a) the H phase lying on  $\{110\}_{\text{Al}}$  planes and (b) the  $\eta^*$  phase lying on  $\{100\}_{\text{Al}}$  planes. The yellow arrows indicate the lengthening directions

for the two Cu-rich phases. The black rectangles highlight the common structural feature between (a) and (b). Atoms with two tones are located at  $(x, y, 0.5)$  and others are at  $(x, y, 0.0)$ ..... 137

## List of Tables

Table 2.1 Solute-vacancy binding energies from experiments and density functional theory calculations for some elements [39, 83]. .....	19
Table 2.2 Summary of $D_0$ and $Q$ for some elements in the Al matrix [84, 113, 114]. .....	28
Table 3.1 Chemical analysis of two micro-alloyed Al-Cu alloys by AES-ICP (atomic percentage). .....	39
Table 3.2 Summary of artificial ageing parameters used in this study.....	40
Table 3.3 Imaging conditions of the used microscopes. The aberrations of Titan <sup>3</sup> 80-300 were corrected by a CEOS Cs probe corrector. ....	42
Table 4.1 Comparison of lattice constants of InSb particles between experimental results and DFT calculations. ....	57
Table 5.1 Cu-rich precipitates in the peak-aged Al-Cu-Ge alloy at 200 °C. ....	80
Table 5.2 Formation energies of the H phase and $\theta'$ type I from DFT calculations (see Appendix 1 for the used supercells). .....	91
Table 5.3 Cu-rich precipitates in the Al-Cu-Ge alloy at the peak aged condition at 200 °C. ....	103
Table 6.1 Comparison of the crystal structure of $\eta^*$ and $\eta_2$ . .....	109
Table 6.2 Formation energies of $\eta^*$ and $\theta'$ from DFT calculations (0K; the supercells used here are shown in Appendix 2; Energy convergence is 0.001 eV/atom). .....	124



# Chapter 1

## Introduction

Phase transformations in metals and alloys are of great fundamental scientific importance and also directly affect the service properties of both structural and functional materials. For example, the second most widely used alloys, aluminium alloys, achieve their broad mechanical properties through a series of complex solid-state phase transformations. Nanoscale precipitates can form in the Al matrix and remarkably strengthen the alloy once supersaturated Al solid solutions are annealed at a moderate temperature. This process is usually called artificial ageing and is the main strengthening method of most wrought Al alloys (excluding 3xxx and 5xxx series Al alloys). There are typically three parameters to optimise the mechanical performances by manipulating phase transformations: composition, temperature and time. The final performance is a complex function of these three parameters, which is far from being understood. Phase diagrams can generally correlate composition and temperature with microstructure and then offer some clues about material properties. However, since phase diagrams usually depict phases at thermodynamic equilibrium, a condition not met in most conventional artificial ageing processes, the phase constituents of an aged alloy cannot be anticipated based on an equilibrium phase diagram. Diagrams describing kinetic information have been developed to describe the change of microstructure with temperature and time, e.g., Continuous Cooling Transformation (CCT) Diagrams for steels. This kind of information is highly helpful in industries but is limited to specific well-known alloys. Once the composition of an alloy changes, new experiments are needed to build a new relationship between processing parameters with microstructure or phase constituents. Therefore, designing new alloys and processing strategies are time-consuming and expensive.

With increasing stringent regulation on carbon emission and fuel economy, light-weight alloys are likely to find greater applications in automotive and aerospace industries. Therefore, designing new light-weight alloys and new processing strategies is urgent. Aluminium alloys are commonly used in these applications to replace ferrous alloys and achieve lower weights for the same strength. Therefore, designing new Al alloys and new processing strategies of Al alloys tend to be industrially driven. However, iterative improvement based on trials and errors

is too slow and too expensive to fulfil industrial requirements. To overcome this problem, a fundamental understanding of the mechanisms of solid-state phase transformations in Al alloys is necessary, which is the basis of designing new alloys in more efficient ways. More specifically, the physical rules that govern the nucleation and growth of nanoscale precipitates in Al alloys need to be explored at the atomic level. Such studies will allow us to design new alloys and processing strategies based on a database (e.g., [1]) and then verify the design by a few experiments. Undoubtedly, such an advance will accelerate the discovery and deployment of light-weight alloys as that envisaged in the Materials Genome Initiative [2]. To understand the physical rules of nucleation and growth of precipitates in Al alloys, we need to study the process at the atomic level by both computer simulations and experimental observations.

Recent advances in computational methods, e.g., classical molecular dynamics simulations and first-principles calculations, offer the opportunity to develop an understanding of phase transformations at the atomic level and even at the electronic level [3-5]. At present, classical molecular dynamics simulations are usually run for  $<1$  ns in a supercell  $\sim 10 \times 10 \times 10$  nm<sup>3</sup>. Therefore, only displacive phase transformations, e.g., martensitic transformations which can occur without any diffusion in a very short time interval, have been investigated by molecular dynamics simulations [6, 7]. First-principles calculations based on density functional theory (DFT) give a highly accurate description of the interatomic interaction [8], thus being a good tool to explain phase transformations [9]. Unfortunately, DFT calculations are computationally expensive, rendering them not appropriate for searching local minima along the free energy surface by itself. Usually, DFT calculations are used to calculate the ground state energies of observed or hypothesized structures. By comparing the ground state energy, the most energetically favourable structure can be found if entropy is assumed not to play an important role [10, 11].

State-of-the-art aberration-corrected scanning transmission electron microscopy improves the spatial resolution to  $<0.1$  nm and in some cases can provide a more directly-interpretable description of the atomic structure. Combining with the above-mentioned DFT calculations, it has successfully explained many phenomena occurring in phase transformations of alloys [12, 13]. As will be discussed in the following, the compositions, the structures and nucleating sites of nanoscale precipitates in Al alloys are not well-understood even in many simple alloy systems. Aberration-corrected scanning transmission electron microscopy can be used to probe the nucleation and growth process of precipitates in Al alloys. Therefore, it is possible to explore the physical rules about precipitate formation at the atomic level, by using aberration-corrected scanning transmission electron microscopy (STEM) observations together with computer simulations.

This study focuses on the change of precipitation mechanism in an Al-Cu alloy upon trace microalloying, which is not well-understood at present. Since the Al-Cu binary alloy is a textbook example of precipitation hardening, such a study will also shed light on nucleation and growth mechanisms of precipitates in other Al alloys. Microalloying in Al alloys can significantly change the precipitation preference of different precipitates, such as Mg and Ag additions promoting the  $\Omega$  phase [14, 15] and Sn additions promoting the  $\theta'$  phase [16]. Characterizing the structure and the composition of the promoted precipitate is important for understanding the promoting mechanism of these microalloying elements. STEM observations together with computer simulations have uncovered that Mg and Ag additions change the structure and the composition of  $\Omega$  nucleus and change the  $\Omega$ /Al interfacial structure, as will be seen in Chapter 2. However, the mechanism by which the  $\theta'$  phase is promoted is still controversial (see Chapter 2). On one hand, this is because the structure and composition of the  $\theta'$  phase near the nucleation stage have never been fully explored. On the other hand, the microalloying additions that promote  $\theta'$  nucleation interact strongly with vacancies. By characterizing the structure and composition of  $\theta'$  precipitates using STEM observations and computer simulations, the promoted nucleation mechanism of the  $\theta'$  phase is unveiled. In addition, the elusive role of vacancies on the structure and the composition of the nuclei of  $\theta'$  precipitates is also revealed for the first time.

# Chapter 2

## Literature review

Precipitation hardening is the main strengthening method for most wrought Al alloys. Precipitates with a high number density usually result in desirable mechanical properties. There are several parameters affecting the precipitation mechanism and precipitation hardening in Al alloys, which will be reviewed in the following in details. Section 2.1 reviews the basic knowledge about precipitation in Al-Cu system and effects of microalloying additions. Section 2.2 discusses the roles of defects on precipitation. In Section 2.3, the effects of processing parameters on precipitation are surveyed, which is followed by the review about the ways to optimise mechanical properties by tuning precipitation. In the end, we raise the open questions in the field and the targeted research.

### 2.1 Precipitation in Al-Cu alloys

Al-Cu alloys are the textbook example of precipitation hardenable alloys. 2000 series Al alloys are Al-Cu based alloys, which have wide applications in the aerospace industry.

#### 2.1.1 Al-Cu binary system

##### 2.1.1.1 Precipitation sequence and crystal structures of precipitate phases

Al-Cu alloys are some of the oldest age-hardenable alloys, which trace back to the first flight of the Wright brothers in 1903 [17]. However, ageing produced precipitates were not recognised until  $\sim 30$  years later. In 1938, Guinier and Preston independently discovered single layer Cu precipitates using X-ray diffraction of Al-Cu solid solutions [18, 19]. After that, precipitates formed at the first stage of ageing in solid solutions have been usually named GP zones, regardless of compositions.

Binary Al-Cu supersaturated solid solutions at the Al-rich side of the Al-Cu phase diagram can decompose into three kinds of metastable and one kind of stable Cu-rich phases depending on the ageing time, temperature and Cu supersaturation. GP zones are single atomic layers of Cu on  $\{100\}_{\text{Al}}$  and usually form streaks on 2D X-ray diffraction patterns and electron diffraction patterns. GP zones have the highest free energy of the four Cu-rich phases [20], but usually, form at the first stage of low-temperature ageing. This is because GP zones and its

successor,  $\theta''$  (multilayer Cu separated by 3 Al layers, Fig. 2.1), are fully coherent with the Al matrix. However, since the radius of Cu atoms is smaller than Al, there is significant strain around GP zones and  $\theta''$ : the nearest Al plane collapsing towards GP zones and  $\theta''$  by  $\sim 10\%$  and the next plane moving away by a similar amount, and these kinds of oscillations vanishing near the fourth or fifth Al planes [21].

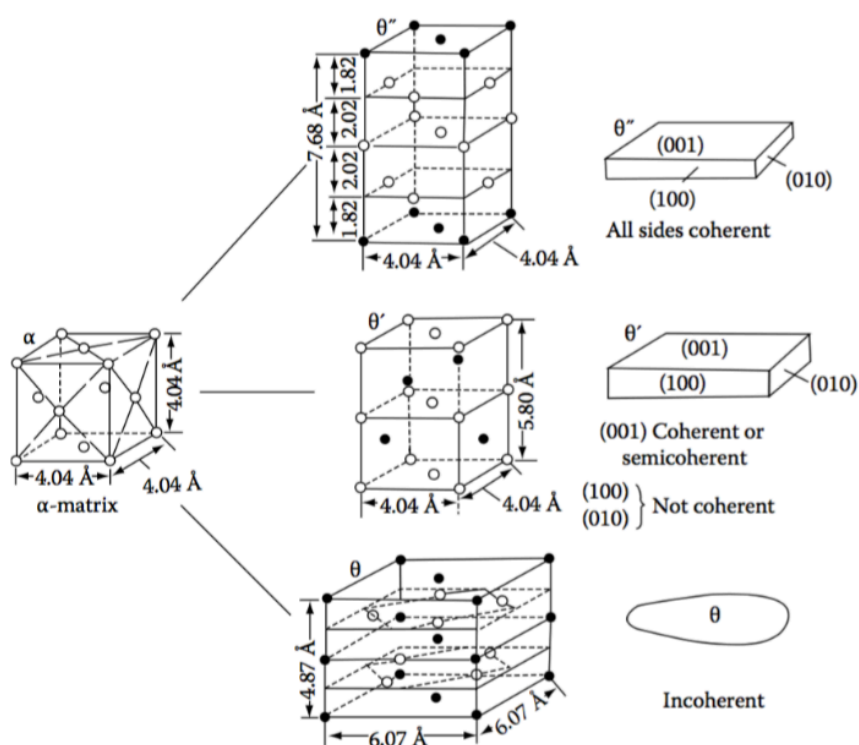


Fig. 2.1 Crystal structures and schematic morphologies of  $\theta''$ ,  $\theta'$  and  $\theta$  precipitates in Al–Cu (filled circles are Cu atoms, open circles are Al atoms). Reproduced with permission from [22].

$\theta'$  is the dominant strengthening phase at the peak ageing condition in Al–Cu binary alloy. It has a different crystal structure compared with the Al matrix, rendering it difficult to fully match the Al matrix. Therefore, there are only two coherent interfaces for one  $\theta'$  precipitate with the Al matrix. The semi-coherent interfaces of  $\theta'$  precipitates are smaller compared with the coherent interfaces and are usually curved or stepped. Since there is a significant mismatch between  $\theta'$  and the Al matrix at the semi-coherent interfaces, solute atoms that can reduce the interfacial energy usually segregate here, as will be reviewed in Section 2.2.2.2. Until now, it is still a mystery how a  $\theta'$  precipitate nucleates. Even though GP zones and  $\theta''$  precipitates nucleate from the Al matrix with ease and tend to form before  $\theta'$  precipitates, especially at low ageing temperatures, they seem to have no positive/negative effects on the nucleation of  $\theta'$  precipitates. There are no solid experimental observations showing the direct transformation from  $\theta''$  to  $\theta'$ . Sometimes, in-situ TEM observations show the formation of a  $\theta'$  precipitate from

a  $\theta''$  precipitate, which may suggest the heterogeneous nucleation of  $\theta'$  from  $\theta''$  [23]. Nevertheless, this phenomenon only occurs in a thin sample ( $\sim 50$  nm) and never in bulk samples. Post mortem TEM observations for bulk samples always show the nucleation of  $\theta'$  precipitates from defects, e.g., dislocation loops, which is usually away from  $\theta''$  precipitates.

$\theta$  is the stable Cu-rich phase that forms in the Al-Cu solid solution [22]. It shares the same composition as  $\theta'$ ,  $\text{Al}_2\text{Cu}$ . However, the crystal structure of  $\theta$  is different from that of  $\theta'$ , as shown in Fig. 2.1.  $\theta$  precipitates form incoherent interfaces with the Al matrix. The large misfit at the  $\theta/\text{Al}$  interfaces means a high interfacial energy and a high nucleation activation energy barrier. Consequently,  $\theta$  is the last phase that can form during ageing. In the literature, the precipitation sequence of Al-Cu supersaturated solid solutions is expressed as: GP zones  $\rightarrow \theta'' \rightarrow \theta' \rightarrow \theta$ . At first glance, this is a good example of multi-step nucleation where nucleation occurs step by step, and Gibbs free energy is reduced step by step. Multi-step nucleation is a kinetically efficient pathway because it gives a lower activation energy barrier of nucleation at every step, as widely observed in liquids and solids [24, 25]. However, here only  $\theta''$  precipitates do nucleate from GP zones, which is consistent with the definition of multi-step nucleation. As mentioned above, there is no evidence that  $\theta'$  precipitates nucleate directly from  $\theta''$  precipitates.  $\theta$  precipitates usually form at grain boundaries and sometimes from the  $\theta'/\text{Al}$  interfaces. This sequence only suggests their relative occurrence in the ageing process, not the transformation pathway. The growth of  $\theta$  precipitates depletes  $\theta'$  precipitates, but this is achieved by the drain of Cu atoms and shrinkage of  $\theta'$  precipitates [22]. The precedent phase generally has no beneficial effects on the later phase, sometimes, even has negative effects. For example, as mentioned above, the formation of GP zones and  $\theta''$  precipitates appear to have no beneficial roles in  $\theta'$  precipitates. The formation of GP zones in Al-Mg-Si alloy even reduces the nucleation frequency of the late precipitates and is deleterious to the peak aged mechanical properties [26]. It is still an open question: how to eliminate the harmful natural ageing effect in Al-Mg-Si alloys because it is impossible to avoid natural ageing when this alloy is used as car body sheets.

### 2.1.1.2 $\theta'/\text{Al}$ interfacial structure

Recent high-resolution scanning transmission electron microscopy images indicate that both the coherent and semi-coherent interfaces between  $\theta'$  precipitates and the Al matrix are more complex than the sharp interfaces that were conceived before. At early stage ageing ( $< 24$  h at  $200^\circ\text{C}$ ), there is significant enrichment of Cu at the coherent interface for thinner  $\theta'$  precipitates, exhibiting a GP-zone like interface (Fig. 2.2) [27]. However, this kind of Cu interstitial occupancy becomes rare for thicker  $\theta'$  plates. Intuitively, the GP zone-like interface

can be regarded to have a lower interfacial energy (and strain energy) compared with the direct  $\theta'$ /matrix interface. Thus it can make  $\theta'$  plates have a lower free energy. As interfacial energy takes a higher proportion of the total free energy for a smaller particle compared with a bigger particle, a lower energy interface can be expected at the initial growth stage. This is also corroborated by DFT calculations that imply interfacial segregation of solute Cu is energetically favourable, but ultimately less so than incorporation of Cu atoms into a new unit of  $\theta'$  through thickening [27].

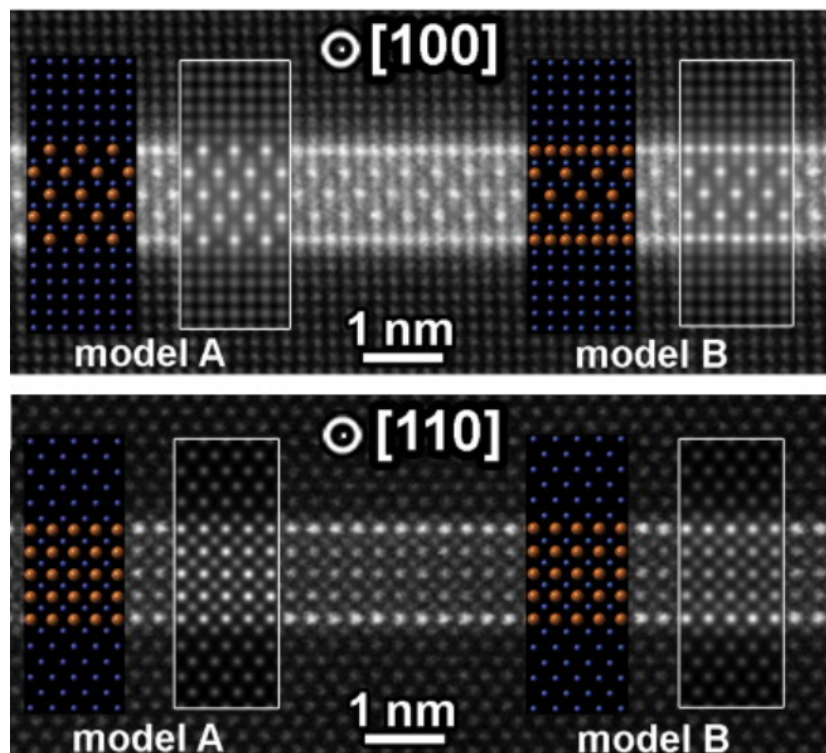


*Fig. 2.2 Experimental HAADF-STEM images with overlaid atomic models and simulated images for the bulk and GP-zone-like interfacial structure of the  $\theta'$ /Al interface. Reproduced with permission from [27].*

The semi-coherent interface between  $\theta'$  precipitates and the Al matrix also exhibits a structure reminiscent of GP zones (more precisely,  $\theta''$ ) at the early stages of ageing as shown in Fig. 2.3 [28]. DFT calculations indicate the intermediate interface increases interfacial energy, which seems counterintuitive (see Fig. 2.3 (a)). This complex interface may be kinetically favourable as it may enable some concerted atom motions to decompose into several single atomic movements with much lower activation energy barriers. This excellently rationalises the more rapid lengthening of  $\theta'$  precipitates at early ageing stages compared with modelling based on the sharp interface with no additional structures. Besides, the absence of the diffuse interface at the late ageing stages at a high temperature (e.g., 350 °C) also confirms

this is a kinetic related process preferred at low temperatures where diffusion is more difficult [10]. However, there are still many mysteries: when does this interfacial structure develop, during nucleation or growth, and how do other solutes affect this? Recent phase-field modelling of the growth of  $\theta'$  precipitates suggests the simulated aspect ratio based on the sharp interface is ten times smaller than experimental observation [29]. This further emphasises the importance of a unique interfacial structure on growth kinetics.

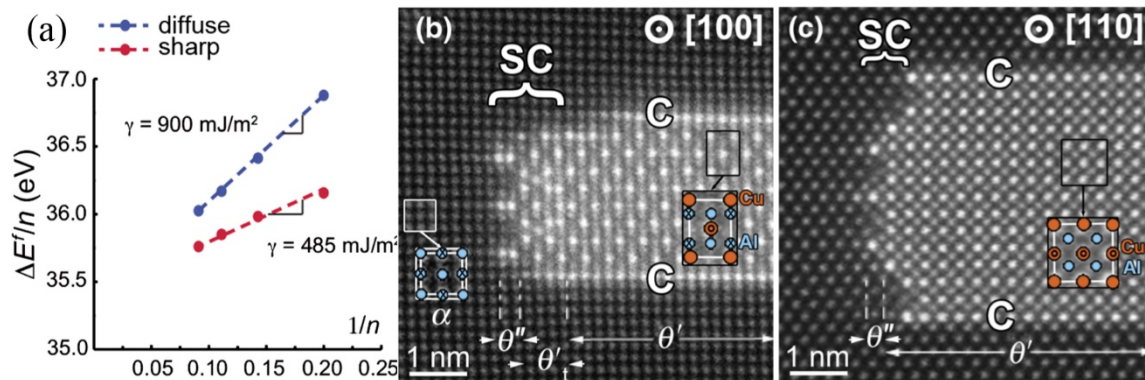


Fig. 2.3 Complex at the semi-coherent  $\theta'$ /Al interface. (a) Interfacial energies, (b) and (c) HAADF-STEM images of the diffuse interface. Reproduced with permission from [28].

## 2.1.2 Trace solute additions enhancing precipitation

About 70 years ago, minor additions of Sn, In and Cd ( $\sim 0.02$  at%) were found to dramatically accelerate precipitation kinetics and increase peak hardness in Al-Cu alloys [30, 31]. These elements cannot form intermetallic compounds with Cu/Al during ageing, and all have a very low solid solubility in the Al matrix. During artificial ageing, their crystalline phases nucleate directly from the Al matrix. For Sn and Cd, the most stable precipitate phases are beta-tin and hexagonal closed packed Cd, respectively [32]. In contrast, face-centred cubic In forms from the Al matrix, instead of the most stable state of bulk In with a body-centred tetragonal structure [32]. Trace additions of Sn have also been used in power metallurgy Al alloys, where the main role of the additions was aiding sintering instead of enhancing precipitation [33].

### 2.1.2.1 Binding with vacancies

There are mainly two rationales for the beneficial effects of trace solute additions on the precipitation of Al-Cu alloys. In the 1950s, it was impossible to get an atomic level observation. The critical role of trace solute additions was explained based on the precipitation kinetics: the presence of these microalloying elements was found to suppress the formation of GP zones during room temperature ageing, which was imputed to the trapping of vacancies by these

elements [34-36]. Electrical resistivity and calorimetric measurements suggest the formation kinetics of GP zones depend on the vacancy concentration in the Al matrix [37].

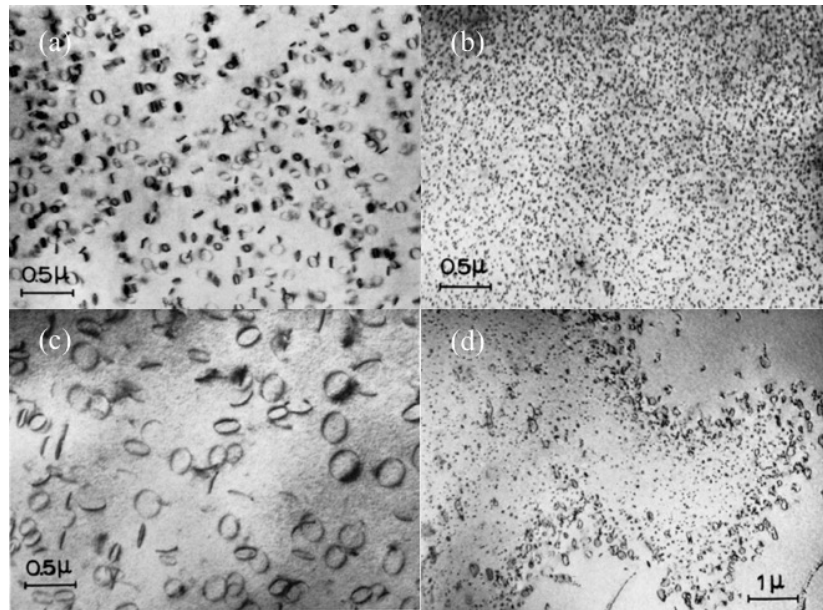


*Fig. 2.4 Dislocation densities in (a) Al-1.7at.% Cu electropolished at -20 °C after quenching, (b) Al-1.7at.% Cu-0.02at.% Cd electropolished at -20 °C after quenching, (c) Al-1.7at.% Cu electropolished at 70 °C, (d), Al-1.7at.% Cu-0.02at.% Cd electropolished at 70 °C. Reproduced with permission from [38].*

Fig. 2.4 shows the comparison of dislocation densities in an Al-Cu binary and an Al-Cu-Cd ternary alloy after quenching [38]. The binary alloy has a lower dislocation density but much bigger dislocation loops, while the ternary alloy has much smaller dislocation loops. A high temperature exposure extends the size of dislocation loops in these two alloys, but the dislocation loops in the binary alloy extend more than that in the ternary alloy. Dislocations are vacancy sinks whose growth consumes the supersaturated vacancies. However, the supersaturated vacancies in the ternary alloy are trapped by Cd atoms and cannot freely participate in the growth of a dislocation. Therefore, these elements can suppress the diffusion of Cu at low temperatures through the buffering of supersaturated vacancies. To jump in the Al lattice, Cu solute atoms in the Al matrix must jump to a vacancy first. These elements are hypothesized to trap vacancies at room temperature because of a relatively high vacancy-solute binding energy, thus suppressing GP zones formation. However, for typical artificial ageing temperatures ( $>100\text{ }^{\circ}\text{C}$ ), the binding energy is not high enough relative to the increased thermal energy. Furthermore, the supersaturated vacancies are released and increase the diffusivity of Cu. There are some drawbacks for this explanation. The first one is using vacancy-solute binding energy neglecting the presence of Cu. Even though both experiments and density

functional theory calculations (shown in the following part) suggest they have a high vacancy binding energy in binary alloys, it is unclear whether they still have high binding energy with a vacancy in a ternary alloy with Cu. This is because density functional theory (DFT) calculations suggest an element with a large radius usually has high binding energy with a vacancy [39]. Here Cu atoms are smaller than Al atoms, therefore Cu atoms may affect the binding energy of these elements with a vacancy. The second shortcoming of the above explanation is a lack of solid corroboration: probing the concentration and distribution of vacancies in the Al matrix remains very difficult. At present, only positron lifetime spectroscopy is available, but it is an indirect method and relies on a lot of assumptions and fittings.

### **2.1.2.2 Microalloying additions as heterogeneous nucleation sites for Cu-rich phases**

The second explanation for the beneficial effect of these elements is providing heterogeneous nucleation sites. Transmission electron microscopy (TEM) and atom probe tomography (APT) have been used routinely to characterise microstructural features in metals and alloys. Both TEM and APT revealed nanoscale particles of these elements at the semi-coherent  $\theta'$ /Al interface (Fig. 2.5) [16, 40]. Thus, it is hypothesized that Cu-rich phases nucleate heterogeneously from these nanoscale particles [41]. This is an intuitive speculation because enhancing heterogeneous nucleation through a lower-energy heterophase interface is a general phenomenon in natural or artificial phenomena. For example, the formation of ice crystals from clouds can be helped by K-rich feldspars particle surface [42]; additive manufacturing can be extended to alloys that have poor weldability by enhancing heterogeneous nucleation through nanoparticle inoculation [43]. Heterogeneous nucleation can also be expressed as epitaxial growth of a new phase from the all-ready existing one [44]. Therefore, the new phase should have good structural matching with the existing one at the atomic level. Usually, we express the structural matching by their crystallographic orientation. Moreover, there is usually a unique crystallographic orientation relationship (OR) between the two phases. However, the crystallographic orientation between Cu-rich phases and nanoscale particles of these elements is variable. In the Al-Cu-Sn alloy, even though TEM observations suggest possible heterogeneous nucleation of  $\theta'$  precipitates from Sn particles, Sn particles show different OR with  $\theta'$  precipitates and the Al matrix [45]. It is more likely suggesting the reverse, namely that nucleation of Sn particles from  $\theta'$  precipitates. Early observations have never distinguished which phase nucleates first from the Al matrix. If it is a  $\theta'$  precipitate that nucleates first and then an Sn particle forms at the semi-coherent  $\theta'$ /Al interface, the observation is not heterogeneous nucleation of a  $\theta'$  precipitate from a Sn particle. Therefore, it is still desirable to

look at the very early stage of precipitation of Al-Cu alloys with the above elements, to find which phase forms first and how it nucleates.

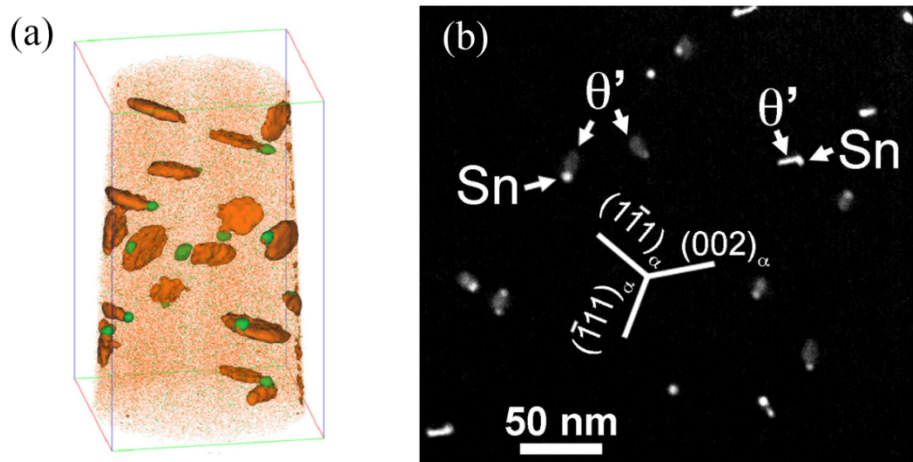


Fig. 2.5 APT and annular dark field STEM (ADF-STEM) observations showing Sn particles at the semi-coherent  $\theta'$ /Al interface. Green particles are Sn particles, and orange particles are  $\theta'$  precipitates. Reproduced with permission from [40, 46].

### 2.1.2.3 New players: Au and Ge

The beneficial roles of Au and Ge additions on the precipitation behaviour of Al-Cu alloys have only been explored in the past two decades [47, 48]. This is partly because they are too expensive to be used as alloying elements and may have limited the exploration of their effects in Al-Cu alloys to date. Au also has a high vacancy binding energy and low solid solubility in the Al matrix. It was once hypothesized to bind with vacancies and suppress the diffusion of Cu at low temperatures. The interaction between Au and vacancies were investigated by positron annihilation spectroscopy and X-ray absorption spectroscopy and verified the important role of vacancies in natural ageing [47]. Recently, advanced aberration-corrected scanning transmission electron microscopy characterisation suggests Au atoms partition into  $\theta'$  precipitates and reduce the nucleation energy barrier of  $\theta'$  precipitates [49]. The segregation of Au into  $\theta'$  precipitates is conceivable because Au forms a similar precipitate regarding crystal structure as the  $\theta'$  phase in the Al matrix [50].

Ge is slightly different from the above-discussed elements because it has a high vacancy binding energy but a high solid solubility in the Al matrix. Its solid solubility at 420 °C is up to 2 at.% and reduces to  $\sim 0$  at room temperature. However, Al-Ge binary alloys show very weak precipitation hardening because the density of Ge precipitates is low [51], which can be increased remarkably by further Si additions [52]. Therefore, combined additions of Ge and Si in Al-Cu alloys were investigated. The precipitates in Al-Si-Ge alloys are a mixture of Si and

Ge elements and adopt a diamond structure [48], which produces a compressive strain in the surrounding Al matrix. The strain field may cancel the transformation strain that will be induced by  $\theta'$  precipitates, therefore enhancing the heterogeneous nucleation of  $\theta'$  precipitates [48, 53].

### 2.1.3 Solute additions changing precipitate phase

#### 2.1.3.1 Mg and Ag

Mg, Li and Zn are the elements that are added in significant amounts into Al-Cu alloys and form new alloy systems with new precipitation characteristics. Mg can be added from 0.1 at.% to 2 at.%, and only large additions can result in new precipitate phases. Fig. 2.6 shows the aluminium-rich corner of the Al-Cu-Mg phase diagram indicating the phases present as a function of composition. In Al-Cu-Mg alloys with a low Mg-Cu ratio, the precipitation sequence is the same as that of Al-Cu binary alloys. Mg additions lower than 0.5 at.% shows no observable changes during ageing relative to Al-Cu (Cu 1-2at.%) binary alloys, except for the rare occurrence of the  $\Omega$  ( $\text{Al}_2\text{Cu}$ ) phase.

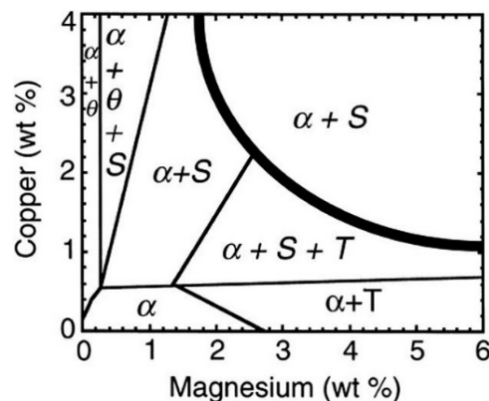


Fig. 2.6 Aluminium-rich corner of the Al-Cu-Mg phase diagram indicating the present phases after long term ageing at 190 °C. Reproduced with permission from [54].

Significant amounts additions of Mg ( $2 > \text{Mg}/\text{Cu} > 0.5$ ) into Al-Cu (Cu, 1-2 at.%) alloys produces a different precipitation sequence. At the early stage of ageing, the hardness increases rapidly within about 60 s, which usually accounts for 70% of the overall hardness increment to peak hardness [55]. Co-clusters of Cu and Mg of about 3-20 atoms are believed to form in this stage, followed by the formation of GPB zones, the  $S'$  phase and finally the S phase [56]. However, a long hardness plateau is observed in Al-Cu-Mg alloys with high Mg additions (see Fig. 2.7), which may mean the transformation from the precipitate phase (GPB zones) at the plateau to the precipitate phases ( $S'$  and S) after the plateau is difficult.

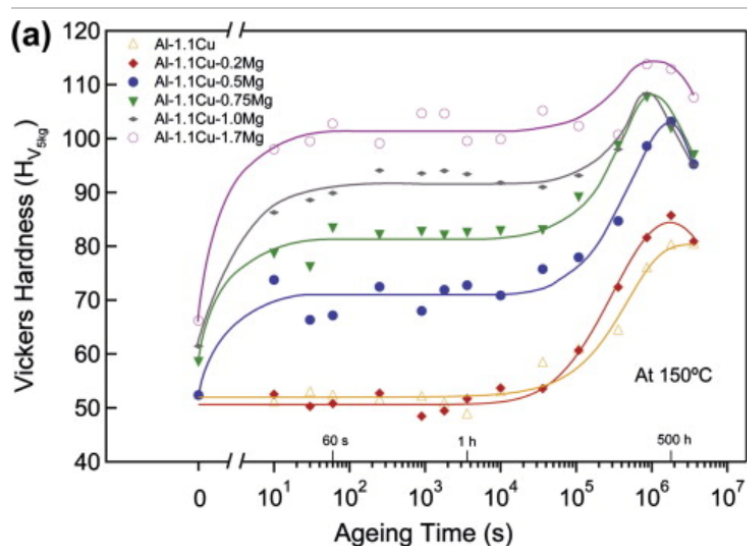


Fig. 2.7 Hardness curves for Al-1.1Cu- $x$ Mg (where  $x=0, 0.2, 0.5, 0.75, 1.0, 1.7$  at.%) aged at 150 °C. Reproduced with permission from [55].

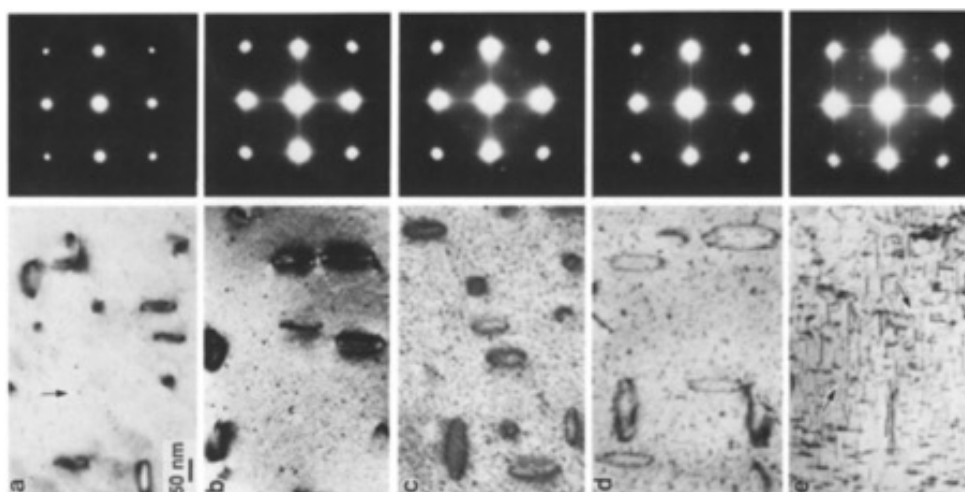


Fig. 2.8 Bright field transmission electron micrographs and corresponding selected area electron diffraction patterns (the top row), showing the evolution of microstructure in the ternary Al-1.7Cu-0.3Mg (at.%) alloy aged at 180 °C for (a) 15 s; (b) 30 s; (c) 120 s; (d) 720 s; (e) 9000 s. The electron beam is parallel to  $\langle 001 \rangle_{Al}$ . Reproduced with permission from [55].

Since Mg has a negligible binding energy with vacancies, it hardly changes the presence of supersaturated vacancies after quenching from high temperature. The supersaturated vacancies in the Al matrix are not stable and tend to diffuse to vacancy sinks. The rapid growth of dislocation loops as shown in Fig. 2.8 suggests the abundance of supersaturated vacancies in quenched state and the rapid diffusion kinetics at artificial ageing temperature. Reducing the artificial ageing temperature from 180 °C to 150 °C extends the growth interval of a dislocation loop to more than 1 h [55]. The diffusion coefficient of vacancy/self-diffusion coefficient of Al at equilibrium vacancy concentration can be expressed as:  $D=D_0\exp(-Q/K_bT)$ , where

$Q=1.25\sim 1.48$  eV [57]. Some positron annihilation spectroscopy studies suggest the vital role of vacancies on precipitation kinetics [58]. Vacancies are believed to co-cluster with Mg and Cu atoms in Al-Cu-Mg alloys [55, 59].

The combined additions of Mg and Ag in small concentrations to Al-Cu (Cu, 1-2 at.%) alloys promote the precipitation of a new phase, named  $\Omega$  ( $\text{Al}_2\text{Cu}$ ), at the expense of  $\theta'$ . The  $\Omega$  phase forms plates on the  $\{111\}_{\text{Al}}$  planes, which results in a good creep resistance of Al-Cu-Mg-Ag alloys.  $\Omega$  precipitates are also present in Al-Cu-Mg ternary alloys but are sparse [60]. However, They are never observed in Al-Cu-Ag ternary alloys [61]. Here both Mg and Ag are at lower concentrations, usually  $< 0.3\text{at.}\%$ . Moreover, neither Mg nor Ag partitions into the interior of  $\Omega$  precipitates but segregates at the coherent  $\Omega/\text{Al}$  interface. The DFT calculated formation energy of  $\Omega$  (-0.15 eV/atom) is higher than  $\theta'$  (-0.19 eV/atom), which means  $\Omega$  is less energetically favourable than  $\theta'$  [62].

Characterization of the early stages of ageing in Al-Cu( $\sim 1.9$ )-Mg( $\sim 0.3$ )-Ag( $\sim 0.2$  at.%) using atom probe field ion microscopy indicates that Ag and Mg co-clusters exist together with Cu-clusters. Thus, it has been proposed that Ag can trap Mg atoms and form co-clusters which can serve as precursors for  $\Omega$  precipitates [15]. Detailed investigations on the evolution of the Ag-Mg co-clusters show that ill-shaped clusters will begin to align on the  $(111)_{\text{Al}}$  planes after 120 s ageing at 180 °C and transform into the  $\Omega$  structure after 2 min [15]. This seems to conflict with the absence of Mg and Ag in the interior of  $\Omega$  precipitates, but not. In the well-defined  $\Omega$  phase, Ag and Mg atoms are strongly segregated at the coherent  $\Omega/\text{Al}$  interface. No Mg and Ag atoms are incorporated within the platelet, and the chemical composition of  $\Omega$  is Al-33 at.% Cu [26]. Scanning transmission electron microscopy (STEM) Z-contrast images show that a remarkably stable double-layered interface covers  $\Omega$  precipitates (see Fig. 2.9), and the interface is composed of Ag and Mg atoms [63]. Therefore, the APT probed Ag-Mg co-clusters aligning on the  $(111)_{\text{Al}}$  planes provide nucleation sites for  $\Omega$  precipitates and separate  $\Omega$  precipitates from the Al matrix. The coverage of  $\Omega$  precipitates by Ag-Mg co-clusters/segregation reduces the interfacial energy of  $\Omega$  precipitates and restricts the thickening of  $\Omega$  precipitates. Even though the formation energy of  $\Omega$  is higher than  $\theta'$ , the lower interfacial energy may compensate it and favour the nucleation of  $\Omega$ .

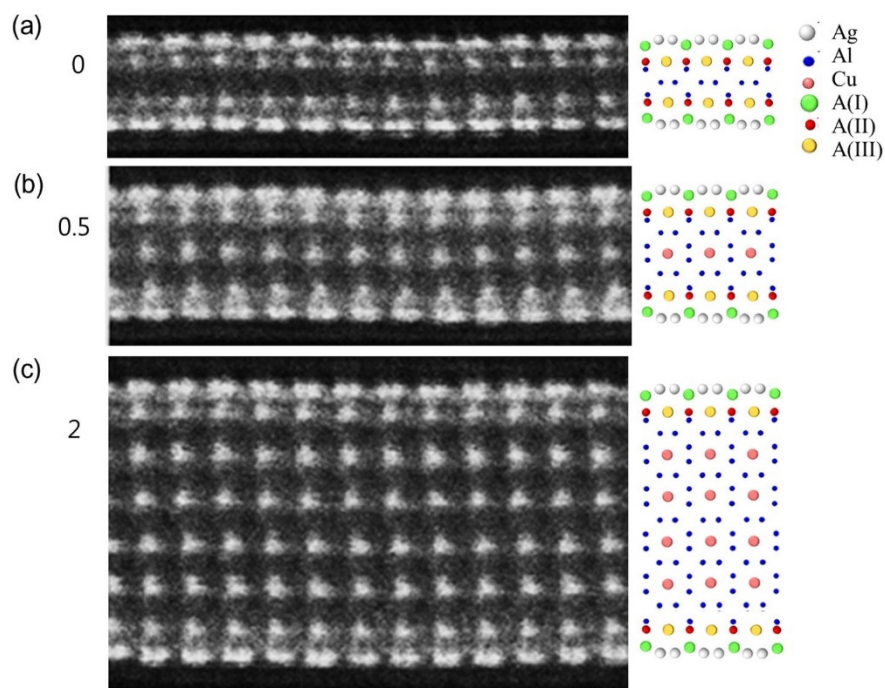


Fig. 2.9 HAADF-STEM images showing the interfacial structures and corresponding atomic models for  $\Omega$  precipitates with different thicknesses in an Al-Cu-Mg-Ag alloy. Reproduced with permission from [63].

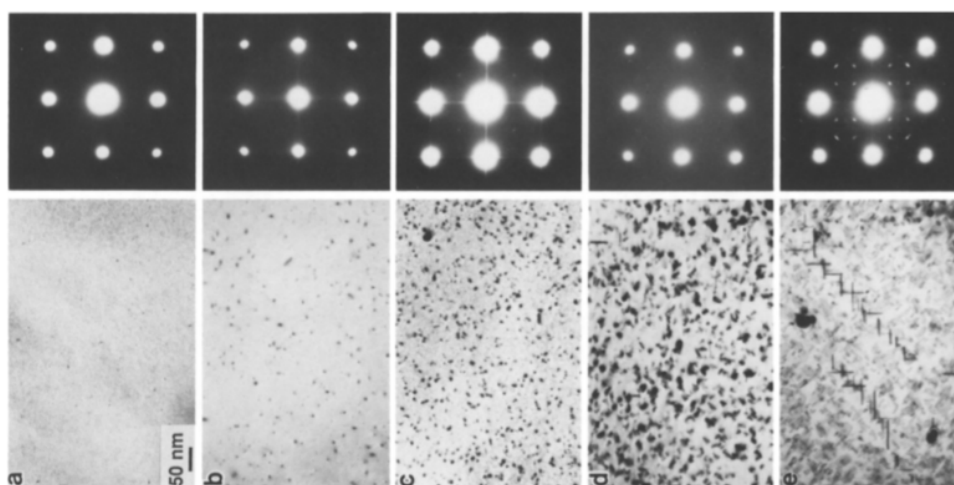


Fig. 2.10 Bright field transmission electron micrographs and corresponding selected area electron diffraction patterns (the top row), showing the evolution of microstructure in a quaternary Al-Cu-Mg-Ag alloy aged at 180 °C for (a) 15 s; (b) 30 s; (c) 120 s; (d) 720 s, and (e) 9000s. The electron beam is near  $\langle 001 \rangle_{Al}$ . Reproduced with permission from [14].

The clustering of Mg and Ag is important for the subsequent formation of a nucleation template aligned on  $\{111\}_{Al}$ , which is also critical for  $\Omega$  to surpass  $\theta'$  regarding total free energy. As discussed above, both Ag and Mg have a very lower vacancy binding energy. However, the combined additions of Ag and Mg significantly suppress the formation of dislocation loops compared with a ternary alloy, as shown in Fig. 2.10 [14]. This implies the clustering of Mg

and Ag during quenching also forms traps for supersaturated vacancies. In other words, the Mg-Ag co-clusters trap vacancies, and the binding energy between co-clusters of elements and vacancies can deviate significantly from the single element case.

### 2.1.3.2 Li

Li is the lightest metal element, and its addition into Al-Cu alloys is attractive for aerospace applications. The most important precipitate phases in the Al-Cu-Li ternary alloy system are the  $T_1$  phase ( $\text{Al}_2\text{CuLi}$ ) and the  $\delta'$  phase ( $\text{Al}_3\text{Li}$ ). Other precipitates, e.g.,  $T_2$ ,  $\theta'$  and TB also form as minor precipitates [64, 65]. The Li content has an important effect on the precipitation sequence. In the high Li content alloy (2196, 1.4-2.1 wt.% Li), the  $\delta'$  phase is present throughout the precipitation sequence, forming after room temperature ageing and coarsening during artificial ageing [65]. In alloys that are lean in Li (2198, 0.8-1.1 wt.% Li), Cu-rich clusters replace the  $\delta'$  phase after natural ageing.  $T_1$  is the dominant strengthening phase in Al-Cu-Li alloys, forming as platelets on the  $\{111\}$  planes of the Al matrix, with plate thickness constantly  $\sim 1.3$  nm unless significantly over-aged; this is much thinner than other precipitates discussed in this study [66].  $T_1$  precipitates can extend up to 100 nm in length on  $\{111\}_{\text{Al}}$  and still retain coherency. Fig. 2.11 shows the atomic structure of  $T_1$  precipitates as recently determined.

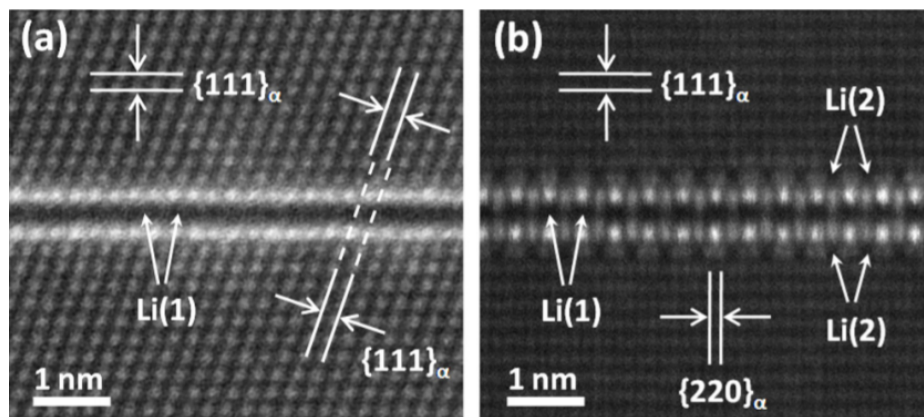


Fig. 2.11 Atomic-resolution HAADF-STEM images of embedded  $T_1$  precipitates, (a) and (b) are images along the  $\langle 110 \rangle_{\text{Al}}$  and  $\langle 112 \rangle_{\text{Al}}$  orientations, respectively. Reproduced with permission from [67].

The combined minor additions of Mg and Ag are also beneficial for the nucleation of  $T_1$  in Al-Cu-Li alloys [68]. Despite the high coherency of  $T_1$  precipitates with the Al matrix, homogeneous nucleation is remarkably difficult for  $T_1$  precipitates. Precipitation of the  $T_1$  phase on the  $\{111\}_{\text{Al}}$  planes is proposed to need one or more partial dislocations bounded by a stacking fault [69]. However, the stacking fault energy of Al is very high ( $\sim 150$  mJ/m<sup>2</sup>), and

the dissociation of dislocations into partials is believed to be necessary to nucleate the  $T_1$  phase. Ag and Mg may reduce the stacking fault energy of Al and are found to be effective in enhancing  $T_1$  nucleation [70]. APT results suggest Mg and Ag segregate to dislocations and the  $T_1$ /Al interface at all ageing times, including the earliest stages [64], which is also verified by scanning transmission electron microscopy observations [71]. The interfacial segregation may occur before  $T_1$  nucleation as for the  $\Omega$  phase in Al-Cu-Mg-Ag alloys. However, if the segregation occurs during the growth of  $T_1$ , as the segregation of Ag around  $\theta'$  precipitates in Al-Cu-Ag alloys [72], it will not affect the nucleation of  $T_1$  precipitates. Further work is desirable to understand the roles of Mg and Ag additions at the atomic level using HAADF-STEM imaging, which can confirm recent reports using small-angle X-ray scattering [73-75].

### **2.1.3.3 Zn**

Zn is usually added into Al-Cu alloys together with Mg at a concentration higher than Cu, forming the Al-Zn-Mg-Cu alloy system. The resulting alloys display the highest strength after proper heat treatment among Al hardenable alloys. The main strengthening phase is  $\eta'$  that is mainly composed of Zn and Mg, not Cu [76]. Here the interesting thing is that  $\eta'$  precipitates mainly transform from small GPI zones [77]. Since this system is not strengthened by Cu-rich phases, it will not be discussed in detail.

## **2.2 Roles of lattice defects in precipitation**

Since precipitates form in the lattice of the Al matrix, the defects in the Al matrix play critical roles in the formation of precipitates. In the following, the roles of vacancies, dislocations, twin/grain boundaries in precipitation will be discussed.

### **2.2.1 Vacancies**

#### **2.2.1.1 Vacancy controlled diffusion and measurement of equilibrium vacancy concentration**

Diffusion of impurities is usually assisted by point defects in most metals, especially for the solute atoms in the Al matrix. A substitutional solute atom rarely diffuses in the Al matrix by direct exchanging its position with neighbours. More commonly, a solute atom jumps into a vacancy on a neighbouring site. The diffusion of a solute atom then is determined by two processes: vacancy formation and vacancy-atom exchange. At finite temperature, vacancy formation can reduce the free energy of the system, and this sets the equilibrium vacancy concentration of the Al matrix. The equilibrium vacancy concentration can be measured experimentally and can also be calculated using first-principles calculations. In experiments, the difference between linear thermal expansion and lattice expansion is used to get the

equilibrium vacancy concentration at a given temperature [78, 79]. The difference is the net added fraction of thermally-generated atomic sites,  $3(\Delta L/L - \Delta a/a)$ . The net added atomic sites relative to 0 K is the equilibrium vacancy at a given temperature. Lattice expansion can be measured by X-ray diffraction with high accuracy. The equilibrium vacancy concentration  $C_v$  in aluminium at a given temperature T is  $C_v = \exp\left(\frac{\Delta S_f}{k_b T}\right) \exp\left(\frac{-\Delta H_f}{k_b T}\right)$ , where  $\Delta H_f$  and  $\Delta S_f$  are the enthalpy and vibrational entropy of vacancy formation. The theoretical calculation of equilibrium vacancy concentration is then the calculation of the thermodynamic parameters by first-principles calculations. Equilibrium vacancy concentration from first-principles calculations (Local-density approximations, LDA and generalized gradient approximations, GGA quasiharmonic calculations) are plotted in comparison with experimental data in Fig. 2.12 [57]. The equilibrium vacancy concentration at the solid solutionising temperature ( $\sim 500$  °C) is  $\sim 10^{-4}$ , which is much higher than the equilibrium vacancy concentration at an artificial ageing temperature (i.e., 100-250 °C),  $\sim 10^{-7}$ .

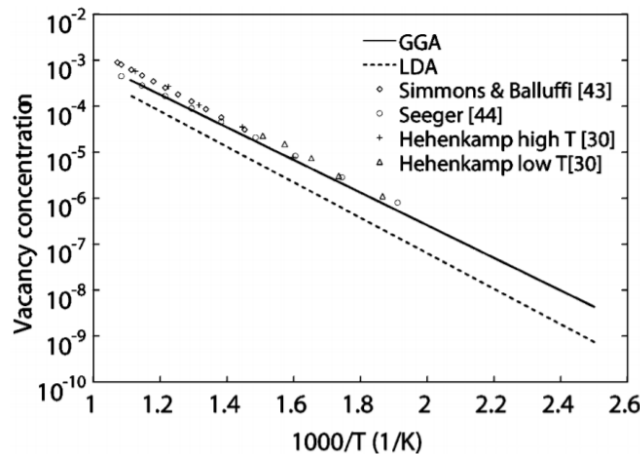


Fig. 2.12 Equilibrium vacancy concentration from first-principles calculations (LDA and GGA quasiharmonic calculations) are plotted in comparison with experimental data. Reproduced with permission from [57]. The references in the figure are from the original paper.

### 2.2.1.2 Interaction between vacancies and solute atoms

The presence of solutes alters the thermodynamics of an alloy and changes the equilibrium vacancy concentration. Assuming there are only isolated monovacancies, isolated solute atoms, and nearest neighbour vacancy-solute pairs, the equilibrium vacancy concentration can be expressed as:  $C_v = C_{v0} \left(1 - 12c_s + 12c_s \exp\left(\frac{-S_{vib}}{k_b T}\right) \exp\left(\frac{-E_b}{k_b T}\right)\right)$ , where  $C_{v0}$  is the equilibrium vacancy concentration without solute presence,  $c_s$  is the solute concentration,  $E_b$

is the vacancy-solute binding energy, and  $S_{vib}$  is the vibrational binding entropy [80, 81]. In most cases,  $S_{vib}$  is assumed to be zero [78]. There are only two variables left,  $C_v$  and  $E_b$ , to describe an alloy system. The vacancy concentration can be measured by  $C_v - C_{v0} = 3 \left( \frac{\Delta L'}{L'} - \frac{\Delta L}{L} \right) - 3 \left( \frac{\Delta a'}{a'} - \frac{\Delta a}{a} \right)$ . The characters with up superscript are for solute-containing Al alloys. By measuring the linear thermal expansion and lattice expansion of pure Al and Al with solutes, the equilibrium vacancy concentration in solute-containing Al can be determined, which consequently gives out the binding energy between a solute atom and a vacancy. The solute-vacancy binding energies for Ag, Mg and Cu in the Al matrix were measured in this way ( -0.08,  $\sim$ -0.01 eV and  $\sim$ 0 eV, respectively) [80-82].

*Table 2.1 Solute-vacancy binding energies from experiments and density functional theory calculations for some elements [39, 83].*

Solute	Binding energy, experiments (eV)	Binding energy, DFT (eV)
Cu	$0.0 \pm 0.1$	0.02
Mg	$-0.01 \pm 0.04$	0.02
Ag	$-0.08 \pm 0.03$	-0.07
Ge	NA	-0.13
In	NA	-0.20
Cd	NA	-0.14
Sb	NA	-0.30
Au	NA	-0.15
Sn	NA	-0.25

First-principles calculations are an alternative way to get the solute-vacancy binding energy. The solute-vacancy binding energy is the energy change of solute-vacancy pair at nearest-neighbour separation relative to that at infinite separation. In this thesis, a negative binding energy means a solute atom prefers to bind to a vacancy. The calculated and experimental solute-vacancy binding energies are summarised in Table 2.1. The good agreement between DFT calculations and experimental results suggests DFT calculations can accurately predict solute-vacancy binding energies. This is very important for some elements whose experimental

binding energies with vacancies are not available. The equilibrium vacancy concentration in an alloy can be predicted using the calculated vacancy binding energy. For an element with a negative binding energy, its presence in the Al matrix can increase the equilibrium vacancy concentration compared with that in pure Al matrix.

### 2.2.1.3 Modulating diffusion by buffering excess vacancies with unique solutes

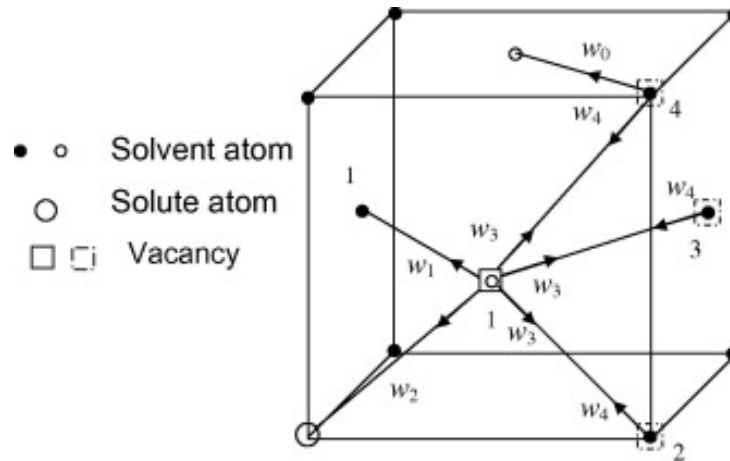


Fig. 2.13 Five frequency model illustration for the case of an fcc system with a dilute impurity concentration. The arrows indicate the direction of the vacancy jump and the numbers  $n$  stand for the  $n$ th nearest neighbouring site to the impurity. Reproduced with permission from [84].

The equilibrium vacancy concentration discussed above sets bounds for the real vacancy concentration that can affect the ageing kinetics. During quenching, the supersaturated vacancies tend to annihilate at vacancy sinks, e.g., dislocations, grain boundaries and sample surfaces. The presence of a solute with a high binding energy can trap many vacancies, thus reserve these vacancies for use at artificial ageing temperature. In the equilibrium condition, the self-diffusion of Al can be described by  $D=a^2C_v\Gamma$ , where  $a$  is the lattice parameter,  $\Gamma$  is the successful atom jump frequency, and  $C_v$  is the equilibrium vacancy concentration [57]. Excess vacancies trapped by solute atoms increase the real vacancy concentration. Solute diffusion in the Al matrix is expressed as  $D_2=D_0(f_2w_4w_1w_2/f_0w_0w_3w_1)$ , where  $D_2$  is the diffusion coefficient of the impurity atom in the host lattice,  $D_0$  is the self-diffusion coefficient of the pure host element,  $f_2$  is the correlation factor for impurity diffusion,  $f_0$  is the self-diffusion correlation factor, and  $w_j(j=0-4)$  are the five jump frequencies as illustrated in Fig. 2.13 [84]. The above discussion suggests extra vacancies trapped by solutes can increase the diffusivity of solute atoms in the Al matrix and benefit precipitation kinetics.

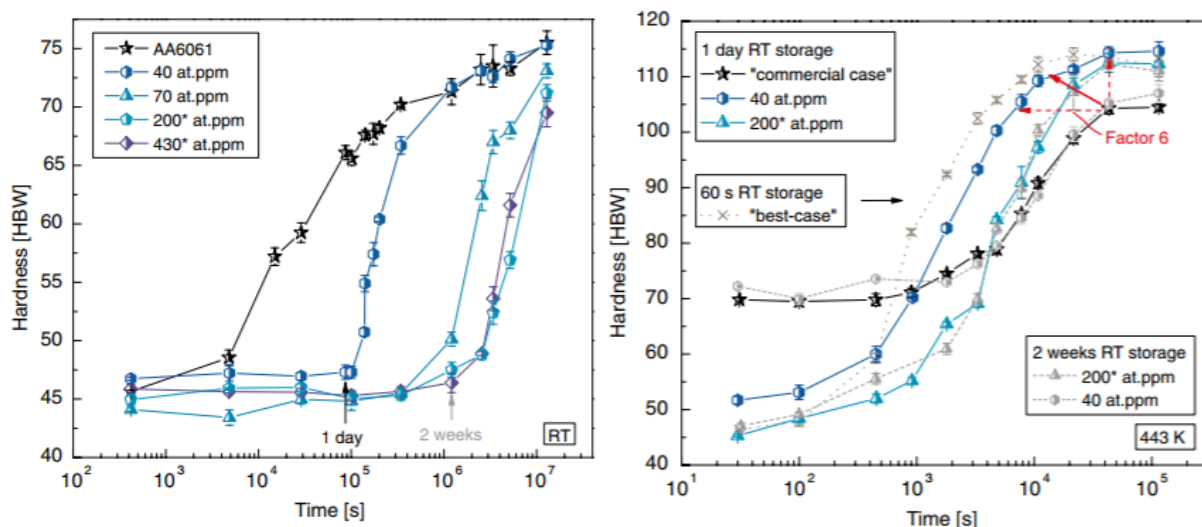


Fig. 2.14 Evolution of hardness during room temperature storage and artificial ageing after quenching for the Al-Mg-Si alloy AA6061 with and without Sn additions. Reproduced with permission from [26].

A solute species having a high solute-vacancy binding energy offers more freedom to control precipitation kinetics. Ageing temperature affects the stability of the binding between solutes and vacancies, and thus affects the diffusivity of atoms. At room temperature, these extra vacancies are bound with solute atoms tightly, thus hardly accelerating diffusion of another kind of solute. The minor additions of Sn ( $\sim 200$  ppm) into an Al-Mg-Si alloy trap the supersaturated vacancies at room temperature, which suppresses the diffusion of Mg and Si by reducing the available vacancy concentration. This delays the onset of hardness increase during natural ageing. However, at artificial ageing temperatures (typically  $170\text{ }^{\circ}\text{C}$ ), the extra vacancies are released from traps because the binding energy is not high enough. Thus, the real vacancy concentration at the ageing temperature is higher than the equilibrium vacancy concentration, consequently, accelerating the diffusion of Mg and Si. Fig. 2.14 shows the buffering effect of Sn on vacancy during room temperature and the release of extra vacancies during artificial ageing [26]. The diffusion-on-demand strategy should be widely applicable in modulating precipitation kinetics in different alloy systems [85-87].

#### 2.2.1.4 Accommodating strain

Vacancies may also affect thermodynamics by accommodating the transformation strain associated with precipitates. Indeed, the nucleation of precipitates in the Al matrix usually comes with volume change. For example, the transformation strain for Ge precipitates is positive. Therefore, vacancies are thought to enhance the nucleation of Ge precipitates [88, 89]. On the other hand, the transformation strain of  $\theta'$  precipitates can be either negative or positive

depending on precipitate thickness [53]. If so, vacancies cannot enhance  $\theta'$  nucleation by accommodating transformation strain.

Precipitates sometimes have magic shapes/sizes, which seems to rely on excess vacancies [90]. A delicate balance of edge energy (excess energy due to the formed edges), interfacial energy and strain energy determines the equilibrium shape/size of a nanoparticle [90]. A precipitate with a magic shape/size has a much higher population compared with other shapes/sizes because the magic shape/size has lower free energy compared with other possibilities. For instance,  $\theta'$  precipitates in Al-Cu alloys show magic sizes (discrete thickness, [40]) and Pb precipitates in an Al-Pb alloy show magic shape [90]. However, these precipitates are inclusions in the Al matrix and cannot grow freely unless copious vacancies are ready to accommodate the volume change of these precipitates [90, 91]. Therefore, vacancies are important to accommodate/lower the strain induced by changes in the shape/size of a precipitate.

## **2.2.2 Dislocations**

### **2.2.2.1 Solute segregation around dislocations**

Dislocations are another kind of defects that significantly affects the precipitation kinetics. Furthermore, they not only affect the diffusion kinetics but can sometimes also alter the nucleation process of precipitates. Solute atoms can interact with the stress field around a dislocation and form remarkable segregation in the vicinity of a dislocation line. Such segregation around a dislocation or in the core of a dislocation has been observed by APT and STEM in alloys [92, 93]. Fig. 2.15 shows the segregation of Mn atoms along dislocations in a Fe-Mn alloy, which takes place during annealing [94]. Cottrell atmospheres are used to describe the tiny clouds of impurity atoms around dislocations in crystals. This kind of solute segregation not only strengthens an alloy by hampering dislocation motions [95] but also can form a favourable site for the nucleation of a precipitate. A lot of Cu-rich precipitates in Al alloys are reported to nucleate near dislocations, such as the  $T_1$  phase in Al-Cu-Li alloys [64] and the  $\theta'$  phase in Al-Cu alloys. These dislocations that nucleate  $T_1$  are enriched with Ag and Mg in Al-Cu-Li-Mg-Ag alloys, which may explain the promoting mechanism of Mg and Ag on precipitation [71, 73, 74].

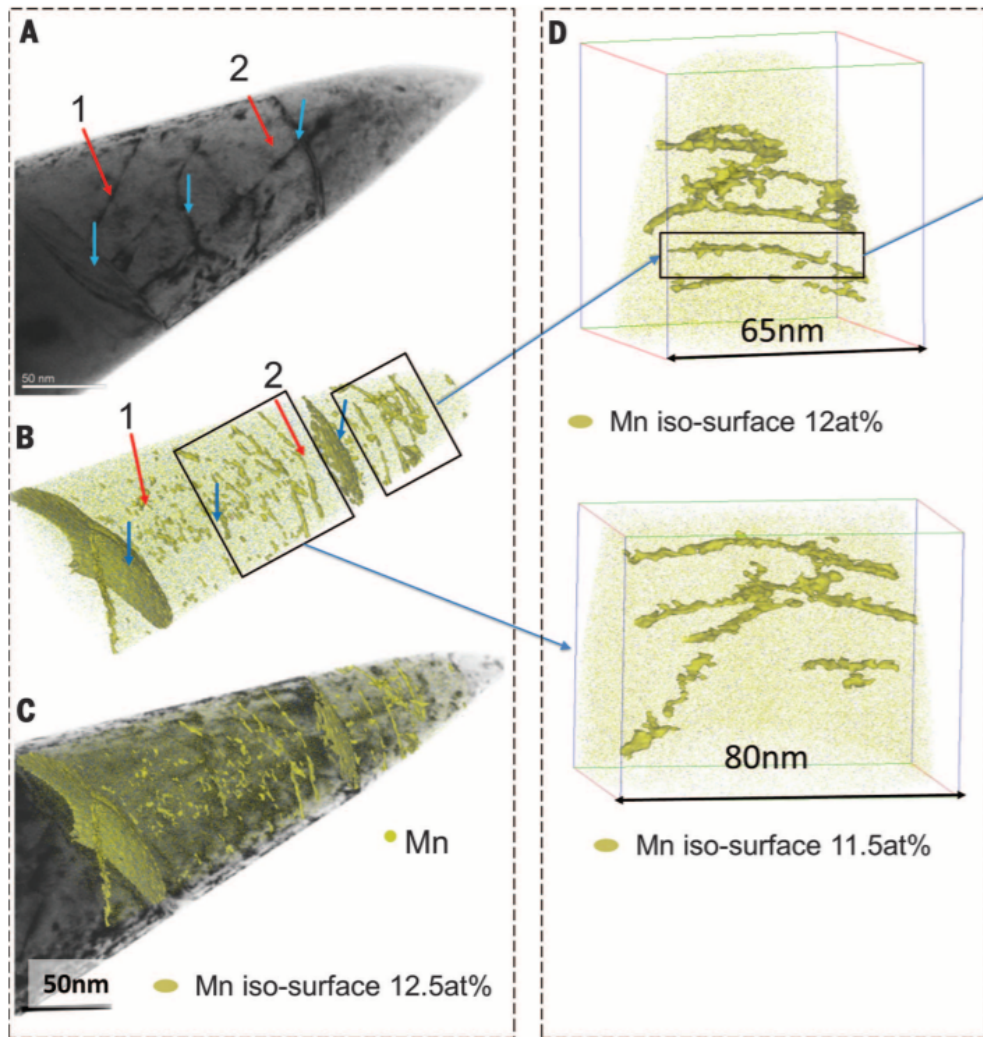


Fig. 2.15 Bright field STEM images and APT reconstructions showing the segregation of Mn atoms along dislocations in a Fe-Mn alloy. Reproduced with permission from [94].

### 2.2.2.2 Diffusion pipeline along dislocations

Dislocations can also provide a fast diffusion pipeline for solute atoms, which can accelerate precipitation kinetics. The disorder in the core region of a dislocation effectively lowers the activation energy for diffusion [96]. The diffusivity of Si in the Al matrix along dislocations was investigated and compared with vacancy-controlled diffusion in bulk, as shown in Fig. 2.16 [97]. The diffusivity is increased by three orders of magnitude along a dislocation compared with that in bulk, also, the activation energy, which indicates how easy diffusion is, is 20% lower than that for bulk diffusion. Diffusion along a dislocation pipeline was found to be important for the precipitation in ultrafine-grained Al alloys [98].

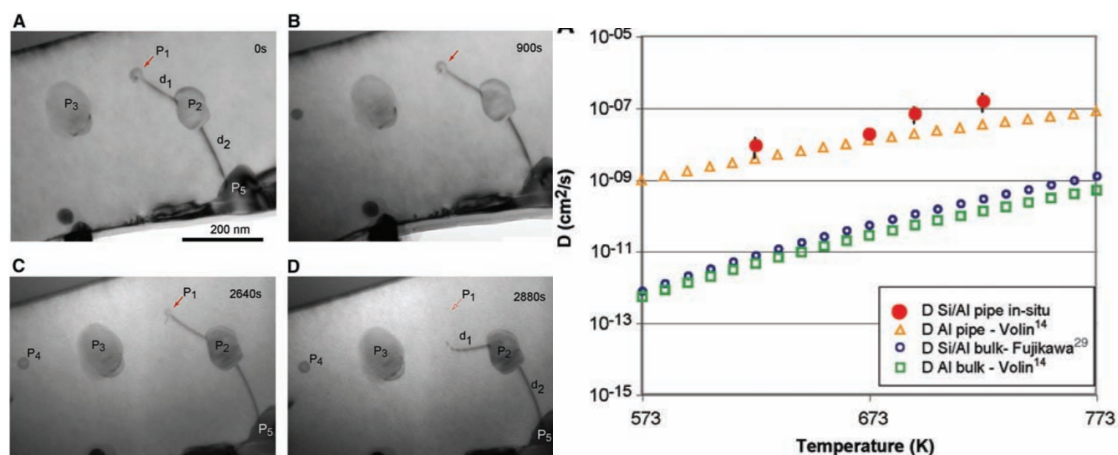


Fig. 2.16 Si diffusion along dislocations in an Al-Si alloy and the diffusion coefficients of Si for diffusion along dislocations and diffusion in the Al matrix. Reproduced with permission from [97]. The references in the figure are from the original paper.

The beneficial effect of dislocations on precipitation through the increased diffusion kinetic is shown vividly by in-situ ageing of an Al-Cu alloy in a TEM [99]. Fig. 2.17 shows snapshots of the ageing process, where the growth of a  $\theta'$  precipitate is accompanied by a moving dislocation. The dislocation connects with the  $\theta'$  precipitate at the semi-coherent  $\theta'$ /Al interface and moves together with the interface. These images are HAADF-STEM images, and the bright contrast of the dislocation segment suggests Cu segregation. The dislocation here definitely provides a fast diffusion pathway of Cu, which can support the fast growth of the  $\theta'$  precipitates.

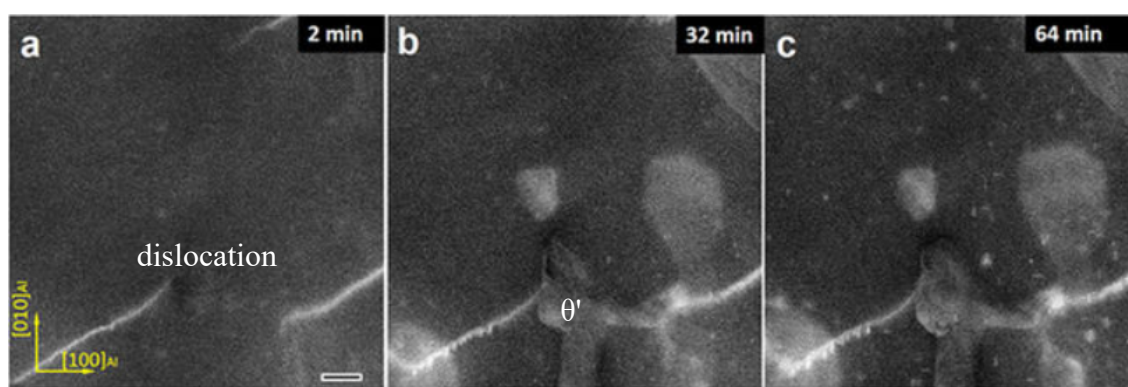


Fig. 2.17 HAADF-STEM images show the growth of a  $\theta'$  precipitate accompanied by a moving dislocation in an Al-Cu alloy. The white line feature is a dislocation. Reproduced with permission from [99].

Misfit dislocations form at the semi-coherent interface of precipitates with the Al matrix. This kind of dislocations can also be associated with solute segregation. The magnitude and spatial distribution of the interfacial solute segregation are strongly correlated with the density of interfacial misfit dislocations. Fig. 2.18 shows the localised solute segregation at the semi-

coherent  $\theta'$ /Al interface and delocalized segregation at the coherent  $\theta'$ /Al interface. DFT calculations suggest that solute segregations reduce the interfacial energy. The segregation of Si at the coherent interface is not confined near the interface, and it is caused by the substitution of Si at the Cu sites of  $\theta'$  [100].

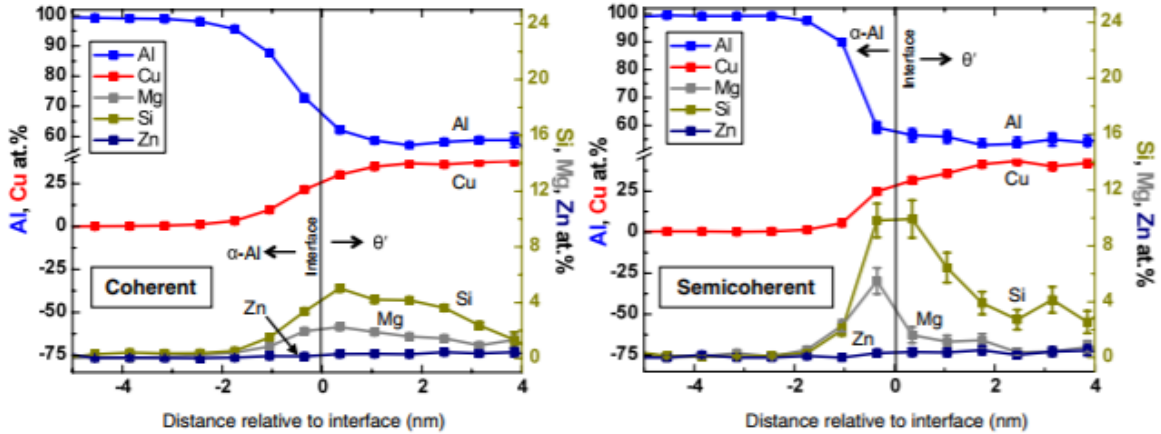


Fig. 2.18 Concentrations of Al, Cu, Mg, Si, and Zn as a function of distance from the coherent (left) and semi-coherent (right)  $\theta'$ /Al interfaces after ageing at 463 K for 8 h in an Al-Si-Cu-Mg alloy. Reproduced with permission from [101].

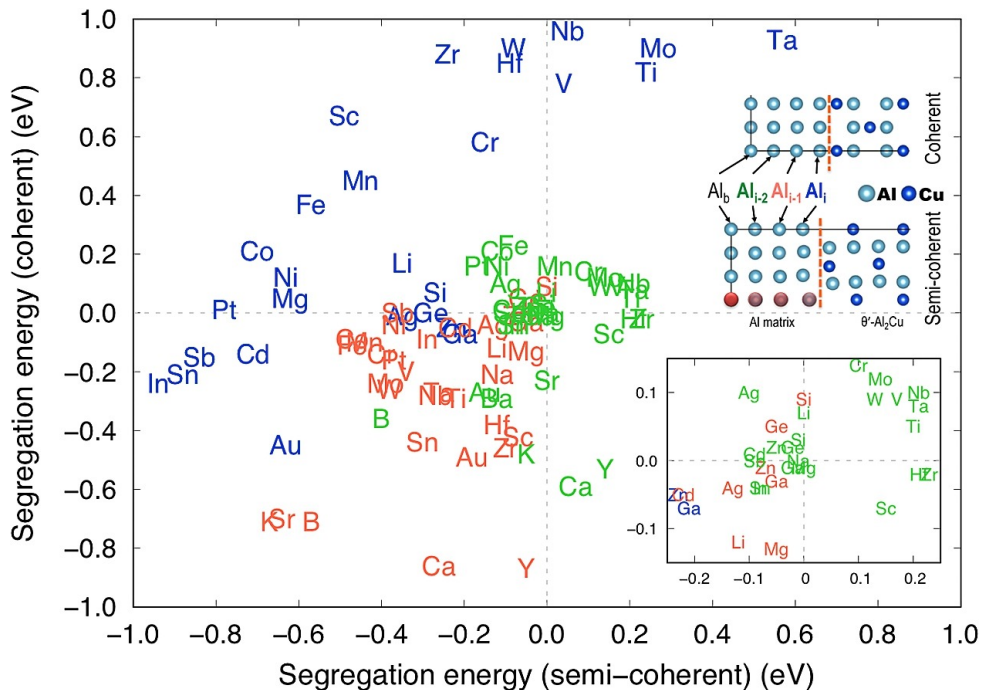


Fig. 2.19 DFT calculated segregation energies of 34 elements at the semi-coherent and coherent  $\theta'$ /Al interfaces. A negative value means energetically favourable segregation. Reproduced with permission from [102].

Recently, the segregation behaviour of 34 elements at the semi-coherent and coherent  $\theta'$ /Al interfaces was investigated by DFT calculations, and the main results are shown in Fig. 2.19 [102]. It is interesting to note that elements having a high vacancy binding energy, e.g., Sn, In, Sb and Cd, are all favoured to segregate at both the semi-coherent and the coherent interface. The tendency to do so at the first layer of the Al matrix near the semi-coherent interface is most remarkable. This may suggest these elements tend to segregate at the semi-coherent  $\theta'$ /Al interface.

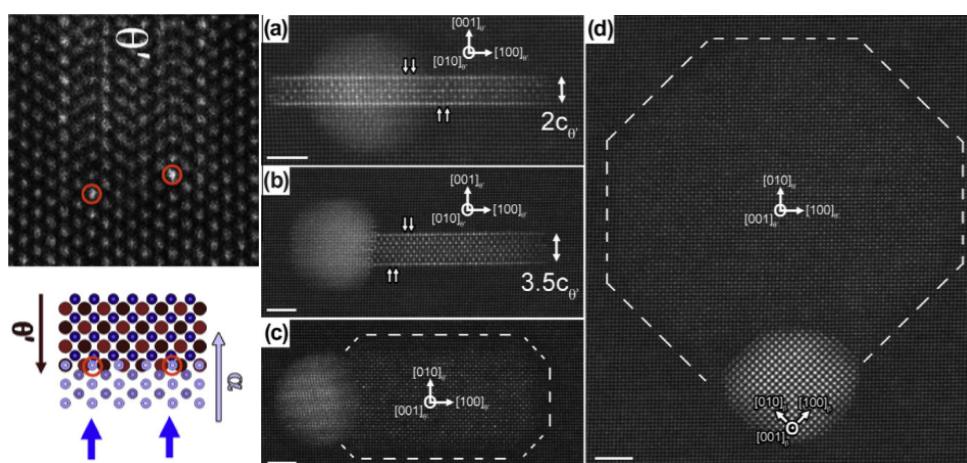


Fig. 2.20 HAADF-STEM images showing the possible segregation of Sn atoms at the semi-coherent  $\theta'$ /Al interface (leftmost, the red circles may indicate the Sn segregation) and the formation of Sn particles (bright big particles in a-d) at the same place in an Al-Cu-Sn alloy. Reproduced with permission from [40].

The semi-coherent precipitate/Al interface is expected to be good nucleation sites for another kind of precipitates, due to the segregation of solutes and the existence of misfit dislocations. On the one hand, the enrichment of solutes and disorder at the semi-coherent interface may provide a nucleation site with a low activation energy barrier. On the other hand, the misfit dislocation provides a fast diffusion pathway for the continuing growth of another kind of precipitates. Fig. 2.20 shows the possible segregation of Sn at the semi-coherent  $\theta'$ /Al interface and formation of Sn particles at the semi-coherent  $\theta'$ /Al interface [40]. In Al-Cu alloys micro-alloyed with Cd, the coarsening rate of  $\theta'$  precipitates was reduced by a factor of 5 compared with that in the binary Al-Cu alloy, which may suggest the Cd segregation at the semi-coherent  $\theta'$ /Al interface [103]. However, the predicted segregation positions from DFT calculations (see Fig. 2.19) sometimes disagree with the experimental observations, such as the Sn segregation shown in Fig. 2.20. Therefore, more detailed studies are needed to understand the segregation behaviour of microalloying elements in Al-Cu alloys.

### 2.2.2.3 Strain field around dislocations

The nucleation energy barrier for a precipitate can be reduced if nucleation takes place in the strain field of a dislocation because the strain field around a dislocation core can cancel, at least in part, the strain caused by the precipitate. This is another reason why dislocations can enhance precipitate nucleation. For the case of  $\theta'$ , the misfit is mainly along the  $c$  axis/the thickness direction, and the misfit strain can be negative or positive depending on the thickness of a  $\theta'$  precipitate. The strain in the direction parallel to the Burgers vector of an edge dislocation can also be positive or negative. Aligning the  $c$  direction of  $\theta'$  precipitates with the Burger vector of a dislocation thus can cancel/minimise the strain, and consequently, lower the activation energy barrier associated with nucleation [104]. There are two kinds of strain referred to in the literature about  $\theta'$  precipitation in the Al matrix, transformation strain and residual volumetric strain. Transformation strain is associated with the matrix-to-precipitate transformation for nucleation or growth, which is because the constituent atoms of a precipitate occupy different volumes in the precipitate and the matrix [40]. The volumetric strain is the residual misfit strain after embedding a precipitate in the Al matrix. The two strains are not strictly distinguished here because both can be accommodated by dislocations and vacancies partially/entirely.

### 2.2.3 2D defects

Twins and stacking faults in aluminium alloys are rare because of the high stacking fault energy ( $\sim 150\text{mJ/m}^2$ ) of FCC Al. Therefore, it is not easy to combine precipitation hardening with twin hardening in aluminium alloys, even though precipitation in severely deformed Al alloys has been investigating for several years [105-108].



*Fig. 2.21 Three boundaries with misorientations of  $4^\circ$  (AB),  $6^\circ$  (BC) and  $9.5^\circ$  (AC) in an Al-4Cu alloy after 2 h ageing at  $240^\circ\text{C}$ . Boundaries AB and BC contain  $\theta'$  precipitates, boundary AC contains  $\theta$  precipitates. Reproduced with permission from [109].*

A grain boundary is an interface between two grains, or crystallites, in a polycrystalline material. Since the misorientation across an interface usually spans a broad range in Al alloys [110, 111], a grain boundary with proper misorientation can provide easy nucleation sites for precipitates. Fig. 2.21 shows the distribution of  $\theta'$  and  $\theta$  precipitates along grain boundaries in an Al-4wt.%Cu alloy [109].

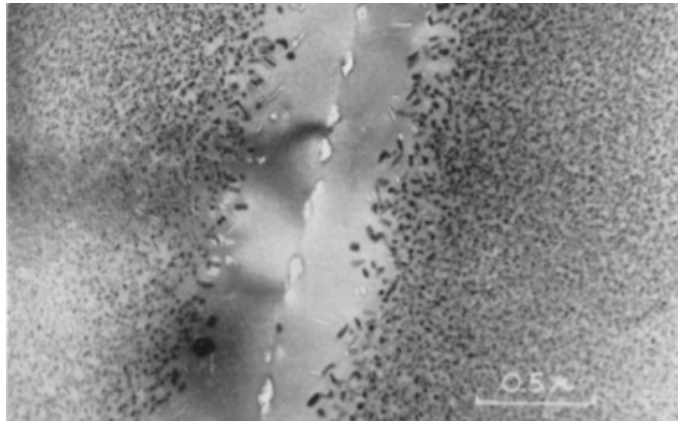


*Fig. 2.22 Precipitate free zone in an Al-Zn-Mg alloy aged 3 h at 180 °C. Reproduced with permission from [112]. The region free of dark particles (precipitates) is a precipitate free zone.*

Precipitate free zones (PFZ) near grain boundaries are widely observed in aged Al alloys, which means the absence of precipitates near grain boundaries. This is usually caused by the depletion of vacancies and solute atoms near grain boundaries. Fig 2.22 shows precipitate free zone in an Al-5.9wt.%Zn -2.5wt.%Mg [112]. Quenching rate and pre-ageing that can affect vacancy concentration and solute concentration near the grain boundary will affect the width of PFZ. PFZ is usually  $<1 \mu\text{m}$  in width and has a deleterious effect on mechanical properties and corrosion resistance.

## 2.3 Effects of processing parameters on precipitation

### 2.3.1 Ageing temperature and time

Ageing temperature and time are the most important parameters that determine precipitation hardening in an alloy and mechanical properties of an alloy. The ageing temperature mainly affects two variables that control precipitate nucleation. The first one is the diffusion coefficient,  $D = D_0 \exp(-Q/K_b T)$ . Here  $D_0$  is a pre-exponential factor,  $K_b$  is Boltzmann constant, and  $Q$  is the activation energy of diffusion. Table 2.2 provides a summary of  $D_0$  and  $Q$  for some elements in the Al matrix. It should be emphasised that the diffusivity of an element in the Al matrix should be compared using  $D$  instead of  $D_0$  or  $Q$ .

*Table 2.2 Summary of  $D_0$  and  $Q$  for some elements in the Al matrix [84, 113, 114].*

Solute	Q (eV), experiment	Q (eV), DFT	$D_0$ (m <sup>2</sup> /s), experiment	$D_0$ (m <sup>2</sup> /s), DFT
Cu	1.24-1.4	1.24-1.25	$6.1 \times 10^{-6}$ - $3 \times 10^{-5}$	$4.4 \times 10^{-6}$
Mg	1.19-1.35	1.21-1.27	$6 \times 10^{-6}$ - $1 \times 10^{-4}$	$1.19 \times 10^{-5}$
Ag	1.20-1.23	1.17	$1.2$ - $1.6 \times 10^{-5}$	NA
Li	1.29	1.31	$3.5 \times 10^{-5}$	NA
Si	1.22-1.41	1.15-1.17	$3.5 \times 10^{-5}$ - $2 \times 10^{-4}$	$3.7 \times 10^{-6}$
Ge	1.25	1.20	$4.8 \times 10^{-5}$	NA
In	1.19-1.28	1.13	$1.2 \times 10^{-4}$ - $1.2 \times 10^{-5}$	NA
Cd	1.29	1.18	$1.04 \times 10^{-4}$	NA
Sb	1.26	1.09	$9 \times 10^{-6}$	NA
Au	1.17-1.25	1.07	$7.7 \times 10^{-6}$ - $2.7 \times 10^{-5}$	NA
Zn	1.20-1.25	1.22	$1.6$ - $3.3 \times 10^{-5}$	$7 \times 10^{-6}$
Sc	1.79	1.52	$5.3 \times 10^{-4}$	$5 \times 10^{-5}$
Zr	2.51	1.89	$7.3 \times 10^{-2}$	NA
Cr	2.62-2.72	2.50	$1.9 \times 10^{-1}$	$7 \times 10^{-5}$
V	3.14	2.47	1.16	$1 \times 10^{-4}$

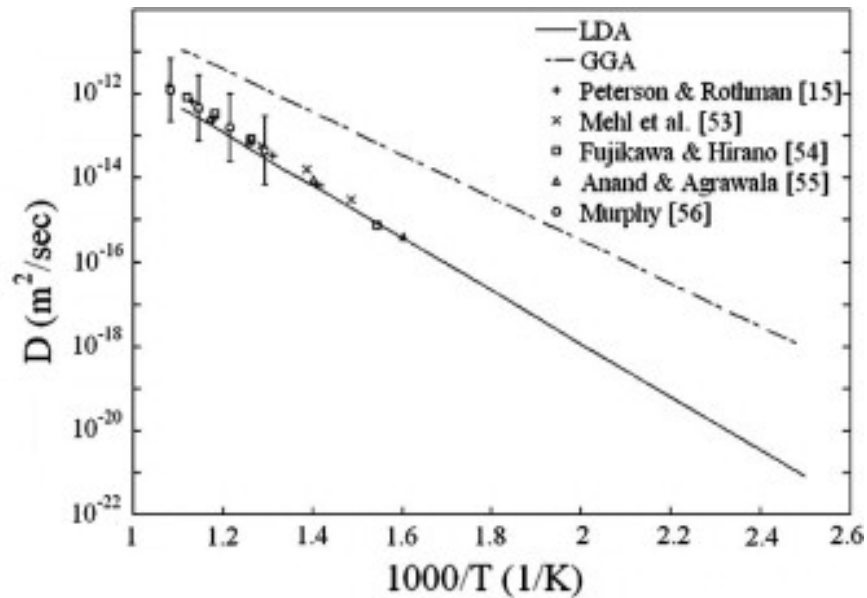


Fig. 2.23 Diffusion coefficient of Cu in the Al matrix from DFT calculations and experiments. Reproduced with permission from [84]. The references in the figure are from the original paper.

Fig. 2.23 shows the change of the diffusion coefficient of Cu as a function of temperature [84]. The coefficient is  $\sim 3 \times 10^{-27}$  m<sup>2</sup>/s at room temperature and is  $\sim 2 \times 10^{-19}$  m<sup>2</sup>/s at 473 K. The big difference indicates the importance of ageing temperature on precipitation kinetics. However, it should be noted that these are just equilibrium diffusion coefficients, which may significantly differ from the real diffusion coefficient. This is because the quenched-in vacancies can increase the diffusion coefficient and the presence of some solute atoms, such as Sn, can modify the vacancy concentration.

Ageing temperature alters the supersaturation of solutes and affects the driving force for nucleation. The solid solubility of an element in the Al matrix is temperature dependent. Usually, the solid solubility decreases with increasing temperature. To the best knowledge of the author, the accurate solid solubility value of a given element in a multicomponent alloy are lacking. The lower the ageing temperature, the higher the driving force for precipitate nucleation. However, this is compromised by a low diffusivity. Therefore, the optimal ageing temperature for an alloy is often determined by trials and errors.

Theoretically, the longer the ageing time, the further the reaction can reach. Usually, the ageing time is determined after continuing ageing at a given temperature until the peak hardness is reached. However, for some multi-step ageing processes, the ageing time can only be chosen based on trial-and-error experiments, except the last step ageing. Multi-step ageing is common for Al-Zn-Mg-Cu alloys [115] and sometimes for Al-Mg-Si alloy [116] but not common for Al-Cu alloys with low concentrations of other elements. This is because GPI zones in Al-Zn-Mg-Cu can transform directly into the main strengthening phase  $\eta'$  [77]. The first stage low-temperature ageing can increase the nucleation rate of GPI zones at the expense of slow diffusion/longer ageing time, which can consequently increase the nucleation rate of  $\eta'$  precipitates [77]. A higher ageing temperature at the second stage (even more stages) is aimed to accelerate the coarsening kinetics and reduce total ageing time. The fact that multi-step ageing has rarely been successful in enhancing  $\theta'$  nucleation may suggest again that the direct transformations between  $\theta''$  and  $\theta'$  precipitates are uncommon in Al-Cu alloys. However, the effect of multi-step ageing on precipitation in Al-Cu alloys remains poorly understood and therefore merits further study.

### **2.3.2 Cold working before artificial ageing**

Plastic deformation applied before ageing has been shown to increase the precipitation kinetics by about one order of magnitude in Al-Cu alloys [117, 118]. The enhanced precipitation kinetics can be attributed to increased diffusivity by the presence of a high density of lattice defects such as vacancies, dislocations and grain boundaries [119]. Slight deformation

is commonly observed to enhance precipitation kinetics and hardly change the precipitation sequence [120]. However, severe plastic deformation can remarkably change the precipitation pathway. Only the equilibrium phase  $\theta$  nucleates at grain boundaries, skipping all the metastable precipitates even at 100 °C in ultrafine-grained Al-Cu solid solution that was processed by equal channel angular pressing (ECAP), as shown in Fig. 2.24 [121]. This is because the supersaturation of Cu in the Al matrix is quickly lost due to fast diffusion of Cu to grain boundaries. Besides, the severe plastic deformation after artificial ageing can dissolve the already formed  $\theta'$  precipitates.

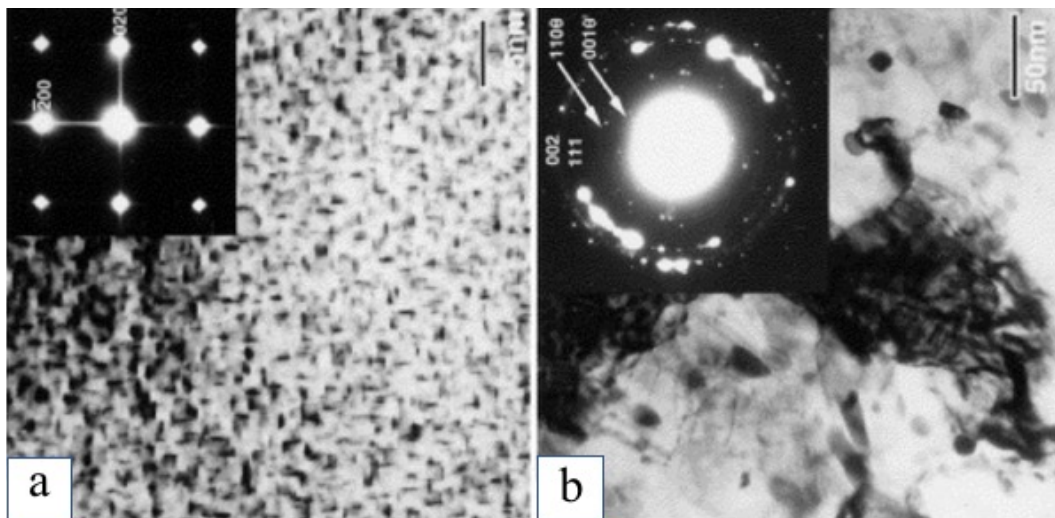


Fig. 2.24 Bright-field TEM images and SAED patterns of an Al-1.7 at% Cu alloy aged at 100 °C for 24 h, (a) without deformation, (b) with eight passes of ECAP. Reproduced with permission from [121].

Slight deformation before artificial ageing can eliminate all the beneficial effects of Sn, In and Cd [32]. This means the beneficial effects of these elements are smeared by deformation, and no additional beneficial effects occur after deformation even if these elements are added. Several reasons have been proposed to explain this. First, deformation produces abundant defects, here mainly vacancies and dislocations. The pronounced enhancing effect of these defects on  $\theta'$  nucleation may surpass that of these elements. Second, these elements may tend to segregate to/around dislocations and thus become unavailable to promote  $\theta'$  nucleation. However, since the functioning mechanisms of Sn additions are not fully understood, further study is required to explore the combined effect of Sn additions and deformation on  $\theta'$  nucleation.

### 2.3.3 Phase selection depending on processing parameters

The phase constituents of a material usually vary with processing conditions, and polymorphic selection often occurs [25]. GP zones,  $\theta''$ ,  $\theta'$  and  $\theta$  are good examples, and the constituent phases at a certain ageing condition are the outcome of their competitions. This kind of phase selection is well known and is documented in the literature as precipitation sequence. In the present work, phase selection mainly concerns the occurrence of new precipitate types that are uncommon in conventional conditions.

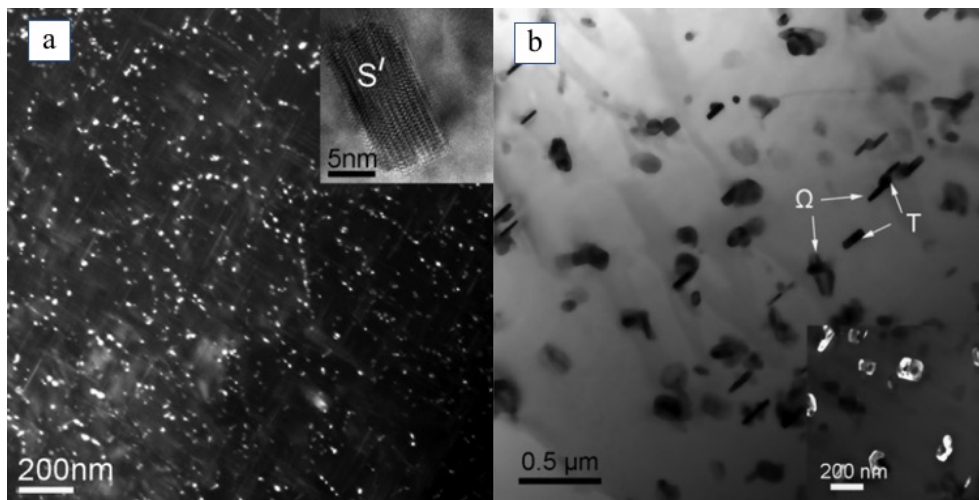


Fig. 2.25 TEM images of 2024 alloy aged for (a) 180 min and (b) 720 min after 70% strain deformation. Reproduced with permission from [56].

Cold rolling between solid solution treatment and artificial ageing can change the precipitation sequence of 2024 Al alloy (Al-4.5wt.% Cu-1.5wt.% Mg-0.5wt.% Mn) [56]. The normal precipitation sequence for this alloy is solid solution  $\rightarrow$  GPB  $\rightarrow$  S' (Al<sub>2</sub>CuMg)  $\rightarrow$  S (Al<sub>2</sub>CuMg) [122]. However, in samples with 20% to 70% thickness reduction, it is the  $\Omega$  phase (Al<sub>2</sub>Cu) that forms after the S' phase [56]. Fig. 2.25 shows the formation of S' precipitates first at 180 min and the dissolution of S' precipitates and formation of  $\Omega$  precipitates at 720 min. Here dislocations are hypothesized to be responsible for the formation of  $\Omega$  precipitates, and it is mainly based on two observations. First, the higher the strain, the faster  $\Omega$  precipitates form at the expense of S' precipitates. Second, when the strain is 20%,  $\theta'$  precipitates occur together with  $\Omega$  precipitates and  $\theta'$  is the dominant phase after 720 min ageing. However, with higher strain and after 720 min ageing, it is the  $\Omega$  phase that almost completely dominates. This may suggest the dislocation density is important for the phase selection. As stated above, the  $\theta'$  phase has lower free energy compared with the  $\Omega$  phase if neglecting interfacial energy. How  $\Omega$  precipitates becomes favoured over  $\theta'$  precipitates remains a mystery. The interfacial

segregation of Mg on  $\Omega$ /Al interface in Al-Cu-Mg alloys (without Ag) is unknown now, and its segregation without Ag may not be enough to offer lower interfacial energy. The nucleation sites of  $\Omega$  precipitates here are interesting: most of the precipitates are found to nucleate heterogeneously from the undissolved T phase (Fig. 2.25). This may bypass the key role of the combined additions of Mg and Ag.

The roles of defects in phase selection are interesting and important. Neither  $\Omega$  nor  $\theta'$  precipitates form in a 2024 alloy processed by deformation at  $-196^\circ\text{C}$  and artificial ageing at  $100^\circ\text{C}$  [123]. Co-clusters of Mg and Cu that form in solid solution may explain the easy formation of  $S'$ . At normal conditions, S precipitates will form at the expense of  $S'$  precipitates, and, in the case in the last paragraph,  $\Omega$  precipitates replace the existing  $S'$  precipitates. The presence of a high density of dislocations/grain boundaries may drain Mg atoms from the matrix [106, 124-126] and thus reduces the stability of  $S'$  and S precipitates. In the latter case, the low ageing temperature,  $100^\circ\text{C}$ , delays the dissolution of  $S'$  to a very long time and stops the formation of  $\Omega$  nor  $\theta'$  precipitates rapidly. Therefore, the deformation generated defects, including grain boundaries and dislocations, are important in changing the stability of phases and inducing new phase selection. In a 7055 alloy (Al-7.76Zn-1.94Mg-2.35Cu), deformation-induced defects also change the stability of  $\eta'$  precipitates and trigger the formation of AlCu and  $\theta$  precipitates [127].

Irradiation is another method to induce new precipitates from well-known Al alloys. Ion irradiation was shown to dissolve  $\beta''$  precipitates and trigger unknown precipitates in a 6061 (Al-Mg-Si) alloy [128].

## **2.4 Ways to optimise mechanical properties by tuning precipitation**

### **2.4.1 Grain refinement**

Precipitation hardening is the major strengthening method for most of wrought Al alloys (2xxx, 6xxx and 7xxx series). Al-Mg and Al-Mn alloys are exceptions because they mainly rely on solute strengthening. There are mainly two approaches in the literature to optimise mechanical properties of age hardenable Al alloys. The first one is combining precipitation hardening with grain refinement. After grain refinement by plastic deformation, the nucleation frequency can be very high, and the space between precipitates can be reduced to  $\sim 10\text{ nm}$  [108]. Thus, strength can be doubled compared with a normal condition, without sacrificing ductility [108, 123]. Fig. 2.26 shows the optimisation of the strength of 2024 Al alloy by grain refinement and precipitation hardening. Such good mechanical properties are achieved by a high number density of very small precipitates ( $< 10\text{ nm}$ ) in grain interiors, not along grain

boundaries. However, in most grain-refined Al alloys by plastic deformation or powder consolidation, defect (including vacancies, dislocations and grain boundaries) densities are significantly increased, and the nucleation of precipitates is preferred from defects [98, 105, 107, 119]. As a result, large precipitates grow along grain boundaries and increase the strength of alloys at the expense of a significant loss of ductility (ductility < 5%) [98, 105, 107]. Therefore, achieving good mechanical properties by grain refinement together with precipitation is only achieved in very limited Al alloys and are not a widely applicable method at present.

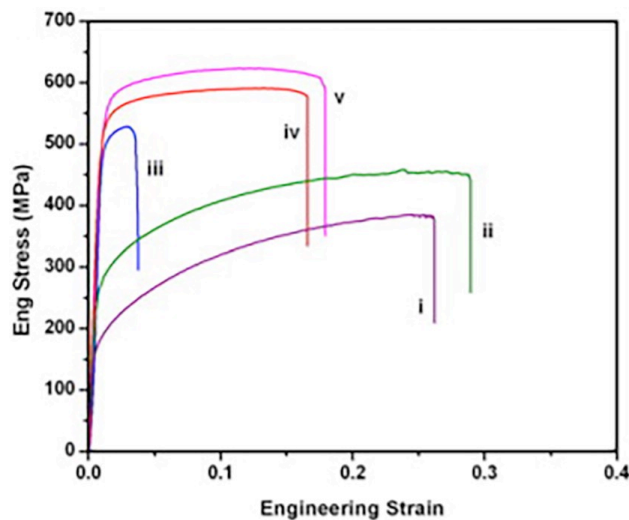


Fig. 2.26 Typical tensile engineering stress-strain curves of 2024 Al alloy under different processing conditions, (i) solid solution treatment (SST) at 493 °C; (ii) SST + aging at 160 °C for 10 h; (iii) SST + cold rolling (CR); (iv) SST + CR + aging at 160 °C for 13 h; (v) SST + CR + aging at 100 °C for 100 h. Reproduced with permission from [123].

#### 2.4.2 Lowering lattice misfit

The second approach for optimising mechanical properties is to maximise the nucleation rate of precipitates by reducing the mismatch between precipitates and the matrix. An additional requirement is that precipitates should be efficient in inhibiting dislocation motion otherwise the high number density of precipitates will be a waste, e.g., GP zones in Al-Cu alloys. The main strengthening precipitates in Al alloys are usually not coherent with the Al matrix, and misfit therefore occurs. Strain energy and interfacial energy that accompany the nucleation and growth of precipitates usually make the nucleation energy barrier very high and the nucleation rate of precipitates low. However, precipitates sometimes can be fully coherent with the matrix, and the nucleation rate of such precipitates is often very high. Fig. 2.27 shows coherent precipitates of  $\text{Al}_3(\text{Sc}_{1-x}\text{Zr}_x)$  and  $\text{Ni}(\text{Al}, \text{Fe})$  in an Al alloy and steel, respectively [129, 130]. In the former case,  $\text{Al}_3(\text{Sc}_{1-x}\text{Zr}_x)$  has an  $\text{L}_{12}$  crystal structure. The lattice parameters of

$\text{Al}_3(\text{Sc}_{1-x}\text{Zr}_x)$  and Al are almost the same. Therefore the nucleation rate can be very high.  $\text{Al}_3\text{Sc}$  is also coherent with Al, but additions of Zr still increase the nucleation rate [129, 131]. This is because the random incorporation of Zr into the  $\text{Al}_3\text{Sc}$  lattice increases the formation entropy and consequently increases the driving force of nucleation [132]. Another example is  $\text{Ni}(\text{Al},\text{Fe})$  precipitates in a recently developed steel, which is associated with a low lattice misfit ( $0.03\pm 0.04\%$ ) and a low nucleation energy barrier [130]. Besides, a low diffusivity of the solute that segregates at the precipitate/matrix interface is important for slowing down the coarsening of precipitates [130, 132]. Therefore, the key question to increase nucleation rate now is to find an element that reduces the misfit between a precipitate and the matrix. It will be better if the element has a slow diffusivity and can be a bottleneck of the coarsening of precipitates.

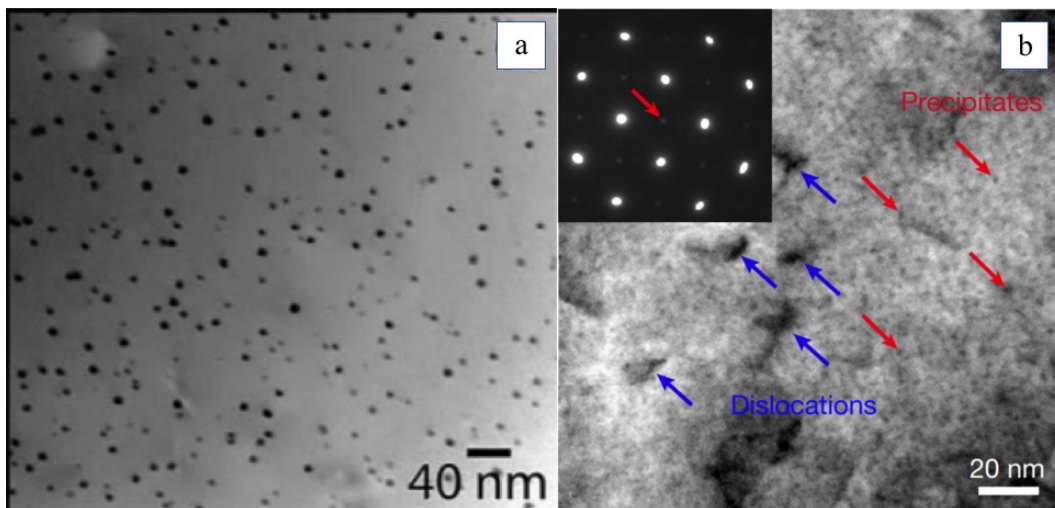


Fig. 2.27 High density of precipitates in alloys due to a low misfit at the precipitate/matrix interface. (a)  $\text{Al}_3(\text{Sc}_{1-x}\text{Zr}_x)$  in an Al-Sc-Zr alloy and (b)  $\text{Ni}(\text{Al},\text{Fe})$  in a steel. Reproduced with permission from [129, 130].

For a given precipitate, although we cannot change its misfit with the matrix, we can reduce the misfit at the interface by elemental segregation. Combined additions of Mg ( $\sim 0.3$  at. %) and Ag ( $\sim 0.2$  at. %) can promote the formation of  $\Omega$  precipitates at the expense of  $\theta'$  precipitates. As stated above, their roles at the  $\Omega/\text{Al}$  interface are to reduce the misfit between  $\Omega$  precipitates and the Al matrix [63]. Another example is the presence of Cu at the  $\beta''/\text{Al}$  interface which removes the misfit dislocations at the interface [133]. This may explain why minor additions of Cu ( $\sim 0.1$  at. %) in an Al-Mg-Si alloy can increase the nucleation rate of  $\beta''$  precipitates remarkably (as shown in Fig. 2. 28) [134]. It is worth noting that the Q phase can form at very high Cu concentration, such as 0.75 wt. % Cu in Fig. 2.28 [134, 135]. As mentioned above, solute (Sn, In and Cd) may segregate around  $\theta'$  precipitates (see Section 2.1.2). Here comes a

question: Is solute (Sn, In and Cd) segregation around  $\theta'$  precipitates responsible for the enhanced nucleation of  $\theta'$  precipitates upon microalloying in Al-Cu alloys? If so, it will be of great interest to explore why such low concentrations of Sn, In or Cd (<0.02 at.%) in Al-Cu alloys can be so effective in reducing the misfit between  $\theta'$  precipitates and the Al matrix.

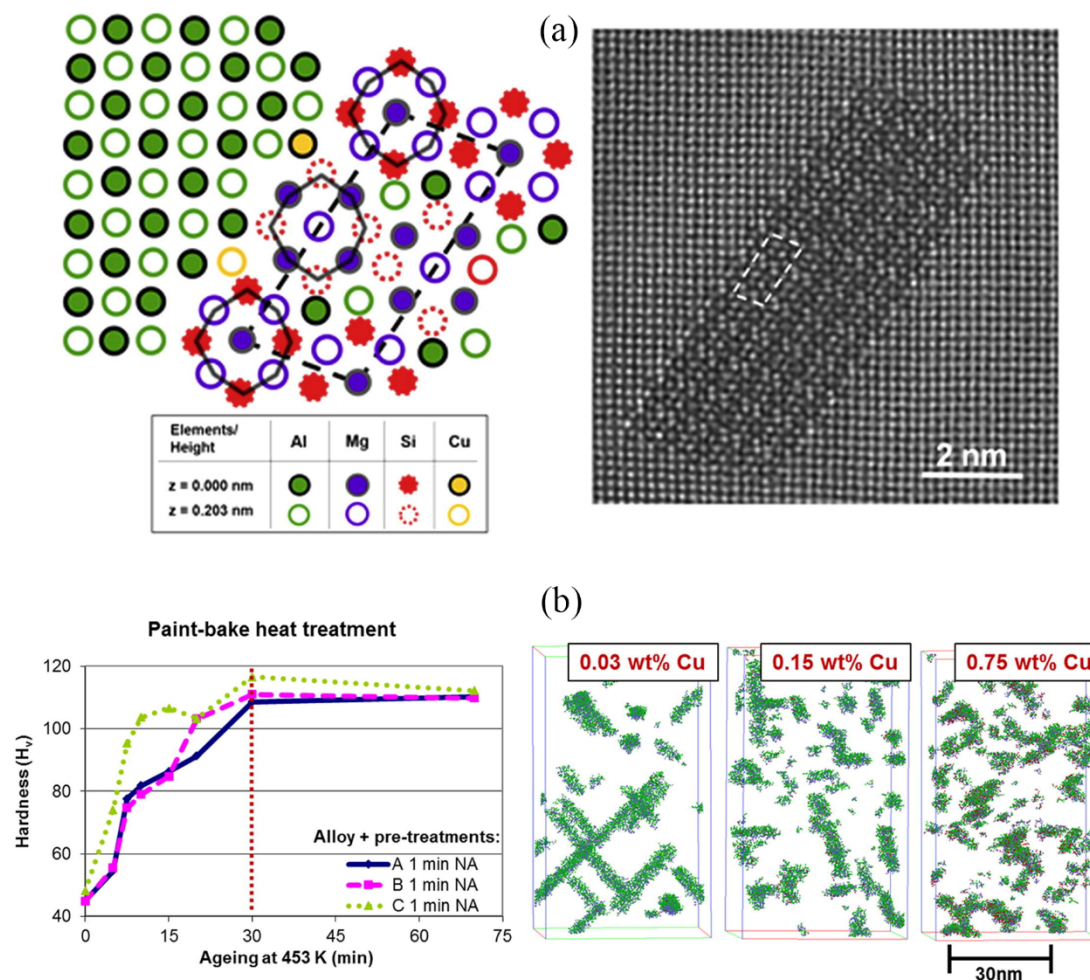


Fig. 2.28 (a) Presence of Cu at the  $\beta''$ /Al interface in an Al-Mg-Si alloy [133] and (b) enhanced nucleation frequency of  $\beta''$  precipitates in an Al-Mg-Si alloy with Cu additions. Reproduced with permission from [134].

## 2.5 Open questions and outline of the research

As stated above, there are several open questions about the nucleation mechanisms of precipitates in Al alloys, especially upon microalloying additions. In this thesis, the following two questions were investigated. First, what is the role of minor solute additions in enhancing  $\theta'$  nucleation in Al-Cu alloys? Second, what are the mechanisms by which vacancies affect phase selection of Cu-rich phases in Al-Cu based alloys? The segregation of solute atoms at

the precipitate/Al interface will also be briefly explored. This thesis aims to understand the nucleation mechanisms of precipitates in Al-Cu solid solutions at the atomic level and develop design guides for optimising mechanical properties by selecting specific precipitation pathways.

The two existing explanations for the role of minor additions of In, Sb and Cd in enhancing precipitation are in part supported by experimental observations, but some degree of ambiguity remains (see section 2.2.2). In this study, the author investigated how typical solute additions affect the ageing responses in Al-Cu alloys and explained the underlying mechanisms at the atomic level. Two kinds of solute additions are selected: combined additions of In and Sb at a low concentration level (0.025 at. %) and Ge additions (0.78 at. %). In the first case, both In and Sb have a high vacancy binding energy (-0.2 eV and -0.3 eV, respectively, comparable to -0.25 eV of Sn [39]), and they tend to form a covalent crystal according to the equilibrium phase diagram. It will be interesting to study how the interaction between these two kinds of solutes affects their role in promoting  $\theta'$  precipitation. Early well-studied solutes, Sn, In and Cd always form metallic crystals. The accumulated addition amount of In and Sb is 0.05 at.%, which is the same as the addition amount of Sn or In in early work [14,30]. The differences between the new Al-1.7Cu-0.025In-0.025Sb (at.%) alloy and the well-studied Al-1.7Cu-0.05Sn or Al-1.7Cu-0.05In alloys (at.%) are thus narrowed to differences in interactions between added solute atoms. Differences in ageing response between the new alloy and the well-studied alloy can be correlated with the difference in interatomic interaction between added solute atoms. In the second case, Ge also tends to bind with vacancies (binding energy=-0.12 eV, much lower than Sn [39]) and has a high solid solubility in the Al matrix. The higher Ge concentration may compensate for its weakness of a lower binding energy with vacancies compared with In and Sb. Thus, we can find whether the vacancy binding energy is a critical parameter.

Defects in the Al matrix can induce the occurrence of new phases (see 2.3.3). The presence of In and Sb or Ge will affect the vacancy concentration in the Al matrix. Therefore, the role of vacancies on phase selection was also studied in these alloys.

Chapter 3 describes the experimental and computational methodologies. Chapter 4 deals with the two precipitation sequences in the Al-1.7Cu-0.025In-0.025Cu (at.%) alloy. Chapter 5 discusses multiple precipitation mechanisms of Cu-rich precipitates in the Al-1.7Cu-1.78Ge alloy. Chapter 6 reports the nucleation precursor (a new Cu-rich phase) of  $\theta'$  precipitates and its dependence on vacancy concentration.

Overall, we find that InSb additions and Ge additions can interact with vacancies, and two different nucleation mechanisms of  $\theta'$  precipitates can be operative depending on the solute-vacancy binding energy.

# Chapter 3

## Experimental and computational methodologies

This chapter describes the preparation of alloys and the experimental and computational methods used in this study. Section 3.1 details the alloy fabrication and heat treatment protocol, which is followed by the hardness testing method in Section 3.2. The direct observation method is scanning transmission electron microscopy, as described in Section 3.3. Computer simulations include two parts, first-principles calculations in Section 3.4 and Computer Coupling of Phase Diagrams and Thermochemistry (CALPHAD) in section 3.5.

### 3.1 Alloy preparation and heat treatment protocols

There are three alloys used in this study, i.e., Al-1.7at.% Cu-0.025at.% In-0.025at.% Sb (Al-Cu-In-Sb), Al-1.7at.% Cu-0.78at.% Ge (Al-Cu-Ge) and Al-1.7at.% Cu (Al-Cu). They were prepared by a casting process using high purity elements and compounds (better than 4N). The raw materials were melted in an electric resistance furnace at 750 °C for 1.5 h, followed by pouring into a cylindrical iron or graphite mould with diameter ~ 30 mm. InSb and Ge single crystal wafers were used. The actual compositions of the two alloys were measured by inductively coupled plasma atomic emission spectroscopy (AES-ICP), which are given in Table 3.1.

*Table 3.1 Chemical analysis of two micro-alloyed Al-Cu alloys by AES-ICP (atomic percentage).*

Samples	Al	Cu	Ge	In	Sb	Fe	Si	others
Al-Cu-In-Sb	Bal	1.721	<0.002	0.027	0.025	0.02	0.06	<0.01
Al-Cu-Ge	Bal	1.797	0.694	<0.002	<0.002	0.03	0.04	<0.01

The ingots were homogenised in a salt bath for 24 h at 520 °C and then quenched into room temperature water. After this, the ingots were sliced into pieces 1.5-3 mm thick pieces. The slices were cold rolled to ~0.5 mm or ~1 mm through 5 passes. The thin slices were used for TEM characterisation, and the thick slices were used for hardness testing.

The heat treatment was carried out in salt baths and oil baths. The prepared slices were first solid solution treated at 520 °C for 1 h to dissolve solute atoms into the Al matrix, and then quenched into room temperature water. Slices for TEM characterisation were punched into disks with 3 mm diameter before solid solution treatment. A mesh tea infuser (made by stainless steel) was used to hold the punched small disks during heat treatment. Natural ageing (NA) was carried out in air at room temperature. The time for natural ageing can be less than 1 min after solution treatment. Unless stated specially, the quenched disks/slices were immediately aged at artificial ageing temperatures in <1 min. The artificial ageing temperatures were 160 °C, 200 °C and 250 °C. Quenching at 160 °C for 1 min (named Interrupted quenching, IQ, in the following) before normal water quenching was also used in some cases. Table 3.2 summarises the ageing parameters for the TEM samples used in this study. For the thick slices used for hardness test, they were aged at a given temperature continuously until the peak hardness was reached.

*Table 3.2 Summary of artificial ageing parameters used in this study.*

Alloys	NA/IQ	Ageing temperatures and times
Al-Cu-In-Sb	NA<1 min	160/200/250 °C, 2 min/10 min/15 min/30 min/1 h/2 h
	NA=10 days	160/200/250 °C, 2 min/10 min/15 min/30 min/1 h/2 h
	IQ, NA<1 min	160/200/250 °C, 2 min/10 min/15 min/30 min/1 h/2 h
Al-Cu-Ge	NA<1 min	160/200/250 °C, 2 min/10 min/15 min/30 min/1 h/2 h
	NA=10 days	160/200/250 °C, 2 min/10 min/15 min/30 min/1 h/2 h
	IQ, NA<1 min	160/200/250 °C, 2 min/10 min/15 min/30 min/1 h/2 h

### 3.2 Hardness measurement

Hardness tests were carried out on an A300 duramin hardness tester. The slices for hardness test were polished on 1200 grit sandpapers before solution treatment. The polished surface was wrapped and protected by aluminium foil when samples were put into a salt bath. The covering aluminium foil hardly affects the temperature of samples but can alleviate the corrosion on sample surfaces caused by salt melts. Any deformation to the slices. e.g., hand polishing on

sandpapers, was avoided after the solid solution treatment. The applied load was 500 g and indentation time was 10 s. The reported values below are averages over 10 measurements. Some slices were deformed between solid solution treatment and artificial ageing in order to investigate the synergetic effect of solute additions and cold working on precipitation. Cold rolling with thickness reduction  $\sim 50\%$  was carried on these slices. These slices were also polished on sandpapers before artificial ageing.

### 3.3 Transmission electron microscopy

The aged samples were characterised mainly by scanning transmission electron microscopy (STEM) imaging in transmission electron microscopes. This is because STEM has shown a powerful capability in studying precipitation phenomena in alloys, as reviewed in Chapter 2. During imaging, a converged electron beam scans on a sample and interacts with the sample. Scattered electrons are picked up by different detectors at different angles off the optic axis. A high angle annular dark field (HAADF) detector collects scattered electrons at a high semi-angle ( $>50\text{mrad}$ ) and provides images with contrast scaling roughly as the atomic number  $Z^{1.7}$  [136]. A bright field detector picks up the direct beam, thus giving a contrast of an image as that of a conventional TEM bright field image. Fig. 3.1 shows a schematic of the HAADF and BF detectors in a STEM.

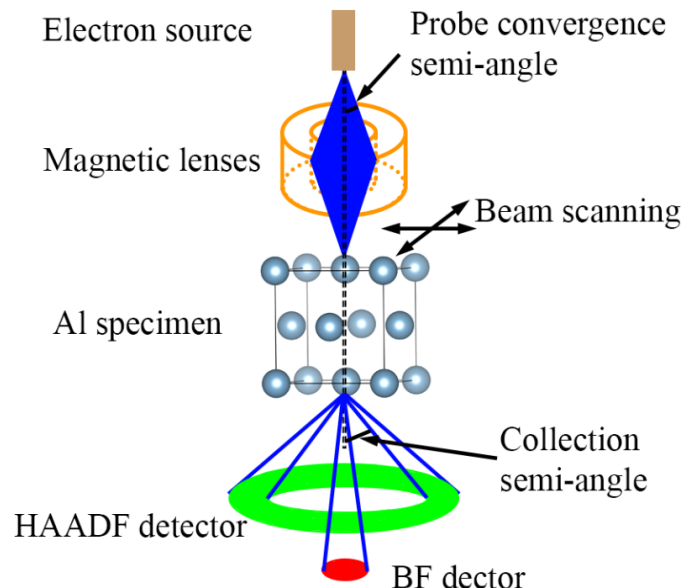


Fig. 3.1 Schematic of imaging a specimen using a HAADF detector and a BF detector in a STEM. The blue region and line indicate electron trajectory.

JEOL JEM 2100F and double-aberration-corrected FEI Titan<sup>3</sup> 80-300 were the TEMs used here for STEM imaging. Detailed imaging conditions are displayed in Table 3.2. The HAADF detector on JEOL 2100F is a JEOL HAADF detector, and BF detector is a Gatan BF detector. The HAADF detector on Titan<sup>3</sup> 80-300 is a Fischione Instruments 3000 annular dark field detector, and the BF detector is an FEI BF detector. Aberrations of Titan<sup>3</sup> 80-300 were corrected up to third order using the CEOS correction software. The measurement and correction of the astigmatisms and spherical aberration were performed on a standard cross-grating specimen consisting of Au nanoparticles on carbon film. The standard specimen was first moved to the eucentric position. The defocus (C1) and second-order astigmatism (A1) were measured by capturing an under-focused image and an over-focused image of the probe. Based on the measurement, C1 and A1 were improved manually to within  $\pm 10$  nm of zero. Then, 17 under-focus and over-focus images of the probe were captured with the beam tilted. The tilt angle of the electron beam was larger than 15 mrad (the probe convergence semi-angle used here), usually being 18-20 mrad. The measured aberrations were then corrected to the confidence interval of the measurement using the correction software. Several iterative measurement and correction steps are needed to reach the confidence interval. After the aberration correction, a resolution of 0.12 nm can be obtained using a convergence semi-angle of 15 mrad. Al specimens were loaded into the FEI Titan<sup>3</sup> 80-300 after the aberration correction. All the Al specimens were cleaned by plasma using a Gatan 950 Solarus Advanced Plasma System. The cleaning recipe used was Ar/O<sub>2</sub> for 2 min.

*Table 3.3 Imaging conditions of the used microscopes. The aberrations of Titan<sup>3</sup> 80-300 were corrected by a CEOS Cs probe corrector.*

Microscopes	Operating voltage (kV)	Probe convergence semi-angle (mrad)	Probe size (nm)	Spherical aberration (mm)	Collection semi-angle (mrad)	
					BF	HAADF
JEOL 2100F	200	10	0.2	1	15	65-185
FEI Titan <sup>3</sup> 80-300	300	15	0.12	<0.001	15	55-200

Energy dispersive X-ray spectroscopy (EDS) was performed to characterise the chemical constituents of the alloys. This was carried out in the JEOL 2100F using a JEOL 50 mm<sup>2</sup> Si(Li) detector with ultra-thin window. The TEM samples were tilted to  $\sim 15^\circ$  to guarantee a maximum collection efficiency of the X-rays. As a result, the incident beam usually is off zone axis. EDS

mapping was carried out in STEM mode using a nominal probe size of 0.7 nm (larger than high-resolution STEM imaging, where a nominal probe size of 0.2 nm was used) to increase signal counts. The scanned area was monitored in real time to avoid significant damages. The mapping time ranged from 30 min to 1 h. Sample drift was corrected by the acquisition software automatically. The acquisition dwell time used was 0.2 ms, and the acquisition map was 256×256 pixels in size.

Nano diffraction and selected area electron diffraction were performed in order to identify the crystal structure of some precipitates. Nano diffraction was carried out in the JEOL JEM 2100F. All the settings were the same as STEM imaging except the smallest condenser aperture (10 μm) was used here to avoid the overlapping of diffraction discs. The convergent electron beam scans over precipitates and produces a diffraction pattern at each position of the probe, which is collected by a Gatan Ultrascan 1000 camera. Selected area diffraction was used to characterise larger areas (typically diameter >200 nm) as well as bigger precipitates. It uses a parallel electron beam and a selected area aperture in the first image plane to select an area. Usually, the smallest selected area aperture was used here. Convergent electron beam diffraction (CBED) was also used to measure sample thickness. The thickness of the TEM sample was measured by comparing the captured CBED patterns with CBED patterns simulated by JEMS (a program simulating images and diffraction patterns in electron microscopy [137]). The parameters for CBED simulation in JEMS were chosen according to the real experiential conditions. The simulated CBED pattern that matches most closely the experimental CBED gives the thickness of the TEM specimen. The accuracy of this method is expected to be better than 10% [138].

### 3.4 First-principles calculations

How the energy of a material changes as its constituent atoms are moved is a common question in material research. In quantum mechanics, we separate the motion of the nuclei from that of the electrons according to Born–Oppenheimer approximation and express the ground-state energy ( $E$ ) of a material as a function of the positions of nuclei ( $(R_1, \dots, R_M, M$  is the number of nuclei). For a system with multiple ( $N$ ) electrons interacting with multiple nuclei ( $M$ ), the Schrödinger equation has the following form,

$$\left[ -\frac{\hbar^2}{2m} \sum_{i=1}^N \nabla_i^2 + \sum_{i=1}^N V(r_i) + \sum_{i=1}^N \sum_{j<i} U(r_i, r_j) \right] \Psi = E\Psi. \quad (3.1)$$

Here,  $m$  is the electron mass,  $\hbar$  is reduced Plank constant,  $E$  is the ground state energy of the electrons and  $\Psi$  is the electronic wave function. The three terms in brackets in this equation define the kinetic energy of each electron, the interaction energy between each electron and the

collection of atomic nuclei, and the interaction energy between different electrons, respectively [139]. The electronic wave function,  $\Psi$ , is a function of each of the spatial coordinates of each of the  $N$  electrons and can be approximated as a product of individual electron wave functions,  $\Psi = \Psi_1(r_1) \Psi_2(r_2) \dots \Psi_N(r_N)$  (Hartree product). However, solving the Schrödinger equation for practical materials is not easy. First, the full wave function is a high-dimensional function ( $3N$ -dimensional for  $N$  electrons). Secondly, individual electron wave function,  $\Psi_i(r_i)$ , cannot be obtained without simultaneously considering the individual electron wave functions associated with all the other electrons [140, 141].

### 3.4.1 Density functional theory

The wave functions for any particular set of coordinates of electrons cannot be directly observed, while density of electrons at a particular position in space,  $n(r)$ , can be (in principle) measured [139].  $n(r)$  can be expressed as:

$$n(r) = 2 \sum_i \Psi_i^*(r) \Psi_i(r), \quad (3.2)$$

where  $\Psi_i^*(r) \Psi_i(r)$  is the probability that an electron in individual wave function  $\Psi_i(r)$  is located at position  $r$ . The factor of 2 appears because the Pauli exclusion principle states that each individual electron wave function can be occupied by two separate electrons if they have different spins [139].

Density functional theory is built on two theorems proved by Kohn and Hohenberg [142] and the derivation of a set of equations proposed by Kohn and Sham [143]. The first theorem of Kohn and Hohenberg is that the ground-state energy from Schrödinger's equation is a unique functional of the electron density. A functional is a function of another function, which here defines the variation of system energy upon the variation of electron density. The second theorem of Kohn and Hohenberg is that the electron density that minimizes the energy of the overall functional is the true electron density corresponding to the full solution of the Schrödinger equation. By varying the electron density until the energy from the functional is minimized, we can solve the Schrödinger equation using three-dimensional variables (the electron density), instead of  $3N$  variables (the wave function). This is why the method is called density functional theory.

The Kohn-Sham equations describe how to obtain single wave function from the electron density in the form of

$$\left[ -\frac{\hbar^2}{2m} \nabla^2 + V(r) + V_H(r) + V_{xc}(r) \right] \Psi_i(r) = \varepsilon_i \Psi_i(r). \quad (3.3)$$

The Kohn-Sham equations are very similar to the Schrödinger equation in (3.1). Here  $V(r)$  defines the interaction between an electron and the collection of atomic nuclei, the same as that

in the Schrödinger equation.  $V_H(r)$  is the Hartree potential, which describes the Coulomb repulsion between the electron being considered in one of the Kohn–Sham equations and the total electron density defined by all electrons in the problem.  $V_{xc}(r)$  defines exchange and correlation contributions to the single electron equations.  $V(r)$ ,  $V_H(r)$  and  $V_{xc}(r)$  are functions of the electron density.

Density functional theory is essentially solving the Kohn–Sham equations in an iterative way:

- (1) Input atomic structure and calculation parameters, and define an initial and trial electron density,  $n(r)$ .
- (2) Solve the Kohn–Sham equations (3.3) using the trial electron density in step 1, and obtain the single-particle wave functions,  $\Psi_i(r)$ .
- (3) Calculate the electron density using the single particle wave functions from step 2 according to equation (3.2).
- (4) Compare the calculated electron density in step 3 with the trial electron density in step 1. If the two densities are the same, then this is the ground-state electron density, and it can be used to compute other ground state properties. Otherwise, the trial electron density in step 1 must be updated according to the calculated electron density in step 3, and the process should be iterated until the two electron densities are the same (self-consistent).

The next question in practical density functional theory applications is what the form of the exchange–correlation functional is. The true form of the exchange–correlation functional is not known. Therefore, approximate exchange–correlation functionals are used in practice. The local density approximation (LDA) assumes locally uniform electron gas [144], which is generally accurate enough but slightly underestimates lattice parameters for metals [145, 146]. The general gradient approximation (GGA) considers the gradient of the electron density, and generally gives a better prediction than LDA, at least in aluminium alloys [146]. Two kinds of GGA functionals are widely used in practical calculations, the Perdew–Wang functional (PW91) and the Perdew–Burke–Ernzerhof functional (PBE) [139].

### 3.4.2 Parameters in DFT calculations

DFT calculations were implemented using the Vienna ab initio Simulation Package (VASP). Pseudopotentials (PAW [147]) based on the GGA method and the PBE parameterisation were used here [148], which shows good reproducibility for various elements [149]. Geometry relaxations were performed with an energy cut-off of 500 eV (for results in Chapter 4) or 600 eV (for results in Chapter 5 and 6), allowing full relaxation with respect to supercell vectors as

well as ionic positions, and were terminated until Hellmann-Feynman forces were less than  $0.01 \text{ eV/\AA}$ . The Methfessel and Paxton smearing method [150] (smearing factor:  $0.05 \text{ eV}$ ) was used for geometry optimization, while the tetrahedron method [151] was used for single-point energy calculations. The convergence of energy with different k-points (meshed by the Monkhorst-Pack method) is shown in Fig. 3.2. The convergence of energy is better than  $0.001 \text{ eV/atom}$  with the chosen k points (labelled in Fig. 3.2). Other supercells were calculated with similar densities of k points in reciprocal space to get similar levels of convergence.

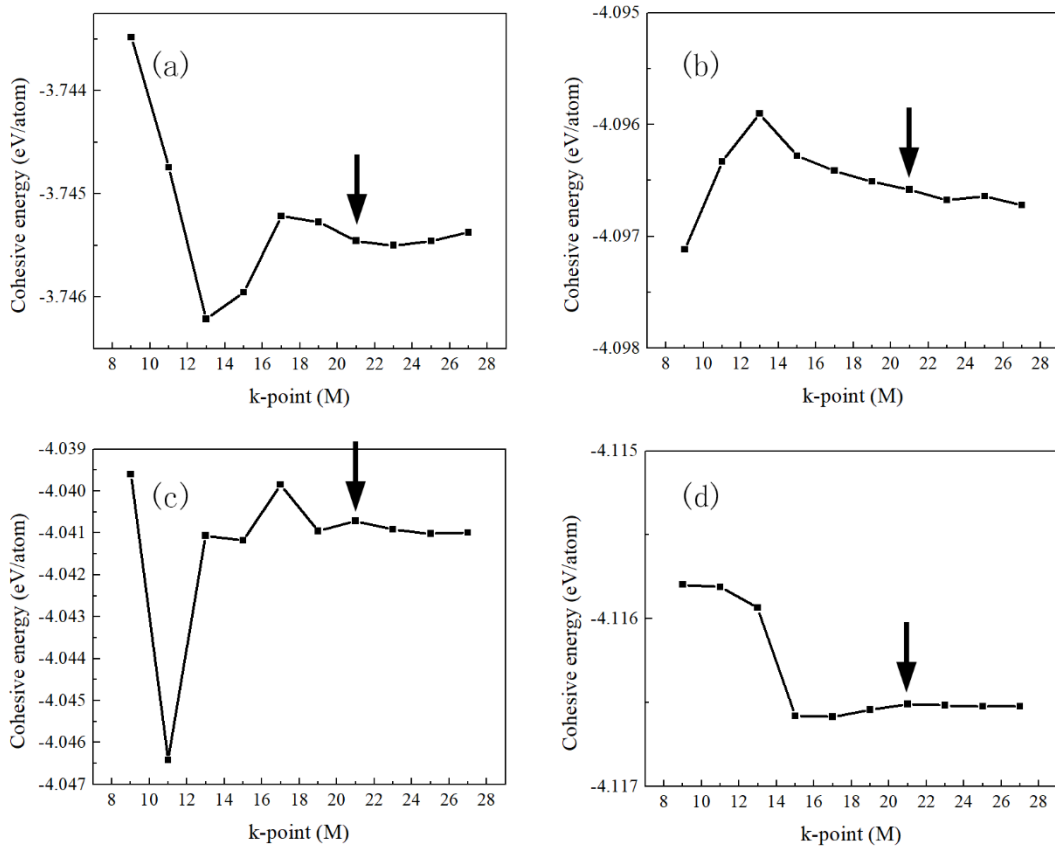


Fig. 3.2 Cohesive energy of FCC Al (a), FCC Cu (b),  $\theta'$  ( $\text{Al}_2\text{Cu}$ , in c) and  $\eta^*$  ( $\text{Al}_1\text{Cu}_1$ , in d) relative to  $M \times M \times M$  ( $M \times M \times N$  for  $\theta'$  and  $M \times L \times O$  for  $\eta^*$ ) k points. The k points labelled by arrows guarantee an energy convergence better than  $0.001 \text{ eV/atom}$ .

### 3.4.3 Formation energy and interfacial energy calculations

The binding energies between a vacancy and different configurations of solute atoms were calculated using 64-atom to 500-atom supercells. Here only first and second nearest neighbour separation between solute atoms and a vacancy were considered. In addition, a solute atom was always put at the first nearest neighbour positions of a vacancy, but it could be at the second nearest neighbour positions of another solute atom. The binding energy is the energy gain or

penalty of putting solute atoms and a vacancy together and is calculated by the following expression:

$$E_b = E(\text{Al}_{N-x-y-1}\text{In}_x\text{Sb}_y\text{V}_1) + (x + y) * E(\text{Al}_N) - xE(\text{Al}_{N-1}\text{In}_1) - yE(\text{Al}_{N-1}\text{Sb}_1) - E(\text{Al}_{N-1}\text{V}_1), \quad (3.4)$$

where  $E$  is the ground state energy of a supercell and the subscripts in parenthesis indicate the numbers of vacancies and atoms. For example,  $E(\text{Al}_{N-x-y-1}\text{In}_x\text{Sb}_y\text{V}_1)$  is the ground state energy of a supercell with  $(N - x - y - 1)$  Al atoms,  $x$  In atoms,  $y$  Sb atoms and 1 vacancy. The binding energies in the Al-Cu-Ge alloy were calculated similarly, by replacing In and Sb with Ge in the expression.

To evaluate the relative stability of different phases, the formation energy per constituent atom is defined as:

$$E_f = \frac{E(\text{Al}_x\text{Cu}_y) - xE(\text{Al}) - yE(\text{Cu})}{x+y}, \quad (3.5)$$

where  $E(\text{Al}_x\text{Cu}_y)$  is the total energy of the relaxed structure,  $E(\text{Al})$  and  $E(\text{Cu})$  are the energy of an Al or Cu atom in their stable crystal structures, respectively. Precipitates with other compositions were calculated similarly. In this thesis, the formation energy of a precipitate embedded in the Al matrix was also compared. In this condition, the calculated formation energy has subtracted the penalties from strain energy and interfacial energy, and is expressed as:

$$E_f = \frac{E(\text{Al}_x\text{Cu}_y) - xE(\text{Al}) - yE(\text{Cu})}{x_{\text{inside}} + y_{\text{inside}}}, \quad (3.6)$$

where  $x_{\text{inside}}$  and  $y_{\text{inside}}$  are Al and Cu numbers inside the precipitate ( $x_{\text{inside}} < x$ ,  $y_{\text{inside}} = y$ ).

Interfacial energy is usually defined as the energy cost when putting two infinitely separated crystals together. However, in DFT calculations, the two crystals will be strained near the interface to achieve a good structural match. Therefore, the coherent strain energy should be separated from the energy cost. Here, the interfacial energy was calculated following the well-established method in the literature [29, 152-155]. The energy cost of putting two crystals together is expressed as:

$$E_{f\text{-interface}} = E(\text{crystal1} + \text{crystal2}) - E(\text{crystal1}) - yE(\text{crystal2}), \quad (3.7)$$

where  $E(\text{crystal1} + \text{crystal2})$  is the energy of a supercell composed of both crystal 1 and crystal 2.  $E(\text{crystal1})$  and  $E(\text{crystal2})$  are the energy of a supercell of crystal 1 or 2, respectively. The calculated energy cost,  $E_{f\text{-interface}}$ , can be decomposed into two parts: the strain energy of deforming the two crystals and the interfacial energy, and is expressed as:

$$E_{f-interface} = N\Delta E_{coherent-strain} + 2A\gamma, \quad (3.8)$$

where  $N$  is the total number of atoms in the supercell,  $\Delta E_{coherent-strain}$  is the coherent strain energy per atom,  $A$  is the area of the interface and  $\gamma$  is the interfacial energy. Dividing the two sides of (3.7) by  $N$ , we can get the following expression,

$$\frac{E_{f-interface}}{N} = \Delta E_{coherent-strain} + \frac{2A\gamma}{N}, \quad (3.9)$$

where the formation energy per atom,  $\frac{E_{f-interface}}{N}$  is a function of  $1/N$ , and the slope is  $2A\gamma$ .

Thus, the interfacial energy can be calculated by plotting  $\frac{E_{f-interface}}{N}$  vs  $1/N$ .

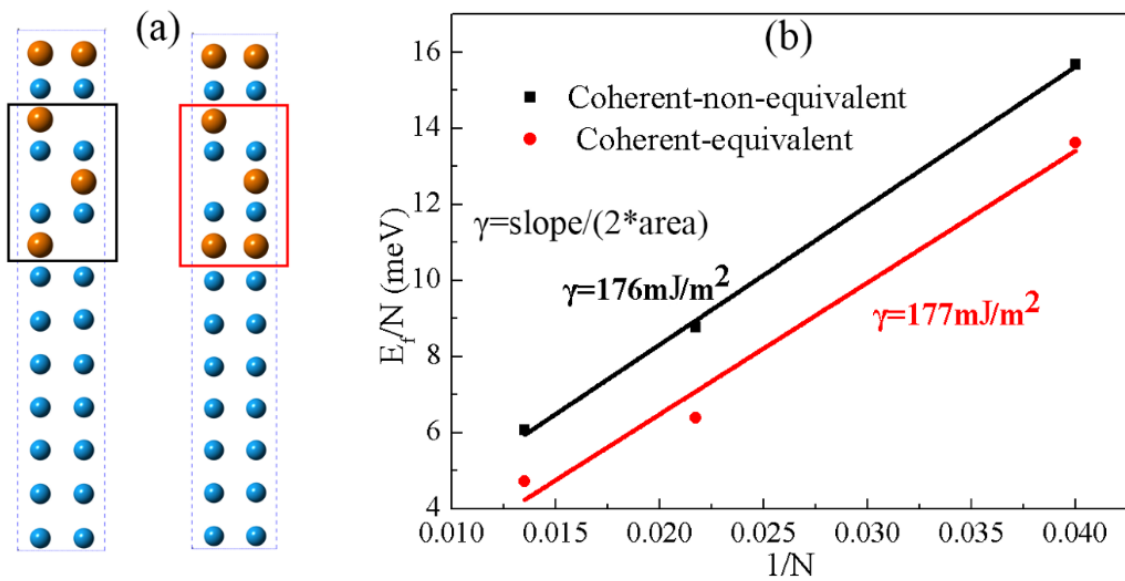


Fig. 3.3 Atomic models of the coherent  $\theta'/Al$  interface and the calculated interfacial energies. (a) Atomic models with equivalent or non-equivalent interfaces (normal unit cell of  $\theta'$  and a modified cell of  $\theta'$  are highlighted by black and red rectangles, respectively), (b) plotting of  $E_f/N$  vs  $1/N$ .

The two interfaces in the above calculations can be equivalent or non-equivalent. If the two interfaces have different atomic structures, the two interfaces will be non-equivalent and have different interfacial energies. As stated in a recent report, it is not easy to calculate the two different interfacial energies separately [153], because precipitates may have a non-integral size of the corresponding unit cell. The Cu-segregation at the coherent  $\theta'/Al$  interface is such a case, which makes the calculation of the coherent interfacial energy difficult, as shown in Fig. 3.3. Here we can use a modified cell of  $\theta'$  (in the red rectangle of Fig. 3.3 (a)) to overcome this. The  $\theta'$  part in the atomic models can be built by a combination of the normal or the new cell of  $\theta'$ , thus making the calculation of the interfacial energy of both the equivalent and non-equivalent interface possible. The calculated interfacial energies in Fig.3.3 (b) show that the

energy difference between the two approaches is small,  $1 \text{ mJ/m}^2$ . For simplicity, in the case that a non-equivalent interface is inevitable, the averaged non-equivalent interfacial energy is used to approximate the real interface energy.

### 3.5 Thermodynamic database for the Al-Cu binary alloy

To validate the calculations from DFT calculations, thermodynamic analysis was also carried out using a thermodynamic database in Thermal-Calc 2018a for the Al-Cu binary alloy [20, 156]. The database was built based on well-verified experimental results. Calculated Al-Cu phase diagram based on the database shows excellent agreement with the experimental Al-Cu phase diagram even for GP I zones,  $\theta''$  and  $\theta'$  precipitates [20], as shown in Fig. 3.4.

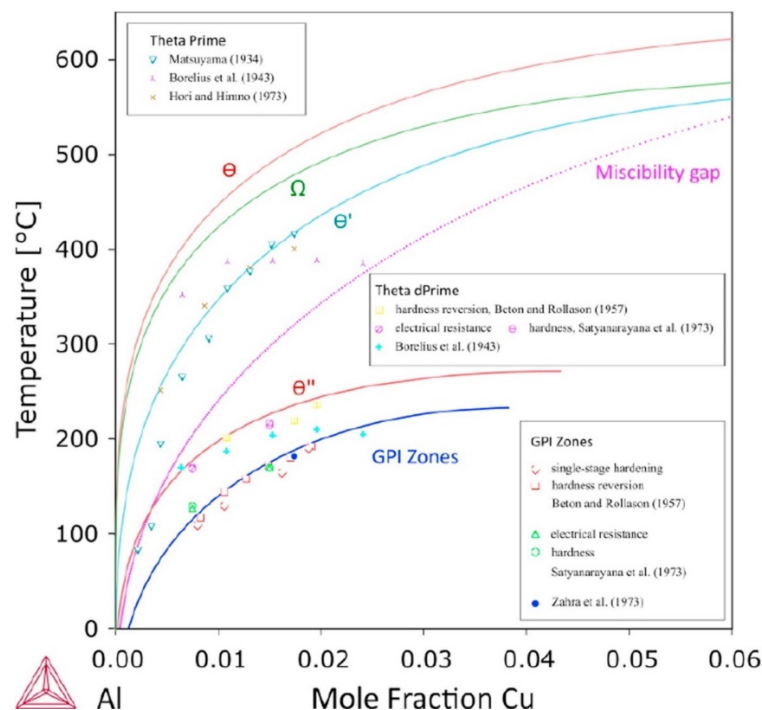


Fig. 3.4 Calculated Al-Cu phase diagram showing precipitates, in comparison with experimental results. Reproduced with permission from [20]. The references in the figure are from the original paper.

## Chapter 4

# Two precipitation sequences in an Al-1.7at.%Cu-0.025at.%In-0.025at.%Sb alloy<sup>1</sup>

About 70 years ago, minor additions of In (~0.05 at. %) into Al-Cu alloys were found to enhance both precipitation kinetics and peak hardness [30, 32]. This was later attributed in part to the high binding energy between In atoms and vacancies [34, 38]. Sb also has a comparably high vacancy binding energy [39] but, to the best knowledge of the author, has never been investigated regarding its potential role in the precipitation of Al-Cu alloys. Early work on the beneficial role of these elements has mainly dealt with a single element [35, 157]. It is still unclear if the precipitates associated with the single microalloying element also contribute to these beneficial effects. The combined additions of In and Sb form a compound instead of single elemental precipitates. This may offer an opportunity to discover if single elemental precipitates containing microalloying elements are critical on the enhancing effects of the microalloying elements.

Here the effects of combined additions of In and Sb on the hardness response and precipitation mechanisms of the classic Al-1.7at.% Cu alloy are reported. The combined additions show a similar enhancing effect on precipitation kinetics and peak hardness as that of a single element addition. There are two nucleation sequences between InSb particles and Cu-rich precipitates. Cu-rich precipitates mainly nucleate heterogeneously from already-formed InSb particles at the common ageing condition (immediate artificial ageing at 200 °C after quenching). However, InSb particles can nucleate after and heterogeneously from Cu-rich precipitates when the ageing conditions are changed. The two nucleation sequences are closely correlated with excess vacancies and can be selectively controlled by quenching rate, ageing temperature and solute-vacancy cluster size.

---

<sup>1</sup> Most of the chapter has been published in *Acta Materialia* 141 (2017): 341-351.

## 4.1 Hardness response

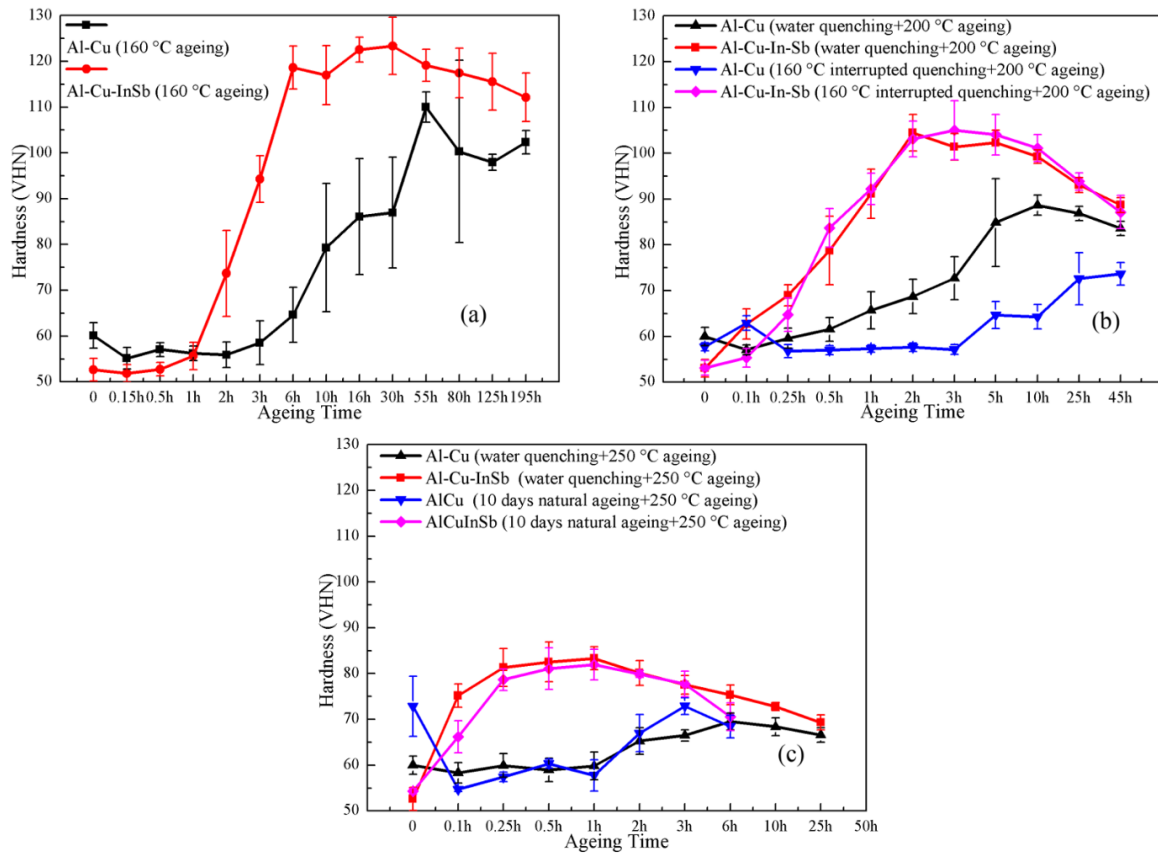


Fig. 4.1 Hardness curves for the Al-Cu alloy and the Al-Cu-In-Sb alloy aged at different temperatures.

The hardness curves for the Al-1.7at.%Cu alloy and the Al-1.7at.%-0.025at.%In-0.025at.%Sb alloy are shown in Fig. 4.1. It can be readily seen that the combined In and Sb additions always accelerate the precipitation kinetics and increase peak hardness compared with the Al-Cu binary alloy when samples were prepared with conventional heat treatments, regardless of the ageing temperature. For the binary alloy aged at 160 °C, there is a two-stage hardness increase, which corresponds to the successive formation of GP zones,  $\theta''$  and  $\theta'$  [22]. According to the literature, this feature is completely suppressed by In or Sn additions [30, 157], but here it may be inherited in the alloy with In and Sb additions though the error bar is very large (Fig. 4.1 a). The two-stage feature of the alloys with In and Sb suggests the enhancing mechanism of the combined additions may be different from that of In and Sn. The hardness curves continuously increase before the peak values for alloys aged at 200 °C and 250 °C. The latter case (250 °C) is in contrast to what has been observed in Al-Cu-Sn/In/Cd alloys, where the additions no longer increase peak hardness though slightly accelerate kinetics [30]. Besides the common ageing conditions, interrupted quenching and natural ageing before

artificial ageing were also investigated. The interrupted quenching at 160 °C makes the ageing kinetics more sluggish in the Al-Cu binary alloy. However, the interrupted quenching does not affect the ageing kinetics significantly in the Al-Cu-In-Sb alloy except for the lower hardness at 0.1 h and 0.25 h. 10 days natural ageing gives a very high initial hardness in the binary alloy aged at 250 °C but does not change the initial hardness in the quaternary alloy. This is consistent with the early observation that In and Sb (and other similar elements) can suppress the formation of GP zones by restricting Cu diffusion [34]. Here 10 days natural ageing also renders a lower hardness at 0.1 h and 0.25 h in the quaternary alloy compared with that with conventional heat treatments, as the interrupted quenching (two steps quenching led by a quenching at 160 °C for 60 s). The lower hardness suggests slow kinetics at the early ageing stage for the Al-Cu-In-Sb alloy undergone interrupted quenching or natural ageing.

## 4.2 Microstructures at different ageing conditions

### 4.2.1 Without natural ageing or interrupted quenching

Fig. 4.2 shows the typical microstructures of the Al-Cu-In-Sb alloy aged to the peak hardness.  $\theta'$  is the main strengthening precipitate with rare GP zones and  $\theta''$  present. The dispersion of  $\theta'$  in the quaternary alloy is uniform for the three ageing temperatures. In contrast, the precipitates in the binary alloy distribute uniformly. According to the statistics of the phase constituents in the binary and quaternary alloy aged at 200 °C for 2 h (Fig. 4.2 (e)), the quaternary alloy is composed of only  $\theta'$ . However, for the binary alloy, half of the precipitates are  $\theta''$ . The number density of precipitates in the binary and quaternary alloy is  $1650 \pm 50 \mu\text{m}^{-3}$  and  $\sim 1890 \pm 40 \mu\text{m}^{-3}$ , respectively. Therefore, the presence of In and Sb significantly enhances the formation of  $\theta'$ . The length distribution of precipitates ( $\theta'$ ) at peak hardness for 200 °C and 250 °C suggests the difference between 200 °C and 250 °C ageing is negligible. The inferior hardness at 250 °C comes from a small length-to-thickness aspect ratio [158] and a low precipitate number density ( $1000 \pm 50 \mu\text{m}^{-3}$ ). The significant thickening of precipitates for 30 min ageing at 250 °C (Fig. 4.2 (c)) suggests the combined additions of In and Sb are not efficient to prevent precipitate thickening, though DFT calculations suggest In and Sb may do this [102].

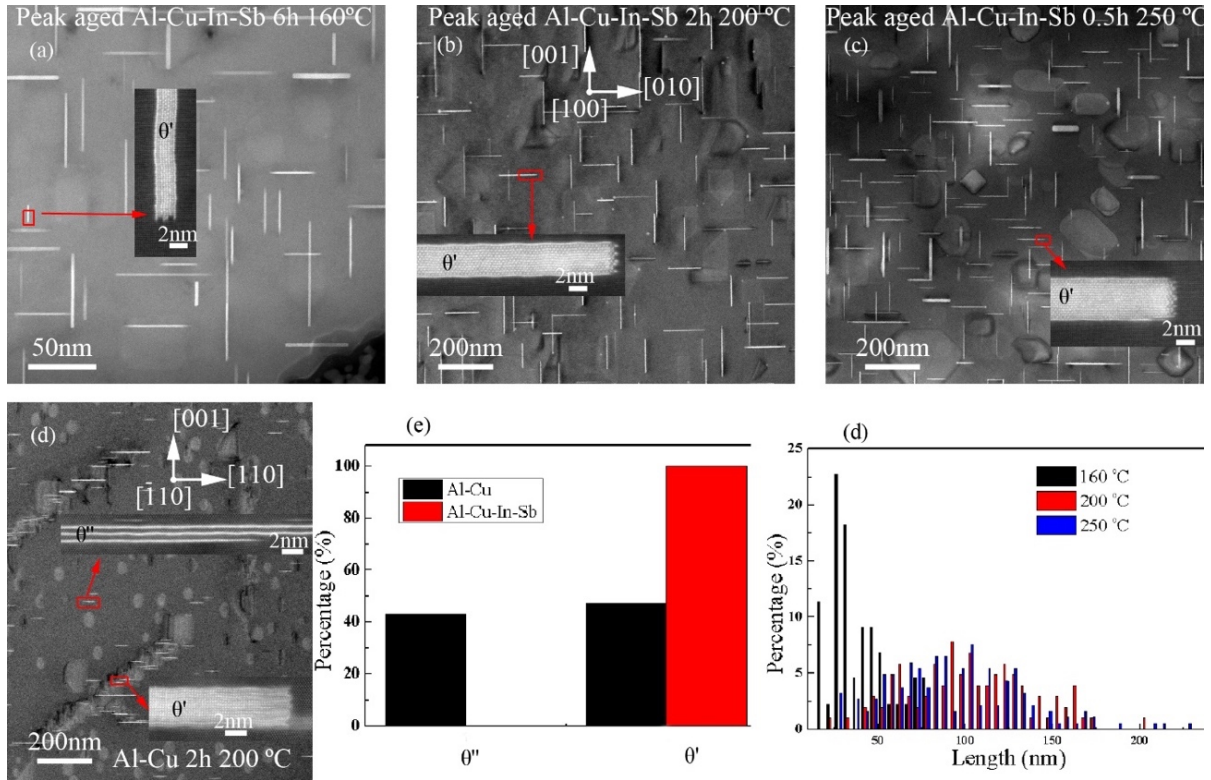


Fig. 4.2 HAADF-STEM images of the alloys and summary of precipitate types and length distribution. (a) the quaternary alloy aged 6 h at 160 °C, (b) the quaternary alloy aged 2 h at 200 °C, (c) the quaternary alloy aged 30 min at 250 °C, (d) the binary alloy aged 2 h at 200 °C, (e) comparison of Cu-rich phases between the binary and quaternary alloys aged 2 h at 200 °C, (f) length distribution for the quaternary alloy at the peak hardness condition. The insets in (a)-(d) are images of typical Cu-rich precipitates.

Fig. 4.3 shows the typical microstructures of Al-Cu-In-Sb alloy aged for 2 min and 10 min at 200 °C, the very early ageing stage. These times correspond to the early stage of precipitation hardening at 200 °C. In HAADF-STEM images, the intensity is roughly proportional to  $Z^{1.7}$  ( $Z$  is the atomic number) in projection. Therefore, atomic columns enriched with Cu, In and Sb are brighter than the aluminium matrix. After 2 min ageing, nanoscale truncated octahedral particles form in the aluminium matrix. The existence of two-dimensional moiré fringes blurs the atomic structure of the nanoscale particles. It is reasonable to view these nanoscale particles as precipitates containing In and Sb atoms, similarly to Al-Cu alloys containing Sn or In [16]. However, the lattice parameter calculated according to the spacings of moiré fringes and the aluminium matrix is different from the stable crystal structure of InSb ( $F\bar{4}3m$ ,  $a=0.648\text{nm}$ ) [159], In ( $I4/mmm$ ,  $a=b=0.325$ ,  $c=0.495$ ) [160] or Sb ( $R\bar{3}m$ ,  $a=b=0.431\text{nm}$ ,  $c=1.1273\text{nm}$ ) [160] and will be discussed in Section 4.3. This means that the InSb precipitates adopt a different crystal structure compared with the most stable structure in the bulk state. Another salient feature of the nanoscale particles is the presence of one atomic layer structure at their truncated

surfaces. Chemical analysis by EDS or electron energy loss spectroscopy (EELS) could not ascertain the composition of these one-layer structures. However, they are likely to be Cu GP zones, as Cu GP zones occur in the first stage of precipitation in Al-Cu alloys but at a temperature lower than 200 °C. It is interesting to note that GP zones are never larger than the truncated surface of the octahedral particles, which means the interface between the octahedral particles and the aluminium matrix stabilises GP zones. Therefore, GP zones nucleate after the octahedral particles and on the truncated surfaces. GP zones and octahedral particles are combining together and are the only precipitates at the very early ageing stage. There are no individual GP zones or InSb particles at the early ageing stage.

With a longer ageing time of 10 min (Fig. 4.3 (b)-(d)) GP zones are replaced by other Cu-rich phases. Fig. 4.3 (b) and (c) reveal a  $\theta''$  precipitate with only one Cu layer covering the truncated surface of the octahedral particles. This special geometry suggests the  $\theta''$  precipitate grows from the GP zones. Besides,  $\theta'$  precipitates also begin to form from the truncated surface of the octahedral particles (see Fig. 4.3 (d)). This seems to be the first direct experimental observation of heterogeneous nucleation of  $\theta'$  on other solute correlated particles. There are always only one  $\theta''$  or  $\theta'$  precipitate on one octahedral particle. The other GP zones docking on the truncated surface disappear with the growth of the octahedral particles. The complete precipitation sequence from GP zones to  $\theta'$  precipitates in the quaternary alloy is different from both the binary alloy and alloys with Sn. For the binary alloy, GP zones cannot form when aged at 200 °C. For the alloys with Sn, both GP zones and  $\theta''$  are skipped at 200 °C [40].

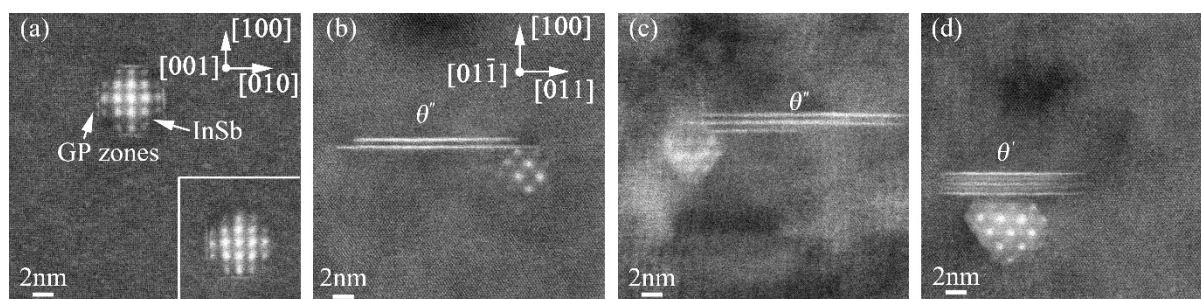


Fig. 4.3 HAADF-STEM images of the quaternary alloys aged at 200 °C for different times. (a) 2 min, the inset is an InSb particle truncated only at two faces, (b) 10 min, (c) 10 min, (d) 10 min.

To further clarify the spatial distribution of In and Sb atoms relative to the Cu rich phases, we present the EDS mappings of a sample aged for 30 min (Fig. 4.4). Note that the measurement was carried out off zone axis in order to minimise channelling effects. It is easy to distinguish the faceted shape of Cu-rich phases and the polyhedral shape of the octahedral

particles. The enrichment of both In and Sb indicates the octahedral particles are a compound of In and Sb. Besides, there are no detectable enrichment of Cu in the octahedral particles and no In/Sb enrichment in Cu precipitates.

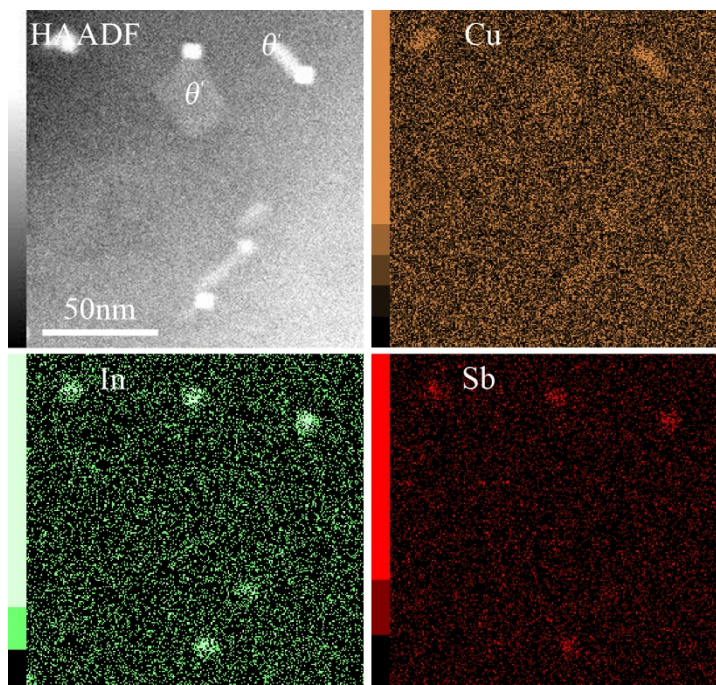


Fig. 4.4 EDS elemental mappings of the quaternary alloy aged for 30 min at 200 °C. The corresponding HAADF-STEM image is at the top left corner.

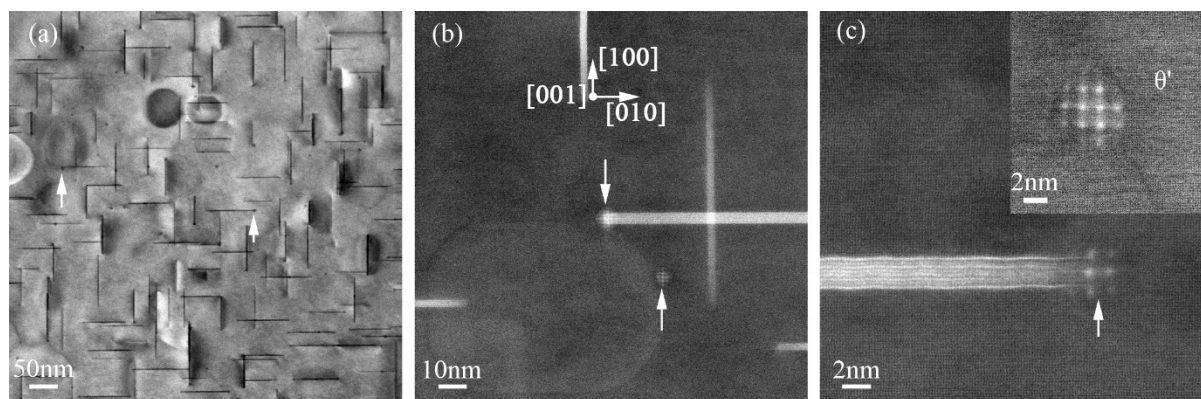


Fig. 4.5 STEM images of the quaternary alloy aged at 250 °C for 2 min. (a) low magnification BF image, (b) and (c) HAADF images, the arrows indicating InSb particles, the inset in (c) showing an InSb particle attaching to a face-on  $\theta'$  precipitate.

The different ageing response of the quaternary alloy aged at 250 °C is manifested more clearly in the microstructure (Fig. 4.5). After only 2 min ageing, there are abundant octahedral particles and  $\theta'$  precipitates (Fig. 4.5 (a)). It is interesting to note that the octahedral particles are mainly located at the periphery of faceted  $\theta'$  precipitates. Instead of attaching to the broad

faces of  $\theta'$  precipitates (see Fig. 4.3 (d)), here the octahedral particles of InSb stick to the edges of  $\theta'$  precipitates. According to the moiré fringe of the octahedral particles (Fig. 4.5 (b) and (c)), the crystal structure of InSb particles is the same as that in the alloy aged at 200 °C. This means that the high ageing temperature cannot change the crystal structure of InSb particles but rather changes their nucleation sequence relative to  $\theta'$  precipitates. Considering the position of the InSb particles relative to  $\theta'$  precipitates, it is reasonable to speculate that InSb particles nucleate at the semi-coherent interface of the already formed  $\theta'$  precipitates.

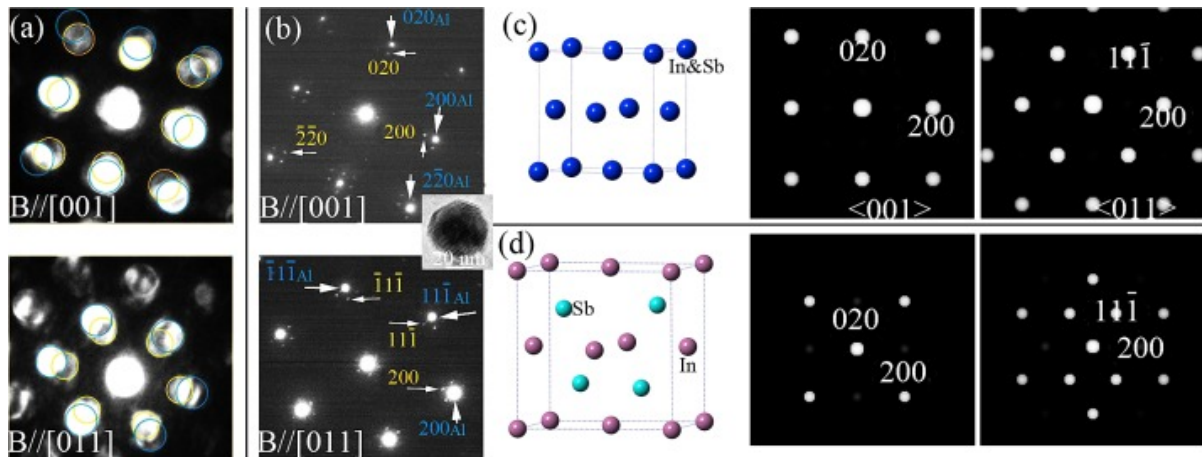


Fig. 4.6 (a) nano diffraction patterns of a  $\sim 5$  nm InSb particle together with the Al matrix in the quaternary alloy aged for 2 h at 200 °C (B in insets means incident beam), (b) selected area electron diffraction patterns of a  $\sim 50$  nm InSb particle together with the Al matrix in the quaternary alloy aged for 30 days at 300 °C, the inset shows the TEM image of the particle, (c) schematics of the measured crystal structure and the corresponding simulated diffraction patterns (left,  $\langle 001 \rangle$ , right,  $\langle 011 \rangle$ ), (d) schematics of InSb bulk stable crystal structure and the corresponding simulated diffraction patterns (left, B along  $\langle 001 \rangle$ , right, B along  $\langle 011 \rangle$ ).

It is difficult to determine the crystal structure of the nanosized octahedral particles using selected area electron diffraction (SAED). Therefore, nano diffraction in scanning transmission electron microscopy mode was used first. The insets in Fig. 4.6 (a) are the nano diffraction patterns with the incident beam parallel to  $\langle 001 \rangle_{\text{Al}}$  and  $\langle 011 \rangle_{\text{Al}}$ , respectively. The convergent beam (nominal probe size 0.2 nm) was focused on a  $\sim 5$  nm nanoscale particle, producing diffraction disks from both the aluminium matrix and the particle. Due to the greater thickness of the matrix, the corresponding diffraction disks are generally brighter than that of the nanoparticles. The similarity of the diffraction patterns of the nanoscale particle and that of the aluminium matrix suggests they share the FCC structure. From the diffraction patterns, the lattice constant of the nanoscale particles is calculated to be  $0.480 \pm 0.004$  nm. After determining the crystal structure, it is possible to calculate the lattice constant from the moiré fringes. Consistent with the diffraction patterns, the lattice constant of the octahedral particles is always

0.480±0.003 nm for all the octahedral particles reported in this work. Therefore, the InSb particles adopt the same crystal structure as the Al matrix but have a bigger lattice constant than Al.

We aged the quaternary alloy for 30 days at 300 °C to investigate the stability of the InSb particles. Surprisingly, the selected area electron diffraction patterns from a ~50 nm particle show that the cubic close-packed structured InSb particles are very stable, with no detectable changes in crystal structure (Fig. 4.6 (b)) compared with what was found at lower ageing temperatures and times. Here the absence of  $\theta'$  around the InSb particle does not mean these two phases precipitate separately. Due to the high ageing temperature and long ageing time,  $\theta'$  or even  $\theta$  precipitates already grow very large, making them vulnerable to electropolishing. Therefore, Cu-rich phases were not found in this sample by TEM.

*Table 4.1 Comparison of lattice constants of InSb particles between experimental results and DFT calculations.*

	Lattice constant (nm)	Formation energy (eV)
Experiment (cubic close-packed)	a=b=c=0.480±0.004	NA
In <sub>1</sub> Sb <sub>3</sub> (cubic close-packed, DFT) [25]	a=b=c=0.481	0.72
In <sub>2</sub> Sb <sub>2</sub> (cubic close-packed before relaxation, DFT)	a=b=0.464, c=0.521 (shape changed)	0.33
In <sub>3</sub> Sb <sub>1</sub> (cubic close-packed, DFT) [25]	a=b=c=0.484 a=b=c=0.480	0.09 0.02
In <sub>4</sub> (Fm $\bar{3}$ m, DFT) [25] Sb <sub>4</sub> (Fm $\bar{3}$ m, DFT) [25]	a=b=c=0.479	1.28
InSb (stable phase, F4 $\bar{3}$ m) [25]	a=b=c=0.663	-1.05
1 solute In atom in Al matrix	NA	0.78
1 solute Sb atom in Al matrix	NA	1.02

In order to investigate the stability of the newly determined close-packed InSb structure, we performed DFT calculation for a range of possible InSb structures. Table 4.1 shows a comparison of the experimentally measured and DFT calculated lattice constants of the InSb particles. The calculated results are consistent with the available DFT database [62]. In an FCC

unit cell, there are four atom sites (1 for the corners and 3 for the face centres). Since the real composition of the InSb particles cannot be accurately measured, there are three possibilities for the composition of the InSb particles, i.e.,  $\text{In}_1\text{Sb}_3$ ,  $\text{In}_2\text{Sb}_2$ , and  $\text{In}_3\text{Sb}_1$ . Except for the composition of  $\text{In}_2\text{Sb}_2$ , the calculated lattice constants are very close to those measured experimentally, which further validates the existence of the cubic close-packed InSb phase. Please note that the DFT calculations used a chemically ordered structure. Chemically disordered  $\text{In}_2\text{Sb}_2$  in FCC lattice is anticipated to give a lattice constant  $\sim 0.48$  nm because both pure In and pure Sb in FCC lattice have a lattice constant of about 0.48 nm. The simulated diffraction patterns of chemically disordered InSb are shown in Fig. 4.6 (c). The excellent agreement between the simulated and experimental diffraction patterns indicates the InSb particles can adopt the cubic close-packed structure. The crystal structure of the most stable structure of bulk InSb ( $F\bar{4}3m$ , not close-packed) and corresponding simulated diffraction patterns are shown in Fig. 4.6 (d). The lattice parameter of the cubic close-packed InSb is smaller than that of the bulk InSb ( $F\bar{4}3m$ ) in real space, as reflected in the diffraction patterns.

The formation energy relative to the stable single element phases suggests the cubic close-packed phase is energetically favourable with more In because pure FCC In has much lower formation energy than that of pure FCC Sb. Even though the formation energies for all the cubic close-packed InSb phases are positive, they are much lower than the formation energy of solute In or Sb atoms in the aluminium matrix (Table 4.1 and [146]). Therefore, In and Sb atoms should be expected to have high driving forces to precipitate from solute atoms in the aluminium matrix into cubic closed-packed precipitates. The significantly positive formation energies of these cubic close-packed InSb phases, especially compared with the negative formation energy of the stable  $F\bar{4}3m$  InSb phase, suggest these cubic close-packed InSb phases hardly form outside the Al matrix at ambient conditions. This is why these InSb phases have never been reported in the literature.

The strain energy accompanying the InSb precipitates in the Al matrix is thought to significantly contribute to the formation of the closed-packed InSb phase. Even though the energy change (volume energy change) from solute In and Sb atoms to the cubic closed-packed InSb phase is negative and is the driving force for the phase transformation (nucleation), the energy change is less negative than the transformation from solute In and Sb atoms to the stable  $F\bar{4}3m$  InSb phase. Therefore, the cubic closed-packed InSb phase is not favoured compared with the  $F\bar{4}3m$  InSb phase, regarding the driving force of nucleation. However, another two important energy costs must be considered for the nucleation of a precipitate in the Al matrix, strain energy and interfacial energy. If InSb precipitates adopt the  $F\bar{4}3m$  structure, each atom

will expand by 105% relative to the Al matrix. In contrast, for the cubic close-packed structure, the expansion is only 67%. Thus, the formation of  $F\bar{4}3m$  InSb phase from the Al matrix will induce a significant strain due to expansion. However, the cubic close-packed InSb phases could have a very low residual strain energy by adopting magic sizes with the help of vacancies, as has been shown in FCC structured Pb precipitates in the Al matrix [90, 91]. The strain energy is widely observed to dictate the nucleating phase taking a matching structure with the confining matrix [44, 161], just as the interfacial energy. Since the interfacial energy is proportional to the square of the particle radius and the volume energy change is proportional to the cube, the interfacial energy determines a phase transition only at small particle sizes. However, the strain energy in our case is also proportional to the cube of the particle radius, similarly to the volume energy change. Therefore, if the strain energy can reverse the energetic stability between two competing phases, the stability trend will be independent of particle size. This is why the cubic close-packed InSb particles are still stable even after the particle radius increases by one order.

#### 4.2.2 With natural ageing or interrupted quenching

Fig. 4.7 displays the microstructure of the quaternary alloy aged for 2 min at 250 °C after 10-days natural ageing at room temperature. In contrast to what was observed for the sample directly aged after solution treatment (Fig. 4.4), there is a significant amount of InSb particles located at the broad face of  $\theta'$  precipitates, even though these precipitates coexist with a comparable amount of InSb particles located at the semi-coherent edges of  $\theta'$  precipitates. Again, the InSb particles are still cubic close-packed according to their moiré fringes in Fig. 4.7 (b). For one face-on  $\theta'$  precipitate in Fig. 4.7 (c), there are 5 InSb particles located at the semi-coherent edge and docked mainly at the corners. One InSb particle is attached to the broad face and is a bit off the face edge. The InSb particles located at the semi-coherent edge nucleate after the  $\theta'$  precipitate as discussed above (see section 4.2.1). Corners have high energy because they have a higher interface/volume ratio than edges, thus being a good nucleation site with a lower nucleation energy barrier [22]. This explains the preferred locations of these edge-located InSb particles. Since dislocations are often observed at the semi-coherent interface between  $\theta'$  and the Al matrix (see Fig. 1 in [28]) and dislocations can significantly accelerate solute diffusion through pipe diffusion [97], diffusion of solute In and Sb atoms will be much easier along the  $\theta'$  periphery than in the Al matrix. The diffusion (segregation) of In and Sb along the  $\theta'$  periphery should change the interfacial energy of the  $\theta'$ /Al semi-coherent interface. This consequently changes the morphologies of  $\theta'$  precipitates at the peak aged condition (see

more discussion in Section 4.5). There are a lot of  $\theta'$  precipitates developing a quadrilateral morphology, as shown in Fig. 4.2. However, in Al-Cu binary alloy or Al-Cu-Au ternary alloy, there are only oval  $\theta'$  precipitates at the peak aged condition [49]. The preferred diffusion of In and Sb atoms along the  $\theta'$  periphery can also partially explain why InSb particles tend to be located at the edge or near the edge, even for those particles nucleating before  $\theta'$  precipitates.

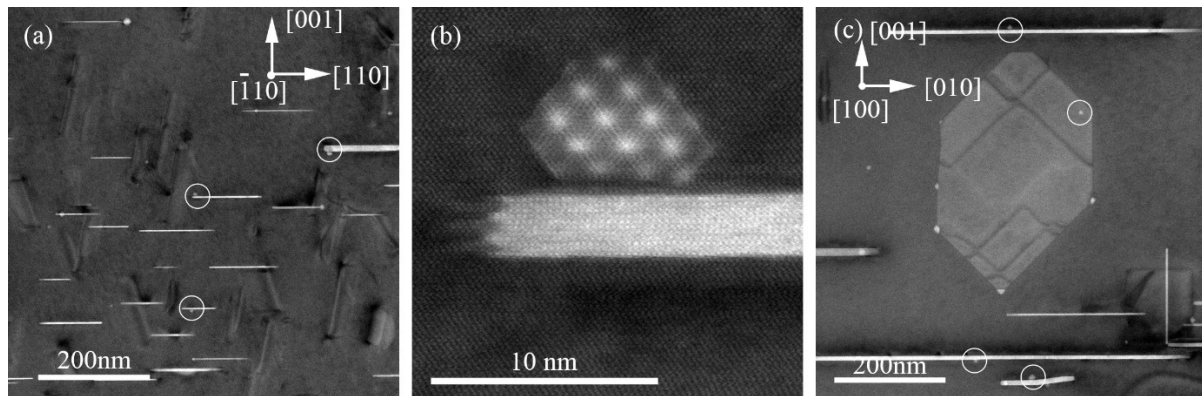


Fig. 4.7 HAADF-STEM images of the quaternary alloys aged at 250 °C for different times after 10 days natural ageing. (a) and (b) 20 min, (c) 1 h. The white circles indicate InSb particles on the broad surface (the coherent interface with the Al matrix) of a  $\theta'$  precipitate.

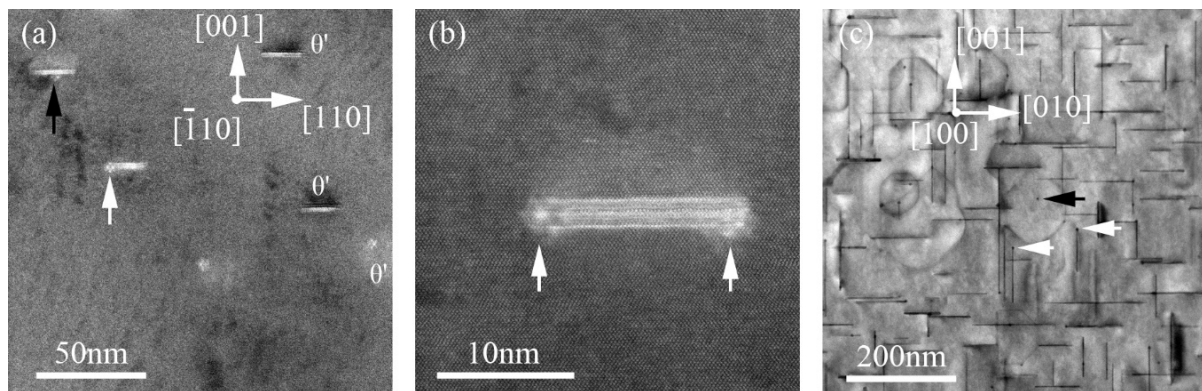


Fig. 4.8 STEM images of the quaternary alloy aged at 200 °C for different times after interrupted quenching; (a) HAADF image for 10 min aged alloy, (b) and (c) HAADF images for 20 min aged alloy, (c) low magnification BF image for 2 h aged alloy. The white and black arrows indicate InSb particles at the semi-coherent and coherent interface of  $\theta'$ , respectively.

Similarly to the effect of natural ageing on InSb locations, the interrupted quenching process also can change the precipitation process. Fig. 4.8 shows the precipitates in the quaternary alloy quenched first in 160 °C oil bath for 60 s and then in room temperature water. 20 min ageing at 200 °C only produces sparse  $\theta'$  precipitates and InSb particles while 10 min ageing could not induce any observable precipitates. This means the precipitation kinetics is much slower than that in normal ageing conditions (Fig. 4.3). This is consistent with the lower

hardness in the interrupted quenched quaternary alloy before 0.25 h (Fig. 4.1 (b)). Interrupted quenching is well known to reduce the supersaturated vacancy concentration [162]. Meanwhile, vacancies play an important role in enhancing diffusion [83, 84, 163]. Thus, after interrupted quenching, the diffusion is more sluggish, and nucleation of any phases is more difficult. As shown in Fig. 4.8 (a) and (b), there are InSb particles at the semi-coherent edges of some  $\theta'$  precipitates, which means these InSb particles nucleate after  $\theta'$  precipitates. Some of  $\theta'$  precipitates grow, without the presence of InSb particles near the edges. However, no InSb particles are found to grow by themselves because their nucleation from the Al matrix is more difficult than that at the  $\theta'$ /Al interface. This can further indicate that  $\theta'$  precipitates nucleate first if InSb particles are not at their broad faces. Even though one InSb particle is located at the broad face of the  $\theta'$  precipitate in Fig. 4.8 (a), it is a rare case according to the low magnification image in Fig. 4.8 (c). The fact that most of InSb particles nucleate after  $\theta'$  precipitates suggests that interrupted quenching makes the diffusion of In and Sb more difficult than that of Cu. In other words, the diffusion of In and Sb relies more on the solute-trapped vacancies compared with the diffusion of Cu.

### 4.3 DFT calculations of solute-vacancy binding energies

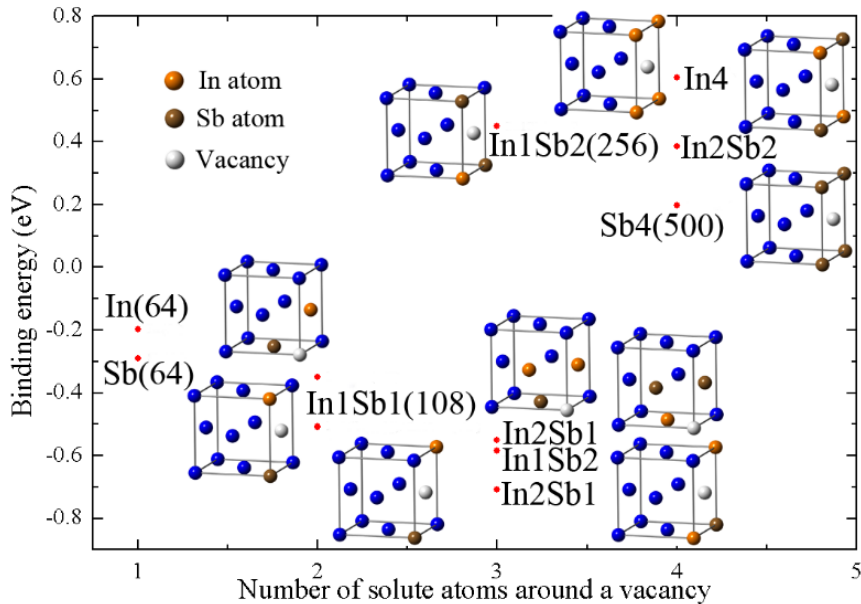


Fig. 4.9 Binding energies between solute atoms and a vacancy calculated from DFT. The inset shows the schematic configurations of solute atoms around a vacancy and the number in parentheses is the size of the supercell.

Fig. 4.9 exhibits DFT calculated binding energies between a vacancy and different numbers of solute In and Sb atoms. The calculated binding energy between a vacancy and a solute In or Sb atom is in good agreement with the literature report [39]. The binding energy becomes more negative with increasing number of solute atoms until four solute atoms. This means that more solute atoms (up to 3) around a vacancy are energetically favourable. Please note that calculations here only consider the scenario that solute atoms are at the first nearest neighbour position of a vacancy. There are also other possible configurations that may be energetically favourable even for solute number bigger than 4. However, the simplification here does not compromise the conclusion that a bigger solute-vacancy cluster can be more energetically favourable. The binding energies between three solute atoms around one vacancy show a very big scatter, which may suggest the interatomic interactions between solute atoms are important on the binding energy between solute atoms and a vacancy.

#### **4.4 A rationale for the two different precipitation sequences: the critical role of vacancies**

As reported above, the combined additions of In and Sb can effectively accelerate precipitation kinetics and increase peak hardness compared with the binary alloy. Even though peak hardness is always increased, independent of the ageing temperature, the atomic microstructures shown above suggest the mechanisms behind the promoted nucleation of  $\theta'$  by In and Sb additions at different ageing temperatures are different. With a normal heat treatment protocol, InSb particles nucleate first from the Al matrix in the samples aged at 200 °C, and GP zones,  $\theta''$  and  $\theta'$  precipitates nucleate on the truncated surfaces of the InSb particles successively. However, 250 °C ageing makes  $\theta'$  become the first nucleating phase, and InSb particles nucleate at the high-energy surfaces on  $\theta'$  precipitates, i.e., the semi-coherent  $\theta'/\text{Al}$  interface. If we change the heat treatment protocol, surprisingly, we can partially reverse the mechanism by which In and Sb additions promote  $\theta'$  precipitation at different ageing temperatures. More specifically, using 10 days natural ageing before ageing at 250 °C, we can make about half of InSb particles nucleate before  $\theta'$  precipitates. These InSb particles offer energetically favourable nucleation sites for  $\theta'$  precipitates. In contrast, by interrupted quenching, we deprive almost all InSb particles of the leading position on the nucleation sequence.  $\theta'$  precipitates nucleate first and then catalyse the nucleation of InSb particles. This phenomenon is controlled by a factor that depends on ageing temperature and heat treatment protocol.

It has been widely observed that Sn/In/Cd additions tend to suppress the formation of GP zones during natural ageing [36] and  $\theta''$  precipitates during artificial ageing [38]. These effects are well explained based on vacancy-mediated diffusion. As the driving force for the decomposition of Al-Cu supersaturated solid solutions is higher at room temperature than during artificial ageing, the retarded formation of GP zones can only be correlated with slower diffusion. Since In and Sb, like Sn, have a high binding energy with vacancies, supersaturated vacancies tend to bind with these solute atoms during quenching. These bound vacancies are no longer free, and can hardly help the diffusion of Cu. Due to the binding energy between a vacancy and a Sn atom is not high enough for the vacancy-Sn pair to remain bound at 200 °C (-0.25 eV), vacancies are released from Sn traps and significantly accelerate diffusion [26, 164]. This can explain why the formation of  $\theta''$  precipitates is usually skipped in alloys containing Sn. The abundant free vacancies significantly accelerate the diffusion of Cu, and probably accommodate the structural change during  $\theta'$  nucleation, thus significantly accelerating  $\theta'$  nucleation. After losing the help from bound vacancies, solute Sn atoms may diffuse difficultly, which needs further verification. However, as stated above, the already formed  $\theta'$  precipitates provide an easy diffusion pathway along the periphery for Sn atoms and easy nucleation sites with a low nucleation energy barrier for Sn precipitates. Therefore, Sn precipitates in an Al-Cu-Sn alloy are always located at the periphery of  $\theta'$  precipitates [40]. Similarly, in the quaternary alloy aged at 250 °C (Fig. 4.5), the binding energy between a solute atom (In and Sb) and a vacancy is not large enough to resist thermal fluctuations, and supersaturated vacancies are released from the solute traps. The abundant free vacancies significantly accelerate the diffusion of Cu and make  $\theta'$  nucleate before InSb precipitates.

The observation that InSb particles nucleate before  $\theta'$  precipitates in the quaternary alloy aged at 200 °C (Fig. 4.2) suggests Cu diffusion is not much helped by excess vacancies. In other words, most supersaturated vacancies are still trapped by In and Sb atoms. The bound vacancies significantly accelerate the diffusion of In and Sb atoms. This is why InSb particles can nucleate quickly. The binding energy between a Sb atom and a vacancy is -0.291 eV (see Fig. 4.9, -0.30 eV in [39]), higher than that of Sn. However, an In atom binds less strongly with a vacancy (-0.20 eV) [39]. Therefore, if a vacancy binds only with an In atom, vacancies trapped by In atoms should be released more easily than that in alloys with Sn. If so, there should be a considerable amount of  $\theta'$  precipitates nucleating first, which is inconsistent with Fig. 4.3. These considerations suggest an In atom also binds with Sb atoms besides a vacancy. This is consistent with the DFT calculations shown in Fig. 4.9. We find that the binding energy between a vacancy and solute atoms continuously becomes more negative as the number of

solute atoms increases to 3. The formation of solute-vacancy clusters is energetically favourable until the binding energy becomes positive. One solute atom binding with two vacancies also results in a more negative binding energy [87], but this seems to be impossible in experiments because there are more solute atoms (0.05at.% In and Sb) than vacancies (equilibrium vacancy concentration is 0.01% at 550 °C [162]) in the quenched state. Therefore, the binding between several solute atoms (In and Sb) and a vacancy is strong enough to trap supersaturated vacancies tightly at 200 °C. With the help of trapped vacancies, In and Sb atoms diffuse easily and, thus, InSb particles nucleate first.

As stated above, the InSb precipitates are cubic close-packed and usually show truncated surfaces. The truncated surfaces are {002} planes of the cubic close-packed crystal. Since we do not know the exact composition of the crystal, we cannot calculate the interfacial energy between the InSb particles and the Al matrix. However, since the cubic close-packed InSb particles tend to form an octahedron terminated by {111} planes to minimize the Gibbs free energy of the system, it is reasonable to assume that the interfacial energy between the {002} planes and the Al matrix is larger than that of {111}, similarly to Pb precipitates in the Al matrix [165]. This is a general trend for FCC crystals [166]. The high energy interface ( $\{002\}_{\text{InSb}}//\{002\}_{\text{Al}}$ ), therefore, tends to attract solute atoms (mainly Cu here) to reduce its energy [101, 167, 168], which may come from the chemical component or the geometrical component of the interfacial energy [169]. The GP zones on the truncated surface of InSb particles should be stabilised by the  $\{002\}_{\text{InSb}}//\{002\}_{\text{Al}}$  interface. Otherwise, GP zones should not occur at 200 °C. With longer ageing time at 200 °C,  $\theta''$  and  $\theta'$  precipitates successively nucleate on the truncated surfaces, because the initially high interfacial energy of the  $\{002\}_{\text{InSb}}//\{002\}_{\text{Al}}$  interface results in a lower nucleation activation energy for these Cu-rich phases. A recent observation in a different system also suggests that ice prefers to nucleate on the high energy surface of feldspars, instead of the low energy surface [170].

The free vacancy concentration at a certain ageing temperature for the Al-Cu-In-Sb alloy is not only determined by the intrinsic binding energy between the solute atoms and a vacancy but also can be changed through the heat treatment protocol. As shown in Fig. 4.9, with increasing solute atoms around a vacancy, the binding becomes much stronger. Therefore, fewer vacancies can be released. During the rapid quenching process, there should not be enough time for several solute atoms to diffuse and surround a vacancy. With a longer natural ageing, it is reasonable that free-standing and supersaturated In and Sb atoms can diffuse to surround a vacancy. Consequently, for the quaternary alloy aged at 250 °C after 10 days natural ageing (Fig. 4.6), more solute-vacancy clusters are stable enough to survive and transform into InSb particles and then help  $\theta'$  nucleation on their truncated surfaces. Correspondingly, the

amount of free vacancies that can help the diffusion of Cu is reduced, which is consistent with the slow kinetics at the early ageing stage (until 0.25 h in Fig. 4.1). Under this condition, we cannot observe GP zones and  $\theta''$  precipitates on the truncated surfaces. This probably results from the rapid precipitation kinetics (relative to that at 200 °C) and/or instability of GP zones and  $\theta''$  precipitates at such high ageing temperature. Note that several solute atoms binding with several vacancies and forming a big solute-vacancy cluster is also possible in the experiment. This should produce similar results as the above discussion. However, such clusters are too large to be the subject of DFT calculations.

The interrupted quenching process was designed to deliberately reduce the number of quenched-in vacancies available to form solute-vacancy clusters. As shown in Fig. 4.1 (b), the hardness response of the binary alloy is remarkably lowered after interrupted quenching. This is likely to originate from a low quenched-in vacancy concentration and concomitant sluggish Cu diffusion. The quaternary alloy also exhibits slower kinetics in the early ageing stages until 0.25 h (Fig. 4.1 (b)). Even though the presence of In and Sb atoms may trap vacancies and restrict the depletion of vacancies, this behaviour is effective only at low temperatures, such as  $\leq 200$  °C [162]: the vacancy concentration decreases significantly before the sample reaches a temperature where In and Sb atoms can bind vacancies tightly. This is why the nucleation of precipitates is delayed compared with normal ageing conditions (Fig. 4.8). Furthermore, the decrease in the quenched-in vacancy concentration caused by interrupted quenching may result in fewer and smaller solute-vacancy clusters, most of which will not survive 200 °C ageing in the quaternary alloy, compared with the conventional heat treatment process. When these small clusters are broken up at 200 °C, the bound vacancies will be released, which could result in the first nucleation of  $\theta'$  precipitates. This may explain why InSb crystals form mainly after  $\theta'$  precipitates (Fig. 4.8). It is interesting to note the rapid recovery of the hardness of the interrupted quenched quaternary alloy to the level seen at normal ageing conditions after 0.25 h (Fig. 4.1 (b)). Hardness should not only be correlated with the number density of precipitates (i.e. the nucleation process) but should also be attributed to the shape of precipitates (i.e. the growth process). The length-to-thickness aspect ratio of  $\theta'$  precipitates at the peak aged condition is slightly higher in the interrupted quenched alloy ( $39 \pm 10$ ) compared with the water quenched alloy ( $30 \pm 8$ ). As reported earlier, a higher aspect ratio will result in a higher hardness for the same precipitate number density [158], which can compensate for the initial inferior hardness in the interrupted quenched alloy. The preferred segregation of In and Sb atoms along the semi-coherent  $\theta'/\text{Al}$  interface may account for this increased aspect ratio at the peak aged condition, but further study is required to understand this part of the ageing curve. Under this

condition,  $\theta'$  precipitates nucleate first and promote the nucleation of InSb particles at the semi-coherent  $\theta'$ /Al interface. Please note here that  $\theta'$  precipitates nucleating earlier than InSb particles may not result only from faster diffusion of Cu atoms compared with In/Sb atoms. The measured diffusion coefficients ( $D = D_0 * e^{\frac{-Q}{RT}}$ ) for Cu, In and Sb at atoms 200 °C are  $6.5 \times 10^{-20} \text{ m}^2/\text{s}$ ,  $3.4 \times 10^{-18} \text{ m}^2/\text{s}$  and  $3.4 \times 10^{-19} \text{ m}^2/\text{s}$ , respectively, which were measured using the same method [171, 172]. These numbers suggest that, with the assistance of free vacancies, Cu atoms diffuse more slowly in the aluminium matrix than that of In and Sb atoms. However, the scattering of the measured diffusion coefficients from different methods are very large, and Cu atoms can diffuse faster than In and Sb atoms according to some reports [83, 173]. Therefore, further study is needed to directly compare the diffusion coefficients of different elements. Since the concentration of Cu solute is 34 times the concentration of In or Sb solute in the studied alloy, it is easier for Cu to enrich a certain number of atoms at a nucleating site than In and Sb. This can, at least partially, explain the earlier nucleation of precipitates than InSb particles. The nucleation energy barriers for  $\theta'$  precipitates and InSb particles may also contribute to this. As will be seen in Chapter 6, free excess vacancies could bring in a new Cu-rich phase which has a lower nucleation energy barrier than the  $\theta'$  phase and is expected to facilitate the nucleation  $\theta'$  precipitates.

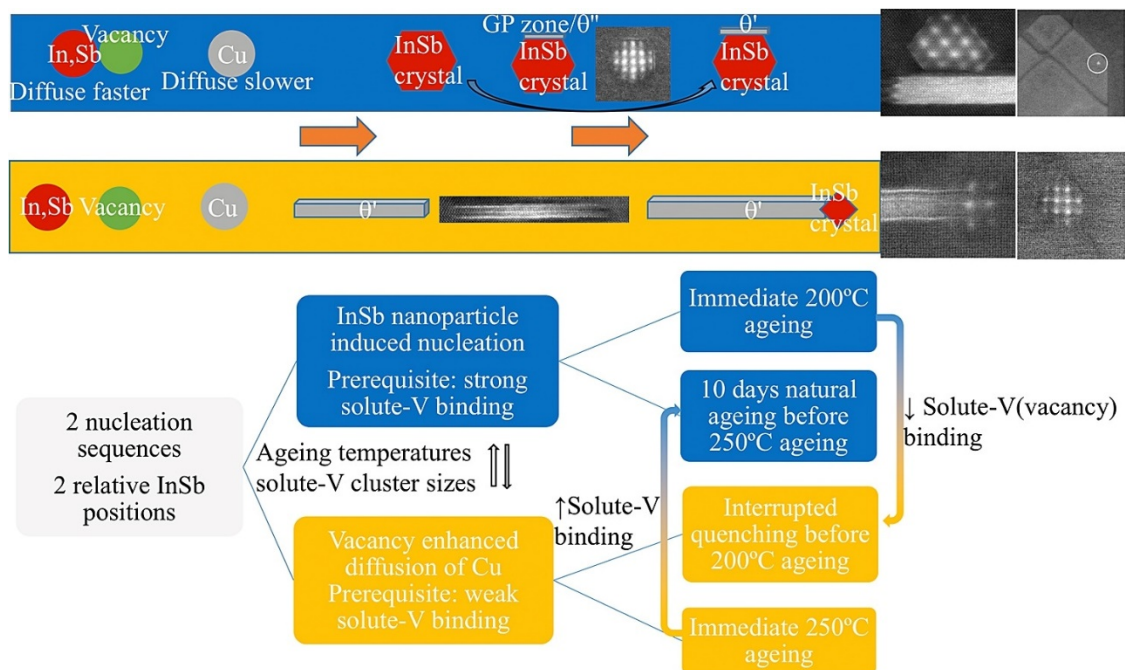


Fig. 4.10 Schematic of nucleation sequence and strategy to change the nucleation sequence using different heat treatments. V indicates a vacancy.

Fig. 4.10 summarises the operating mechanisms of vacancies on the nucleation of  $\theta'$  precipitates. If vacancies are mainly binding with In and Sb atoms, In and Sb atoms seem to diffuse faster than Cu atoms, and InSb particles nucleate first. If vacancies are free, In, Sb and Cu all can benefit from the free vacancies. However, the diffusivity of Cu is increased compared with that in the first case, while the diffusivities of In and Sb are lowered. Consequently,  $\theta'$  precipitates can nucleate first. The bottom panel in Fig. 4.10 shows how to alter the free vacancy concentration by changing the solute-vacancy cluster size and ageing temperature. The successful control of the operational modes on demand, as shown above, support the proposed mechanisms.

#### 4.5 Possible segregation of In and Sb solutes at the $\theta'$ /Al semi-coherent interface

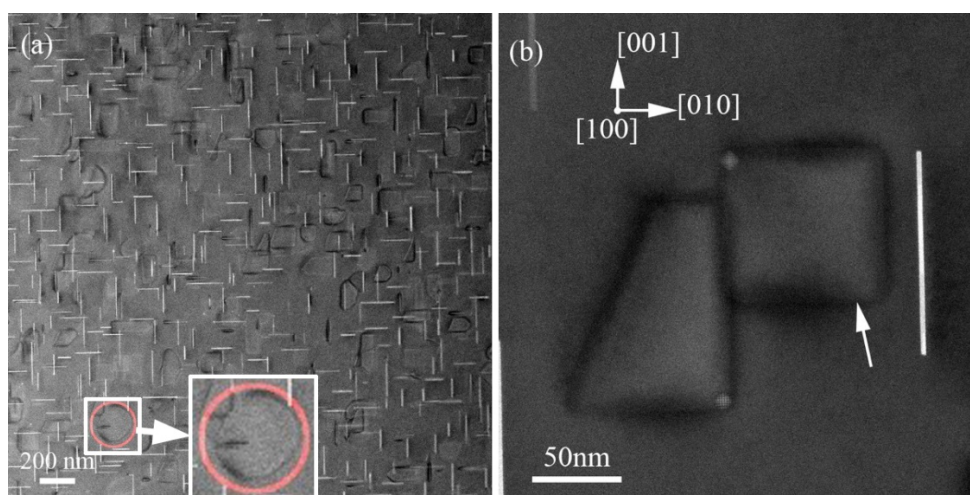


Fig. 4.11 HAADF-STEM images showing projected morphology  $\theta'$  precipitates in the Al-Cu-In-Sb alloy aged for 30 min at 200 °C. The pink circle highlights a  $\theta'$  precipitate with a circular shape. The white arrow indicates a squared  $\theta'$  precipitate.

Fig. 4.11 shows the projected morphologies of  $\theta'$  precipitates along  $\langle 100 \rangle_{\text{Al}}$  at under-aged condition as imaged by HAADF-STEM. More than 80% of  $\theta'$  precipitates can be seen to exhibit near square/rectangular morphologies with straight edges of precipitates parallel with  $\langle 001 \rangle_{\text{Al}}$ . However,  $\theta'$  precipitates mainly display an oval morphology at under-aged condition in Al-Cu binary alloys [49]. Square or rectangular  $\theta'$  precipitates with edges parallel with  $\langle 001 \rangle_{\text{Al}}$  are never observed in Al-Cu binary alloys even at peak-aged condition [28]. Another conspicuous feature is the location of the InSb particle relative to a given  $\theta'$  precipitate: it is always at the coherent  $\theta'$ /Al interface and a corner of the square-shaped  $\theta'$  precipitate. The morphology change may be correlated with In and Sb solute segregation at the semi-coherent  $\theta'$ /Al interface.

However, if an InSb particle is located at the semi-coherent  $\theta'/\text{Al}$  interface, the given  $\theta'$  precipitate does not adopt a square or rectangular shape, such as the  $\theta'$  precipitate in the pink circle of Fig. 4.11 (a).

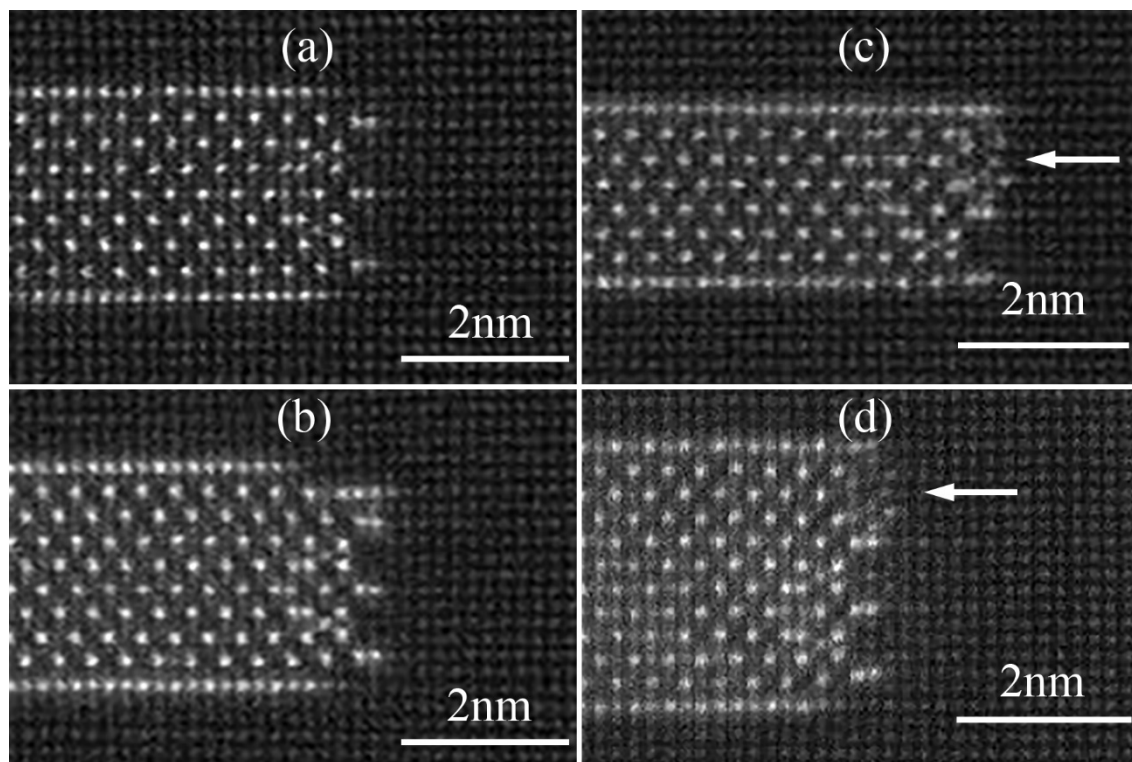


Fig. 4.12 HAADF-STEM images showing possible In and Sb segregation at the semi-coherent  $\theta'/\text{Al}$  interface in the aged Al-Cu-In-Sb alloy, (a) and (c) 30 min at 200 °C, (b) and (d) 60 min at 160 °C. (a) and (b) exhibit the typical  $\theta'/\text{Al}$  semi-coherent interface that also occurs in Al-Cu binary alloys [28]. (c) and (d) display different interfacial structures with arrows highlighting possible In and Sb segregation.

Fig. 4.12 shows two different atomic structures of the semi-coherent  $\theta'/\text{Al}$  interface along  $\langle 001 \rangle_{\text{Al}}$ . The interfacial structure shown in Fig. 4.12 (a) and (b) is the same as that in Al-Cu binary alloys [28], which is very common in the Al-Cu-In-Sb alloy. However, the interfacial structures shown in (c) and (d) are quite different from that in (a) and (b). The upper parts indicated by arrows are different from the atomic structure at the  $\theta'/\text{Al}$  interface shown in (a) and (b), which may suggest In and Sb segregation at the  $\theta'/\text{Al}$  semi-coherent interface. Even though In and Sb have a higher atomic number  $Z$  than Cu, their segregation in an Al atomic column may result in an average  $Z$  lower than that of Cu due to low concentrations along the column (viewing direction). This is why the atomic columns which are possibly In and Sb enriched have a lower contrast than a Cu column. Unfortunately, attempts to determine the chemical identity of such solute segregation using EDS all failed due to the low collection efficiency of the X-ray signal in the current MCEM microscopes and beam damage.  $\theta'$

precipitates with such a different semi-coherent  $\theta'$ /Al interfacial structure account for  $\sim 10\%$  of all  $\theta'$  precipitates in the Al-Cu-In-Sb alloy, independent of the ageing temperatures. However, the solute segregation of In and Sb is expected to occur at most of  $\theta'$  precipitates because most of  $\theta'$  precipitates undergo a shape change upon In and Sb microalloying.

#### 4.6 Interfacial structure between an InSb particle and a $\theta'$ precipitate

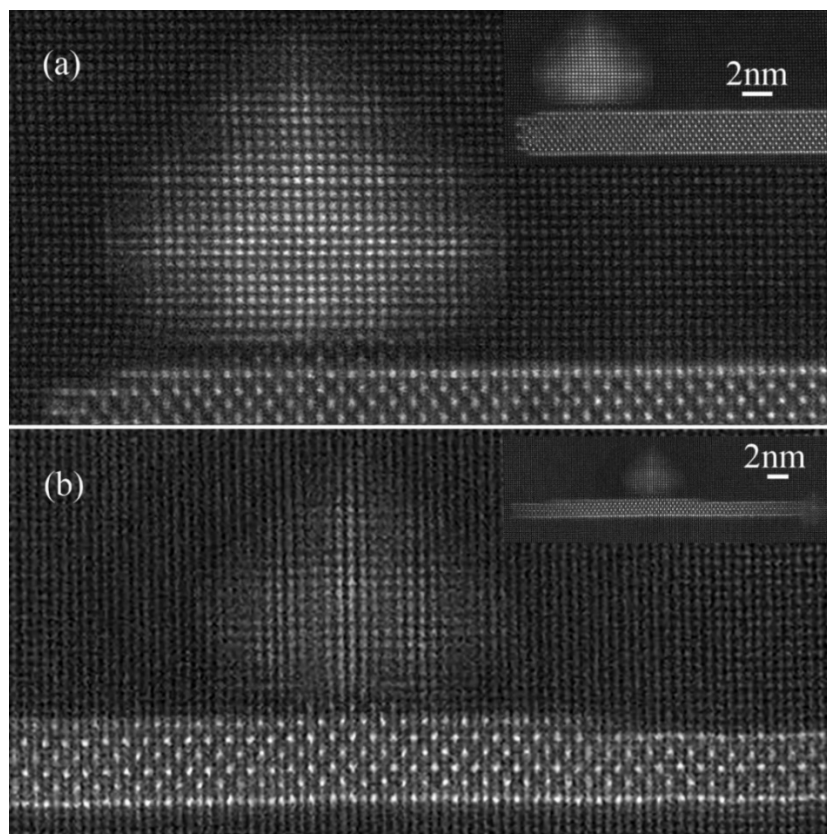


Fig. 4.13 HAADF-STEM images show the interface between an InSb particle and a  $\theta'$  precipitate in the Al-Cu-In-Sb alloy aged for 60 min at 160 °C (a) and 15 min at 200 °C (b). The insets are low magnification images of precipitates.

Heterogeneous nucleation of  $\theta'$  precipitates from pre-existing InSb particles is an important nucleation mechanism of  $\theta'$  in the Al-Cu-In-Sb alloy. Fig. 4.13 shows the interface between an InSb particle and a  $\theta'$  precipitate which is undoubtedly important for the heterogeneous nucleation process. Here the atomic structure near the interface between InSb and  $\theta'$  does not change and generally copies the projected structure of  $\theta'$  along  $\langle 100 \rangle$ . The part between the InSb particle and the big  $\theta'$  precipitate is proposed to be a small  $\theta'$  precipitate, sandwiched between the InSb particle and the big  $\theta'$  precipitate. The lattice mismatch between the  $\theta'$  phase ( $a=0.405\pm 0.004$  nm) and the InSb phase ( $a=0.480\pm 0.004$  nm) is up to 20%, which is much larger than commonly observed mismatches ( $<10\%$ ) at an interface for heterogeneous nucleation [174, 175]. At present, it is impossible to figure out how the large mismatch is

accommodated at the interface because moiré fringes blur the atomic columns of InSb particles. Therefore, further study on the structural matching at the  $\theta'$ /InSb interface is still needed.

## 4.7 Conclusions

The effects of combined additions of In and Sb on the precipitation in an Al-1.7at.%Cu alloy were investigated, and the corresponding mechanisms were proposed based on HAADF-STEM observations and DFT calculations. The main conclusions are the following:

- (1) The combined In and Sb additions increase both precipitation kinetics and peak hardness.
- (2) There are two different nucleation sequences depending on the binding states between a vacancy and In and Sb solute atoms. It is suggested that both ageing temperature and solute-vacancy cluster size can change the binding state between a vacancy and solutes. In one condition when supersaturated vacancies are bound to In and Sb atoms, InSb crystals nucleate first and promote the heterogeneous nucleation of GP zones,  $\theta''$  and  $\theta'$  precipitates. In the other condition when supersaturated vacancies are free and are able to enhance the diffusion of Cu atoms, the nucleation of  $\theta'$  precipitates occurs first, thus providing heterogeneous nucleation sites at the semi-coherent  $\theta'$ /Al interface for InSb particles.
- (3) Three parameters, i.e., interrupted quenching at 160 °C, natural ageing and artificial ageing temperature, were used to alter the operative nucleation sequence. Through appropriate interrupted quenching or natural ageing, the two different nucleation sequences both can be achieved in the Al-Cu-In-Sb alloy artificially aged at 200 °C or 250 °C.
- (4) In and Sb additions significantly change the morphologies of  $\theta'$  precipitates.  $\theta'$  precipitates tend to be square or rectangular when an InSb particle is located on the coherent  $\theta'$ /Al interface and near the edge of a  $\theta'$  precipitate. However,  $\theta'$  precipitates tend to be circular when an InSb particle is located at the semi-coherent  $\theta'$ /Al interface. These observations may suggest the segregation of In and Sb atoms at the semi-coherent  $\theta'$ /Al interface.

## Chapter 5

# Multiple precipitation mechanisms of Cu-rich precipitates in an Al-1.7at.%Cu-0.78at.%Ge alloy

The present chapter deals with additions of Ge to an Al-1.7at.%Cu alloy. Two conclusions from the literature suggest Ge additions may promote the precipitation of  $\theta'$  in Al-Cu alloys. First, the combined additions of Ge and Si significantly increase the nucleation rate of  $\theta'$  precipitates by providing heterogeneous nucleation sites [48]. Secondly, many solutes (e.g., In, Cd and Sn) that have a high solute-vacancy binding energy are very useful in enhancing precipitation in Al-Cu alloys [30], and Ge has a high solute-vacancy binding energy [39]. Therefore, the study of the independent effect of Ge will be as important as the study of the synergetic effects of two elements (In and Sb). The two studies may provide a comprehensive insight into the mechanisms of the enhanced precipitation upon solute additions.

Our observations show that the high Ge concentration results in higher peak hardness but similar precipitation kinetics compared with the combined In and Sb additions. The main Cu-rich precipitates (>80%) are  $\theta'$ , and most of  $\theta'$  precipitates (>80%) are free of the attachment of a Ge crystal. The dominant nucleation mechanism for the common  $\theta'$  precipitates was found to be correlated with vacancies trapped by Ge solutes, instead of heterogeneous nucleation on a Ge particle. Cu-rich precipitates different from  $\theta'$  and GP zones, in terms of crystallographic orientation and crystal structure, also form as minorities (<20%). Four kinds of  $\theta'$  precipitates with new crystallographic orientations as well as  $\Omega$  precipitates are found, which was determined, in most cases, to be associated with heterogeneous nucleation on Ge particles. However, for one kind of minority  $\theta'$  precipitates, a second nucleation mechanism is transforming an unexpected Cu-rich phase (named H in the following).

## 5.1 Hardness response

Fig. 5.1 shows the hardness curves of the Al-Cu-Ge alloy during artificial ageing at 200 °C, in comparison with the Al-1.7at.%Cu alloy and the Al-1.7Cu-0.025%In-0.025Sb (at.%) alloy. Ge additions result in a remarkable increase in both precipitation kinetics and peak hardness compared with the binary alloy. The hardness increase associated with Ge additions is more remarkable than that of In and Sb additions. The Ge containing alloy reaches the peak hardness at nearly the same ageing time as In and Sb additions. However, this alloy has a poor coarsening resistance because it displays a rapid hardness decline during over-ageing.

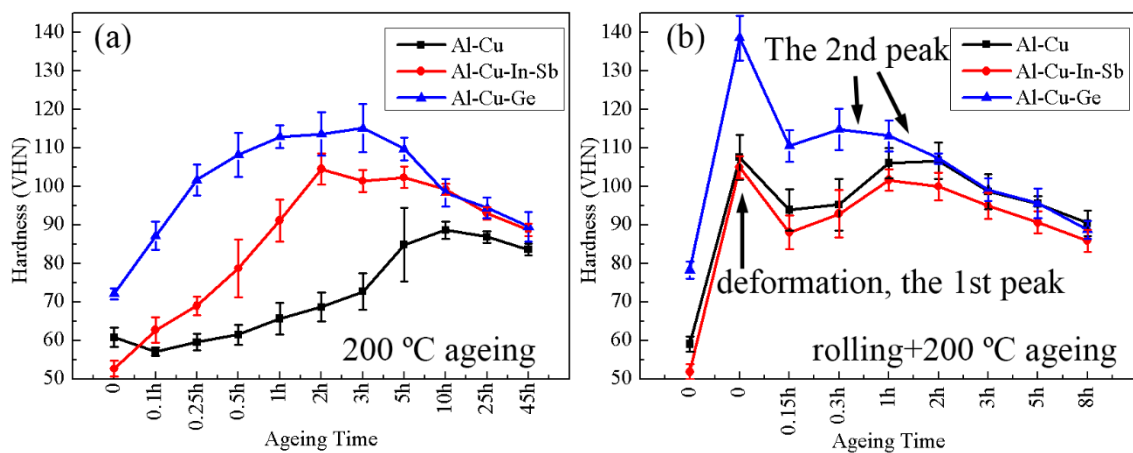


Fig. 5.1 Hardness curves for the Al-Cu-Ge, Al-Cu-In-Sb and Al-Cu alloys aged at 200 °C (a) and 200 °C after cold rolling (b).

Deformation after solid solution treatment and before isothermal ageing strengthens the three alloys to a level comparable with the alloys peak-aged at 200 °C, as shown in Fig. 5.1 (b). Deformation results in a more significant hardness increase in the Al-Cu-Ge alloy than in the other two alloys. However, the hardness of the three alloys does not further increase but reduces with short artificial ageing. This suggests precipitation strengthening cannot compensate for the hardness loss from dislocation annihilation and grain coarsening during artificial ageing, which is nontrivial as shown in other deformed Al alloys [105]. The second peak on the hardness curves implies the hardening effect of precipitation. The second peak hardness of the Al-Cu-In-Sb alloy and the Al-Cu-Ge alloy in Fig. 5.1 (b) is nearly the same as their peak hardness in Fig. 5.1 (a). However, the second peak hardness of the binary alloy in Fig. 5.1 (b) is higher than its peak hardness in Fig. 5.1 (a). Therefore, deformation smears the net beneficial roles of Ge or In and Sb additions on precipitation hardening completely. Even though both solute additions and deformation are well-known in promoting precipitation, their synergetic

effects on promoting precipitation are not achieved here. The non-synergy of deformation and Ge/InSb additions is conceivable because it has been observed in Al-Cu-Sn alloys [31, 32].

The ageing responses of the three alloys at 160 °C and 250 °C are shown in Fig. 5.2. When aged at 160 °C, the Al-Cu-Ge alloy reaches almost the same peak hardness as the Al-Cu-In-Sb alloy. However, the two alloys are different in the ramping rate of hardness. The hardness of the Al-Cu-Ge alloy continuously increases before the peak hardness, while for the Al-Cu-In-Sb alloy, the hardness does not increase until 30 min and then increases rapidly. The Al-Cu-Ge alloy shows a reduced hardness at the initial ageing stage at 250 °C, which is different from both the binary alloy and the Al-Cu-In-Sb alloy. The Al-Cu-Ge alloy has a comparable peak hardness as that of the Al-Cu-In-Sb alloy at the expense of slightly longer ageing time at 250 °C.

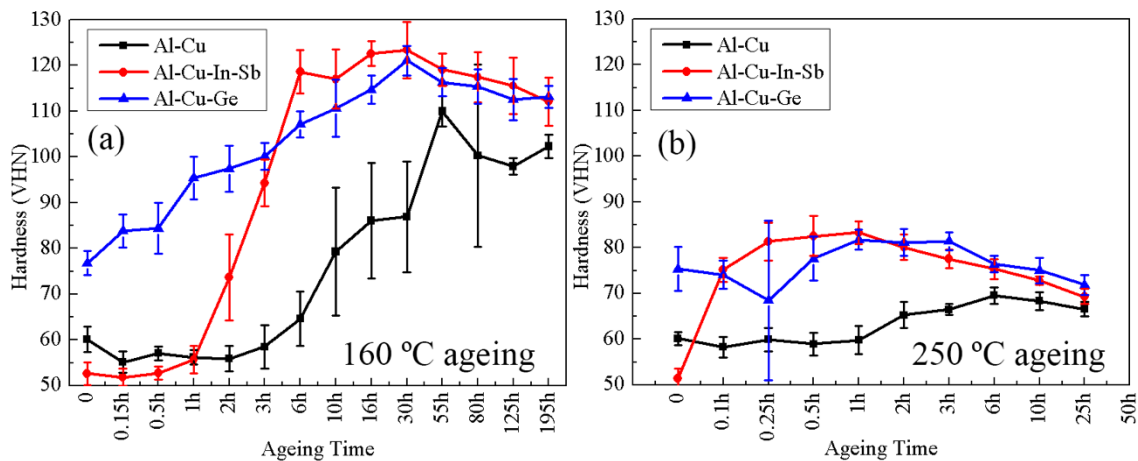


Fig. 5.2 Hardness curves for the Al-Cu-Ge, Al-Cu-In-Sb and Al-Cu alloys aged at 160 °C (a) and 250 °C (b).

## 5.2 Main precipitate phases and their crystallography at different ageing temperatures

### 5.2.1 200 °C ageing

Fig. 5.3 displays the typical precipitates observed by HAADF-STEM in the Al-Cu-Ge alloy aged 2 min at 200 °C. Half of all  $\theta'$  precipitates exists without the decoration of a Ge particle, while all Ge particles are decorated by regions exhibiting low image brightness. Sometimes the low-brightness region has a clear structure of  $\theta'$  (Fig. 5.3 (b) and (d)), but, in most cases, the low-brightness region has a structure different from the well-known Cu-rich phases in Al-Cu alloys (Fig. 5.3 (c)-(d)). The unidentified low-brightness regions are suspected to be a Cu-rich region because they have a comparable atomic-number ( $Z$ -) contrast to  $\theta'$  precipitates and

transform into  $\theta'$  precipitates with longer ageing time (shown below). The chemical composition of these regions could not be determined due to their small size. The much brighter contrast of Ge atomic columns is expected to be an illusion because Ge columns have almost the same integrated intensity as Cu columns, as shown in the insets in Fig. 5.3 (b). The illusion is due to the much smaller spacing between two dumbbell Ge atoms than that between two neighbouring Cu atoms. Theoretically speaking, Ge columns and Cu columns should have similar brightness/intensity because they have a similar atomic number (32 vs 29) and the same atom density viewed along  $\langle 100 \rangle_{\theta'} // \langle 110 \rangle_{\text{Ge}}$  (generally  $// \langle 001 \rangle_{\text{Al}}$ ). In addition, all Ge particles were found to display at least one twin plane.

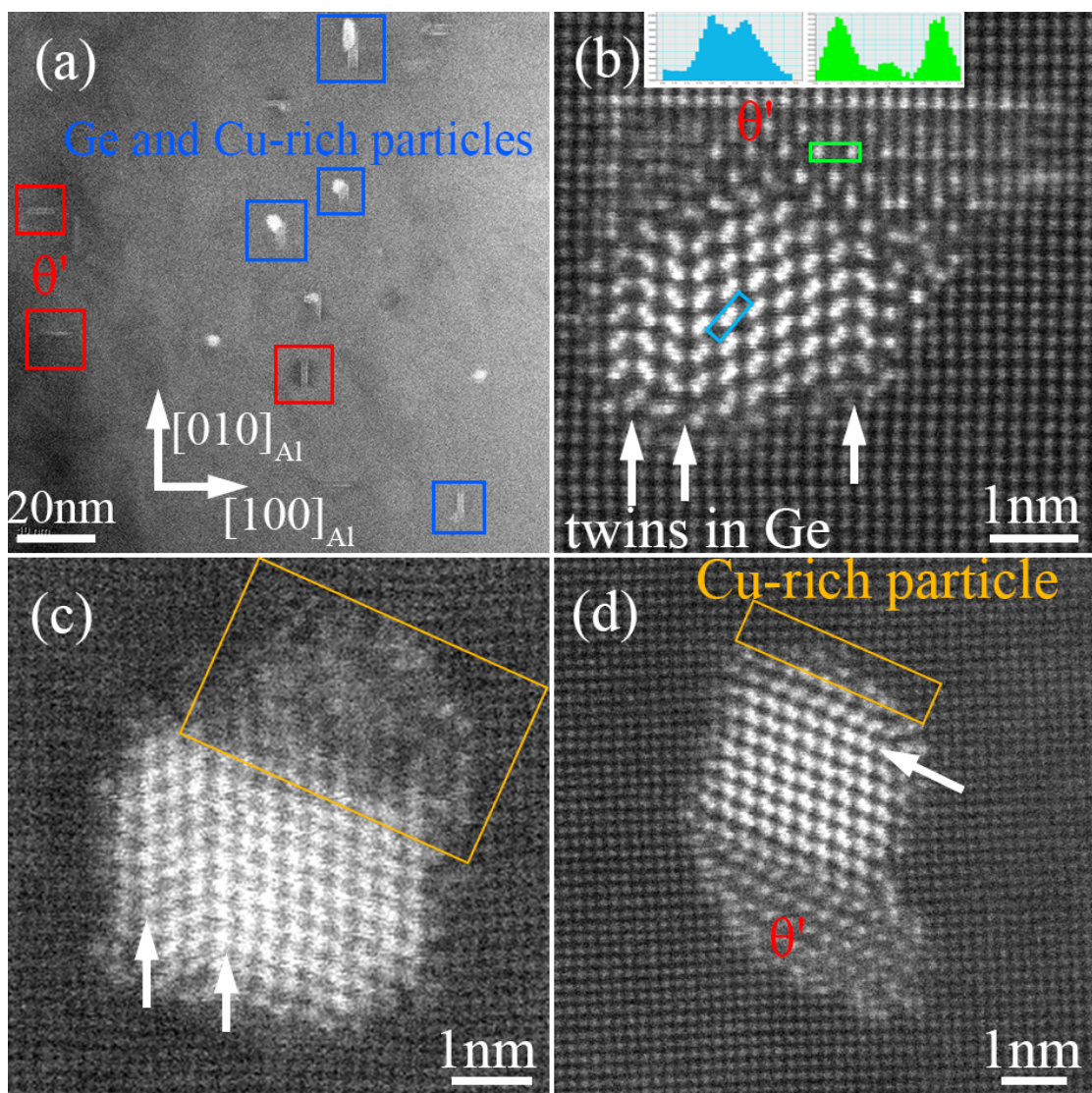


Fig. 5.3 HAADF-STEM images of the Al-Cu-Ge alloy aged 2 min at 200 °C. Low-brightness regions (expected to be Cu-rich particles based on image contrast) always decorate Ge particles, but half of  $\theta'$  precipitates are free of Ge particles. The insets in (b) are integrated intensity in the green rectangle and the light blue rectangle.

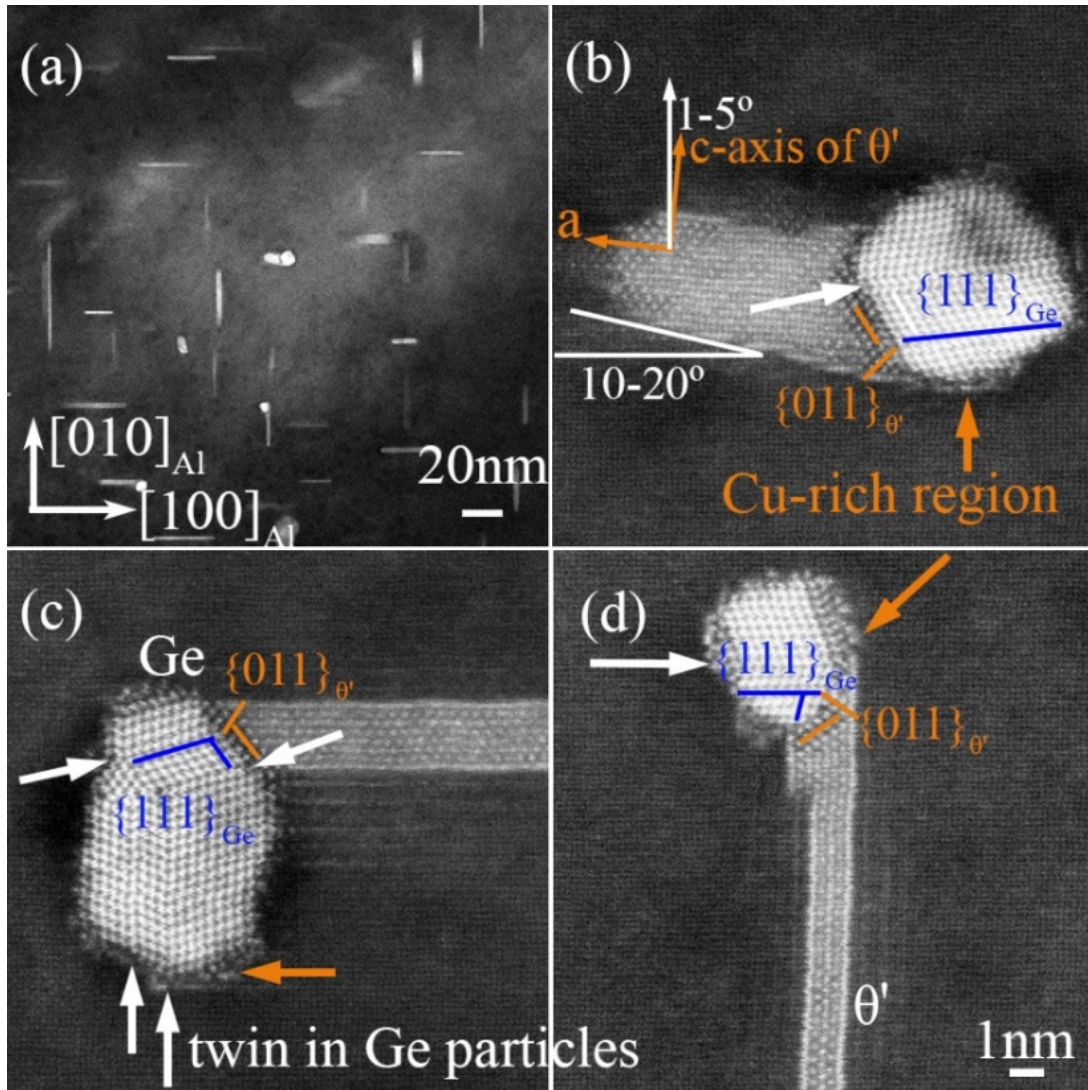


Fig. 5.4 HAADF-STEM images of the Al-Cu-Ge alloy aged 10 min at 200 °C. Ge particles are always decorated with Cu-rich particles, but more than half of  $\theta'$  precipitates are free of Ge particles. The blue lines and orange lines are parallel with  $\{111\}_{\text{Ge}}$  and  $\{011\}_{\theta'}$ , respectively.

With a longer ageing time (10 min), more than 50% of  $\theta'$  precipitates exist free of the direct attachment of Ge particles, as shown in Fig. 5.4 (a). The remaining  $\theta'$  precipitates have one and only one Ge particle adjoined at one end. There is a minority of precipitates (less than 5%) forming a stair-like interface with the Al matrix (Fig. 5.4 (b)). They have the same atomic structure as  $\theta'$  but have a different crystallographic orientation with the Al matrix (named  $\theta'$  type II in the following). The a-axis and c-axis of  $\theta'$  are off  $\langle 100 \rangle_{\text{Al}}$  by 1-5° (measured in 24 precipitates), and the habit planes are off  $\{100\}_{\text{Al}}$  by 10-20°. However, each step at the interface is still parallel with  $\{100\}_{\text{Al}}$ , though the growth direction of this kind of precipitates deviates from  $\langle 010 \rangle_{\text{Al}}$  direction by 10-20°. This kind of  $\theta'$  precipitates was also found in an Al-3.2wt.%Cu-1.6wt.%Li alloy [176].  $\theta'$  type II precipitates generally have a thickness

comparable to the attaching Ge particles, which may suggest  $\theta'$  type II precipitates nucleate heterogeneously from Ge particles. The  $\{011\}$  planes of  $\theta'$  and  $\{111\}$  planes of Ge crystal are always matched together because they have a very small interplanar spacing discrepancy ( $d_{\{011\}\theta'}=0.332$  nm,  $d_{\{111\}\text{Ge}}=0.326$  nm). However,  $\{011\}\theta'$  are not always parallel with  $\{111\}\text{Ge}$ , and usually only one pair of planes between them are parallel, as shown in Fig. 5.4 (b)-(d). The good matching  $\theta'/\text{Ge}$  interface suggests Ge particles may be good heterogeneous nucleation sites for both common  $\theta'$  (type I) and  $\theta'$  type II. A  $\theta'$  type I precipitate starts to thicken at the  $\theta'/\text{Ge}$  interface as displayed in Fig. 5.4 (d), which also implies the  $\theta'/\text{Ge}$  interface has a lower interfacial energy compared with the  $\theta'/\text{Al}$  semi-coherent interface. All Ge particles at this stage are still covered by low- brightness regions and at the same time are attached by a  $\theta'$  precipitate. The low- brightness regions labelled in Fig. 5.4 (b) and (d) form an integer with the corresponding  $\theta'$  precipitate. Therefore, the low- brightness regions covering Ge particles are Cu-rich zones, and they will transform into  $\theta'$  precipitates with longer ageing time.

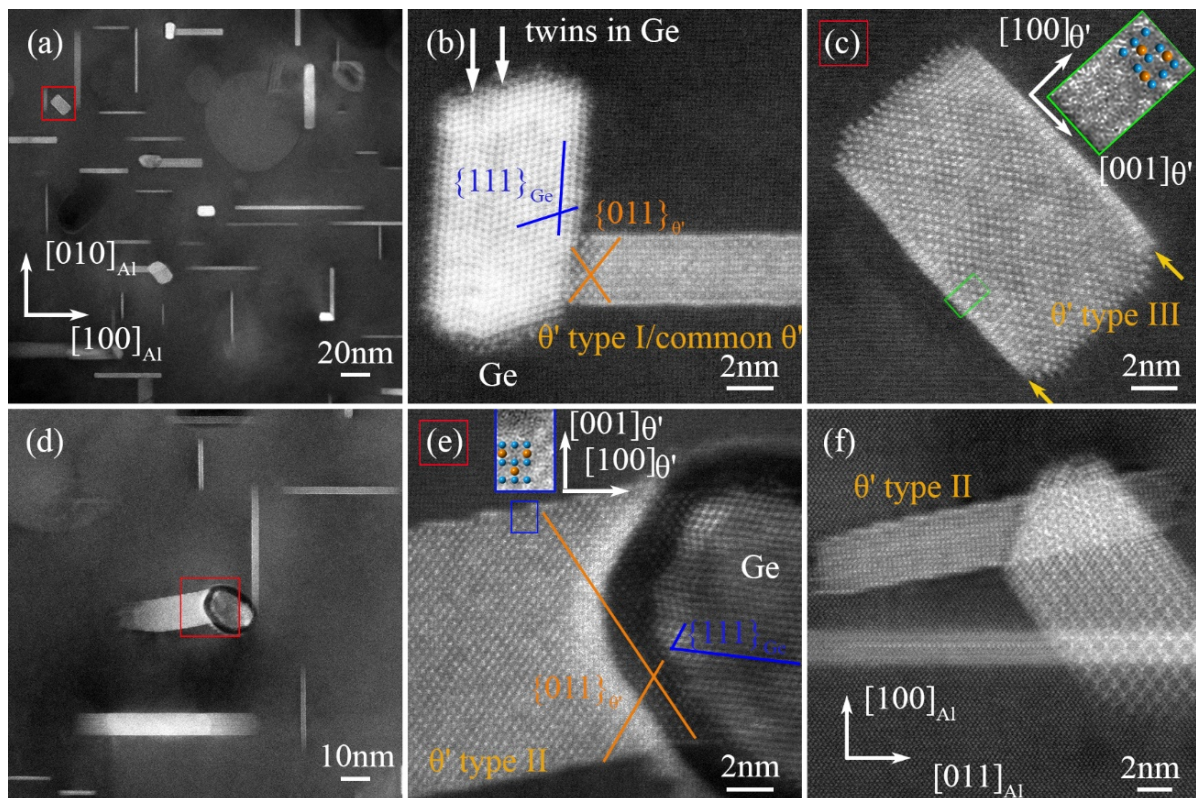


Fig. 5.5 HAADF-STEM images of the Al-Cu-Ge alloy aged 2 h at 200 °C showing  $\theta'$  type I,  $\theta'$  type II and  $\theta'$  type III precipitates. (c) is an enlargement of the red rectangle in (a) and shows  $\theta'$  type III, (e) is an enlargement of the red rectangle in (d) and shows  $\theta'$  type II. (f) shows  $\theta'$  type II from another zone axis. The atomic model of  $\theta'$  is overlapped in the insets. The blue lines and orange lines are parallel with  $\{111\}\text{Ge}$  and  $\{011\}\theta'$ , respectively.

At the peak-aged condition (Fig. 5.5), 87% of the  $\theta'$  type I precipitates (lying on  $\{100\}_{\text{Al}}$ ) nucleate without Ge particle attachment in the Al-Cu-Ge alloy. The remaining  $\theta'$  type I precipitates have a Ge precipitate at one end. In contrast, almost all of  $\theta'$  precipitates are decorated with InSb particles in the Al-Cu-In-Sb alloy at the peak aged condition at 200 °C. These Ge precipitates are laths, and their crystallographic orientation relationship with the Al matrix generally is  $[001]_{\text{Al}}//[011]_{\text{Ge}}$ ,  $(100)_{\text{Al}}//(11\bar{1})_{\text{Ge}}$ ,  $(010)_{\text{Al}}//(112)_{\text{Ge}}$ . This kind of Ge orientation with respect to the Al matrix is not the dominant orientation in the Al-Ge binary alloy [177, 178]. The misfit along  $\langle 011 \rangle_{\text{Ge}}$  and  $\langle 001 \rangle_{\text{Al}}$  is very low, only 1.2%, which was once proposed to result in the broad  $\{111\}_{\text{Ge}}//\{100\}_{\text{Al}}$  interface [177]. The growth twins in Ge precipitates exist from the very beginning of artificial ageing to the peak aged condition. The growth twins in Ge precipitates can change the crystallographic orientation relationship between Ge precipitates and the Al matrix. For example, several Ge segments in Fig. 5.4 (c) have different crystallographic orientations with the Al matrix.

Fig. 5.5 (c) shows another rare kind of  $\theta'$  (type III) precipitates in the Al-Cu-Ge alloy. Its number fraction can be roughly estimated from Fig. 5.5 (a), namely, <5% of Cu-rich precipitates. The broad surface of  $\theta'$  type III is parallel with  $\{110\}_{\text{Al}}$ , instead of  $\{100\}_{\text{Al}}$ . The new crystallographic orientation relationship between  $\theta'$  type III and the Al matrix is  $[010]_{\theta'}/[100]_{\text{Al}}$ ,  $(001)_{\theta'}/(01\bar{1})_{\text{Al}}$ ,  $(100)_{\theta'}/(011)_{\text{Al}}$ . Here the lengthening direction of the  $\theta'$  type III is along  $\langle 001 \rangle_{\theta'}$ , which is the thickening direction of the common  $\theta'$  (type I). Interestingly, the interfacial structure at  $(100)_{\theta'}/(011)_{\text{Al}}$  interface is different from that inside the  $\theta'$  type III precipitates, as highlighted by the yellow arrows and the green box in Fig. 5.5 (c).

$\theta'$  type II precipitates grow into big sizes accompanied by the growing Ge particles at the peak aged condition, as shown in Fig. 5.5 (d). The zooming of the Ge/ $\theta'$  interface suggests a  $\theta'$  precipitate forms a coherent interface with a Ge particle, even though the matched  $\{011\}_{\theta'}$  and  $\{111\}_{\text{Ge}}$  are not always parallel (Fig. 5.5 (e)). The dark area around the Ge particle in Fig. 5.5 (e) is caused by non-uniform thinning during electro-polishing. Fig. 5.5 (f) shows a  $\theta'$  type II precipitate with a stair-like interface viewed from  $\langle 011 \rangle_{\text{Al}}$ . The  $\theta'$  precipitate is still accompanied by a Ge particle. The short lengths of  $\theta'$  type II precipitates suggest their lengthening always from the anchoring Ge particles is not energetically favourable.

Fig. 5.6 shows the peak aged Al-Cu-Ge alloy observed along  $\langle 011 \rangle_{\text{Al}}$  zone axis.  $\theta'$  precipitates with the fourth and fifth kinds of orientations with the Al matrix can be observed. First of all, they take up < 5% of all Cu-rich precipitates (see the inset in Fig. 5.6 (b)). The  $\theta'$  type IV precipitate in Fig. 5.6 (a) lies on  $\{111\}_{\text{Al}}$  and adopts an crystallographic orientation of

$[100]_{\theta'}/[011]_{Al}$ ,  $(011)_{\theta'}/(1\bar{1}\bar{1})_{Al}$ . Since  $\{011\}_{\theta'}$  can form a low-mismatched interface with  $\{111\}_{Ge}$  (the atomic model will be shown in Section 5.4), a  $\theta'$  type IV precipitate can form a coherent but tilted interface with the attaching Ge particle (Fig. 5.6 (a)). Fig. 5.6 (b) shows the fifth kind of  $\theta'$  (type V) which is a particle rather than a lath or a plate. The author could not identify any parallel crystal planes between the  $\theta'$  type V precipitate and the Al matrix.  $\{011\}_{\theta'}$  planes are always tilted from  $\{111\}_{Al}$  planes, as shown in Fig. 5.6 (b). The two Ge precipitates in Fig. 5.6 share the same crystallographic orientation relationship with the Al matrix:  $[011]_{Al}/[011]_{Ge}$ ,  $(11\bar{1})_{Al}/(11\bar{1})_{Ge}$ . However, Ge particles with this orientation are a minority in the Al-Cu-Ge alloy (<5% of Ge precipitates).

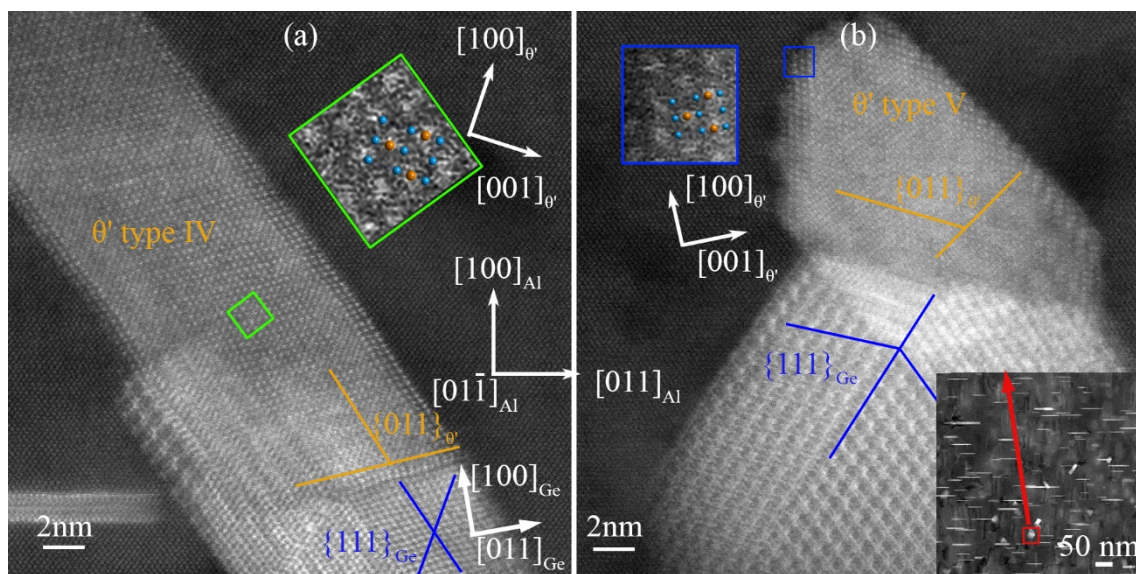


Fig. 5.6 HAADF-STEM images of  $\theta'$  type IV (a) and type V (b) precipitates in the Al-Cu-Ge alloy aged 2 h at 200 °C viewed along  $\langle 011 \rangle_{Al}$ . The blue lines and orange lines are parallel with  $\{111\}_{Ge}$  and  $\{011\}_{\theta'}$ , respectively.

Fig. 5.7 shows the  $\Omega$  precipitates (of  $Al_2Cu$  stoichiometry but with a different structure compared with  $\theta'$ ) in the Al-Cu-Ge alloy aged 2 h at 200 °C. These  $\Omega$  precipitates exist by themselves or are accompanied by a Ge particle. The number density of  $\Omega$  precipitates in the Al-Cu-Ge alloy is very low, lower than any of the above-discussed Cu-rich phases. They are stubby here, while  $\Omega$  precipitates are usually thin and long in Al-Cu-Mg-Ag alloys. The  $\Omega/Al$  coherent interface shows bright Z-contrast, as shown in Fig. 5.7 (b) and (d), which may suggest Ge segregation at the interface. Therefore, Ge additions may have a similar effect as Mg additions in Al-Cu binary alloys because they both can induce very rare  $\Omega$  precipitates.

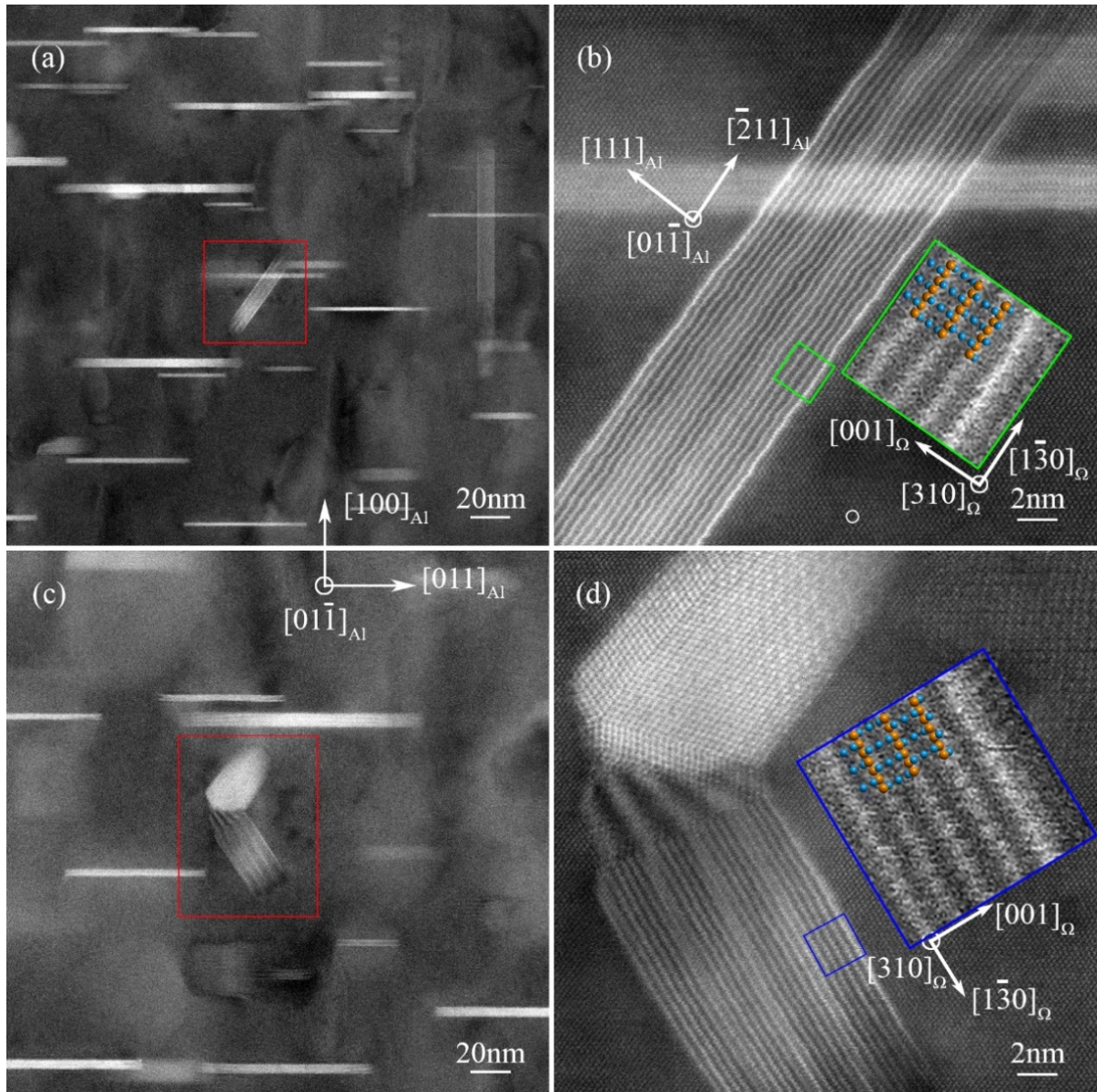


Fig. 5.7 HAADF-STEM images of  $\Omega$  precipitates in the Al-Cu-Ge alloy aged 2 h at 200 °C. The precipitates in red rectangles (a) and (c) are zoomed in and shown in (b) and (d), respectively. The overlaid atomic model of  $\Omega$  is bigger than one unit cell.

The main Cu-rich precipitates found in the Al-Cu-Ge alloy are summarised in Table 5.1. They have the same chemical composition ( $Al_2Cu$ ) but different crystal structures or crystallographic orientations with the Al matrix. The fractions of Cu-rich precipitates other than  $\theta'$  type I are very lower compared with precipitates of  $\theta'$  type I. In other words, even though Ge additions result in new precipitates ( $\Omega$  and  $\theta'$  type II to type V), the main strengthening precipitates in the Al-Cu-Ge alloy are expected to still be common  $\theta'$  precipitates (type I here). The nucleation mechanisms of these Cu-rich precipitates will be discussed in Section 5.3-5.6 based on whether a Ge crystal decorates them.

Table 5.1 Cu-rich precipitates in the peak-aged Al-Cu-Ge alloy at 200 °C.

Types	Orientation relationships	Fractions	Fraction of precipitates attached to a Ge crystal
$\theta'$ type I (habit planes, $\{100\}_{Al}$ )	$[100]_{\theta'}/[100]_{Al}$ , $(001)_{\theta'}/(001)_{Al}$	>80%	13% (counting 512 precipitates)
$\theta'$ type II (habit planes off 10-20° from $\{100\}_{Al}$ )	$[100]_{\theta'}/[100]_{Al}$ , 1-5° between $(001)_{\theta'}$ and $(001)_{Al}$	<5%	100% (counting 24 precipitates)
$\theta'$ type III (habit planes, $\{110\}_{Al}$ )	$[100]_{\theta'}/[100]_{Al}$ , $(001)_{\theta'}/(01\bar{1})_{Al}$	<5%	40% (counting 30 precipitates)
$\theta'$ type IV (habit planes, $\{111\}_{Al}$ )	$[100]_{\theta'}/[011]_{Al}$ , $(011)_{\theta'}/(1\bar{1}\bar{1})_{Al}$	<5%	100% (counting 25 precipitates)
$\theta'$ type V (no clear habit planes)	$[100]_{\theta'}/[011]_{Al}$ , coherent but tilted interface between $(011)_{\theta'}$ and $(1\bar{1}\bar{1})_{Al}$	<5%	100% (counting 23 precipitates)
$\Omega$ (habit planes, $\{111\}_{Al}$ )	$[310]_{\Omega}/[011]_{Al}$ $(001)_{\Omega}/(11\bar{1})_{Al}$	<1%	50% (counting 2 precipitates)

### 5.2.1 160 °C ageing

Al-Cu based alloys are usually artificially aged at ~200 °C [179, 180]. Therefore, the microstructural characterisation was carried out to a lesser extent in the Al-Cu-Ge alloy aged at 160 °C and 250 °C.

Fig. 5.8 shows the precipitates in the Al-Cu-Ge alloy aged 2 h at 160 °C. GP zones are the main precipitates and are distributed uniformly in the Al matrix.  $\theta'$  type I precipitates already form at this stage but have a very low number density. The fraction of  $\theta'$  precipitates free of a Ge particle is similar to the fraction of  $\theta'$  decorated by a Ge particle. Ge particles also have at least one twin inside and are mainly distributed at the semi-coherent  $\theta'/Al$  interface (Fig. 5.8 (b)). However, a Ge particle located at the coherent  $\theta'/Al$  interface is also possible, as shown in Fig. 5.8 (c), though is much rarer than the former location.

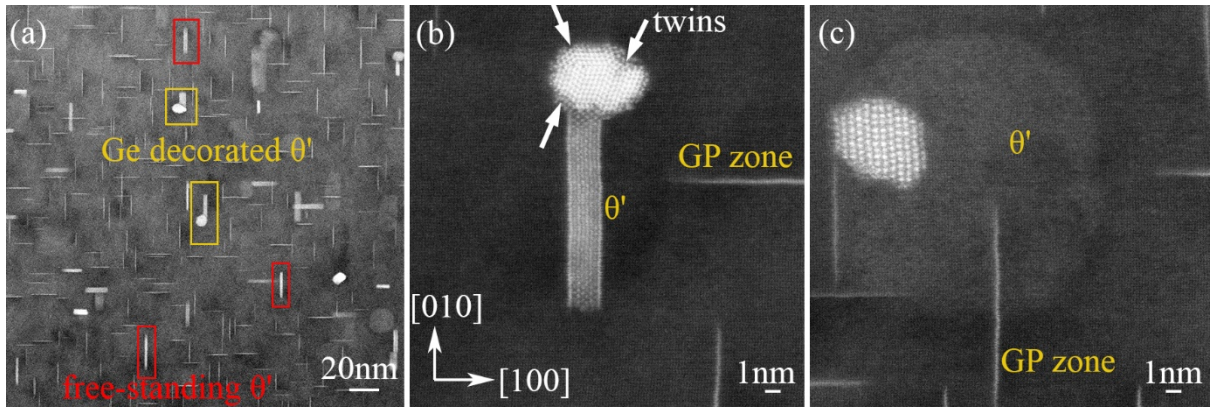


Fig. 5.8 HAADF-STEM images of Ge particles, GP zones and  $\theta'$  precipitates in the Al-Cu-Ge alloy aged for 2 h at 160 °C.

### 5.2.3 250 °C ageing

The Al-Cu-Ge solid solution decomposes quickly when aged at 250 °C, as reflected by the high number density of precipitates in Fig. 5.9. High-resolution images confirm that the precipitates lying on  $\{100\}_{\text{Al}}$  are  $\theta'$  type I. Most of  $\theta'$  type I precipitates exist without the attachment of Ge particles. Nearly all the  $\theta'$  particles decorated by a Ge particle do not lie on  $\{100\}_{\text{Al}}$ . Fig. 5.9 (b) and (c) show  $\theta'$  precipitates having a Ge particle at one end. The  $\theta'$  precipitate in Fig. 5.9 (b) is type III and is lying on  $\{110\}_{\text{Al}}$ , like that shown in Fig. 5.5 (c) (200 °C ageing). The  $\theta'$  type III particle also has a different structure at its coherent interface with the Al matrix compared with the interior, the same as that observed at 200 °C. The  $\theta'$  precipitate in Fig. 5.9 (c) is type II and has a stair-like interface, like the ones shown in Fig. 5.4 (b) and Fig. 5.5 (e) (200 °C ageing). The  $\theta'$  type II precipitate is still very small, while common  $\theta'$  (type I) precipitates already grow up to 100 nm.

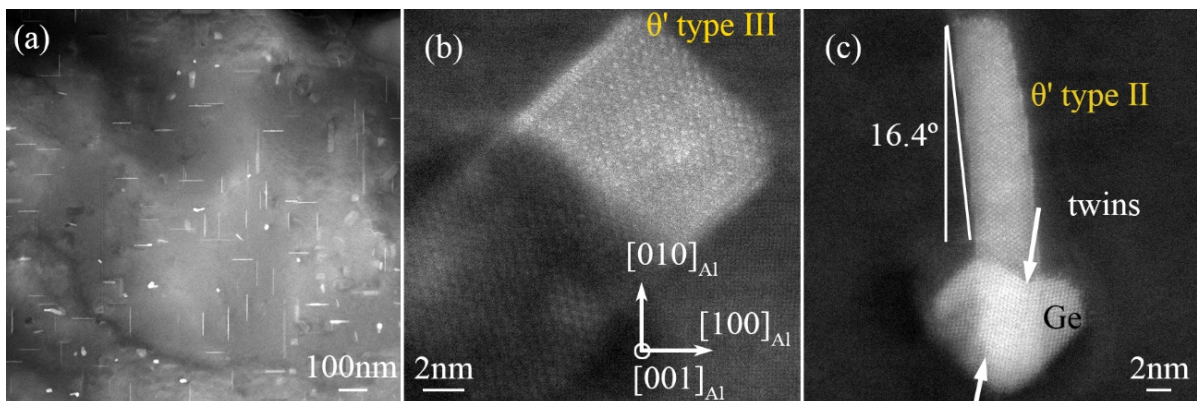


Fig. 5.9 HAADF-STEM images of  $\theta'$  (type I, II and III) precipitates and Ge particles in the Al-Cu-Ge alloy aged for 2 min at 250 °C. (b)  $\theta'$  type II and (c)  $\theta'$  type III.

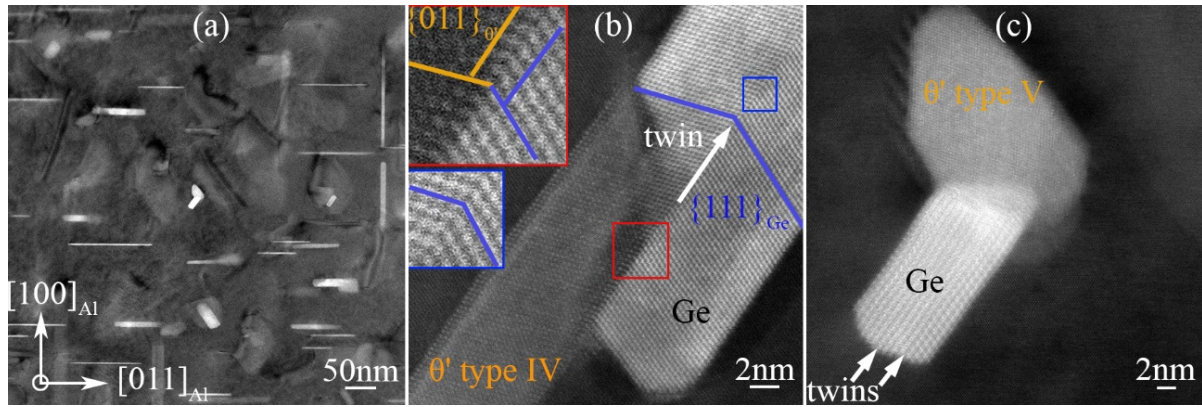


Fig. 5.10 HAADF-STEM images of  $\theta'$  type I (a), type IV (b) and type V (c) precipitates in the Al-Cu-Ge alloy aged 15 min at 250 °C. The blue and yellow lines are parallel with  $\{111\}_{\text{Ge}}$  and  $\{011\}_{\theta'}$ , respectively.

Fig. 5.10 shows the Al-Cu-Ge alloy aged for 15 min at 250 °C. The Al-Cu-Ge alloy shows a large error bar on the hardness curve at this point (Fig. 5.2), but the microstructure does not show too much difference compared with that for 2 min ageing. Fig. 5.10 (b) and (c) show  $\theta'$  type IV and V precipitates, respectively, which are the same as that observed in the 200 °C aged Al-Cu-Ge alloy. The heterophase boundary between  $\theta'$ /Ge in Fig. 5.10 (b) is almost the same as the twin boundary in the Ge part, except a lower Z-contrast at the  $\theta'$  side. Besides, the number fraction of  $\theta'$  type II-V precipitate is very low (each <5%), similar to the fraction observed in the alloy aged at 200 °C.

### 5.3 Nucleation mechanism of $\theta'$ type I without the attachment of a Ge crystal: the critical role of vacancies

As shown in Table 5.1, 87% of  $\theta'$  type I precipitates are free of the attachment of a Ge crystal in the Al-Cu-Ge alloy peak-aged at 200 °C. This suggests Ge crystals hardly affect the nucleation of 87%  $\theta'$  type I precipitates. However, the nucleation of  $\theta'$  type I is facilitated by Ge additions. Firstly, the hardness curves in Fig. 5.1 show that Ge additions increase both precipitation kinetics and peak hardness. Secondly,  $\theta'$  type I precipitates has formed after 2 min ageing, which takes a much longer time in Al-Cu binary alloys. The rapid formation of  $\theta'$  type I precipitates in the Al-Cu-Ge alloy is proposed to be correlated with the released vacancies from Ge atoms and the consequently increased diffusivity of Cu, as that discussed in the Al-Cu-In-Sb alloy. The Ge solutes can trap vacancies during the quenching process and reserve more excess vacancies. Since the binding energies between vacancies and Ge atoms are much weaker than that between InSb and vacancies, even in big solute-vacancy clusters (see Fig. 5.12). Most of Ge atoms release the trapped vacancies during 200 °C ageing, which enhances

the diffusion of Cu and promotes the formation of free-standing  $\theta'$  type I precipitates. A minority of Ge atoms keep binding with vacancies, which can result in the formation of Ge particles before  $\theta'$  type I precipitates and facilitate the heterogeneous nucleation of  $\theta'$  type I precipitates (see Section 5.4 for more discussion). Therefore, the nucleation mechanism of  $\theta'$  type I precipitates in the Al-Cu-Ge alloy is the same as that in the Al-Cu-In-Sb alloy. However, releasing vacancies is the primary functioning mechanism of Ge solutes at **200 °C** in the Al-Cu-Ge alloy, while this mechanism is mainly operative at **250 °C** in the Al-Cu-In-Sb alloy. The reason for the difference has been proposed in the last chapter: a tighter binding between Ge/InSb and vacancies make the mechanism operative at a higher ageing temperature.

Natural ageing before artificial ageing has also been carried out in the Al-Cu-Ge alloy, aiming to change the nucleation sequence between Ge particles and  $\theta'$ , like that in the Al-Cu-In-Sb alloy. Fig. 5.11 shows the microstructures of the peak-aged Al-Cu-Ge alloy with and without natural ageing. The 10-day natural ageing hardly changes the fraction of Cu-rich precipitates decorated by a Ge particle. The red boxes in Fig. 5.11 highlight  $\theta'$  type II, IV and V precipitates that are always decorated by a Ge particle (see Table 5.1). There are not any recognisable changes in the fraction of  $\theta'$  type II, IV and V precipitates. The fraction of  $\theta'$  type I precipitates decorated by a Ge particle is 15% in the Al-Cu-Ge alloy with 10-day natural ageing (it is 13% without the natural ageing).

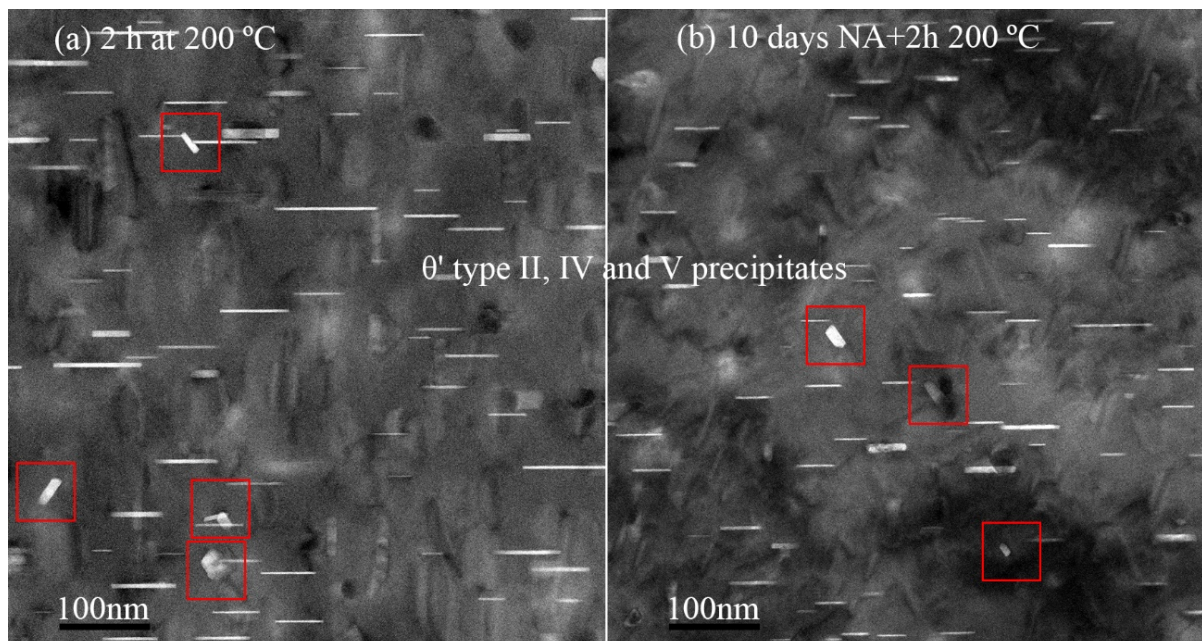


*Fig. 5.11 HAADF-STEM images of the Al-Cu-Ge alloy without (a) and with 10-day natural ageing before aged at 200 °C (b). Natural ageing hardly changes the fraction of Cu-rich precipitates decorated with a Ge particle.*

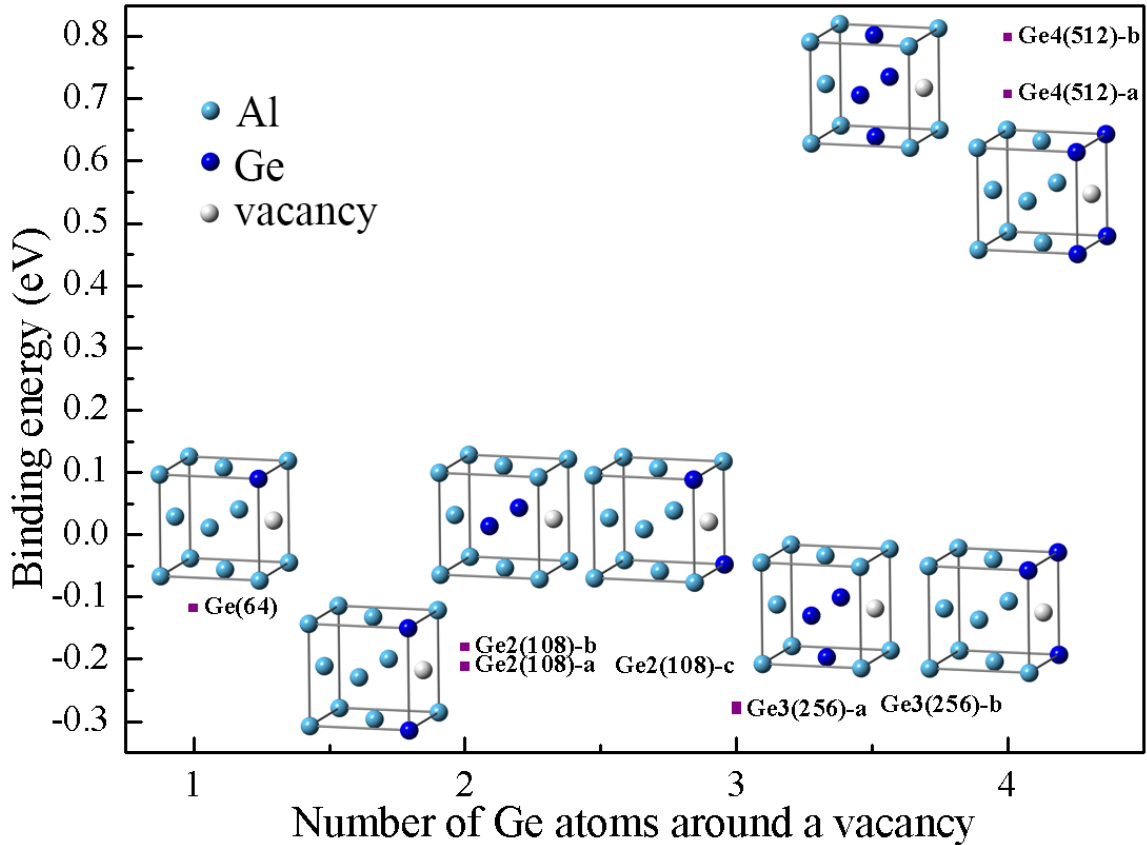


Fig. 5.12 Binding energies between solute Ge atoms and a vacancy calculated from DFT. The inset shows the schematic configurations of solute atoms around a vacancy and the number in parentheses is the size of the supercell.

Fig. 5.12 exhibits DFT-calculated binding energies between a vacancy and different numbers of Ge atoms. The calculated binding energy between a vacancy and a Ge atom is in good agreement with the literature report [39]. The binding energy becomes more negative with the increasing number of Ge atoms (up to 3), which is the same trend as that in In-Sb-vacancy co-clusters. However, the binding energy of the most favourable Ge-vacancy cluster is only -0.282 eV, while the binding energy of the most favourable In-Sb-vacancy cluster is -0.708 eV. The binding energy between an Sb atom and a vacancy (only 1 solute atom, -0.291 eV) is already more negative than that in the most favourable Ge-vacancy cluster (3 atoms, -0.282 eV). Therefore, natural ageing can hardly increase the binding strength of Ge atoms with a vacancy to a level comparable with the binding strength between In and Sb atoms with a vacancy. The low binding energies of Ge-vacancy clusters are the reason why natural ageing cannot significantly increase the fraction of  $\theta'$  precipitates decorated by a Ge crystal.

### 5.4 Heterogeneous nucleation of $\theta'$ (type I, II, IV and V) on Ge particles

The Cu-rich regions on the surface of Ge particles always transform into  $\theta'$  with a longer ageing time. The formation of  $\theta'$  from Cu-rich regions implies heterogeneous nucleation of a  $\theta'$  precipitate on a Ge particle starts with segregation of Cu atoms at the Ge/Al interface. The segregated Cu atoms at the beginning do not adopt the structure of  $\theta'$  but adopt an ill-defined structure at the Ge/Al interface (Fig. 5.3 and 5.4).

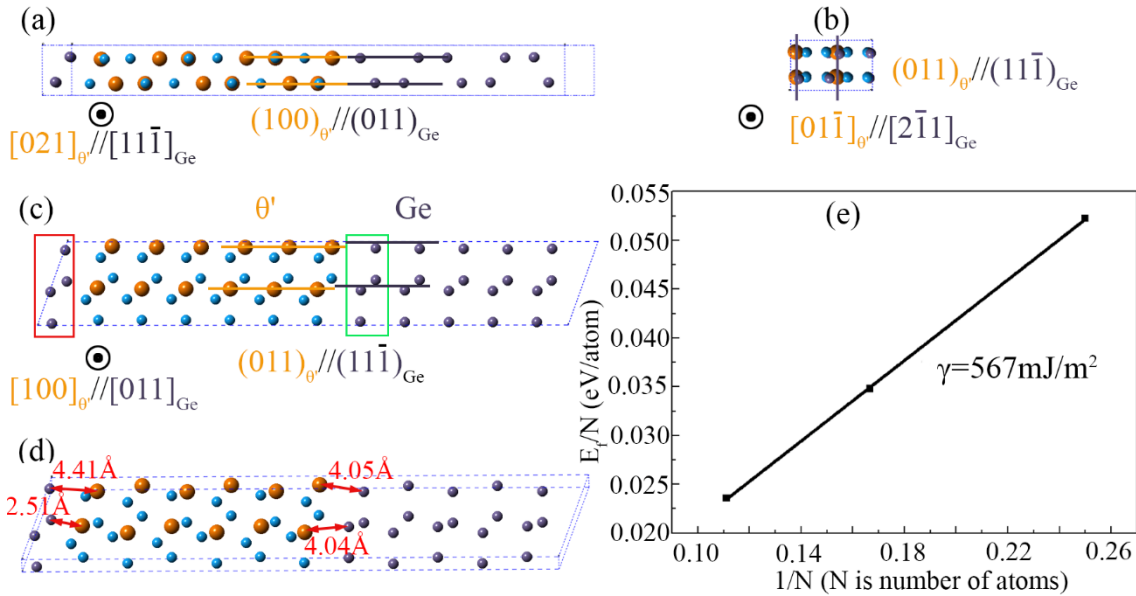


Fig. 5.13 Atomic model for the well-matching Ge/ $\theta'$  interface and DFT calculated interfacial energy. (a-d) atomic model of the interface (e) DFT calculated interfacial energy. The red rectangles indicate distortion at the left interface relative to the right one in the green rectangle. The orange and grey lines indicate the crystal planes of  $\theta'$  and Ge crystals, respectively.

To understand why Ge particles can facilitate the heterogeneous nucleation of  $\theta'$  precipitates, the atomic model (supercell) of the coherent  $\theta'$ /Ge interface was built according to Fig. 5.10 (b) and relaxed by DFT calculations, as shown in Fig. 5.13. The crystallographic orientation between Ge and  $\theta'$  can be expressed as  $[100]_{\theta'} // [011]_{Ge}$ ,  $(011)_{\theta'} // (11\bar{1})_{Ge}$ ,  $(01\bar{1})_{\theta'} // (2\bar{1}1)_{Ge}$ . Here one thing is important to be emphasised: the left interface in the red box is different from the right one in the green box. The right interface is in good agreement with the experimental observation (Fig. 5.14), but the left interface has significant distortion. The distortion essentially is caused by the unphysical distances between Ge and Cu atoms at the left interface, as shown in Fig. 5.13 (d). However, the deficiency at the left interface cannot be overcome easily at present due to the limitations of the periodic boundary condition in DFT calculations and the crystal structure of Ge and  $\theta'$  phases. In this atomic model, the Ge phase matches coherently with the  $\theta'$  phase at the right interface. However, due to the distortion at the left

interface, the calculated Ge/ $\theta'$  interfacial energy (the average of the left and right interfacial energies) should overestimate the real interfacial energy, and the real one is expected to be  $<520 \text{ mJ/m}^2$  ( $520 \text{ mJ/m}^2$  is the accepted interfacial energy of the  $\theta'$ /Al semi-coherent interface calculated by DFT).

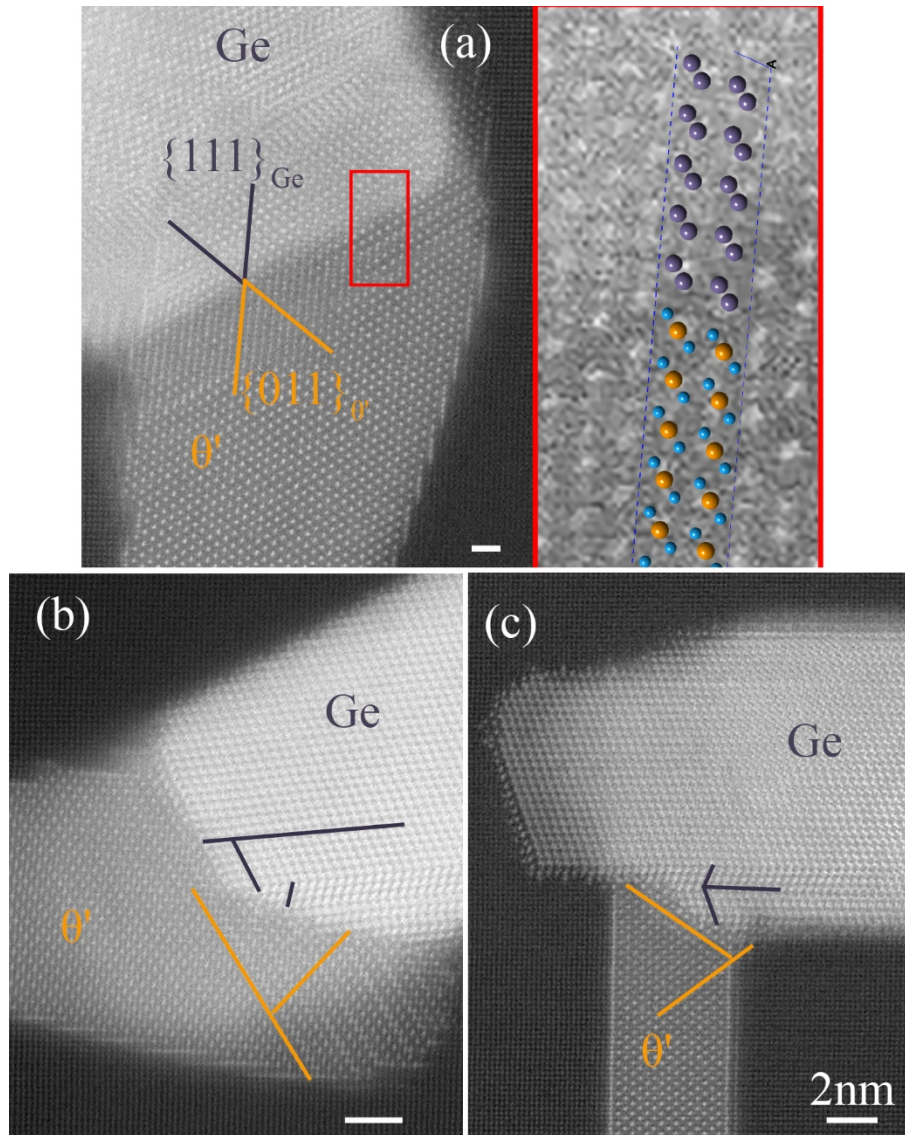


Fig. 5.14 HAADF-STEM images of the  $\theta'$ /Ge interface in the Al-Cu-Ge aged for 2 h at 200 °C. The orange lines and grey lines are parallel with the  $\{011\}_{\theta'}$  and  $\{111\}_{\text{Ge}}$  planes, respectively. The two planes are not always parallel but also form different angles. The DFT relaxed atomic model in Fig. 5.13 is overlapped as the inset in (a).

Fig. 5.14 shows the coherent Ge/ $\theta'$  interface. The DFT-relaxed atomic model (the right interface of Fig. 5.13) is in good agreement with the HAADF images, which further corroborates the above conclusion. In Fig. 5.14, the orange and grey lines are parallel with the  $\{011\}_{\theta'}$  and  $\{111\}_{\text{Ge}}$  planes, respectively, which indicates the  $\{011\}_{\theta'}$  and  $\{111\}_{\text{Ge}}$  planes are

not always parallel but form variable tilting angles. There are two possible reasons. First, the tilting angle between the two planes may hardly change the Ge/ $\theta'$  interfacial energy. Secondly, during the nucleation process, not only the Ge/ $\theta'$  interfacial energy but also the  $\theta'$ /Al interfacial energy contributes significantly to the nucleation energy barrier of  $\theta'$  precipitates. Therefore, the tilting angle may lower the total interfacial energy penalty of  $\theta'$  precipitates by reducing the  $\theta'$ /Al interfacial energy at the expense of forming tilting angles at the Ge/ $\theta'$  interface. Besides, strain energy may also play a critical role because Ge precipitates compress the Al matrix significantly, which further complicates the process of calculating the total free energy change associated with the nucleation of  $\theta'$  precipitates. Therefore, no further analysis was attempted in the present work.

Now we can propose that a Ge particle can be a heterogeneous nucleation site for a  $\theta'$  precipitate especially for  $\theta'$  type II, IV and V. There are two reasons. First, a  $\theta'$  precipitate is always preceded by a Cu-rich region at the surface of Ge particles which always transforms into a  $\theta'$  precipitate with ageing. Second, a  $\theta'$  precipitate can form a coherent interface with a Ge particle, which is expected to have an interfacial energy lower than the  $\theta'$ /Al semi-coherent interfacial energy.  $\theta'$  precipitates are never thicker than the attached Ge particles, which also suggests the  $\theta'$ /Ge coherent interfacial energy is lower than the  $\theta'$ /Al semi-coherent interfacial energy. Therefore,  $\theta'$  (type I, II, IV and V) precipitates decorated by a Ge particle are proposed to nucleate heterogeneously from pre-existing Ge particles.

### 5.5 Two nucleation mechanisms of $\theta'$ type III

$\theta'$  type III precipitates can be categorized into two kinds according to their morphologies. The first kind of precipitates is long and thin (see Fig. 5.24), while the second kind of precipitates is short and fat (Fig. 5.25). Moreover, the second kind of precipitates is always decorated with a big Ge particle, while the first kind of precipitates is usually free of a big Ge particle. The two kinds of  $\theta'$  type III precipitates are correlated with two different nucleation mechanisms, which is discussed in Section 5.5.4 and Section 5.5.5. In the following, the special interfacial structure of  $\theta'$  type III is shown to be an independent phase (named H phase in Section 5.5.1) and its crystal structure is determined in Section 5.5.2. To understand the formation mechanism of the H phase, the interfacial energy of the H/Al coherent interface was calculated by DFT calculations and is compared with  $\theta'$ /Al interfacial energies in Section 5.5.3. Finally, the two nucleation mechanisms of  $\theta'$  type III precipitates are discussed based on the discussion in Section 5.5.1 to 5.5.3.

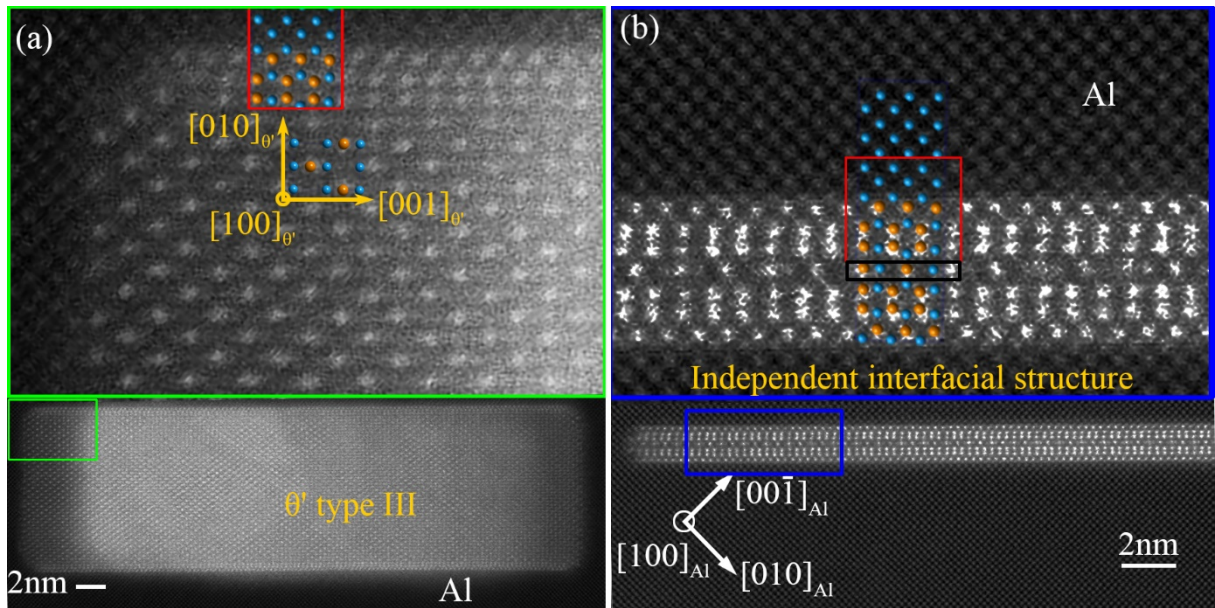
5.5.1 The H phase located at the  $\theta'$  type III/Al coherent interface

Fig. 5.15 HAADF-STEM images of the interfacial structure of  $\theta'$  type III precipitates in the Al-Cu-Ge alloy aged at 200 °C for 2 h. (a) a thick  $\theta'$  type III precipitate, (b) an independent H phase precipitate. The atomic models of the H phase and the  $\theta'$  phase are overlapped with the HAADF images. The red rectangles mark the structurally common part between the independent H phase precipitate and the special structure at the  $\theta'$ /Al interface, and the black rectangle highlights the difference between them.

Fig. 5.15 shows the special interfacial structure of  $\theta'$  type III precipitates, which is always present in the Al-Cu-Ge alloy but has never been reported before. Fig. 5.15 (a) shows a thick  $\theta'$  type III precipitate covered by the interfacial structure. The interfacial structure has a constant thickness in all the observed 30  $\theta'$  type III precipitates. The interfacial structure also exists as an independent precipitate without  $\theta'$  type III embedded inside, as shown in Fig. 5.15 (b), which suggests the special interfacial structure is an independent phase (named H phase here) rather than an interfacial correlated structure. The centre atomic layer (in black rectangle) of the independent precipitate in Fig. 5.15 (b) does not exist in the interfacial structure of  $\theta'$  type III precipitates. There are not any other differences between the independent H precipitate and the interfacial structure of  $\theta'$  type III precipitates. It is important to note that both the independent H precipitate and the interfacial structure are very similar to the special structure observed at the semi-coherent  $\{100\}_{\theta'}/\{100\}_{Al}$  interface in an Al-Cu binary alloy [28].  $\theta'$  type III precipitates can also directly contact with the Al matrix without the interfacial structure coverage, but this only extends two Cu columns along the lengthening direction (see the corner of the precipitate in Fig. 5.15 (a)). This may suggest the H phase coverage can lower the

interfacial energy of the Al/ $\theta'$  type III interface. The atomic models of the special interfacial structure and the H phase will be discussed in detail in Section 5.5.2.

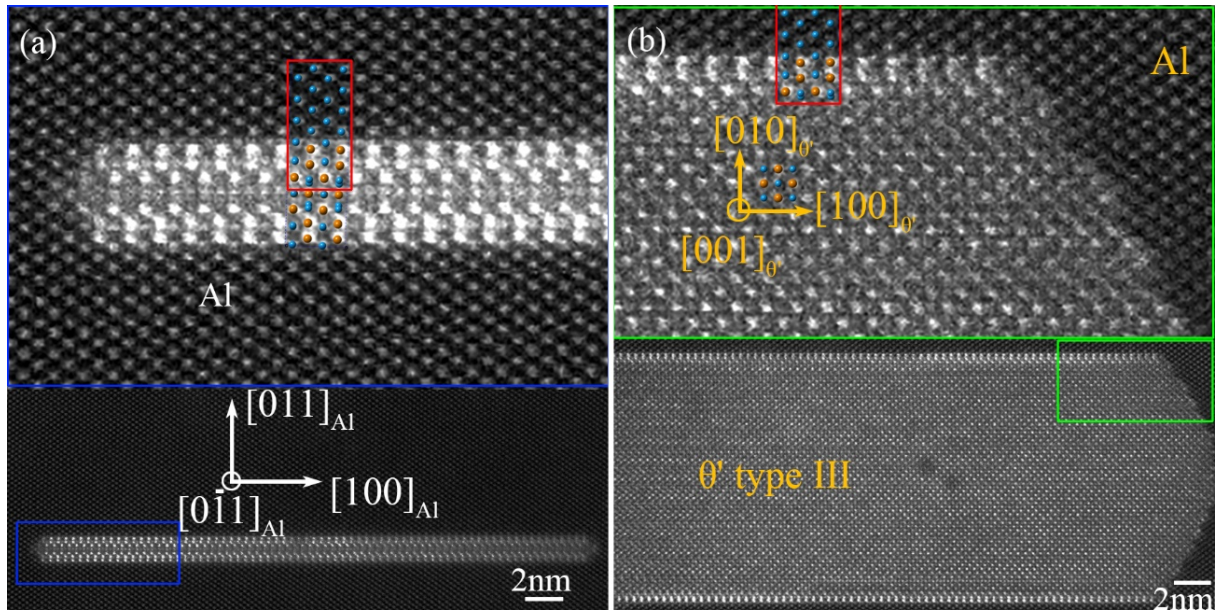


Fig. 5.16 HAADF-STEM images of (a) an independent H phase precipitate and (b) a thick  $\theta'$  type III precipitate covered by the H phase in the Al-Cu-Ge alloy aged at 200 °C for 1 h. The atomic models for the H phase and the  $\theta'$  phase are overlapped onto the HAADF images. The red rectangles mark the structurally common part between the H phase precipitate and the structure at the  $\theta'$ /Al interface.

Fig. 5.16 shows the interfacial structure of  $\theta'$  type III precipitates and an independent H phase precipitate viewed along  $\langle 011 \rangle_{\text{Al}}$ . The interfacial structure of  $\theta'$  type III precipitates is still different from that of  $\theta'$  precipitates but has almost the same structure as the independent H precipitate. The red rectangles highlight the shared structure between the Al/ $\theta'$  type III interface and the independent H phase precipitate. The  $\{100\}_{\theta'}$  planes can contact directly with the Al matrix but only at the narrow corners of  $\theta'$  type III precipitates, as shown in Fig. 5.16 (b).

There remains an ambiguity as to whether the special interfacial structure and H phase precipitates contain Ge atoms. Fig. 5.17 shows by energy dispersive X-ray spectroscopy (EDS) elemental mappings of a  $\theta'$  type III precipitate and an independent H phase precipitate. There is no detectable Ge segregation at the coherent interfaces for the two precipitates. However, the segregation of Ge element at the other interface is observable, which suggests EDS here is sensitive enough to detect interfacial solute segregation. Therefore, the special interfacial structure and the H phase are composed of Al and Cu atoms, though a very low concentration of Ge that is lower than the detectable limit may be present as an impurity.

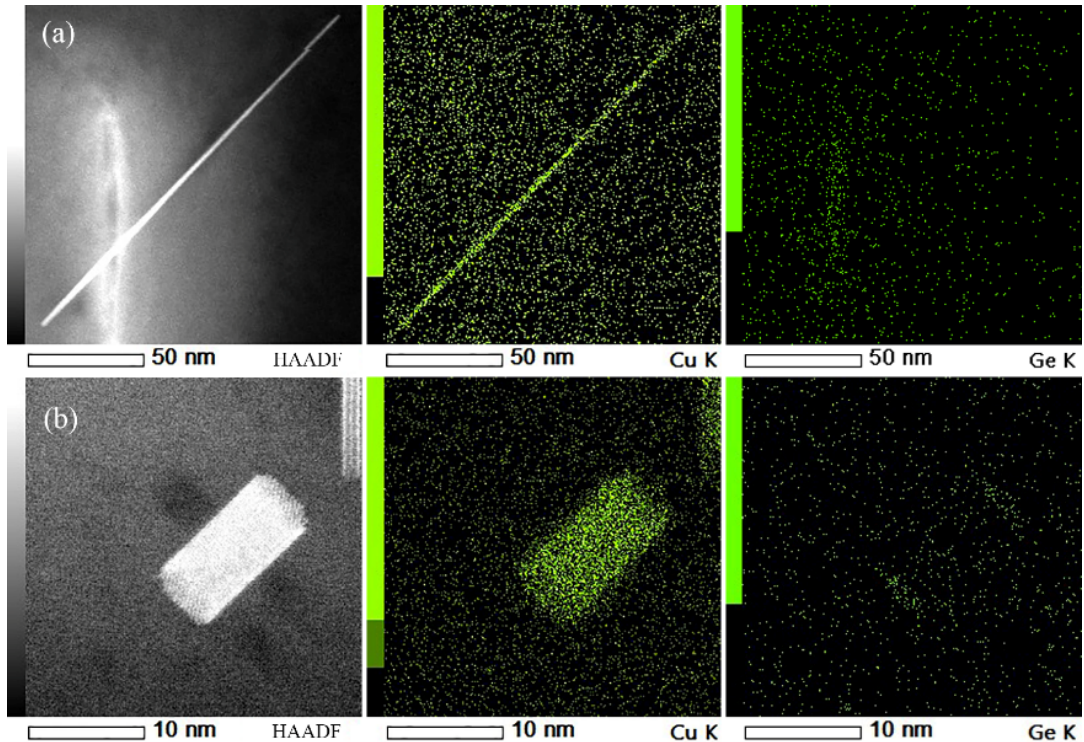


Fig. 5.17 EDS elemental mappings of (a) an independent H phase precipitate and (b) a  $\theta'$  type III precipitate in the Al-Cu-Ge alloy aged 2 h at 200 °C. The incident electron beam was near  $\langle 001 \rangle_{Al}$  zone axis (deviation  $< 2^\circ$ ).

### 5.5.2 Crystal structure and formation energy of the H phase

The atomic model of the H phase and its interface with the Al matrix were built according to Fig. 5.15 and Fig. 5.16, using a similar structure at the semi-coherent  $\theta'/Al$  interface in an Al-Cu binary alloy [28] as a starting point. The built atomic models were then relaxed using DFT calculations and compared with HAADF-STEM images. Iterative optimization was carried out by comparing the DFT relaxed structure with HAADF-STEM images. Fig. 5.18 shows the finally determined atomic models of the H phase and the H/Al interface which show excellent agreement with HAADF-STEM images, as displayed in Fig. 5.15 and Fig. 5.16. The determined atomic model for the H/Al coherent interface (in Fig. 5.18 (a) and (b)) is also applicable for the  $\theta'$  type III/Al interface because  $\theta'$  type III precipitates are always covered by a segment of the H phase. The segment of the H phase on the interface of  $\theta'$  type III precipitates is about a half unit cell in thickness along  $[001]_H$ , as highlighted by red rectangles in Fig. 5.15, Fig. 5.16 and Fig. 18. The two segments (at two  $\theta'$  type III/Al coherent interfaces) of the H phase can be viewed as an H precipitate separating along the black rectangle. Except for the difference highlighted by the black rectangles, the structure of the H phase is the same as the structure at the  $\theta'$  type III/Al coherent interface.

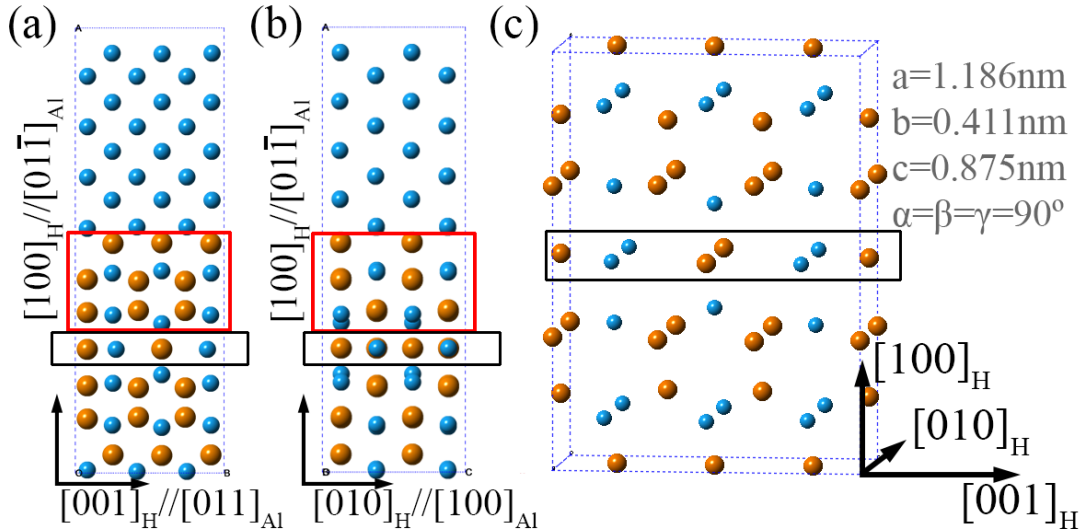


Fig. 5.18 Atomic models of the H/Al interface and the H phase. (a) and (b) are the atomic models of the interface viewed along  $[100]_{Al}$  and  $[011]_{Al}$ , respectively. (c) a unit cell of the H phase and the corresponding lattice parameters. The structure in red rectangles is observed at the  $\theta'$  type III/Al coherent interface, while the structure in black rectangles is not observed at the  $\theta'$  type III/Al coherent interface. CIF file for the H phase is given in Appendix 3.

Table 5.2 Formation energies of the H phase and  $\theta'$  type I from DFT calculations (see Appendix 1 for the used supercells).

Phases	Compositions	Formation energies <sup>§</sup>	Formation energies <sup>¶</sup>
		(eV/atom)	(eV/atom)
The H phase	$Al_{14}Cu_{17}$	-0.182	/
#Embedded H	$Al_{14}Cu_{20}^{#+}$	-0.201	-0.142
$\theta'$	$Al_2Cu$	-0.174	/
Embedded $\theta'$	$Al_{10}Cu_7^{#\times}$	-0.171	-0.130

<sup>§</sup> Formation energies relative to pure Al and Cu crystals.

<sup>¶</sup> Formation energies relative to Al and Cu solutes. The chemical potential of a Cu atom is approximated by the formation energy of a Cu atom together with 47 Al atoms in a fully relaxed FCC lattice.

<sup>#</sup> Compositions of embedded phases do not include the Al matrix. Formation energies are also averaged over atoms in precipitates only.

<sup>+</sup> The greater Cu-enrichment for the embedded H phase can be found in Appendix 1: there are two outmost Cu layers but only one in the bulk state one.

<sup>×</sup> The composition of  $\theta'$  is more Cu-enriched because the coherent interface is fully Cu occupied, it will be close to  $Al_2Cu$  for thick precipitates [27].

The formation energy of the H phase is compared with that of  $\theta'$  type I, as shown in Table 5.2. Here the formation energies are calculated relative to both pure elements and to solute atoms in the Al matrix. The H phase has a lower formation energy per atom compared to  $\theta'$  type I, whether in bulk state or as an embedded phase in the Al matrix. Therefore, ignoring the contribution of entropy [28, 63, 146], the DFT calculated formation enthalpies suggest that the H phase has a higher driving force of nucleation compared with  $\theta'$  type I. However, the thermodynamic favourability of the H phase is achieved at the expense of a higher Cu concentration ( $\sim\text{Al}_1\text{Cu}_1$ ), which means that the H phase is expected to rely more on Cu diffusion than  $\theta'$  type I ( $\text{Al}_2\text{Cu}$ ). Therefore, it is anticipated that H phase precipitates can form only if fast Cu diffusion is possible.

One important thing should be emphasized: the above formation energies/enthalpies cannot be used to predict the thermodynamic stability of a system consisting of a precipitate and the Al matrix. Therefore, even though DFT calculations suggest the H phase has a high driving force of nucleation than  $\theta'$  type I, it is still an open question which precipitation product, H precipitates or  $\theta'$  type I precipitates, can lower the energy of an Al-Cu solid solution more.

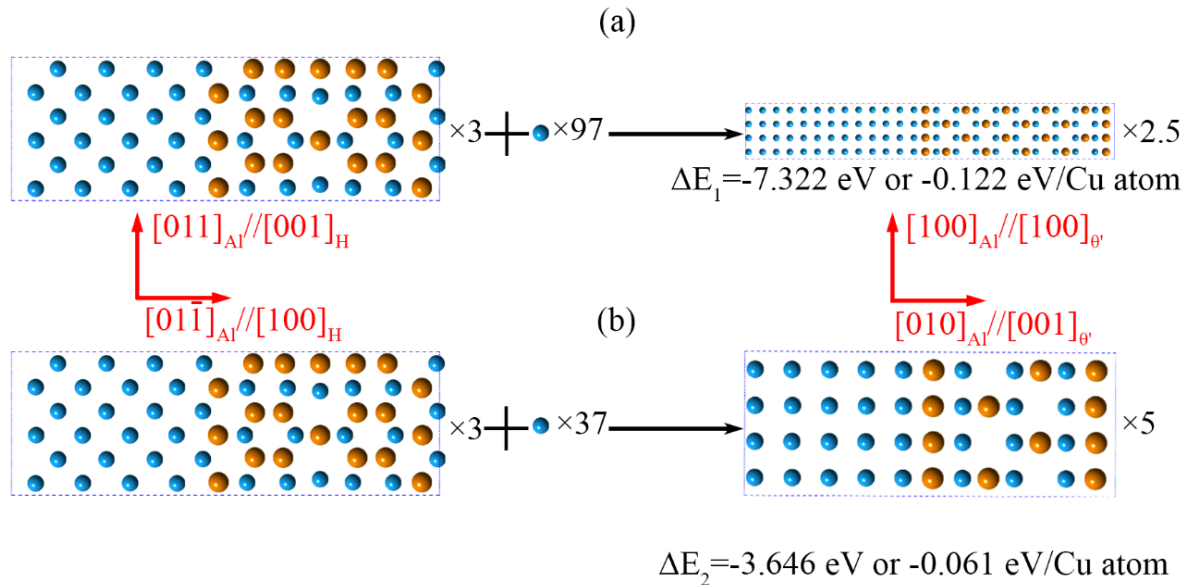


Fig. 5.19 Transformation energy from (an H phase precipitate and the Al matrix) to (a  $\theta'$  type I precipitate and the Al matrix). (a) 4.5 unit cell thick  $\theta'$ , (b) 1.5 unit cell thick  $\theta'$ . The blue spheres are Al atoms and orange ones are Cu atoms. The single blue atom after + is an Al atom, and its energy is the ground state energy in the FCC lattice. The supercells and Al atoms are multiplied (indicated by  $\times$ ) by different times to make sure the numbers of Al and Cu atoms are the same on the left and right sides of the black arrows.

Inspired by the concept of convex hull analysis in the literature [1, 181, 182], the thermodynamic stability of the Al matrix with either the H phase or  $\theta'$  type I precipitates can be compared by calculating the transformation energy from one to the other. The transformation energy is the formation energy difference of supercells in the form of either (the Al matrix and an H phase precipitate) or (the Al matrix and a  $\theta'$  precipitate). It is very difficult to build two supercells with the same numbers of Al and Cu atoms with different precipitate types (H or  $\theta'$  type I) embedded in the Al matrix. Assuming an Al atom in the Al matrix has the same energy as an Al atom in its ground state (FCC lattice), additional Al atoms can be added to keep the numbers of Al and Cu atoms the same in the transformation (see Fig. 5.19). The assumption has been widely used in convex hull analysis in the literature [1, 181, 182]. A negative transformation energy suggests precipitation in the form of  $\theta'$  precipitates and the Al matrix is more thermodynamically stable than in the form of H phase precipitates and the Al matrix. The transformation energy is more negative for the thicker embedded  $\theta'$  precipitate (see Fig. 5.19), which is consistent with the energy lowering process of  $\theta'$  coarsening in experiments. Thus, it is valid to compare the thermodynamic stability of the system (the Al matrix and precipitates) using the transformation energy.

In conclusion, a precipitate in the form of the H phase has a higher nucleation driving force compared with in the form of  $\theta'$  type I, but this is achieved at the expense of less lowering the energy of the Al-Cu solid solution system. In contrast, a precipitate in the form of  $\theta'$  type I results in a system (precipitates and the Al matrix) with a lower energy compared with that in the form of the H phase, though the nucleation driving force of  $\theta'$  is lower than the H phase. The nucleation of the H phase is expected to be more kinetically favourable due to a high driving force of nucleation if Cu diffusion is not a bottleneck. Excess vacancies released from Ge atoms are expected to play a critical role in enhancing Cu diffusion and making the nucleation of the H phase possible. The critical role of vacancies in the nucleation of the H phase will be further discussed in Chapter 6.

### 5.5.3 Low interfacial energy of the H/Al coherent interface

$\theta'$  type III precipitates are always covered by the H phase at the  $\theta'$  type III/Al coherent interface in the Al-Cu-Ge alloy, which may suggest the H/Al interfacial energy is lower than the  $\theta'$ /Al interfacial energy. In the following, the interfacial energy of the coherent H/Al interface will be compared with that of two cases of coherent  $\theta'$ /Al interfaces. The first coherent  $\theta'$ /Al interface is  $\{001\}_{\theta'}/\{001\}_{Al}$  (the coherent interface for  $\theta'$  type I, the most common coherent  $\theta'$ /Al interface in Al-Cu alloys). The second coherent  $\theta'$ /Al interface is

$\{010\}_{\theta'}/\{011\}_{\text{Al}}$ , which has been observed only at corners of  $\theta'$  type III precipitates (see Fig. 5.15 and 5.16).

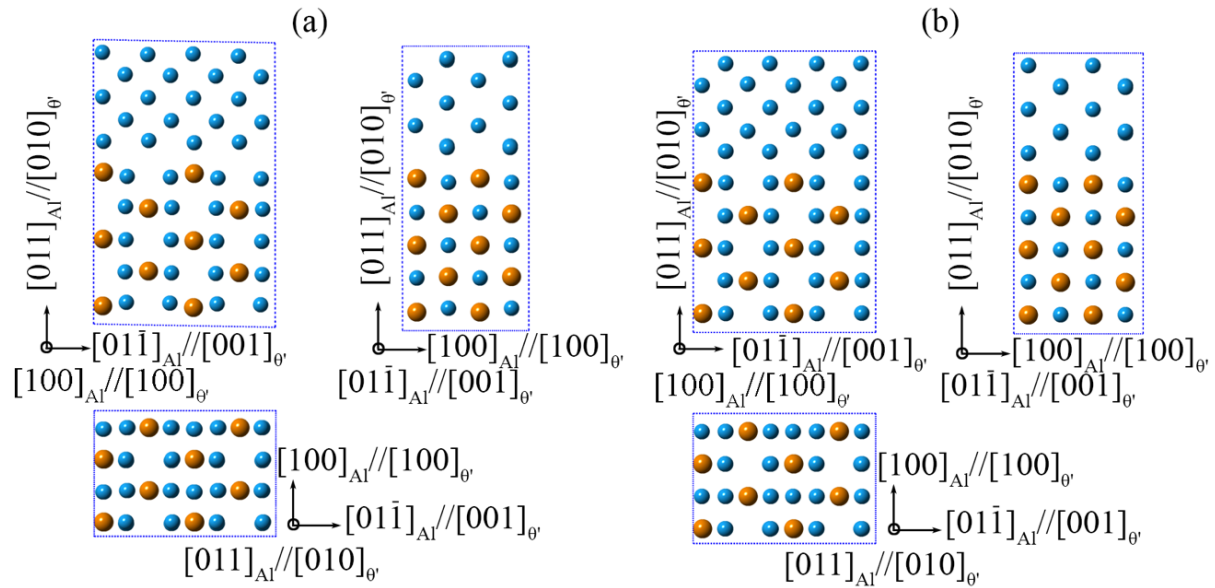


Fig. 5.20 Possible atomic models of the direct interface between the Al matrix and a  $\theta'$  type III precipitate. (a) the first possible atomic model, (b) the second possible atomic model.

Before further going, it is necessary to discuss how  $\theta'$  type III precipitates (habit planes are  $\{011\}_{\text{Al}}$ ) match with the Al matrix without the H phase coverage. Two possible atomic models of the direct coherent  $\theta'$  type III/Al interface were built based on the crystallographic orientation relationship observed experimentally. The DFT-relaxed atomic models are shown in Fig. 5.20. The two models are very similar. Shifting the Al matrix part by  $\sim 0.14$  nm (half of the nearest neighbour distance among Al atoms) along  $[01\bar{1}]_{\text{Al}}$  in Fig. 5.20 (a) will produce the atomic model shown in Fig. 5.20 (b). In the two possible models,  $\theta'$  matches coherently with the Al matrix. The mismatching at the interface is  $\sim 0\%$ , which is surprisingly low. Such a low mismatch is comparable with that at the coherent interface of  $\theta'$ /Al for  $\theta'$  type I. If a low mismatch is a good indicator of a low interfacial energy [183-185],  $\theta'$  type III precipitates should be common in Al-Cu binary alloys. However, to the best knowledge of the author,  $\theta'$  type III precipitates have never been reported in Al-Cu alloys.

The interfacial energies of the coherent H/Al interface (atomic model shown in Fig. 5.18) and the two possible direct  $\theta'$  type III/Al interfaces (atomic model shown in Fig. 5.20) were calculated using first-principles calculations, as shown in Fig. 5.21. The coherent H/Al interface has the lowest interfacial energy, even lower than the  $\{001\}_{\theta'}/\{001\}_{\text{Al}}$  coherent interface; while the direct interface between a  $\theta'$  type III precipitate and the Al matrix

( $\{010\}_{\theta'}/\{011\}_{\text{Al}}$ ) has the highest interfacial energy. Therefore, the high interfacial energy renders  $\theta'$  type III precipitates rare to occur in Al-Cu binary alloys. The coverage of the H phase on  $\theta'$  type III precipitates is expected to significantly reduce the interfacial energy of  $\theta'$  type III precipitates. The nearly full coverage of  $\theta'$  type III precipitates by the H phase also suggests the coverage results in a lower interfacial energy.

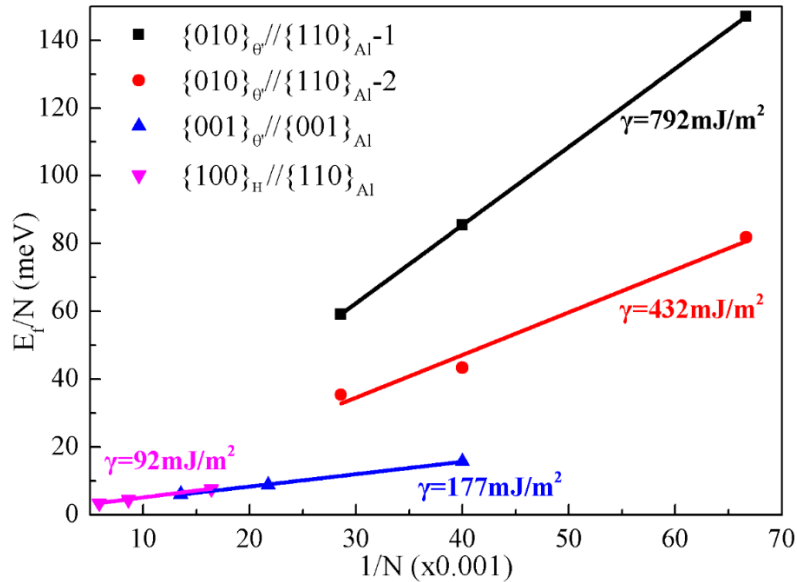


Fig. 5.21 DFT calculated interfacial energies of four different interfacial models. The coherent H/Al interface has the lowest interfacial energy.  $N$  is the number of atoms in a supercell and  $E_f$  is the formation energies of the supercell (supercells are shown in Appendix 1).

An atomic model of a thick  $\theta'$  type III precipitate covered by the H phase at the coherent interface with the Al matrix was also built and relaxed by DFT calculations (see Fig. 5.22). The atomic columns in the model are in good agreement with the HAADF-STEM image. The interfacial energy for such a complex interface cannot be directly calculated using the method described in Section 3.4.3 because the extra atomic columns in the black rectangle of the H phase (see Fig. 5.18) will be unnecessarily but inevitably subtracted. Such an unreasonable subtraction will result in an overestimation of the interfacial energy [186]. Therefore, interfacial energy for such a complex interface is not calculated here, and formation energy of the Cu-rich part will be used for discussion instead. DFT calculated formation energy of the Cu-rich part in the model is -0.176 eV per atom. It is lower than the formation energy of  $\theta'$  type III with a direct interface with the Al matrix (-0.081 eV/atom for the 1st model and -0.120 eV/atom for the 2nd model) but slightly higher than an embedded  $\theta'$  type I precipitate (-0.186 eV/atom).

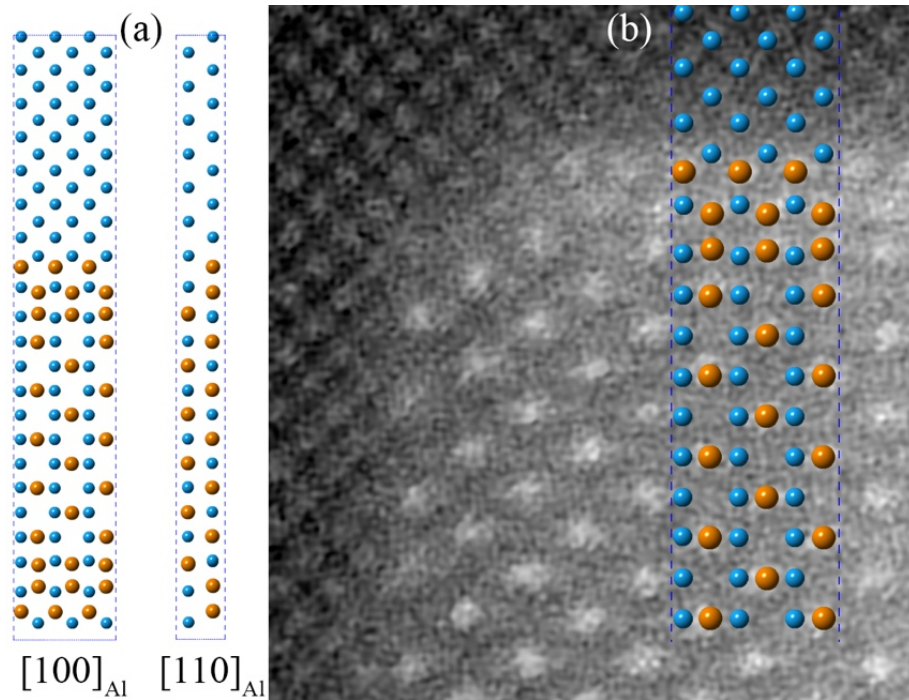


Fig. 5.22 Atomic model of a thick  $\theta'$  type III precipitate covered by the H phase viewed from  $[100]_{Al}$  and  $[110]_{Al}$ , (b) comparison between the relaxed atomic model and the HAADF-STEM image (The viewing direction is  $[100]_{\theta'}/[100]_{Al}$ ).

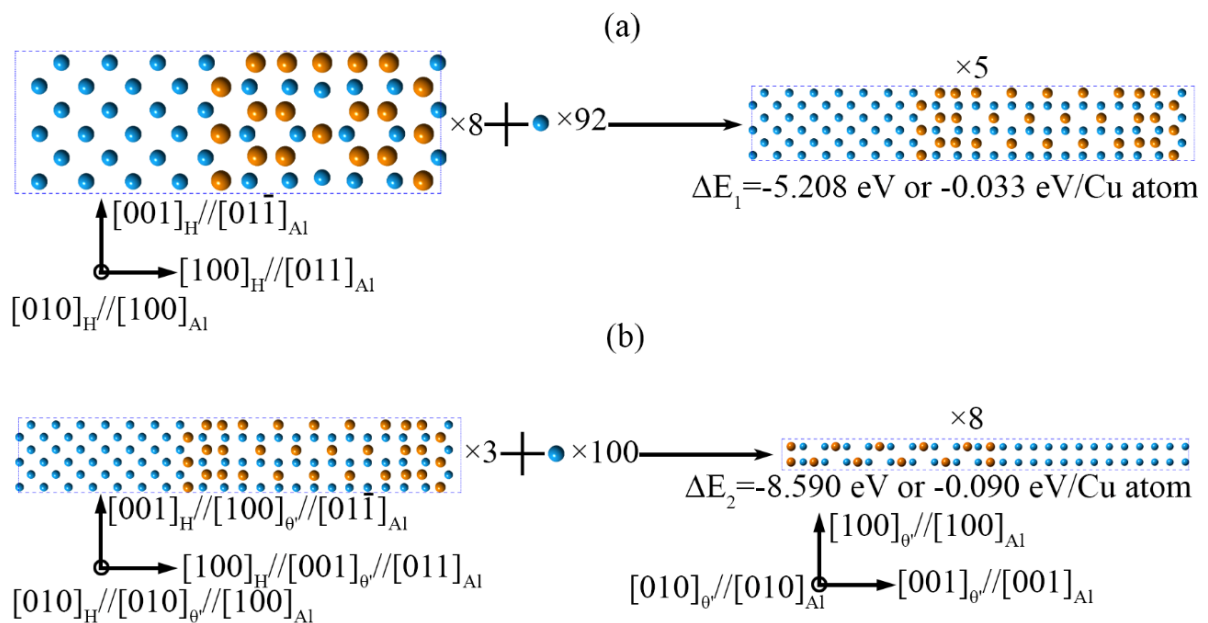


Fig. 5.23 Transformation energies for (a) the transformation from an embedded H phase precipitate to a thick  $\theta'$  type III precipitate covered by the H phase and (b) the transformation from an embedded thick  $\theta'$  type III precipitate covered by the H phase to an embedded 4.5 unit cell thick  $\theta'$  type I precipitate. The blue spheres are Al atoms and orange ones are Cu atoms. The single blue atom before + is an Al atom, and its energy is the ground state energy in the FCC lattice. The supercells and Al atoms are multiplied (indicated by  $\times$ ) by different times to make sure the numbers of Al and Cu atoms are the same on the left and right sides of the black arrows.

Fig. 5.23 displays the transformation energies involving a thick  $\theta'$  type III precipitate covered by the H phase. The negative transformation energy in Fig. 5.23 (a) suggests precipitation in the form of a thick  $\theta'$  type III precipitate covered by the H phase in the Al matrix is more thermodynamically stable than that in the form of the H phase in the Al matrix. Therefore, the formation of a thick  $\theta'$  precipitate inside an existing H phase precipitate is thermodynamically driven. The negative transformation energy from a thick  $\theta'$  type III precipitate covered by the H phase together in the Al matrix to a  $\theta'$  type I precipitate in the Al matrix indicates that  $\theta'$  type I precipitates is more thermodynamically stable than  $\theta'$  type III precipitates in the Al matrix.

In summary, an H phase precipitate has a driving force of nucleation and a lower coherent interfacial energy compared with both a  $\theta'$  type I or  $\theta'$  type III precipitate with a direct interface (see Fig. 5.20). Therefore, the H phase is expected to form first from the Al-Cu solid solution because it has a lower nucleation energy barrier compared with  $\theta'$  type I (strain energy is not considered here).  $\theta'$  type III precipitates are anticipated to form inside existing H phase precipitates (as shown in Fig. 5.15 and Fig. 5.16) because this can lower the energy of the system consisting of precipitates and the Al matrix (a negative transformation energy).  $\theta'$  type I precipitates in the Al matrix are always preferred in terms of the thermodynamic stability of the system of precipitates and the Al matrix (see Fig. 5.19 and Fig. 5.23), but H phase precipitates and  $\theta'$  type III precipitates are kinetically favoured due to a lower nucleation energy barrier. The reason for the lower number density of H phase precipitates and  $\theta'$  type III precipitates is correlated with excess vacancies, which will be discussed in Chapter 6.

#### 5.5.4 Long and thin $\theta'$ type III precipitates nucleating inside H phase precipitates

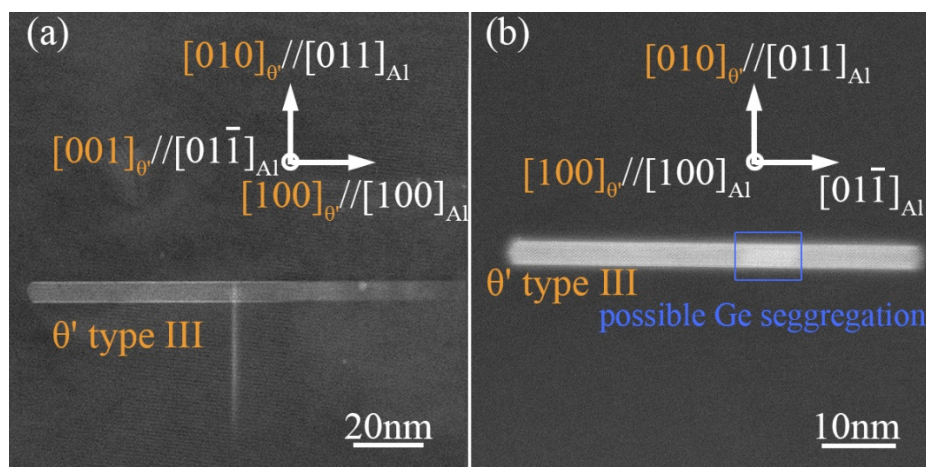


Fig. 5.24 Long and thin  $\theta'$  type III precipitates in the Al-Cu-Ge alloy aged for 1 h (a) and 2 h (b) at 200 °C. These precipitates are free of a big Ge particle.

Fig. 5.24 shows long and thin  $\theta'$  type III precipitates. These precipitates exist without the decoration of a Ge particle. However, there may be Ge solute segregation at the semi-coherent interface. The segregation of Ge atoms at the semi-coherent interface may finally induce the nucleation and growth of Ge particles, as shown by the brighter region in the precipitate in Fig. 5.24 (b). The dimensions of the  $\theta'$  type III precipitates are much greater than the possible Ge particles, which means the nucleation of the Ge particle must occur much later.

The nucleation of long and thin  $\theta'$  type III precipitates is hypothesized to start inside the H phase precipitates. H phase precipitates form first from the Al matrix as shown in Fig. 5.15 and 5.16, which provide heterogeneous nucleation sites for  $\theta'$  type III precipitates, because the H phase has a lower nucleation energy barrier. This process is similar to the formation process of the  $\Omega$  phase in Al-Cu-Mg-Ag alloys, where a special interfacial structure consisting of Mg and Ag forms first and then the  $\Omega$  phase forms inside [63]. Please note H phase precipitates are always only 1 unit cell thick along  $[100]_H$ . The formation of  $\theta'$  type III precipitates is proposed to start by transforming half thickness of H phase precipitates into  $\theta'$  precipitates. A new half unit cell thick H precipitate is expected to form at the  $\theta'$  type III/Al coherent interface to lower the interfacial energy. The transformation of the H phase into  $\theta'$  type III is also thermodynamically driven, as shown in Fig. 5.23. If H phase precipitates cannot form first,  $\theta'$  type III precipitates cannot form by themselves due to the high interfacial energy cost. The constant thickness of the H phase segment at the coherent  $\theta'$  type III/Al interface suggests the transformation from the H phase segment (half unit cell along  $[100]_H$ ) to  $\theta'$  type III is very easy.

The interface-mediated nucleation and growth are not uncommon. The first report may be the nucleation of FCC crystal covered by BCC structured interface in many single elemental liquids [187]. This theory was validated 30 years later by computer simulations: BCC crystals act as precursors for the nucleation of FCC crystals and continuously locate at the interface of FCC crystals [188, 189]. As discussed here, the BCC part at the interface also results in a lower nucleation energy barrier and a lower interfacial energy [188, 189]. The interfacial phase must be both thermodynamically metastable (a local minimum on the free energy landscape) and mechanically stable and always has a lower interfacial energy than the phase in the core [11, 190-192].

### 5.5.5 Short and thick $\theta'$ type III precipitates nucleating heterogeneously on Ge particles

Fig. 5.25 shows short and thick  $\theta'$  type III precipitates. They are always attached to a big Ge particle which is usually bigger than or comparable with the  $\theta'$  type III precipitates. Ge particles always have twins inside and are free of the H phase segment at the interface, which

makes it easy to distinguish Ge particles from  $\theta'$  type III precipitates. The high-resolution images clearly show that  $\{011\}_{\theta'}$  planes are coherent with  $\{111\}_{\text{Ge}}$  planes. The superimposed atomic model (Ge/ $\theta'$  interface model shown in Fig. 5.13) generally matches well with the atomic columns of the Ge/ $\theta'$  interface in Fig. 5.25 (c). Therefore, these  $\theta'$  type III precipitates are expected to nucleate heterogeneously on a Ge particle, as that discussed for  $\theta'$  type I, II, IV and V precipitates. The crystal orientation relationship between a Ge particle and a  $\theta'$  type III precipitate is, in essence, the same as that for other  $\theta'$  types. However, here both Ge precipitates and  $\theta'$  type III precipitates have a new orientation relationship with the Al matrix. Since a  $\theta'$  type III precipitate nucleates heterogeneously from a Ge particle, the semi-coherent Al/ $\theta'$  type III interface is replaced by a coherent Ge/ $\theta'$  interface at one end. Thus,  $\theta'$  type III precipitates can thicken more easily but cannot exceed the thickness of the attached Ge particle. The H phase coverage on the coherent Al/ $\theta'$  type III interface may not be very important at the heterogeneous nucleation stage of a  $\theta'$  type III precipitate on a Ge particle, as suggested by the bareness of the H phase at the corners of thick  $\theta'$  type III precipitates, but the H phase will form to reduce the interfacial energy of Al/ $\theta'$  type III interface later.

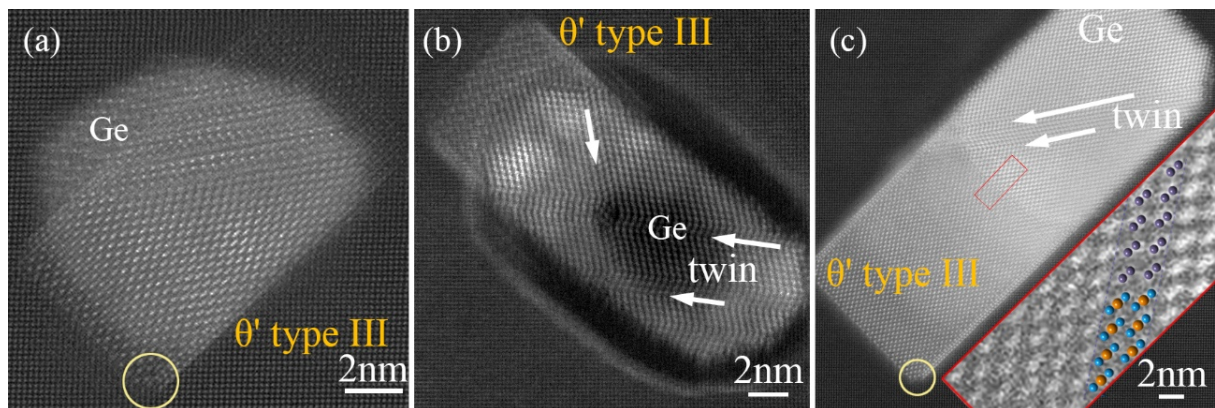


Fig. 5.25 Short and thick  $\theta'$  type III precipitates nucleating heterogeneously on Ge particles in the Al-Cu-Ge alloy aged for 15 min (a) and 1 h (b) and 2 h (c) at 200 °C. The inset in (c) is the enlargement of the area in the small red rectangle and the superimposed Ge/ $\theta'$  interfacial atomic model. Circles highlight the regions free of the interfacial H phase coverage. The viewing direction is  $[100]_{\theta'} // [100]_{Al}$ .

## 5.6 Possible formation mechanism of $\Omega$ precipitates

Long  $\Omega$  precipitates are the main precipitates in Al-Cu-Mg-Ag alloys but are rare precipitates in Al-Cu-Mg alloys [61]. Recent atomic characterisations suggest Mg and Ag together segregate at the  $\Omega$ /Al coherent interface and form a distinct interfacial structure [63]. However,  $\Omega$  precipitates were found recently as main precipitates in the cold-worked 2024 Al alloy (Al-4.5wt.%Cu-1.5wt.%Mg-0.5wt.%Mn) [56]. Short  $\Omega$  precipitates form at the second

ageing peak in the cold-worked 2024 Al alloy, with the first peak dominated by normal S' precipitates. These short  $\Omega$  precipitates mainly nucleate heterogeneously from undissolved T phase precipitates (see Fig. 2.25) in the 2024 Al alloy. Here  $\Omega$  precipitates are also short and sometimes also seem to nucleate heterogeneously on a Ge particle (see Fig. 5.7). The coherent  $\Omega$ /Al interface shows a bright Z-contrast (Fig. 5.7), which may suggest interfacial segregation of Ge, just like Ag and Mg. However, the interfacial structure and composition of  $\Omega$  precipitates in the Al-Cu-Ge alloy have not been resolved because only two  $\Omega$  precipitates were found. Further study is desired to understand the role of a Ge particle and interfacial Ge segregation on  $\Omega$  formation.

### 5.7 Possible Ge segregation at the semi-coherent $\theta'$ type I/Al interface

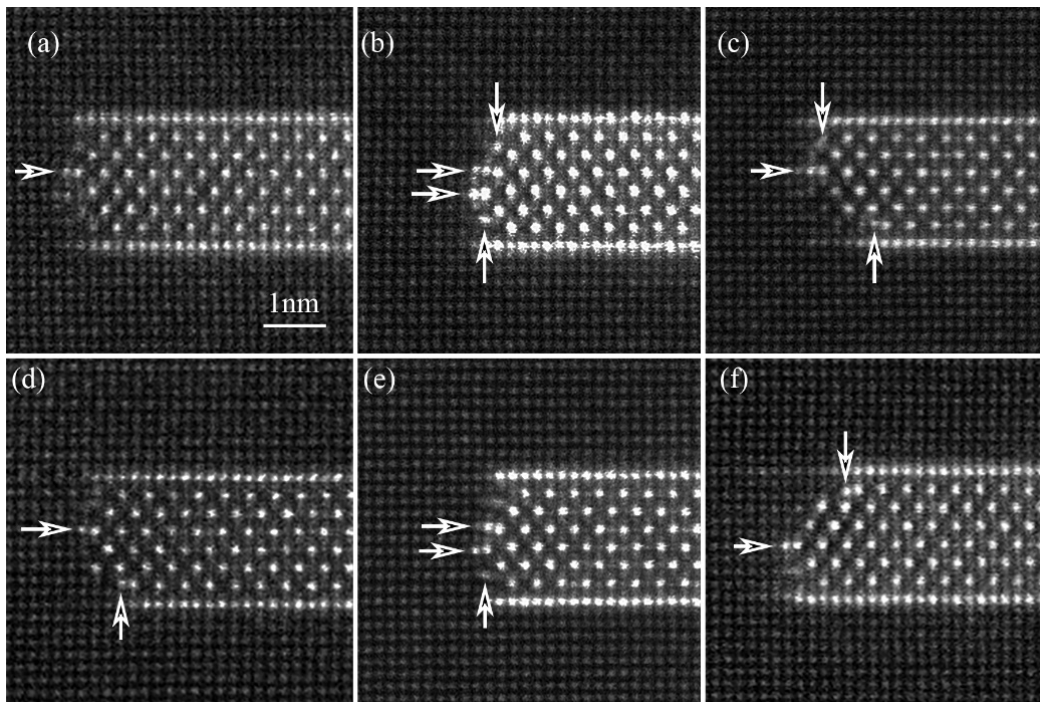


Fig. 5.26 HAADF-STEM images of the semi-coherent  $\theta'$  type I/Al interface in the Al-Cu-Ge alloy aged for 1 h at 200 °C. Arrows highlight extra atomic columns that have never been observed in Al-Cu alloys.

Fig. 5.26 shows the semi-coherent  $\theta'$  type I/Al interface in the Al-Cu-Ge alloy, which is different from the common semi-coherent  $\theta'$ /Al interface in Al-Cu binary alloys [28]. The arrows in Fig. 5.26 indicate extra atomic columns that have never been observed in equilibrium lattice positions of both the Al matrix and  $\theta'$  precipitates. These columns should be enriched with Ge, Cu or their mixture because they have a higher Z-contrast than Al columns. These extra atomic columns may be correlated with Ge solute segregation. Here it is worth to mention

that the observed possible Ge segregation positions (the extra atomic columns) are different from the favourable positions retrieved from DFT calculations [102]. Further work that can distinguish elemental distribution at the atomic scale is necessary. Both ordered solute segregation and solute-induced reconfiguration at interfaces can be expected but not commonly observed [193, 194].

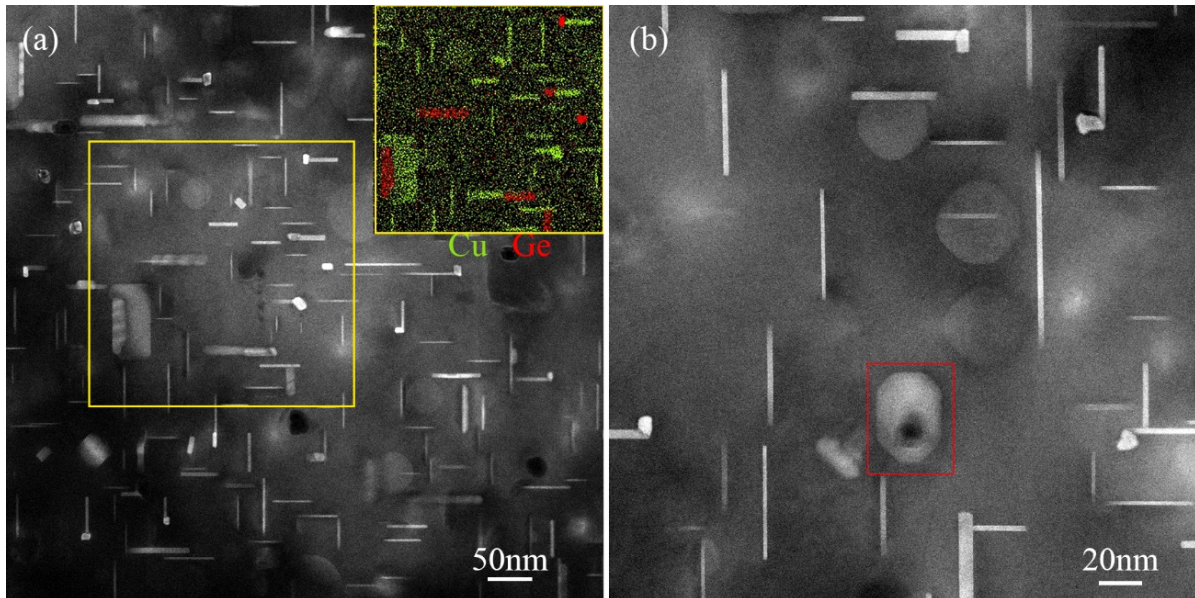


Fig. 5.27 HAADF-STEM images showing the rounding of  $\theta'$  precipitates (type I) in the Al-Cu-Ge alloy aged for 2 h at 200 °C. EDS elemental mapping of the area in the yellow square is shown as the inset in (a). The  $\theta'$  precipitate in the red rectangle is the common morphology of  $\theta'$  precipitates in Al-Cu binary alloys at the peak aged condition.

Fig. 5.27 shows the typical morphologies of Cu-rich precipitates in the Al-Cu-Ge alloy. Most of the face-on  $\theta'$  precipitates are circular. However, the common projection morphology of  $\theta'$  precipitates in Al-Cu binary alloys looks like the one in the red rectangle of Fig. 5.27 (b). The morphology change is proposed to be correlated with Ge segregation at the semi-coherent  $\theta'$  type I/Al interface, which changes the interfacial energy differently along different crystallographic directions (i.e.,  $[100]_{\theta'}$  and  $[110]_{\theta'}$ ). The Ge solute segregation at the semi-coherent interface may be uneven along the periphery of a  $\theta'$  precipitate, and it will be interesting to probe the concentration profile along the periphery in the future. There are also rare  $\theta'$  precipitates with a rectangular/square morphology which are always decorated by a Ge precipitate on **the  $\theta'$ /Al coherent interface and near the edge of  $\theta'$**  (see 5.27(a)).  $\theta'$  precipitates in the Al-Cu-In-Sb alloy are also rectangular/square when an InSb particle is located at **the  $\theta'$ /Al coherent interface and near the edge of  $\theta'$** . The author believes that a Ge/InSb particle can modulate the solute concentration distribution along the periphery of  $\theta'$  precipitates because

they consume the solutes that segregate at the semi-coherent  $\theta'/\text{Al}$  interface. However, more work is needed to fully understand the solute segregation at the semi-coherent  $\theta'/\text{Al}$  interface.

## 5.8 Conclusions

The effects and roles of Ge additions on the precipitation of Al-Cu alloy were investigated and compared with In and Sb additions. The conclusions are the followings:

1. Ge additions can increase precipitation kinetics and peak hardness in the Al-1.7at.%Cu alloy.
2. As for In and Sb additions, Ge additions are associated with two mechanisms for promoting the nucleation of Cu-rich phases: (a) releasing excess vacancies and increasing the diffusivity of Cu and (b) providing Ge particles as heterogeneous nucleation sites for  $\theta'$  precipitates. However, the binding energy between Ge atoms and a vacancy is much smaller than that in the Al-Cu-In-Sb alloy, even after natural ageing. As a result, <20% of  $\theta'$  precipitates form due to the heterogeneous nucleation on a Ge particle, while >80% of  $\theta'$  precipitates benefit from the released excess vacancies and the increased Cu diffusivity. The critical role of vacancies in  $\theta'$  nucleation will be further discussed in Chapter 6.
3. Six kinds of  $\text{Al}_2\text{Cu}$  precipitates were found in the aged Al-Cu-Ge alloys. They are  $\theta'$  precipitates with five kinds of crystallographic orientations with the Al matrix and  $\Omega$  precipitates. Only the common  $\theta'$  precipitates (lying on  $\{100\}_{\text{Al}}$ ) are the dominant precipitates, with the remaining being in the minority. Their number fractions, habit planes and nucleation mechanisms are summarised in Table 5.3 (see the next page).
4. Ge particles can form a coherent interface with  $\theta'$  precipitates and provide heterogeneous nucleation sites for all  $\theta'$  precipitates. This is the only nucleation mechanism for  $\theta'$  type II, IV and V precipitates.
5.  $\theta'$  type III precipitates have a distinct interfacial structure at its coherent interface with the Al matrix. The interfacial structure also exists in the form of independent precipitates lying on  $\{110\}_{\text{Al}}$  (named H phase). The H phase has a lower interfacial energy with the Al matrix and a higher driving force for nucleation compared with  $\theta'$ . Thus, the H phase is proposed to form before  $\theta'$  type III and facilitates the nucleation of  $\theta'$  type III. Vacancies also play a critical role in the formation of the H phase, which will be further discussed in Chapter 6.

Table 5.3 Cu-rich precipitates in the Al-Cu-Ge alloy at the peak aged condition at 200 °C.

Types	Orientation relationships	Fractions	Nucleation mechanisms
$\theta'$ type I (habit planes, $\{100\}_{Al}$ )	$[100]_{\theta'}/[100]_{Al}$ , $(001)_{\theta'}/(001)_{Al}$	>80%	13% heterogeneous nucleation on a Ge particle
$\theta'$ type II (habit planes inclined 10-20° from $\{100\}_{Al}$ )	$[100]_{\theta'}/[100]_{Al}$ , 1-5° between $(001)_{\theta'}$ and $(001)_{Al}$	<5%	100% heterogeneous nucleation on a Ge particle
$\theta'$ type III (habit planes, $\{110\}_{Al}$ )	$[100]_{\theta'}/[100]_{Al}$ , $(001)_{\theta'}/(01\bar{1})_{Al}$	<5%	40% heterogeneous nucleation on a Ge particle 60% nucleation starting in the H phase
$\theta'$ type IV (habit planes, $\{111\}_{Al}$ )	$[100]_{\theta'}/[011]_{Al}$ , $(011)_{\theta'}/(1\bar{1}\bar{1})_{Al}$	<5%	100% heterogeneous nucleation on a Ge particle
$\theta'$ type V (no clear habit planes)	$[100]_{\theta'}/[011]_{Al}$ , coherent but tilted interface between $(011)_{\theta'}$ and $(1\bar{1}\bar{1})_{Al}$	<5%	100% heterogeneous nucleation on a Ge particle
$\Omega$ (habit planes, $\{111\}_{Al}$ )	$[310]_{\Omega}/[011]_{Al}$ , $(001)_{\Omega}/(111)_{Al}$	<1%	Not sure

## Chapter 6

# An unexpected phase ( $\eta^*$ ) preceding $\theta'$ in Al-Cu alloys with abundant vacancies

The above observations in Chapter 4 and Chapter 5 suggest Ge or InSb additions promote  $\theta'$  nucleation by two mechanisms. The first one is providing heterogeneous nucleation sites (Ge or InSb particles) for  $\theta'$ . However, heterogeneous nucleation is not the primary mechanism of  $\theta'$  nucleation in the Al-Cu-Ge alloy aged at  $\geq 160$  °C and in the Al-Cu-In-Sb alloy aged at 250 °C. The second mechanism is releasing excess vacancies and enhancing Cu diffusion. However, the mechanism by which excess vacancies enhance  $\theta'$  nucleation is not fully understood. In particular, the involvement of vacancies in precipitates has never been studied.

In the following, an unexpected and rare Cu-rich phase ( $\eta^*$ ) will be reported in the Al-Cu-In-Sb and Al-Cu-Ge alloys, which is more difficult to form in the Al-Cu binary alloy at the same ageing condition. The  $\eta^*$  phase is found at three locations: as free-standing precipitates in the Al matrix, embedded within large  $\theta'$  precipitates or located (with half unit cell size) at the semi-coherent  $\theta'$ /Al interface. The  $\eta^*$  phase has a very similar (and sometimes even the same) structure and composition as the bulk  $\eta_2$  ( $\text{Al}_1\text{Cu}_1$ ) phase. However,  $\eta^*/\eta_2$  are rarely observed in dilute Al-Cu alloys in the past. Thermodynamic analysis suggests that the  $\eta^*$  phase has a higher driving force of nucleation and a lower interfacial energy compared with  $\theta'$ . However,  $\eta^*$  nucleation and growth appear to be restricted by diffusion kinetics because  $\eta^*$  ( $\text{Al}_1\text{Cu}_1$ ) is more Cu-enriched than  $\theta'$  ( $\text{Al}_2\text{Cu}$ ) and relies more on fast Cu diffusion. As a result, the  $\eta^*$  phase can be expected to nucleate more easily than  $\theta'$  from the Al-Cu solid solutions only at the condition that Cu diffusivity is increased by abundant vacancies. Ge and InSb additions bring more excess vacancies and render the formation of  $\eta^*$  possible at some local regions. Moreover, the H phase discussed in Chapter 5 shows strong similarities with the  $\eta^*$  phase. Both H and  $\eta^*$  precipitates are hypothesized to be nucleation sites for, and possibly, the precursors of  $\theta'$  when abundant vacancies are available.

## 6.1 $\eta^*$ in the Al-Cu-In-Sb alloy and its crystal structure

> 99% of all Cu-rich precipitates are  $\theta'$  in the Al-Cu-In-Sb alloy aged at 200 °C or 250 °C; the fraction is lower for ageing at 160 °C due to the presence of GP I zones and  $\theta''$ . Besides these well-known Cu-rich precipitates, a kind of unexpected Cu-rich precipitates is observed (called  $\eta^*$ , and making up <1% of all Cu-rich precipitates). Fig. 6.1 displays the distribution of the unexpected Cu-rich precipitates together with  $\theta'$  precipitates. Please note that the distribution of the unexpected Cu-rich precipitates is not uniform. All of the precipitates in Fig. 6.1 (a) are  $\theta'$  according to high magnification observations, while there is only one precipitate as the unexpected Cu-rich phase in Fig. 6.1 (b). The unexpected Cu-rich precipitates cannot be distinguished from  $\theta'$  precipitates at low magnification: they have almost the same morphology and atomic number (Z-) contrast. A precipitate can only be ascertained to be the unexpected Cu-rich phase until atomic columns in the precipitate are observed along  $\langle 100 \rangle_{\text{Al}}$ .

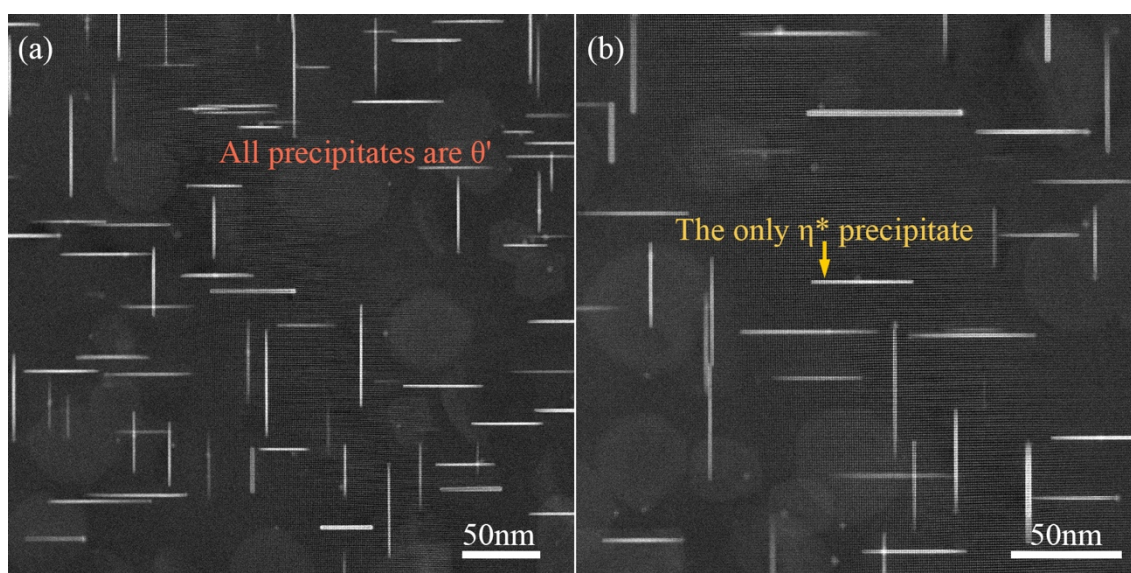


Fig. 6.1 HAADF-STEM images displaying one unexpected Cu-rich precipitate in the Al-Cu-In-Sb alloy aged 20 min at 200 °C. The unexpected Cu-rich phase precipitates are rare and not uniformly distributed.

$\eta^*$  precipitates in the Al-Cu-In-Sb alloy were observed in three different locations. The first location is in the Al matrix as free-standing precipitates at least several tens of nanometers in length. The second location is at the semi-coherent  $\theta'/\text{Al}$  interface as a small segment less than 1 nm in length. The third location is within large  $\theta'$  precipitates.

### 6.1.1 Isolated $\eta^*$ precipitates

Fig. 6.2 shows the HAADF-STEM images of the unexpected Cu-rich phase. It is different from the common Cu-rich precipitates ( $\theta''$ ,  $\theta'$  and  $\Omega$ ) in Al-Cu alloys. The unexpected Cu-rich

phase was imaged along two  $\langle 100 \rangle_{\text{Al}}$  directions and could not be imaged from the third  $\langle 100 \rangle_{\text{Al}}$  direction because it is too thin in that direction.

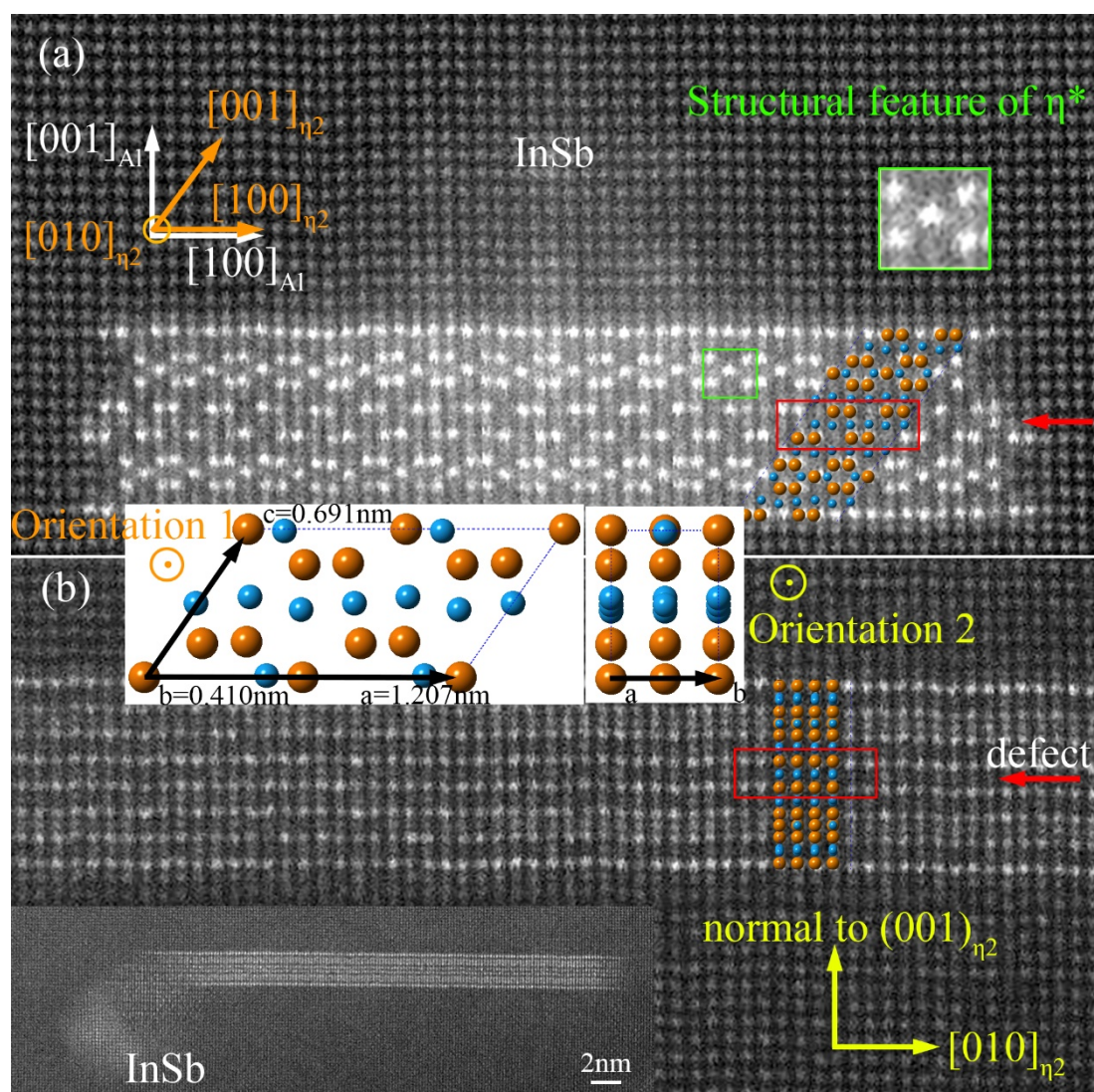


Fig. 6.2 HAADF-STEM images of the  $\eta^*$  phase precipitates with two orientations in the Al-Cu-In-Sb alloy aged for 15 min at 200 °C. The inset between (a) and (b) is the atomic model of perfect  $\eta_2$ , and the superimposed atomic model on Cu-rich precipitates is  $\eta_2$  with a defect (the red rectangles highlight the defect).

The unexpected Cu-rich phase is found to be very similar to the bulk  $\eta_2$  phase (private communication with Laure Bourgeois). The atomic model of  $\eta_2$  with a defect in Fig. 6.2 shows excellent agreement with the HAADF-STEM image of the precipitates, except for the difference at the coherent interface with the Al matrix. The defect is highlighted in red rectangles, which will be discussed in detail at the end of the section (see Appendix 3 for the CIF file of the atomic model).  $\eta_2$  has never been observed in dilute Al-Cu alloys (Cu < 30 at.%) and is a phase in the middle of the Al-Cu phase diagram (50 at.%) with a composition of  $\text{Al}_1\text{Cu}_1$

(see the Al-Cu phase diagram in Fig. 6.3).  $\eta_2$  is not expected to form in an Al-1.7at.% Cu alloy because Cu concentration in the alloy is too low. It should be mentioned that the difference between the observed precipitates and the *perfect* bulk  $\eta_2$  phase is caused by a defect (highlighted in red rectangle in Fig. 6.2), which sometimes does not occur at all (see Fig. 6.5). As will be seen in the following, three common defect types are associated with the structural differences between this kind of precipitates and perfect  $\eta_2$ ; these are correlated with the thickening process of those precipitates (see Section 6.5.3). Hereafter, for simplicity, all precipitates adopting such a structure will be called  $\eta^*$  whether defects are present or not inside.

The  $\eta^*/\text{Al}$  coherent interface is fully occupied by Cu atoms, forming a GP zone like that for  $\theta'$  precipitates, and this is different from the atomic model of defected  $\eta_2$  (Fig. 6.2). It is interesting to note that the atomic structure of  $\eta^*$  precipitates near the semi-coherent  $\eta^*/\text{Al}$  interface is the same as that inside  $\eta^*$  (Fig. 6.2). This is different from the semi-coherent  $\theta'/\text{Al}$  interface where a special interfacial structure forms [28]. These  $\eta^*$  precipitates usually have an InSb particle attached on their broad surface. The green square in Fig. 6.2 (a) highlights a structural feature of  $\eta^*$  precipitates, which will be called structural feature of  $\eta^*$  for simple structural comparison based on HAADF-STEM images.

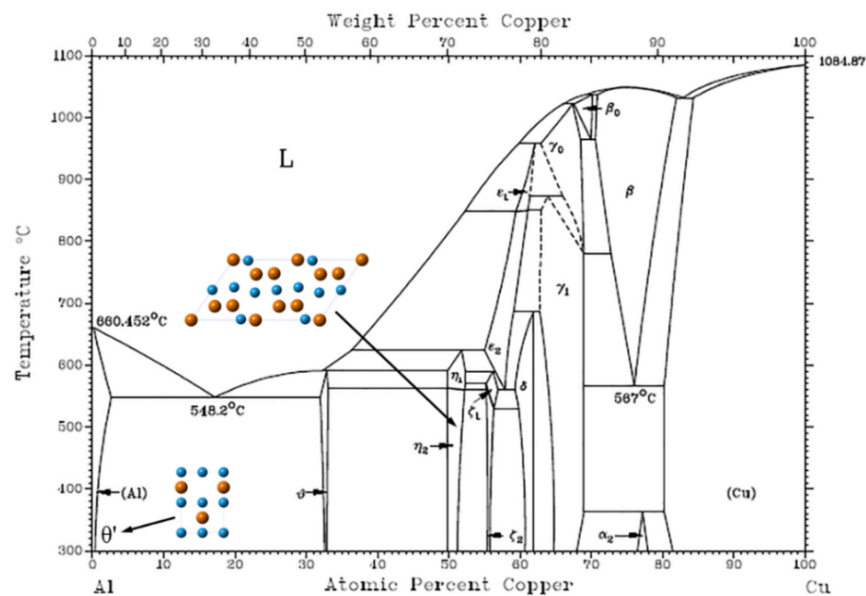


Fig. 6.3 The equilibrium Al-Cu phase diagram and the unit cells of  $\theta'$  (metastable phase) and  $\eta_2$  viewed along  $[010]_{\theta'/\eta_2}$ . Reproduced with permission from [156].

Fig. 6.3 displays the equilibrium Al-Cu phase diagram [156] which shows that  $\eta_2$  (the bulk equilibrium phase on which  $\eta^*$  is based) is far away from the compositional range of the studied alloys (Al-1.7at.%Cu). Therefore, the  $\eta^*$  phase is clearly a highly non-equilibrium product in

the investigated alloys. The formation mechanism of  $\eta^*$  precipitates will be discussed in Section 6.4 and 6.5.

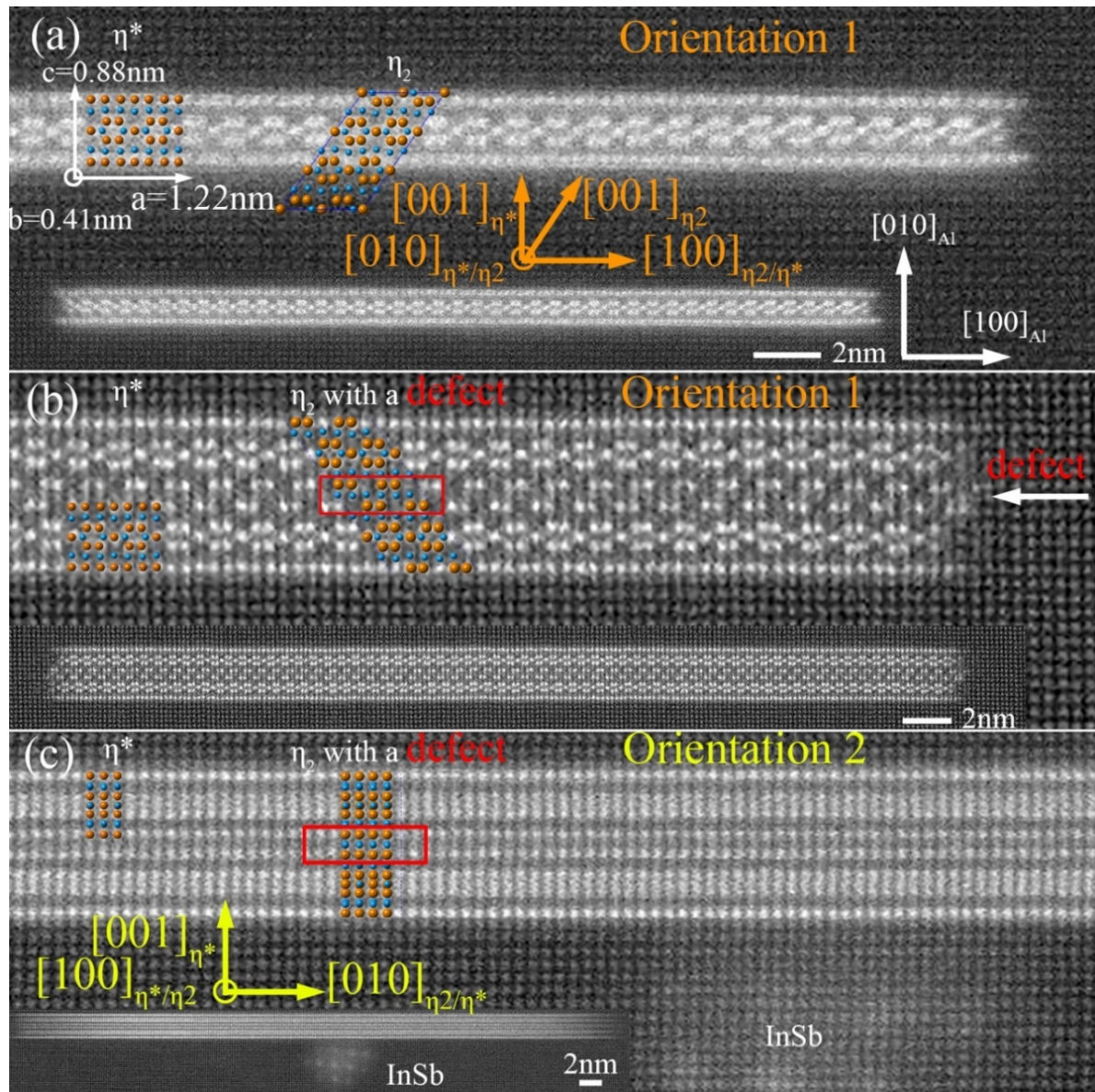


Fig. 6.4 HAADF-STEM images of  $\eta^*$  precipitates in the Al-Cu-In-Sb alloy aged for 1 h at 160 °C. The inserted atomic models were relaxed by DFT calculations. Low magnification images of the  $\eta^*$  precipitates are also shown as insets.

Fig. 6.4 displays several examples of the unexpected  $\eta^*$  phase precipitates found in the Al-Cu-In-Sb alloy aged at 160 °C. The Cu-rich precipitate shown in Fig. 6.4 (a) is the thinnest one with the basic structural feature of  $\eta^*$ . An atomic model of the thinnest precipitate then was built accordingly and was relaxed by DFT calculations, which also shows excellent agreement with the HAADF image (see the left atomic model in Fig. 6.4 (a)). This atomic model is viewed as the unit cell of  $\eta^*$  in the following, though defects sometimes must be included to match

observed thick precipitates. Both  $\eta^*$  and  $\theta'$  precipitates lie on  $\{100\}_{\text{Al}}$  planes and prefer a GP zone-like coherent interface with the Al matrix (see Fig.6.4 and Fig. 6.8). Fig. 6.4 (b) and (c) show thick  $\eta^*$  precipitates with a defect viewed from two crystallographic orientations,  $\langle 010 \rangle_{\eta^*}$  and  $\langle 100 \rangle_{\eta^*}$ . The defect is planar and consists of three atomic layers (parallel with  $\{001\}_{\eta^*}$ ). The defect results in two changes in the  $\eta^*$  precipitate compared with perfect  $\eta_2$ : (1) Cu is impoverished at the middle atomic layer (parallel with  $\{001\}_{\eta^*}$ ) of the defect and (2) the top Cu layer (parallel with  $\{001\}_{\eta^*}$ ) is shifted laterally by  $\sim 0.2$  nm along  $[100]_{\eta^*}$ .

Here it is interesting to compare the semi-coherent  $\eta^*/\text{Al}$  interface from two orientations of  $\eta^*$  precipitates. The transition from  $\eta^*$  to Al is much clearer in Fig. 6.4 (b) (viewed along  $\langle 010 \rangle_{\eta^*}$ ) than that in Fig. 6.4 (c) (viewed along  $\langle 100 \rangle_{\eta^*}$ ). The long interfacial region in Fig. 6.4 (c) may suggest the interface is a diffuse interface or an inclined interface instead of a sharp interface parallel with the viewing direction like the one in Fig. 6.4 (b). The different interfacial structure between the two orientations is conceivable because the atomic structures  $\eta^*$  viewed from the two orientations are different. The semi-coherent  $\eta^*/\text{Al}$  interface viewed along  $\langle 100 \rangle_{\eta^*}$ , such as the one in Fig. 6.4 (c), is never imaged clearly enough to identify the atomic structure. Therefore, the semi-coherent interfacial structure viewed along  $\langle 100 \rangle_{\eta^*}$  will not be further discussed because no experimental observations are available at present.

Before going further, the crystal structures of  $\eta^*$  and  $\eta_2$  are compared in Table 6.1. It should be emphasized that the observed  $\eta^*$  precipitates show strong similarities with the  $\eta_2$  phase despite the different lattice parameters and crystal systems between  $\eta^*$  and  $\eta_2$ . It is not necessary to regard the  $\eta^*$  phase as a new phase different from  $\eta_2$ . The  $\eta^*$  phase has the basic structural feature of  $\eta_2$ , which is used here for simplicity to describe all the observed unexpected precipitates.

*Table 6.1 Comparison of the crystal structure of  $\eta^*$  and  $\eta_2$ .*

Phases	Crystal system	Lattice parameters (Å)	Number of atoms in a unit cell	Atomic positions
$\eta_2$ [195]	Monoclinic	12.066, 4.105, 6.913 ( $\beta=55.12^\circ$ )	10 (Al)+10 (Cu)	See Appendix 3
$\eta^*$	Orthorhombic	12.167, 4.136, 8.794	16 (Al)+16 (Cu)	See Appendix 3

Fig. 6.5 shows much thicker  $\eta^*$  precipitates found in the Al-Cu-In-Sb alloy aged at 160 °C and 250 °C. These precipitates can be viewed as thick  $\eta_2$  with different defects at the top interface. A GP zone like coherent interface occurs at the bottom of the precipitates, which can

be achieved by the upward movement (along  $\langle 001 \rangle_{\eta_2}$ ) of the two Cu columns in the atomic model of  $\eta_2$  (indicated by red arrows). The top interface is different from the bottom interface. In Fig. 6.5 (a), the defect at the top interface is the same as the ones in Fig. 6.2 and Fig. 6.4. Therefore, this kind of defect (named type 1 in the following) is hypothesized to occur first at the interface (as shown in Fig. 6.5 (a)) and then become buried inside as thickening takes place (see Fig. 6.2 and Fig. 6.4). The defect on the top surface of the  $\eta^*$  precipitate in Fig. 6.5 (b) is a stacking fault of the top three Cu layers (named type 2 in the following).

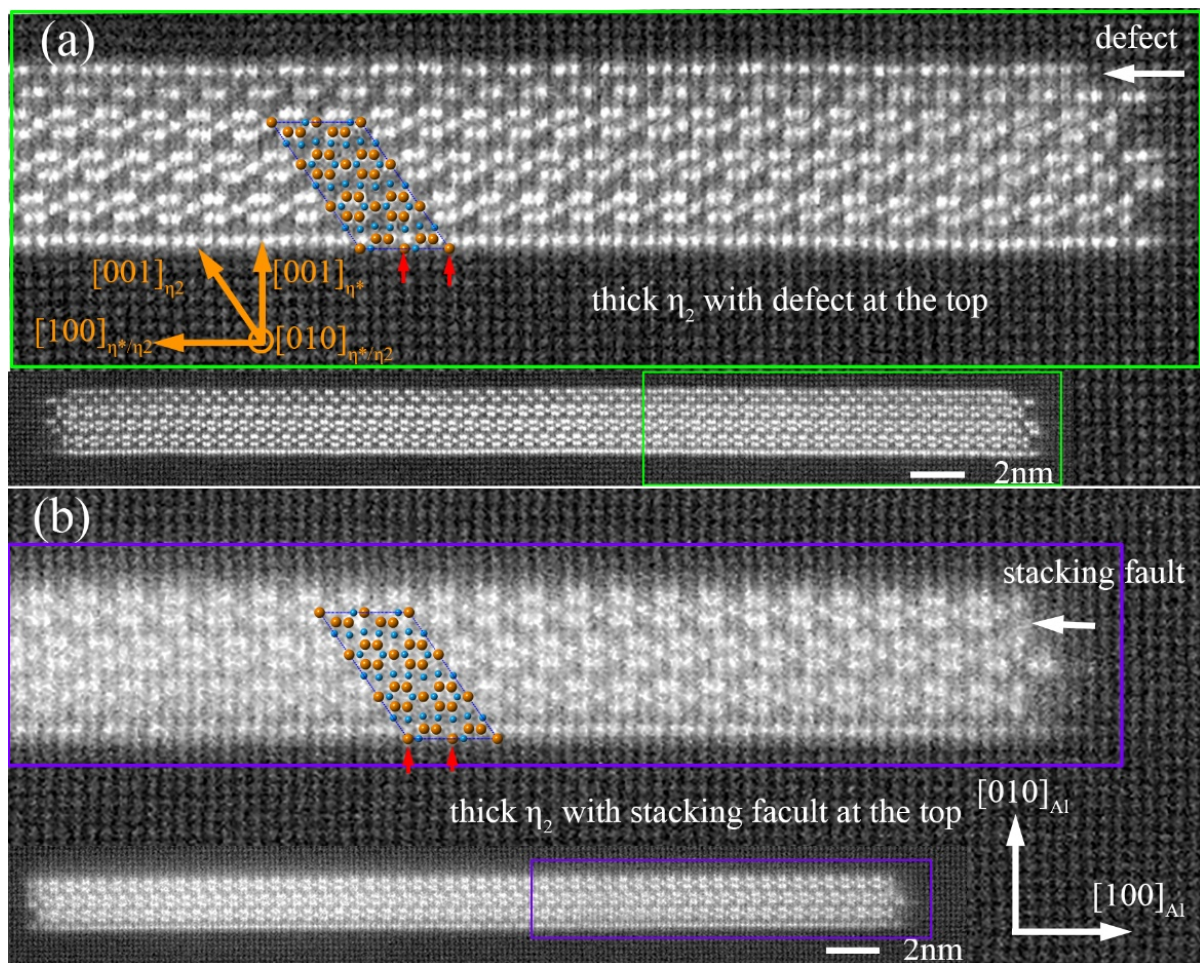


Fig. 6.5 HAADF-STEM images of  $\eta^*$  precipitates in the Al-Cu-In-Sb aged for 1 h at 160 °C and 10 min at 250 °C. DFT relaxed atomic model of  $\eta_2$  are also overlapped. A defect is located at the top surface of these  $\eta^*$  precipitates.

Based on our observations, it is safe to conclude that the  $\eta^*$  phase is a general precipitate phase in the Al-Cu-In-Sb alloy, although it only accounts for <1% of all Cu-rich precipitates. The ageing temperature has no recognisable effects on the structure and number density of  $\eta^*$  precipitates in the Al-Cu-In-Sb alloy. All the  $\eta^*$  precipitates share the same structural features of  $\eta^*$ , and the differences among them appear to be only thickening induced defects.

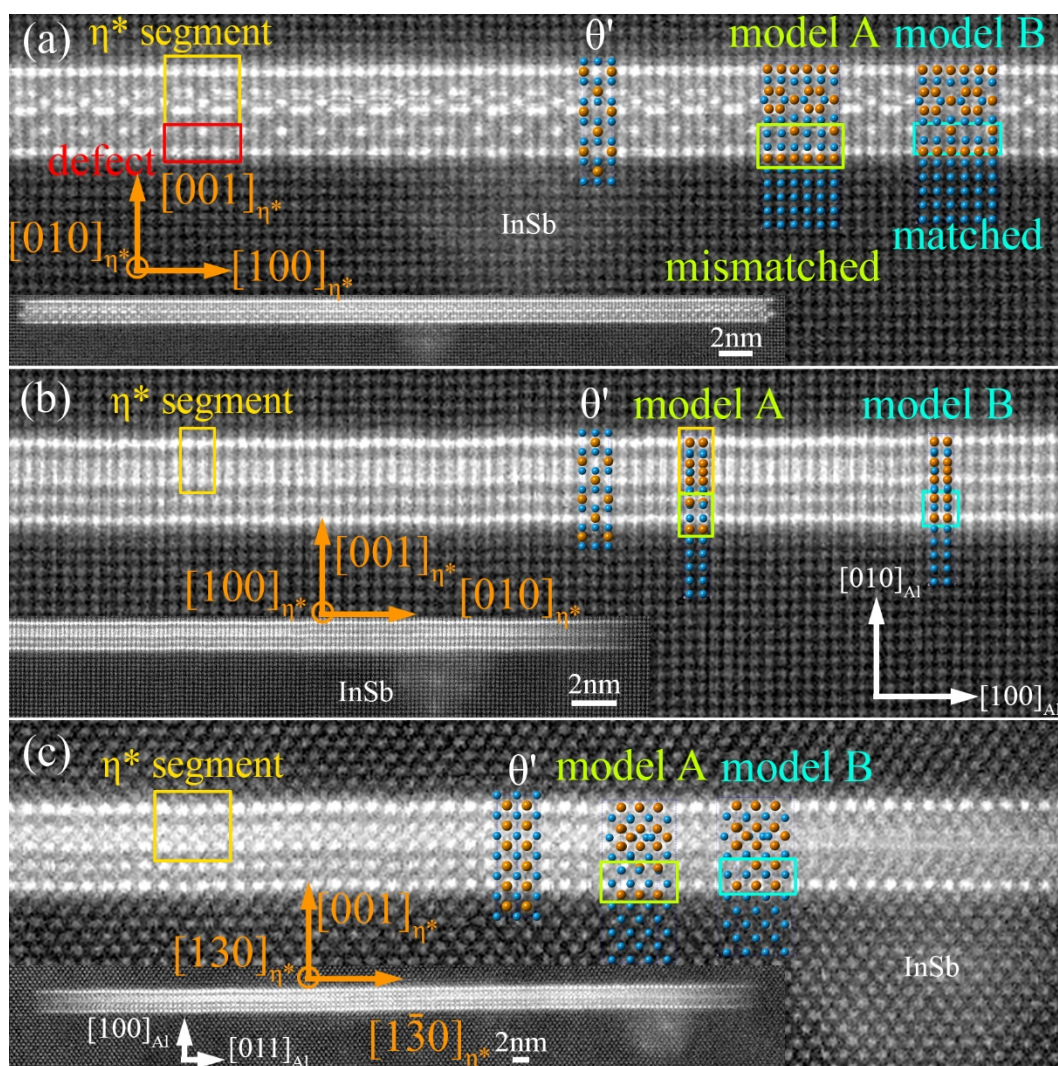


Fig. 6.6 HAADF-STEM images of  $\eta^*$  precipitates with the third kind of defect in the Al-Cu-In-Sb alloy aged for 20 min at 200 °C. Two atomic models of the precipitates are superimposed on the HAADF images. The red rectangles indicate the defect part, and the yellow ones highlight a segment of  $\eta^*$ . Model A and Model B have the same structural feature as the HAADF-STEM images, but only Model B matches the positions of atomic columns in HAADF-STEM images.

Fig. 6.6 shows  $\eta^*$  precipitates with the third kind of defect near the coherent  $\eta^*/\text{Al}$  interface. This kind of defect was imaged from three orientations ( $\langle 010 \rangle_{\eta^*}$ ,  $\langle 100 \rangle_{\eta^*}$  and  $\langle 130 \rangle_{\eta^*}$ ) and is less common regarding the number density than the one in Fig. 6.5 (a). The top part in the yellow rectangles is a segment of  $\eta^*$ . The defect in the red rectangles is different from both  $\eta^*$  and  $\theta'$ . Please note that  $\eta^*$  cannot be distinguished from  $\theta'$  in HAADF-STEM images along  $\langle 011 \rangle_{\text{Al}}$  unless a defect is presented (see Fig. 6.6 (c)). Two atomic models were built based on the HAADF images and were relaxed by DFT calculations (more details in Fig. 6.18). Both model A and model B have the same structural feature as that of the HAADF images, but only model B shows good agreement with observations regarding atomic column positions. The

lower part of model A (in green rectangles) is much thicker than the observation, which induces displacements of atomic columns between the atomic model and the HAADF images. Difference and correlation between the defect shown here and the one shown above will be discussed in section 6.5.3.

### 6.1.2 $\eta^*$ segment at the semi-coherent $\theta'$ /Al interface

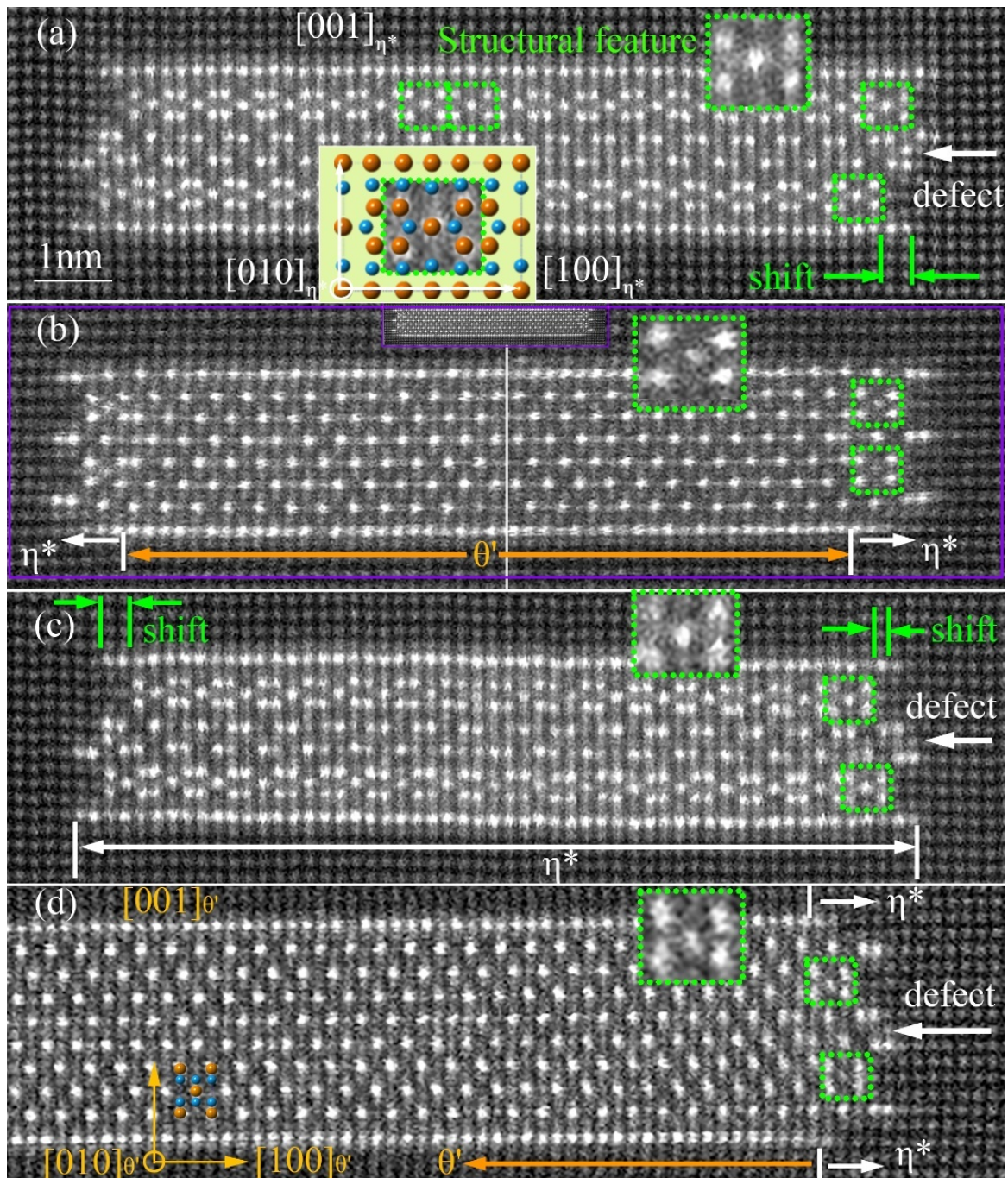


Fig. 6.7 HAADF-STEM images displaying a  $\eta^*$  segment (half unit cell in size along  $[100]_{\eta^*}$ ) at the semi-coherent  $\theta'$ /Al interface in the Al-Cu-In-Sb alloy aged for 15 min (a-c) or 30 min (d) at 200 °C. (a) and (c) show  $\eta^*$  precipitates, and (b) and (d) show  $\theta'$  precipitates.

Fig. 6.7 displays a small  $\eta^*$  segment at the  $\theta'/\text{Al}$  semi-coherent interface as imaged by HAADF-STEM along  $\langle 100 \rangle_{\text{Al}}$ . The structural feature of  $\eta^*$  (in green rectangles) viewed along  $[010]_{\eta^*}$  is also located at the  $\theta'/\text{Al}$  semi-coherent interface, which suggests a  $\eta^*$  featured segment seems to be located at the  $\theta'/\text{Al}$  semi-coherent interface. A unit cell of  $\eta^*$  is also shown here, and it suggests that the size of the  $\eta^*$  featured segment at the  $\theta'/\text{Al}$  semi-coherent interface is half unit cell ( $\sim 0.4$  nm) in the direction of  $[100]_{\eta^*}$ . The labelled defect in the  $\eta^*$  precipitate in Fig. 6.7 (a) makes the positions of the two structural features of  $\eta^*$  shift at the semi-coherent  $\eta^*/\text{Al}$  interface, which is different from the  $\theta'/\text{Al}$  semi-coherent interface in Fig. 6.7 (b). The shift between structural features at the right  $\eta^*/\text{Al}$  semi-coherent interface of Fig. 6.7 (c) is the same as that at the right  $\theta'/\text{Al}$  semi-coherent interface in Fig. 6.7 (d). Thus, the  $\eta^*$  and  $\theta'$  precipitates share the same semi-coherent interfacial structure, and defects cannot degrade the structural similarity between the  $\eta^*/\text{Al}$  and the  $\theta'/\text{Al}$  semi-coherent interfaces.

At present, the  $\eta^*$  featured segment at the  $\theta'/\text{Al}$  semi-coherent interface has not been observed along  $[001]_{\eta^*}$  and  $[100]_{\eta^*}$ , but this does not exclude the existence of the  $\eta^*$  featured segment at the  $\theta'/\text{Al}$  semi-coherent interface.  $\eta^*$  precipitates can be observed and distinguished from  $\theta'$  from two  $\langle 001 \rangle_{\text{Al}}$  directions (parallel with  $[100]_{\eta^*}$  and  $[010]_{\eta^*}$ , see Fig. 6.2). However, the  $\eta^*$  featured segment at the  $\theta'/\text{Al}$  semi-coherent interface cannot be observed along  $[100]_{\eta^*}$  due to its small dimension (only half unit cell) relative to the thickness of a TEM sample (generally 50-200nm). When imaged along  $[110]_{\text{Al}}$  (parallel with  $[130]_{\eta^*}$  and  $[110]_{\theta'}$ ),  $\eta^*$  precipitates cannot be distinguished from  $\theta'$  precipitates (see Fig. 6.6 (c) and Appendix 4) because they show almost the same structure and contrast features. Therefore, it is safe to conclude that a  $\eta^*$  featured segment (half unit cell along  $[100]_{\eta^*}$ ) is located at the  $\theta'/\text{Al}$  semi-coherent interface.

The  $\eta^*$  featured segment at the semi-coherent  $\theta'/\text{Al}$  interface has been observed in an Al-Cu binary alloy along  $\langle 100 \rangle_{\text{Al}}$  and  $\langle 110 \rangle_{\text{Al}}$  directions, but it was not designated as a  $\eta^*$  correlated structure [28]. Please note that the  $\eta^*$  featured segment at the semi-coherent  $\theta'/\text{Al}$  interface also shows the same features as  $\theta'$  when imaged along  $\langle 110 \rangle_{\text{Al}}$  [28].

### 6.1.3 $\eta^*$ precipitates embedded in $\theta'$ precipitates

The  $\eta^*$  phase not only appears as stand-alone precipitates but also inside or attached to  $\theta'$  precipitates. This further supports the idea that the  $\eta^*$ -like region at the semi-coherent  $\theta'/\text{Al}$  interface is a  $\eta^*$  related structure. A thin  $\eta^*$  precipitate is embedded in a relatively longer and thicker  $\theta'$  precipitate in Fig. 6.8 (a). The thin  $\eta^*$  precipitate is the same as the thinnest  $\eta^*$  precipitate shown in Fig. 6.4 (a), ignoring Cu impoverishment at the  $\eta^*/\theta'$  interface (labelled by red arrows). The embedded  $\eta^*$  precipitates in Fig. 6.8 (b) and (c) have the same thickness

as the covering  $\theta'$  precipitates. The  $\theta'$  precipitates in Fig. 6.8 (d)-(f) also have a region that looks like  $\eta^*$ . However, these  $\eta^*$  precipitates in Fig. 6.8 (d)-(f) are very short relative to their thicknesses and have different defects inside. Since a  $\eta^*$  segment (half unit cell along  $[100]_{\eta^*}$ ) is always found at the semi-coherent  $\theta'/\text{Al}$  interface in the Al-Cu-In-Sb alloy aged at between 160 °C and 250 °C, the continuing  $\eta^*$  growth eliminates the nucleation process and thus is expected to have a lower thermodynamic energy barrier compared with the nucleation and growth of  $\theta'$  from the  $\eta^*$  segment. However, big (larger than one unit cell along  $[100]_{\eta^*}$ )  $\eta^*$  precipitates are rare (<1 % of Cu-rich precipitates) in the Al-Cu-In-Sb alloy. The rarity of  $\eta^*$  precipitates implies that the formation of  $\eta^*$  seems to be bottlenecked by a second reason, at least not only the energy barrier (thermodynamics) associated with the nucleation and growth process, which will be discussed in Section 6.3 and 6.5.

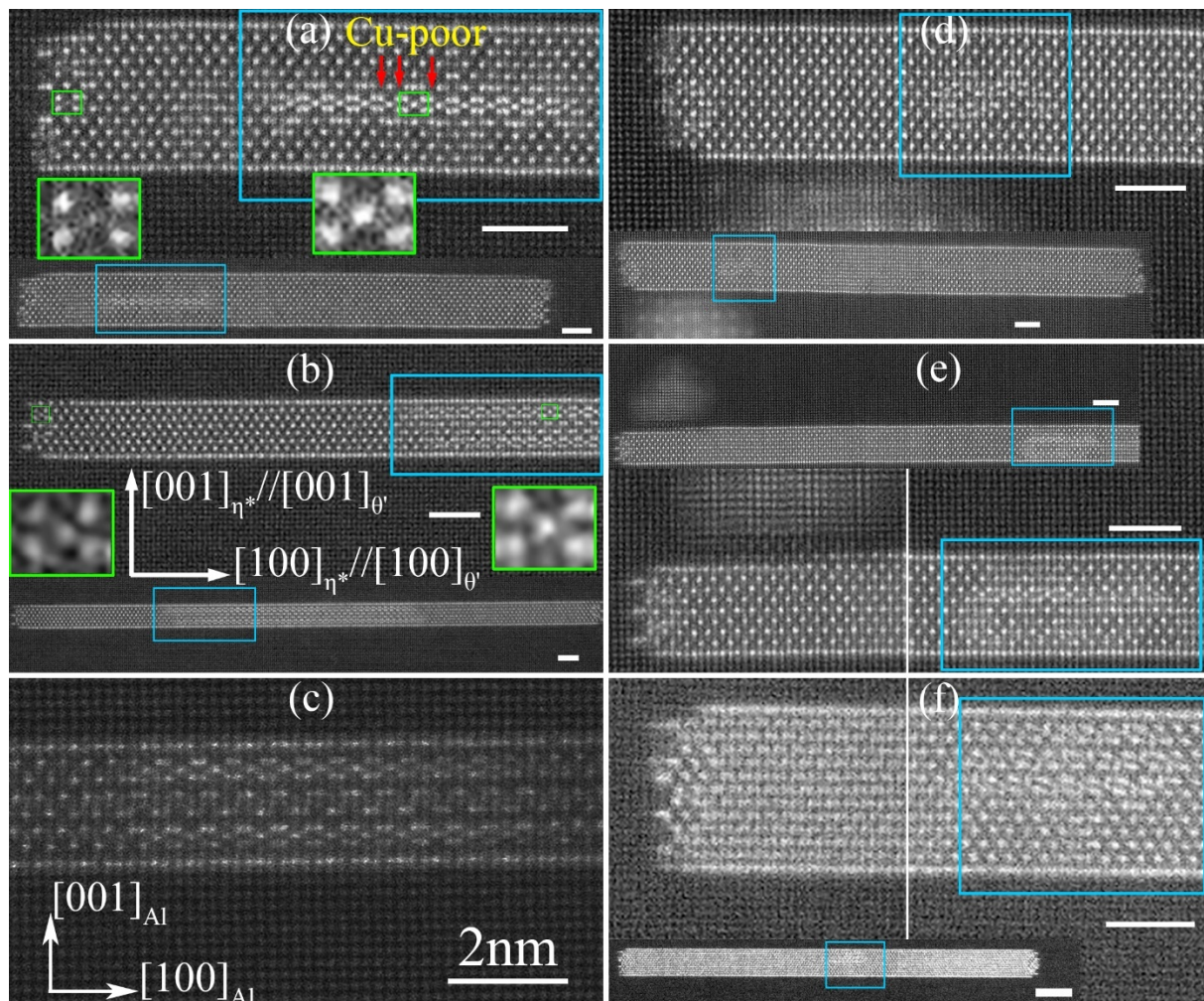


Fig. 6.8 HAADF-STEM images showing  $\eta^*$  precipitates embedded in or attached to  $\theta'$  precipitates in the Al-Cu-In-Sb alloy. (a), (b), (d) and (e) aged for 1 h at 160 °C, (c) 15 min at 200 °C, (f) 10 min at 200 °C. The green rectangles highlight the 2D structural feature of  $\eta^*$

## 6.2 $\eta^*$ in the Al-Cu-Ge alloy and its crystal structure

Fig. 6.9 shows  $\eta^*$  precipitates in the Al-Cu-Ge alloy with different orientations and thicknesses. The precipitates in Fig. 6.9 (a) and (b) have different orientations but the same thickness, being the thinnest one with the structural feature of  $\eta^*$  (see Fig. 6.4 (a)). The precipitate in Fig. 6.9 (c) is a 2-unit-cell thick  $\eta^*$  except for the defect in the middle Cu layer which is not fully occupied by Cu in the image (based on the reduced atomic column intensity observed in the image). It is interesting to note all these precipitates have a shrinking thickness near the semi-coherent  $\eta^*/\text{Al}$  interface. The shrinking thickness means these  $\eta^*$  precipitates expand in the vertical direction of the image compared with the Al matrix (imposing compression strain in the Al matrix), see Fig. 6.9 (c).

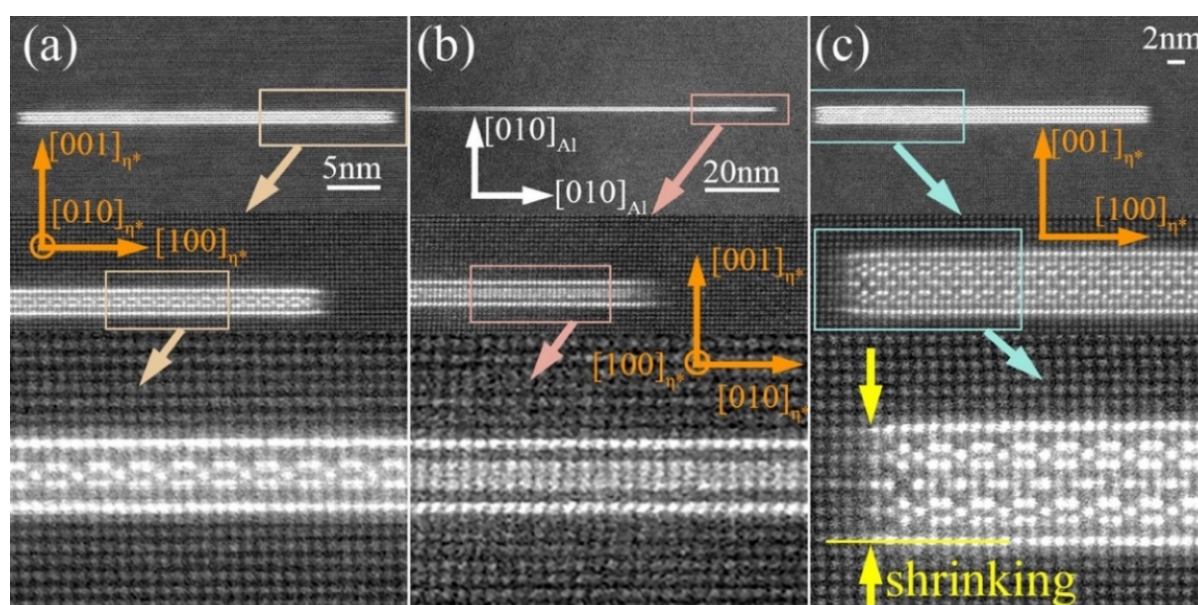


Fig. 6.9 HAADF-STEM images of  $\eta^*$  precipitates in the Al-Cu-Ge alloy aged 1 h at 200 °C.  $\eta^*$  precipitates show the same crystal structure as that observed in the Al-Cu-In-Sb alloy.

Fig. 6.10 shows thick  $\eta^*$  precipitates with defects in the Al-Cu-Ge alloy. The precipitate in Fig. 6.10 (a) is  $\eta^*$  with defect type 1 as that shown in Fig. 6.4. The precipitate in Fig. 6.10 (b) could be a perfect  $\eta_2$  precipitate with full Cu occupation at the coherent  $\eta_2/\text{Al}$  interface and could also be  $\eta_2$  with defect type 2 as that shown in Fig. 6.5 (b). The  $\eta^*$  precipitate in Fig. 6.10 (c) appears to have the third kind of defect which is also observed in the Al-Cu-In-Sb alloy in Fig. 6.6. Therefore,  $\eta^*$  precipitates in the Al-Cu-In-Sb and the Al-Cu-Ge alloys appear to have the same crystal structure and the same kind of defects. There is only one recognised difference in the two alloys:  $\eta^*$  precipitates in the Al-Cu-In-Sb alloy usually have an InSb particle attached, whereas they are always free-standing in the Al-Cu-Ge alloy.

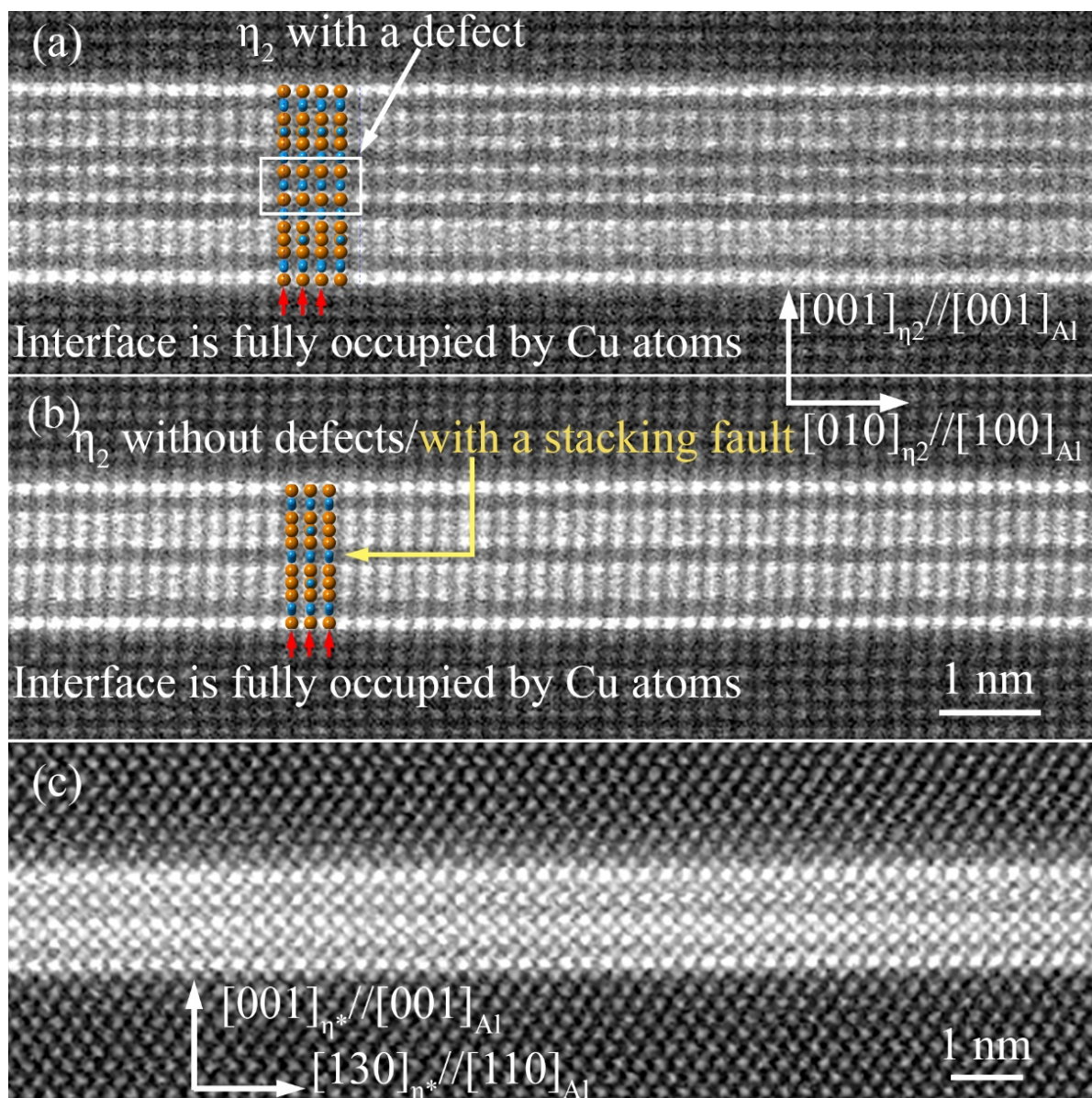


Fig. 6.10 HAADF-STEM images of thick  $\eta^*$  precipitates with a defect in the Al-Cu-Ge alloy aged 1 h at 200 °C. The insets are DFT relaxed atom models overlaid on HAADF-STEM images.

Fig. 6.11 shows two  $\eta^*$  precipitates in the Al-Cu-Ge alloy at the peak aged condition at 200 °C. The semi-coherent  $\eta^*/\text{Al}$  interface is the same as the  $\eta^*/\text{Al}$  interface in the Al-Cu-In-Sb alloy. Therefore, the semi-coherent interfacial structure of  $\eta^*/\text{Al}$  always has the structural feature of  $\eta^*$  and does not change with solutes (In, Sb and Ge), ageing times and ageing temperatures (160-250 °C). It is interesting to compare the semi-coherent  $\eta^*/\text{Al}$  interfacial structure with the semi-coherent  $\theta'/\text{Al}$  interfacial structure in peak aged Al-Cu-Ge alloy. As discussed in Chapter 5,  $\theta'$  precipitates (type I) in the Al-Cu-Ge alloy do not adopt a  $\eta^*$ -like semi-coherent interfacial structure but take a  $\theta'$ -like semi-coherent interfacial structure (see Fig. 5.26). The semi-coherent interfacial structure of  $\theta'$  in the Al-Cu-Ge alloy should have a  $\eta^*$ -like structure without Ge segregation (see Appendix 4), as in the case of  $\theta'$  precipitates in Al-Cu

binary alloys [28] and in the Al-Cu-In-Sb alloy. It is still a mystery why Ge additions can destroy the  $\eta^*$ -like semi-coherent interfacial structure of  $\theta'$  precipitates but hardly change the semi-coherent interfacial structure of  $\eta^*$  precipitate (see Section 6.4.2 for more details).

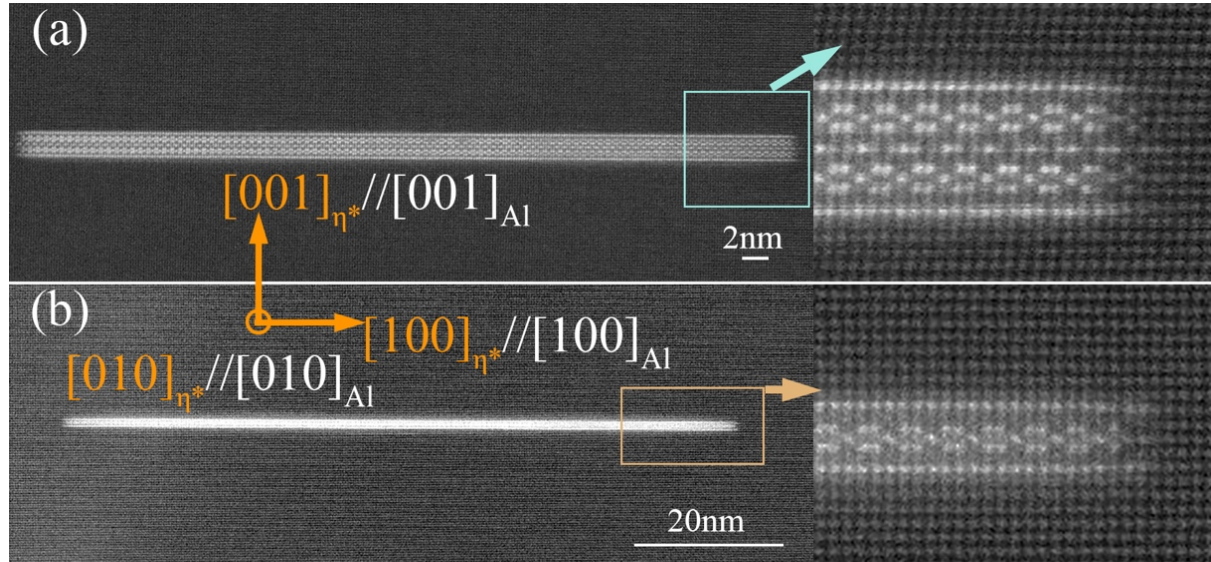


Fig. 6.11 HAADF-STEM images showing the semi-coherent  $\eta^*/Al$  interface in the Al-Cu-Ge alloy aged 2 h at 200 °C. The interfacial structure is different from the  $\theta'/Al$  semi-coherent interface in the same alloy.

### 6.3 Phase transformations at the $\eta^*$ decorated $\theta'/Al$ semi-coherent interface

#### 6.3.1 Proposed growth (lengthening) mechanism of $\theta'$ at the $\eta^*$ decorated $\theta'/Al$ semi-coherent interface

The  $\eta^*$  decorated semi-coherent  $\theta'/Al$  interfaces shown in Fig. 6.12 (a-c) suggest the growth process of  $\theta'$  intermediated by a segment of  $\eta^*$ . Please note that the  $\eta^*$  segment at the semi-coherent  $\theta'/Al$  interface has the same atomic structure of the thinnest  $\eta^*$  precipitates but its size is half of the unit cell along  $[100]_{\eta^*}$  (see Fig. 6.7). During the growth process of  $\theta'$  from the interface, a new structural feature of  $\eta^*$  (in yellow dot rectangle) forms at the front of the interface, but this cannot result in a genuine  $\eta^*$  precipitate (Fig. 6.12 (a-c)). Here the existing structural feature of  $\eta^*$  (in green dot rectangle) at the interface shares two Cu columns and one Al column with the new structural feature of  $\eta^*$  (in yellow dot rectangle). Atomic structures in the yellow and green dot rectangles are the same in three dimensions here. In contrast, two neighbouring structural features of  $\eta^*$  are separated (also shifted by  $\sim 0.4$  nm in the direction perpendicular to the paper) and are not intersected in a real  $\eta^*$  precipitate (see Fig. 6.13 (a)). The new structural feature of  $\eta^*$  can be Cu-impoverished at the centre Cu column (see 6.12

(a)), but gradual Cu accumulation at this site is also observed before the existing structural feature of  $\eta^*$  completely transforms into the structure of  $\theta'$ , as shown in Fig. 6.12 (b)-(c).

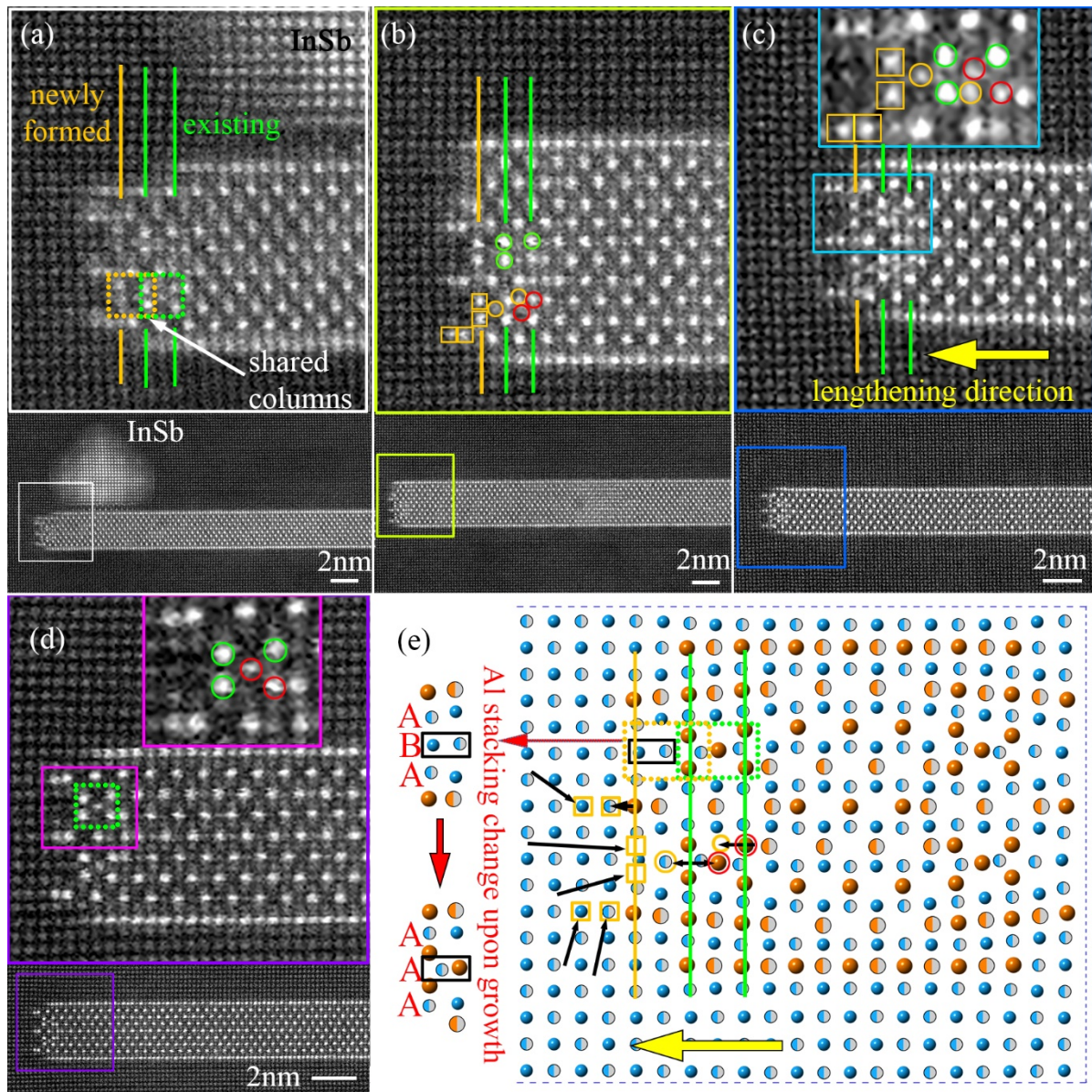


Fig. 6.12 HAADF-STEM images (a-d) and atomic model (e) depicting the growth of  $\theta'$  at the  $\eta^*$  decorated semi-coherent  $\theta'$ /Al interface in the Al-Cu-In-Sb alloy. (a-c) show the growth intermediate (aged 1 h at 160 °C), (d) shows the typical interface before/after the growth intermediate (aged 30 min at 200 °C). Atoms with two tones are located at  $(x, y, 0.5)$  and others are at  $(x, y, 0.0)$ . Cu columns in green circles remain intact during the growth process; atomic columns in yellow squares are expected to be filled by Cu atoms from the Al matrix; Cu atoms in the red circles are expected to diffuse into the yellow circles. The black arrows indicate the possible movement directions of Cu atoms. Each atomic column in (e) is filled by only Al or Cu atoms before and after the transformation.

The structural and compositional changes that take place at the interface can be identified roughly by comparing the interfaces shown in Fig. 6.12 (a-d). Three out of five Cu columns in

the existing structural feature of  $\eta^*$  seem to remain intact and are indicated by green circles, and the remaining two Cu columns in red circles are becoming Cu impoverished (losing Cu atoms) gradually. The Z-contrast for the three intact Cu columns is usually as bright as those columns inside  $\theta'$ . Six columns appear to be gradually enriched with Cu and are labelled in yellow: 1 in the existing structural feature of  $\eta^*$ , 3 in the new structural feature of  $\eta^*$  and 2 in the new GP zone like feature. The four Cu columns closest to the Al matrix at the interface (in yellow squares) are speculated to accumulate Cu atoms from the Al matrix, while the rest two columns in yellow circles are conjectured to be filled by Cu atoms from the red circles. The Cu columns in red circles and yellow circles are usually darker than the three intact Cu columns in green circles, which suggests the transformation process is diffusive instead of displacive. The intermediate contrast implies a gradual filling/draining of Cu atoms in these columns. The semi-coherent  $\theta'$ /Al interface in Fig. 6.12 (a) is decorated by an InSb particle, which shows no differences with the semi-coherent  $\theta'$ /Al interfaces free of InSb particles (Fig. 6.12 (b-c)).

The step-by-step growth process of  $\theta'$  lengthening at the interface can be schematically depicted in Fig. 6.12 (e). The black arrows indicate the possible movement directions of Cu atoms. Cu atoms from the red circles will fill the two columns in yellow circles. The diffusion of Cu atoms in the existing structural feature of  $\eta^*$  is expected to be more difficult than Cu diffusion in the Al matrix because the newly-filled Cu columns in the Al matrix are brighter than that in the existing structural feature of  $\eta^*$  (Fig. 6.12 (a-c)). In other words, it takes a longer time to complete the structural reordering (through Cu diffusion) in the existing structural feature of  $\eta^*$  than to build a new structural feature of  $\eta^*$  in front of the interface. Two parameters,  $D_0$  and  $Q$ , determine the diffusivity of an element according to  $D=D_0\exp(-Q/K_bT)$ . The activation energy for diffusion,  $Q$ , is mainly composed of two equal contributions (both  $\sim 0.6$  eV for Cu diffusion in Al) which are the migration barrier for an atom and the activation energy for vacancy formation [57, 84]. Here the top yellow circle in the existing structural feature of  $\eta^*$  is empty (vacancies present) before the transformation, and the activation energy for vacancy formation is 0. Thus, the more difficult diffusion of Cu atom inside the existing structural feature of  $\eta^*$  than in the Al matrix could be correlated with the increased migration energy barrier of Cu and the changed jump frequency of Cu. The diffusion from the bottom red circle to the yellow circle requires the introduction of a vacancy, which may be the main barrier for the structural reordering in the existing structural feature of  $\eta^*$ . The slow diffusion from the bottom red circle to the yellow circle is also supported by HAADF-STEM images: the two atomic columns are always darker in contrast than other Cu columns. Besides the structural changes correlated with Cu diffusion, the stacking sequence of atoms in the black rectangle should also be changed from ABA to AAA relative to the top and bottom

Al layers (parallel with  $(002)_{\text{Al}}$  see Fig. 6.12 (e)). The concerted movement (or shear) of one atomic layer (though only two atomic columns) should result in a very high energy barrier because shearing the Al matrix or GP zones in this direction is very difficult and may never happen in reality [196, 197]. As will be shown in Section 6.5.1, the stacking change is expected to be easily achieved by vacancy and Cu diffusion if abundant vacancies are present.

The growth mechanism at the semi-coherent  $\theta'/\text{Al}$  interface proposed here is different from an early report [28], which is because different atomic models are used for the same interfacial structure. Firstly, Cu columns in the structural feature of  $\eta^*$  are put at different positions along the direction perpendicular to the paper (parallel with  $[010]_{\eta^*}$ ). Secondly, a misfit dislocation is present at the interface and is hypothesized to be necessary for the stacking change of ABA to AAA (achieved by  $a/2\langle 100 \rangle$  gliding) in the early report. In contrast, such a misfit dislocation is not present in the atomic model in Fig. 6.12 (e). The stacking sequence change is expected to be achieved by vacancy condensation and refilling of atoms in the new stacking sequence, which will be discussed in Section 6.5.1. The author does not deny the early report but proposes a more reasonable interfacial structure and growth mechanism. The atomic model in the early report results in an unexpected high interfacial energy (thermodynamically unfavored), which was proposed to be compromised by a kinetically efficient growth mechanism. In contrast, the present growth mechanism based on the new atomic structure does not need such a dislocation, which is both kinetically efficient and is thermodynamically favoured (associated with a much lower interfacial energy, see Fig. 6.16).

### 6.3.2 Proposed growth (lengthening) mechanism of $\eta^*$ at the $\eta^*$ decorated $\theta'/\text{Al}$ semi-coherent interface

There are two possibilities to form the embedded  $\eta^*$  precipitates in  $\theta'$  precipitates. The first one is that a big  $\eta^*$  precipitate forms first and then transforms into  $\theta'$  partially. However, this possibility is unlikely based on the above observations. There are not any reasons that the transformation from a big  $\eta^*$  precipitate to a  $\theta'$  precipitate can stop just before the end and leave a tiny untransformed  $\eta^*$  embedded inside the  $\theta'$  precipitate. Sometimes, the untransformed  $\eta^*$  is only 1 or 2 unit cells along  $[100]_{\eta^*}$  (see Fig. 6.8(d) and (e)). Moreover, the transformation from a big  $\eta^*$  precipitate to a  $\theta'$  precipitate seems to be difficult, otherwise, no big  $\eta^*$  precipitates can be left. The second possibility is that a  $\eta^*$  precipitate grows from the  $\eta^*$  segment at the  $\theta'/\text{Al}$  semi-coherent interface and is followed by the second stage of  $\theta'$  growth at the  $\eta^*/\text{Al}$  semi-coherent interface. The growth process of  $\eta^*$  from the  $\eta^*$  segment at the  $\theta'/\text{Al}$  semi-coherent interface will be discussed in the following. However, this process has not yet

been imaged directly, but its atomic mechanism can be imagined based on the embedded  $\eta^*/\theta'$  interface sometimes observed (Fig. 6.13 (a)).

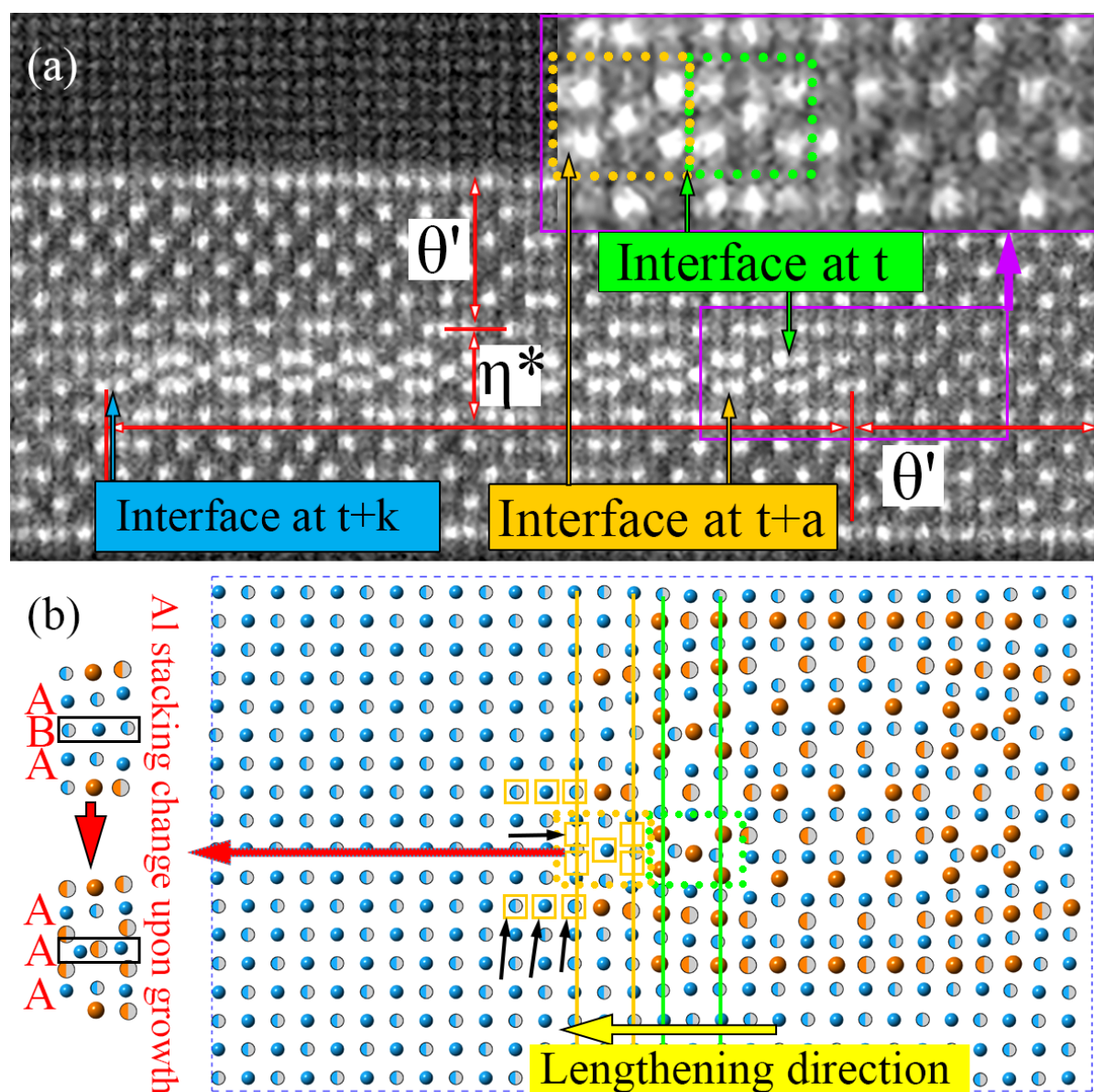


Fig. 6.13 (a) HAADF-STEM images indicating the growth of  $\eta^*$  at the  $\eta^*$  decorated semi-coherent  $\theta'/\text{Al}$  interface from  $t$  ( $t$  is time) to  $t+a$  ( $0 < a < k$ ), (b) atomic model depicting the growth mechanism of  $\eta^*$  at the semi-coherent  $\theta'/\text{Al}$  interface from  $t$  (the atomic model at  $t$  is the same as that in Fig. 6.12 for easy comparison) to  $t+a$ . Atomic columns in yellow squares are expected to be filled by Cu atoms from the Al matrix. The black arrows indicate the possible movement directions of Cu atoms.

Before a  $\eta^*$  precipitate begins to form at the  $\theta'/\text{Al}$  interface at  $t$  ( $t$  is time), the left part of the interface is still the Al matrix or Al-Cu solid solution (see Fig. 6.13), as that shown in Fig. 6.12 (d). There is only one existing structural feature of  $\eta^*$  (in dot green rectangle), thus forming a typical  $\eta^*$ -decorated  $\theta'/\text{Al}$  semi-coherent interface with the Al matrix on the left (not

shown in the HAADF-STEM image but in the atomic model). A new structural feature of  $\eta^*$  forms in the Al matrix from  $t$  to  $t+a$  (in the yellow dot rectangle in Fig. 6.13), and the interface moves forward. The structures in the green dot and yellow dot rectangles stand separately and result in a genuine  $\eta^*$  precipitate (one unit cell in size along  $[100]_{\eta^*}$ ). No further changes are required in the part in the green dot rectangle to complete the growth of  $\eta^*$ , which is different from  $\theta'$  growth at the same place (Fig. 6.12). Cu atoms in the yellow dot rectangle (and the new GP zone feature) are thought to be diffused from the Al matrix. The growth and extension of  $\eta^*$  can be expressed schematically by Fig. 6.13 (b). The black arrows show the possible movement directions of Cu atoms from the Al solid solution. The atoms highlighted by the black rectangle are also displaced (by  $\sim 0.2$  nm along  $\langle 100 \rangle_{\text{Al}}$ ) to change the stacking sequence from ABA to AAA. The newly-formed part in the yellow dot rectangle has the same three-dimensional atomic structure as that of the existing part in the green dot rectangle, but they are shifted by  $\sim 0.2$  nm in the direction perpendicular to the paper ( $[010]_{\eta^*}$ ).

Before going further, it will be helpful to compare the two growth processes,  $\theta'$  growth and  $\eta^*$  growth at the same  $\eta^*$ -decorated  $\theta'/\text{Al}$  semi-coherent interface. First, the Cu consumption for  $\eta^*$  ( $\text{Al}_1\text{Cu}_1$ , 50at.% Cu) growth is 1.5 times of that for  $\theta'$  ( $\text{Al}_2\text{Cu}$ , 33at.% Cu) growth. In the atomic model of  $\theta'$  growth in Fig. 6.12 (e), *two* Cu columns need to be filled by Cu atoms from the Al matrix to move the interface forward two atomic layers (ignoring the Cu atoms to build the GP zone feature). However, in the atomic model of  $\eta^*$  growth in Fig. 6.13 (b), *three* Cu columns need to be filled by Cu atoms from the Al matrix to move the interface forward two atomic layers (the number of Cu atoms per Cu columns in Fig. 6.12 (e) and Fig. 6.13 (b) are the same). Therefore, the bottleneck for the growth of  $\eta^*$  is Cu supply from the Al matrix because  $\eta^*$  consumes more Cu atoms than  $\theta'$  per volume, which relies on the diffusivity of Cu. Second, there is a complicated rearrangement of Cu columns in the existing structural feature of  $\eta^*$  during the growth of  $\theta'$  but not during the growth of  $\eta^*$ , as can be seen in Fig. 6.12 (e) and 6.13 (b). Third, the stacking change (from ABA to AAA) of atoms in the black rectangles is the same for both  $\theta'$  and  $\eta^*$  growth. Therefore, the constraint for  $\theta'$  growth is whether the structural rearrangement in the existing structural feature of  $\eta^*$  is easy, while the constraint for  $\eta^*$  growth is whether Cu supply from the Al matrix is sufficient and timely.

#### 6.4 Discussion: thermodynamic analysis of $\theta'$ and $\eta^*$

The above results suggest that  $\theta'$  and  $\eta^*$  compete during both the nucleation stage and the growth stage. Moreover,  $\eta^*$  precipitates have never been observed in Al-Cu alloys with a low Cu concentration ( $<30\text{at.}\%$ ) aged with conventional methods. A pre-deformed Al-Cu binary alloy seems to show similar precipitates in a recent report in 2018 [198], but the atomic

structure of precipitates in the report is different from the HAADF-STEM images in the thesis. To understanding the competition between  $\theta'$  and  $\eta^*$ , the formation thermodynamics of the two phases are first analyzed in the following.

The well-known metastable phases in the composition range of the investigated alloys (with 1.7at.%Cu) are GP I zones,  $\theta''$  ( $\text{Al}_3\text{Cu}$ ) and  $\theta'$  ( $\text{Al}_2\text{Cu}$ ).  $\eta^*$  has a much higher Cu concentration ( $\text{Al}_1\text{Cu}_1$ ), and its formation in such a dilute alloy seems to be inconceivable at first glance. No remarkable In, Sb and Ge segregation in or around  $\eta^*$  precipitates have been detected. Yet these solute elements are critical for the formation of  $\eta^*$  since  $\eta^*$  precipitates have not been observed in conventionally aged binary Al-Cu alloys both in this study and in others' work [28]. As has been shown in the last two chapters, excess vacancies associated with these microalloying additions are important for the precipitation in the two alloys, which is conjectured to play a key role in the formation of  $\eta^*$  (discussed in Section 6.5). In the following,  $\eta^*$  will first be compared with  $\theta'$  regarding formation energy (and driving force of nucleation), interfacial energy and strain energy, which will be the basis of the discussion on the key role of vacancies regarding formation kinetics (in Section 6.5).

#### **6.4.1 Driving force of nucleation from DFT calculations and a thermodynamic database**

The driving force of nucleation for  $\eta^*$  and  $\theta'$  was calculated using first-principles calculations and a thermodynamic database for Al-Cu system (in Thermo-Calc Software 2018a [20]). As will be seen in the following, the two methods give the same trend, which gives the author confidence about the thermodynamic analysis.

##### **6.4.1.1 Driving force of nucleation from DFT calculations**

Table 6.2 presents the results from DFT calculations. The formation energies relative to pure elements are the commonly used parameters to assess the stability of different phases (with similar compositions) in the literature [62, 76, 199, 200].  $\eta^*$  has a lower formation energy relative to pure elements for both the free-standing one and the embedded one (see Appendix 2 for the atomic models).  $\eta_2$ , the stable bulk phase found in the middle of the Al-Cu phase diagram, is the most stable here based on the formation energy relative to pure elements, and a defect inside it (as shown in Fig. 6.2) will most likely increase the formation energy. This is what is found through the DFT calculations: a thick  $\eta^*$  precipitate with a defect (see Appendix 2) is slightly less energetically favourable compared with perfect  $\eta_2$ , but it is more favourable compared with a  $\theta'$  precipitate. The formation energies from DFT calculations also suggest a  $\eta^*$  precipitate is always more energetically favourable than a  $\theta'$  precipitate.

Table 6.2 Formation energies of  $\eta^*$  and  $\theta'$  from DFT calculations (0K; the supercells used here are shown in Appendix 2; Energy convergence is 0.001 eV/atom).

Phases	Compositions	Formation energies relative to pure elements, $E_f$ (eV/atom)	Formation energies relative to solutes, $E_f$ (eV/atom)
Thin $\eta^*$	$\text{Al}_{16}\text{Cu}_{16}$ <sup>1</sup>	-0.194	/
Embedded thin $\eta^*$	$\text{Al}_{16}\text{Cu}_{22}$ <sup>2,3</sup>	-0.207	-0.150
$\eta_2$	$\text{Al}_{30}\text{Cu}_{30}$	-0.215	/
$\eta_2$ /thick $\eta^*$ with a defect	$\text{Al}_{32}\text{Cu}_{28}$ <sup>4</sup>	-0.199	/
Embedded thick $\eta^*$ with a defect	$\text{Al}_{22}\text{Cu}_{24}$	-0.195	-0.143
$\theta'$	$\text{Al}_2\text{Cu}$	-0.174	/
Embedded $\theta'$	$\text{Al}_{10}\text{Cu}_7$ <sup>2,5</sup>	-0.171	-0.130

<sup>1</sup>  $\eta^*$  has many variants due to defects inside and Cu-enrichment at the coherent interface with the Al matrix. A model built based on Fig. 6.4 (a) was used for simplicity.

<sup>2</sup> Composition for embedded phase does not include the Al matrix. Formation energy is also averaged over atoms in the precipitate only.

<sup>3</sup> The reason for more Cu-enrichment in the embedded  $\eta^*$  can be found in Appendix 2: there are two outmost Cu layers but only one in the free-standing  $\eta^*$ .

<sup>4</sup> The atomic model was built based on Fig. 6.2 (a).

<sup>5</sup> The composition for  $\theta'$  is more Cu-enriched because the coherent interface is fully Cu occupied, it will be close to  $\text{Al}_2\text{Cu}$  for very thick precipitates.

The formation energies of embedded phases relative to the chemical potentials of Cu and Al in the Al-1.7 at.% Cu solid solution can approximate the enthalpy contribution to the driving force of nucleation at 0 K. The chemical potential of Cu is approximated by the formation energy of one Cu atom together with 47 Al atoms in the FCC Al lattice (forming an Al-2.1 at.%Cu solid solution, see Appendix 2), and the chemical potential of Al solute is the formation energy of an Al atom in the Al crystal. Such an approximation in the calculations of chemical potentials of Al and Cu is widely used in the literature and shows very good agreement with experimental results [1, 155, 181]. The formation energies of embedded phases relative to Cu and Al atoms in the Al-Cu solid solution can be divided into two parts, i.e., the driving force of nucleation ( $\Delta G_v V < 0$ , see equation 6.1) and the energy cost of forming the coherent interface between the embedded phase and the Al matrix ( $\gamma A > 0$ , see equation 6.1). Since

energy costs of forming coherent interfaces are similar for  $\eta^*$  and  $\theta'$  (see Fig. 6.16 for interfacial energies), it is reasonable to use the formation energies relative to Cu and Al atoms in the Al-Cu solid solution to approximate the driving force of nucleation ( $\Delta G_v V$ , see below). According to the classical nucleation theory [201, 202], the nucleation energy barrier can be expressed as:

$$\Delta G = \Delta G_v V + \gamma A + wV, \quad (6.1)$$

where  $\Delta G_v$  is the free energy change per unit volume from the parent phase to the product phase ( $\Delta G_v < 0$ ),  $V$  is the volume of the product phase,  $\gamma$  is the interfacial energy of the interface between the parent phase and product phase,  $A$  is the area of the interface between parent phase and product phase,  $w$  is strain energy per volume (for the product phase in a rough approximation). The first term is the only driving force for nucleation, and the last two terms are energy costs. The formation energies of embedded  $\eta^*$  relative to Cu and Al atoms in the Al-Cu solid solution is lower than that of embedded  $\theta'$ . Therefore,  $\eta^*$  has a high driving force (enthalpy at 0K) of nucleation compared with  $\theta'$ . This conclusion is consistent with the analysis based on formation energies relative to pure elements discussed above. Therefore, formation energies relative to pure elements can be used to approximate the driving force of nucleation, at least for the studied case here.

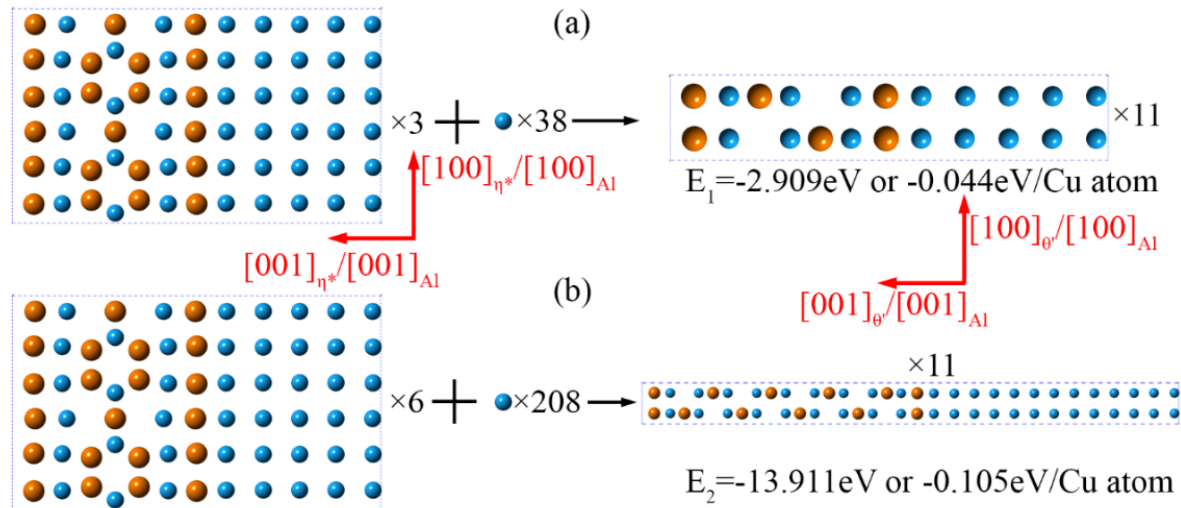


Fig. 6.14 DFT calculated transformation energy from an embedded  $\eta^*$  precipitate in the Al matrix to an embedded  $\theta'$  precipitate in the Al matrix with different thicknesses. (a) 1.5 unit-cell  $\theta'$ , (b) 4.5 unit-cell  $\theta'$ . The blue spheres are Al atoms and orange ones are Cu atoms. The single blue atom is an Al atom, and its energy is the ground state energy in the FCC lattice. The supercells and Al atoms are multiplied (indicated by  $\times$ ) by different times to make sure the numbers of Al and Cu atoms are the same on the left and right sides of the black arrows.

The high energetical preference of  $\eta^*$  compared with  $\theta'$  seems to conflict with the Al-Cu phase diagram. To further check if it is an artefact in DFT calculations, the formation energy

difference of a supercell with Al matrix and  $\eta^*$  and a supercell with Al matrix and  $\theta'$  were calculated and named as transformation energy. The transformation energy means the energy change for the transformation of a  $\eta^*$  precipitate to a  $\theta'$  precipitate in the Al matrix at the same numbers of Al and Cu atoms. A negative transformation energy suggests precipitation in the form of  $\theta'$  can lower the energy of the whole Al matrix and precipitates system more than precipitation in the form of  $\eta^*$ . This idea is the same as the convex hull analysis in the literature [1, 154]. Fig. 6.14 shows the DFT calculated transformation energy from  $\eta^*$  to  $\theta'$ , where the number of Cu atoms is the same on the left and right sides of the black arrows. The transformation energy is negative and becomes more negative for a thicker  $\theta'$  precipitate. The negative transformation energy suggests precipitation in the form of  $\theta'$  results in a more thermodynamically stable system (a precipitate and the Al matrix), though its nucleation driving force is lower than in the form of the  $\eta^*$  phase. In contrast, a precipitate in the form of  $\eta^*$  has a higher nucleation driving force compared with in the form of  $\theta'$ , but this is achieved at the expense of less lowering the energy of the system of the precipitate and the Al matrix.

#### 6.4.1.2 Driving force of nucleation from a thermodynamic database

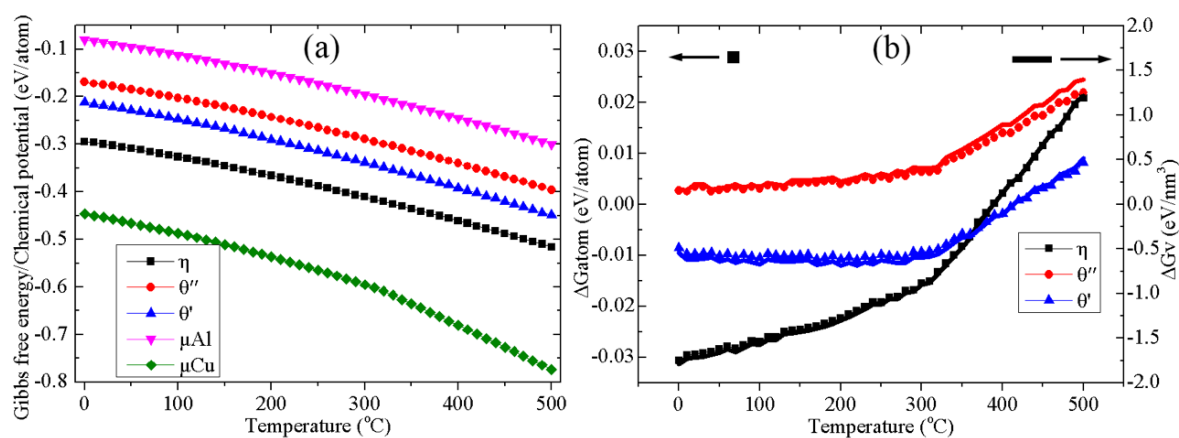


Fig. 6.15 (a) Gibbs free energies for  $\theta''$ ,  $\theta'$  and  $\eta_2$  phases and chemical potentials for Al and Cu atoms in the Al-1.7at.%Cu solid solution. (b) free energy change for the formation of  $\theta''$ ,  $\theta'$  and  $\eta_2$  phases from the Al-1.7at.%Cu solid solution. The  $\eta_2$  phase has a higher driving force of nucleation than  $\theta'$ .

The Gibbs free energies of  $\theta''$ ,  $\theta'$  and  $\eta_2$  (named  $\eta$  in Thermo-Calc Software 2018a [20]) and the chemical potentials of Al and Cu atoms in an Al-1.7 at.%Cu solid solution are shown in Fig. 6.15 (a).  $\eta_2$  is the most stable phase and GP I zones are the least stable phase, in terms of their Gibbs free energies. Here the Gibbs free energy of a phase in the thermodynamic database has the same physical meaning as the DFT calculated formation energy relative to pure

elements. They both indicate the energy change of forming a compound from stable single elemental crystals (here Al and Cu crystals). Precipitation in the form of  $\theta'$  lowers the solid solution system energy more because more Al atoms are incorporated into  $\theta'$  precipitates at the same amount of Cu atoms than in the form of  $\eta_2$ . Therefore, even though  $\eta_2$  has the lowest Gibbs free energy for itself, the calculated Al-Cu phase diagram suggests  $\theta'$  is a more energetically favourable precipitate for the system consisting of precipitates and the Al matrix than  $\eta_2$  [20]. This is consistent with the analysis using the transformation energies from DFT calculations.

The Gibbs free energy change per unit volume is calculated from Fig. 6.15 (a) according to the following expression:

$$\Delta G_v = \frac{G_{precipitate} - x\mu_{Al} - y\mu_{Cu}}{V_{atom}}, \quad (6.2)$$

Where  $G_{precipitate}$  is the Gibbs free energy of a precipitate ( $Al_3Cu$ ,  $Al_2Cu_1$  or  $Al_1Cu_1$ ),  $x$  and  $y$  are the atomic concentrations of Al and Cu in the precipitate ( $x+y=1$ ),  $V_{atom}$  is the average atomic volume in the precipitate ( $\Delta G_{atom} = \Delta G_v \times V_{atom}$ ). The Gibbs free energy change per unit volume for  $\eta_2$  is the most negative among the three precipitates, which means  $\eta_2$  has the highest driving force for nucleation as suggested by the above DFT calculations. However, the thermodynamic parameters of  $\theta''$  in the database may be wrong because the driving force of nucleation is positive for  $\theta''$ , which is in contradiction with the classical nucleation theory. This is not inconceivable because the Gibbs free energy of  $\theta''$  in the thermodynamic database has been artificially modified [20].

The driving force of nucleation calculated using the DFT calculations and the thermodynamic database gives the same trend that  $\eta^*$  has a higher driving force of nucleation than  $\theta'$ .

#### 6.4.2 Interfacial energies of the $\eta^*/Al$ and $\theta'/Al$ interfaces: the first energy cost of nucleation

Interfacial energy cost due to the formation of a new phase is against the nucleation. It is necessary to compare the interfacial energies of the  $\eta^*/Al$  and  $\theta'/Al$  interfaces to understand the competition between  $\eta^*$  and  $\theta'$ . However, the accurate interfacial energies of the  $\eta^*/Al$  and  $\theta'/Al$  interfaces are difficult to be measured experimentally. DFT calculations are used here to calculate the interfacial energies, following the common method in the literature [28, 153]. Please note that the second  $\eta^*/Al$  semi-coherent interface (viewed along  $[100]_{\eta^*}$  see Fig. 6.4 (b)) is not considered here because its atomic structure is not available now.

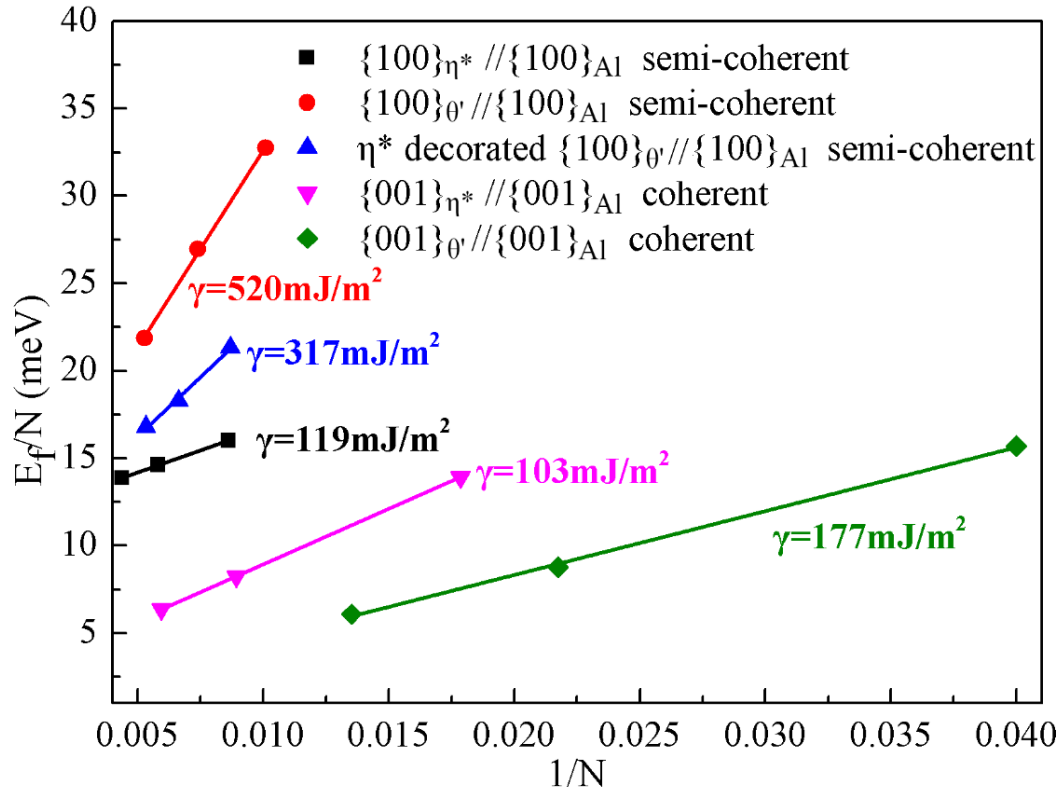


Fig. 6.16 Interfacial energies of  $\eta^*/Al$  and  $\theta'/Al$  interfaces calculated using DFT calculations.  $E_f$  is the formation energy of a supercell and  $N$  is the total number of Cu and Al atoms in the supercells. A  $\eta^*$  precipitate has a lower interfacial energy compared with that of a  $\theta'$  precipitate without  $\eta^*$  decoration.  $\eta^*$  decoration at the semi-coherent  $\theta'/Al$  interface lowers the semi-coherent interfacial energy of a  $\theta'$  precipitate. The atomic models of different interfaces are shown in Appendix 2.

Fig. 6.16 displays DFT calculated interfacial energies of the  $\eta^*/Al$  and  $\theta'/Al$  interfaces (the atomic models of different interfaces are shown in Appendix 2). Compared with  $\theta'$ ,  $\eta^*$  has lower interfacial energies with the Al matrix, especially for the semi-coherent interface (119 mJ/m<sup>2</sup>). The remarkably low interfacial energy of the  $\eta^*/Al$  semi-coherent interface may rationalise the formation of the  $\eta^*$  segment at the  $\theta'/Al$  semi-coherent interface. The decoration of  $\eta^*$  (only half unit cell in size along  $[100]_{\eta^*}$ ) at the  $\theta'/Al$  semi-coherent interface should lower the semi-coherent interfacial energy of  $\theta'$  precipitates. As shown in Fig. 6.16, the interfacial energy of the semi-coherent  $\theta'/Al$  interface is lowered from 520 mJ/m<sup>2</sup> (without  $\eta^*$  decoration, the sharp interface) to 317 mJ/m<sup>2</sup> (with  $\eta^*$  decoration). As suggested by the classical nucleation theory, there are two energy costs for nucleation, interfacial energy and strain energy. The lower semi-coherent and coherent interfacial energies of  $\eta^*$ , compared with  $\theta'$ , thus imply a lower nucleation energy penalty from the interfacial energy term. The first two terms of the nucleation energy barrier (see equation 6.1, the nucleation driving force and the interfacial energy cost) thus both favour the nucleation of  $\eta^*$  over  $\theta'$ .

It is interesting to note the  $\eta^*/\text{Al}$  semi-coherent interface has a much lower interfacial energy ( $119 \text{ mJ/m}^2$ ) than the  $\theta'/\text{Al}$  semi-coherent interface with or without  $\eta^*$  decoration ( $317$  or  $520 \text{ mJ/m}^2$ ). Please remember that we have found Ge additions cannot change the structure of the  $\eta^*/\text{Al}$  semi-coherent interface but change the structure of the semi-coherent  $\theta'/\text{Al}$  interface remarkably (see Fig. 5.26 and Fig. 6.11). The difference may be correlated with the differences in interfacial energies: an interface with a lower interfacial energy needs less solute segregation to reduce its excess energy [101, 203].

#### 6.4.3 Strain energy: the second energy cost of nucleation

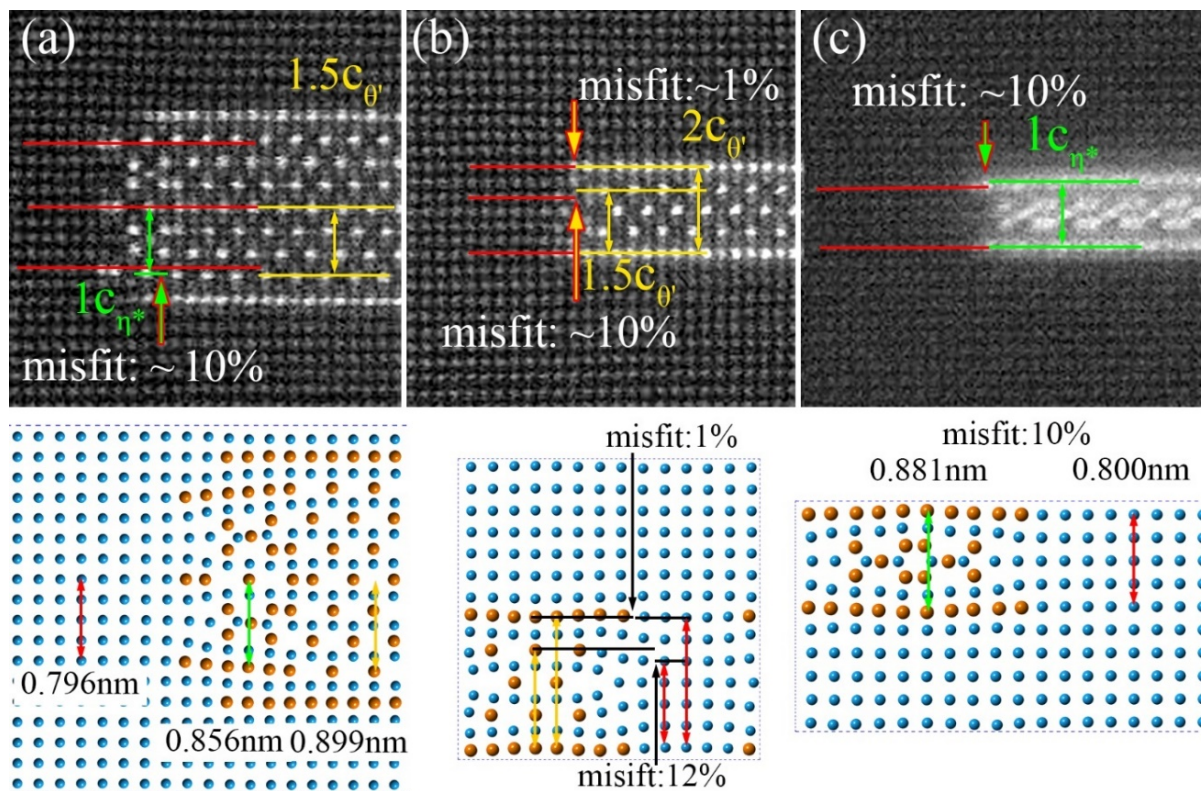


Fig. 6.17 HAADF-STEM images and atomic models showing the misfits between precipitates and the Al matrix. (a) and (b) are  $\theta'$  precipitates in the Al-Cu-In-Sb alloy aged for 30 min at  $200^\circ\text{C}$ , (c) is a  $\eta^*$  precipitate in the Al-Cu-In-Sb alloy aged for 1 h at  $160^\circ\text{C}$ . The red, yellow and green lines indicate the atomic planes for Al,  $\theta'$  and  $\eta^*$ , respectively.

Strain energy should play an important role in the nucleation process for both  $\theta'$  and  $\eta^*$  precipitates because residual misfit strain is inevitable [40]. Fig. 6.17 shows experimental HAADF-STEM images and DFT-relaxed atomic models, both displaying misfit strains between precipitates and the Al matrix. Here the misfit strains of the thinnest  $\eta^*$  precipitates (1 unit cell in thickness) and  $\theta'$  precipitates (1.5 and 2 unit-cell in thickness) are compared. Both experimental observations and DFT-relaxed structures suggest the  $1.5c_{\theta'}$  and  $1c_{\eta^*}$

precipitates exert a compressive strain on the Al matrix in the direction perpendicular to the coherent interface. The lattice misfit between 1c  $\eta^*$  and the Al matrix is  $\sim 10\%$  from both HAADF-STEM images and the DFT-relaxed atomic model. The lattice misfit between 1.5c  $\theta'$  and the Al matrix is also  $\sim 10\%$ . Such large strains may introduce a remarkable strain energy cost which may prohibit the start of nucleation. This may be why  $\eta^*$  and  $\theta'$  precipitates with such thicknesses have never been observed experimentally in normally aged Al-Cu binary alloys at  $>160^\circ\text{C}$  [49]. The thinnest  $\theta'$  precipitates observed here in experiments have a 2 unit-cell thickness (2c), with a lattice misfit being  $\sim 1\%$  relative to the Al matrix, as shown in Fig. 6.17. These analyses suggest a low strain energy is important for precipitate nucleation [204]. 1-unit-cell thick  $\eta^*$  introduces  $\sim 10\%$  compression strain on the Al matrix, larger than that of a 2-unit-cell thick  $\theta'$ , which may cancel the advantage of  $\eta^*$  regarding a higher driving force of nucleation and a lower interfacial energy.

Strain energy in a phase transformation is usually calculated based on the assumption that the matrix and the precipitate have the same Young's modulus and Poisson's ratio [90, 202]. In this condition, strain energy per volume,  $w$ , is generally expressed as:

$$(w = \frac{E\varepsilon^2}{1-\nu}), \quad (6.3) [202]$$

Where  $E$  is Young's modulus ( $E_{\theta'}=127\text{GPa}$ ,  $E_{\eta^*}=170\text{GPa}$  and  $E_{\text{Al}}=69\text{GPa}$ ) and  $\nu$  is Poisson's ratio ( $\nu_{\theta'}=0.30$ ,  $\nu_{\eta^*}=0.25$  and  $\nu_{\text{Al}}=0.37$ ) [62]. If we assume the Al matrix has the same  $E$  and  $\nu$  as  $\theta'$  or  $\eta^*$ ,  $w_{\theta'}$  is  $0.11\text{ eV/nm}^3$  (2-unit-cell thick) and  $w_{\eta^*}$  is  $14.14\text{ eV/nm}^3$  (1-unit-cell thick). However, if we use the  $E$  and  $\nu$  for Al in calculations, we get  $w_{\theta'}=0.07\text{ eV/nm}^3$  (2-unit-cell thick) and  $w_{\eta^*}=6.84\text{ eV/nm}^3$  (1-unit-cell thick). Now the question is which value should be used for comparison? Due to the limitation of assuming the same  $E$  and  $\nu$  for the precipitate and the matrix in the conventional treatment, the author thinks such a simple mathematical treatment of strain energy is not accurate enough for the comparison between  $\eta^*$  and  $\theta'$ . More mathematical work is needed in this direction, which should include the anisotropy of Young's modulus [205-207] and the difference of Young's modulus between the precipitate and the matrix [208]. Instead, the strain effect on nucleation energy barrier will be roughly estimated by DFT calculations in the following.

The DFT calculated formation energies of the embedded precipitates in Fig. 6.17 relative to the chemical potentials of Cu and Al atoms in the Al-Cu solid solution are the estimates of the nucleation energy barriers for the embedded  $\eta^*$  and  $\theta'$  precipitates. The estimated nucleation energy barriers incorporate the contributions from the nucleation driving force (enthalpy change due to phase change), interfacial energy cost (ignoring the unavailable  $(010)_{\eta^*}/(010)_{\text{Al}}$  interface contribution) and the strain energy cost. The chemical potential of Cu is approximated

by the energy of one Cu solute atom in a 47-atom Al matrix (Al-2.1 at.%Cu, atomic model see Appendix 2). The ground state energy of an Al atom in the equilibrium FCC lattice is used as the chemical potential of Al. The calculated nucleation energy barriers for the 2-unit-cell  $\theta'$  and 1-unit-cell  $\eta^*$  precipitates in Fig. 6.17 are -0.035 eV/atom and -0.100 eV/atom, respectively. Their formation energies are both negative, indicating the precipitates in the atomic models are larger than the corresponding critical sizes of nuclei. The more negative formation energy of the  $\eta^*$  precipitate roughly suggests the residual strain energy cost cannot favour  $\theta'$  over  $\eta^*$ , at least for the investigated precipitate thicknesses in the atomic models. Regarding nucleation energy barrier/energy change for the phase transformation,  $\eta^*$  is always preferred than  $\theta'$ , at least based on the DFT calculations. However, this analysis does not deny the importance of lowering the strain energy cost. If excess vacancies can present and lower the strain energy cost, the nucleation of  $\eta^*$  precipitates will be much easier. Besides, a more accurate estimation of the strain energy is also necessary in the future to accurately compare the nucleation energy barriers for  $\eta^*$  and  $\theta'$  precipitates.

To summarise, thermodynamic analysis according to both DFT calculations and the Al-Cu thermodynamic database primarily suggests  $\eta^*$  is preferred over  $\theta'$  from the perspective of nucleation energy barrier. The lower nucleation energy barrier of  $\eta^*$  compared with  $\theta'$  is also supported by the observation that  $\eta_2$  (the bulk state of  $\eta^*$ ) phase nucleates first and before  $\theta$  (and  $\theta'$ ) during rapid solidification in Al-31.5at.%Cu, where the  $\theta$  phase is expected to form according to the Al-Cu phase diagram [209]. If there are no other limiting factors,  $\eta^*$  phase is anticipated to nucleate more easily than  $\theta'$  and form widely in aged Al-Cu alloys. However, to the best knowledge of the author,  $\eta^*$  precipitates are never observed in the normally aged Al-Cu alloys and have never be reported until now. Therefore, kinetics are expected to be critical on the phase selection between  $\eta^*$  and  $\theta'$ .

## 6.5 Discussion: kinetic analysis of the phase selection between $\theta'$ and $\eta^*$

The above thermodynamic discussion suggests  $\eta^*$  appears to be always favoured over  $\theta'$  during precipitation. The following discussion from the perspective of kinetics will show that  $\eta^*$  formation depends on abundant vacancies in the Al matrix.

### 6.5.1 Role of vacancies on the formation of $\theta'$ and $\eta^*$ at the $\eta^*$ decorated $\theta'$ /Al semi-coherent interface

As shown in Fig. 6.12 and 6.13, the stacking sequence of three Al layers at the interface should be changed from ABA to AAA, for the growth of both  $\theta'$  and  $\eta^*$ . Gliding of a misfit dislocation was once proposed to be necessary for the stacking change [28], which is difficult

to occur according to molecular dynamics simulations [196, 197, 210]. Moreover, the atomic model with such a dislocation is not thermodynamically favourable because it results in an unexpected high interfacial energy [28]. In contrast, the new growth mechanism at the  $\theta'$ /Al semi-coherent interface (see Fig. 6.12 and 6.13) features a much lower interfacial energy (see Fig. 6.16), which is more reasonable than the mechanism in the early report [28]. Now the question is how the stacking sequence is changed without gliding a misfit dislocation. We propose that vacancy condensation at the interface can make the stacking change very easy.

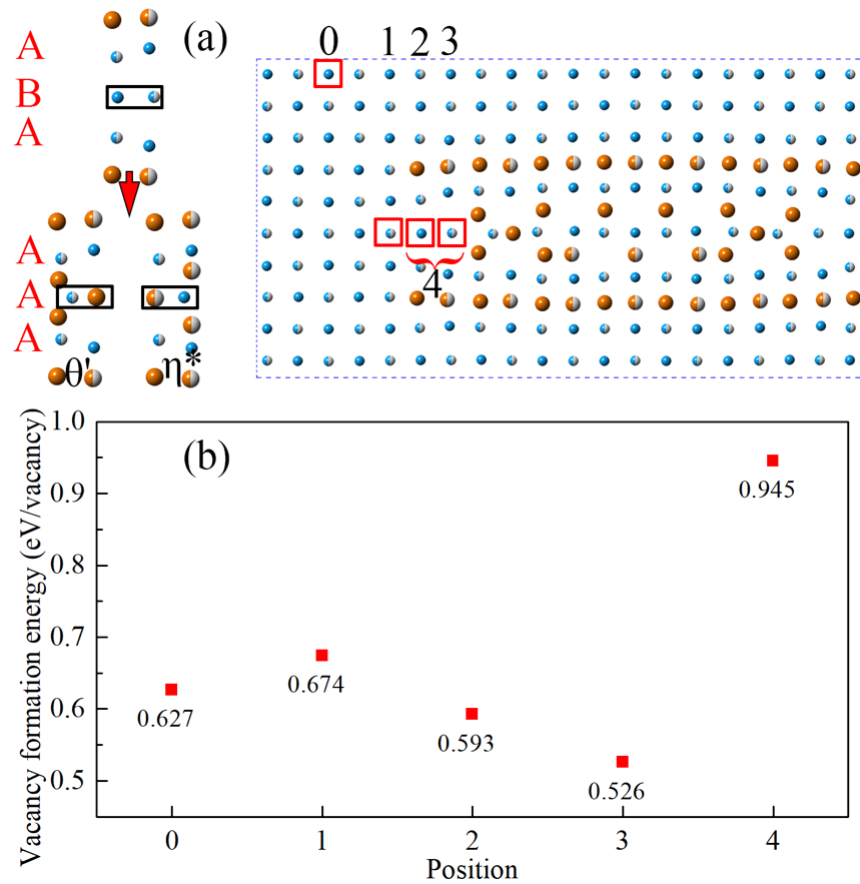


Fig. 6.18 DFT calculated vacancy formation energies at different positions near the  $\eta^*$ -decorated  $\theta'$ /Al semi-coherent interface. (a) schematic of the stacking change and the five possible positions for vacancy formation, (b) vacancy formation energies at different positions. Vacancy formation energy is lower near the interface than far away from the interface.

Firstly, vacancy condensation at the semi-coherent  $\theta'$ /Al interface is energetically preferred compared with random vacancy distribution in the Al matrix. The formation energies of vacancy at five possible locations were calculated by DFT calculations and are shown in Fig. 6.18. The positions with lower vacancy formation energies are the atomic columns that change stacking sequence (see the black rectangle in Fig. 6.18). During the growth process of either  $\theta'$  or  $\eta^*$ , these sites are expected to be refilled by Al and Cu atoms. The stacking change together

with the chemical change required for both the growth of  $\theta'$  and  $\eta^*$  can be achieved by discrete atomic movements. The discrete movements of atoms and vacancies can be expected to be energetically more favourable than shearing. It is basically a diffusion process with an energy barrier of  $\sim 1.3$  eV (typical energy barrier of Cu and vacancy diffusion in the Al matrix [57, 84, 211]). However, a concerted motion of one atomic layer (shearing) on  $\{100\}_{\text{Al}}$  planes should be very difficult. To the best knowledge of the author, the gliding/shearing on  $\{100\}_{\text{Al}}$  planes in the Al matrix or GP I zones has never been reported based on experimental observations or computer simulations [196, 197, 210, 212, 213]. In fact, vacancy condensation at the same positions during the transition from  $\theta''$  to  $\theta'$  has been proposed to be a pathway to avoid the difficult shearing [104]. Therefore, the segregation of vacancies at the semi-coherent interface is expected to facilitate the structural transformation at the interface. Moreover, the segregated vacancies do not annihilate at the interface because they are moved to the new interface and facilitate the next-step transformation once the transformation is completed at the existing interface.

Secondly, solute (In, Sb and Ge) additions increase the local and temporal concentration of vacancy in the Al-Cu-In-Sb and Al-Cu-Ge alloys. As discussed in the last two chapters, solutes (In, Sb and Ge) trap vacancies during quenching and release excess vacancies during ageing. The buffering role of these solutes can increase the local and temporal concentration of vacancy, which has also been experimentally verified by Sn additions in an Al-Mg-Si alloy [26]. The released vacancies have been shown to be the second mechanism by which solute additions enhance the nucleation of  $\theta'$  precipitates in the last two chapters. Now we can improve the second mechanism. Excess vacancies are hypothesized to segregate at the  $\theta'/\text{Al}$  semi-coherent interface and eliminate the concerted shearing at the interface. As shown in Fig. 6.12 and 6.13, the  $\theta'/\text{Al}$  and  $\eta^*/\text{Al}$  semi-coherent interfaces have the same stacking change. Therefore, vacancy segregation is expected to be critical for the lengthening of both  $\theta'$  and  $\eta^*$ . However, vacancy segregation cannot explain the phase selection between  $\theta'$  and  $\eta^*$ , which will be further discussed in Section 6.5.2.

### 6.5.2 Roles of vacancies on the phase selection between $\eta^*$ and $\theta'$

Now it is clear that vacancies appear to be critical for the formation of both  $\eta^*$  and  $\theta'$ . However, the formation of  $\eta^*$  is more sensitive to vacancies than  $\theta'$ . Vacancies play the same critical role for  $\eta^*$  and  $\theta'$  growth at the  $\eta^*$ -decorated  $\theta'/\text{Al}$  semi-coherent interface by changing the stacking sequence (see section 6.5.1). The second critical role of vacancies in  $\eta^*$  formation is proposed to be accelerating Cu diffusion, which is hypothesized to be the origin of the phase selection between  $\eta^*$  and  $\theta'$ .

As analysed in Section 6.3.2, the bottleneck for  $\theta'$  growth is whether the structural rearrangement in the existing structural feature of  $\eta^*$  is easy, while the bottleneck for  $\eta^*$  growth is whether Cu supply from the Al matrix is sufficient and timely. Therefore, the phase selection between  $\eta^*$  and  $\theta'$  at the  $\theta'/\text{Al}$  semi-coherent interface is controlled by the two bottlenecks. The two bottlenecks are both energy-barrier-climbing processes. The time to overcome either of the bottlenecks will be proportional to  $\exp\left(\frac{-\Delta E}{K_b T}\right)$ , where  $\Delta E$  is the energy barrier of overcoming one of the bottlenecks. Since more vacancies can increase the diffusivity of Cu atoms, the bottleneck for  $\eta^*$  growth can thus be eased by excess vacancies. When the diffusivity of Cu in the Al matrix is increased by excess vacancies, the growth of  $\eta^*$  will be preferred over  $\theta'$ . In the Al-Cu-In-Sb alloy, excess vacancies are released from In and Sb atoms during ageing, which can result in locally increased diffusivity of Cu and favour the growth of  $\eta^*$ . However, such locally increased vacancies will disappear later due to annihilation at defects, and the growth of  $\eta^*$  will not continue. In contrast,  $\theta'$  growth can start after vacancy annihilation because the bottleneck for  $\theta'$  growth is not correlated with excess vacancies in the Al matrix. This is why we can observe  $\eta^*$  precipitates embedded in big  $\theta'$  precipitates. We can understand the phase selection between  $\eta^*$  and  $\theta'$  at the  $\theta'/\text{Al}$  semi-coherent interface by comparing the time to overcome the two bottlenecks. In most conditions without abundant excess vacancies,  $\theta'$  growth at the  $\theta'/\text{Al}$  semi-coherent interface is preferred over  $\eta^*$  because the time for  $\theta'$  to overcome its bottleneck is expected to be shorter than that for  $\eta^*$ . However, once the diffusivity of Cu is increased with abundant excess vacancies, the time for  $\eta^*$  to overcome its bottleneck will be shortened, and  $\eta^*$  is expected to be preferred over  $\theta'$ . Estimating the energy barriers for the two bottlenecks will be beneficial for a deep understanding about the phase selection, but it needs future work. Here please note that the two energy barriers are kinetics-related because they are correlated with atomic motion, while the nucleation energy barrier discussed in Section 6.4 incorporates nothing about atomic vibration and motion.

The competition between  $\eta^*$  and  $\theta'$  at the nucleation stage from the Al-Cu solid solution is expected to be similar to the above discussion about the growth at the  $\eta^*$ -decorated  $\theta'/\text{Al}$  semi-coherent interface. In the Al-Cu-In-Sb and Al-Cu-Ge alloys, Cu diffusion in some local regions is increased due to excess vacancies. In this condition,  $\eta^*$  is proposed to nucleate first due to a shorter nucleation incubation time ( $\propto \exp(-\Delta G/K_b T)$ ,  $\Delta G$  is the nucleation energy barrier and  $>0$ , see Section 6.4). While in the remaining sites or in other alloys without enough excess vacancies,  $\theta'$  (consumes less Cu per volume than  $\eta^*$ ) nucleates before  $\eta^*$  because the nucleation incubation time of  $\theta'$  is shorter than the time to accumulate enough Cu for a  $\eta^*$  nucleus. Even

though the expected nucleation incubation time of  $\eta^*$  which is derived from the thermodynamic analysis is always shorter than that of  $\theta'$ , the formation of  $\eta^*$  is impossible when Cu diffusivity is not increased by excess vacancies. Therefore, both the nucleation thermodynamics and diffusion kinetics are proposed to be important on the phase selection between  $\eta^*$  and  $\theta'$ . In the classical nucleation theory, diffusion is determined by temperature-dependent equilibrium diffusion coefficient and is usually not critical for nucleation phenomena in gases and liquids [201] because diffusion is generally not changed at different conditions significantly. Therefore, non-equilibrium diffusion kinetics are generally ignored in the past, and thermodynamic nucleation energy barrier is enough to analyse phase selections in liquids [25, 214, 215]. However, in solid-state phase transformations, diffusion (atomic motion) can be significantly affected by defects, and thermodynamic nucleation energy barrier is not enough to understand phase selections. A more accurate way is to compare nucleation rate,  $I = A^* \exp\left(\frac{-\Delta G}{k_b T}\right)$ , where  $A^*$  incorporates the contributions of atomic movements [201]. However, the theoretical framework about nucleation rate is not well-established for the conditions where diffusion changes with processing conditions [201, 202].

### 6.5.3 Role of vacancies on $\eta^*$ thickening

There is another clue which suggests vacancies are important for  $\eta^*$  formation. In Section 6.1 and 6.2, we have shown that three kinds of defects are common in thick  $\eta^*$  precipitates in both the Al-Cu-In-Sb alloy and the Al-Cu-Ge alloy. As will be seen in the following, two kinds of defects are correlated with vacancies. This may explain why most of the observed thick  $\eta^*$  precipitates have defects though a defect seems to lower their thermodynamic stability (see Table 6.2).

Fig. 6.19 shows the atomic models of the thickening process of a  $\eta^*$  precipitate. The atomic models in Fig. 6.19 (a) and (b) were built according to the precipitates with the third kind of defect in Fig. 6.6. After DFT relaxation, model B (Fig. 6.19 (b)) matches with the HAADF images well from three crystallographic orientations, but model A is too thick to match the HAADF images (misfit by about one  $\{020\}_{Al}$  atomic plane spacing, see Fig. 6.6). The atomic model in Fig. 6.19 (c) is built according to precipitates with defect type 1 (see Fig. 6.4 (b-c)). We propose that the atomic models in 6.19 (a) and (b) can be viewed as intermediates of  $\eta^*$  thickening. The difference between (a) and (b) is the presence of vacancies in (b) but not in (a). It is interesting to note the concomitant decrease of the formation energy and the increasing matching of the precipitate with six  $(002)_{Al}$  planes ( $\sim 1.215$  nm) from (a) to (c).

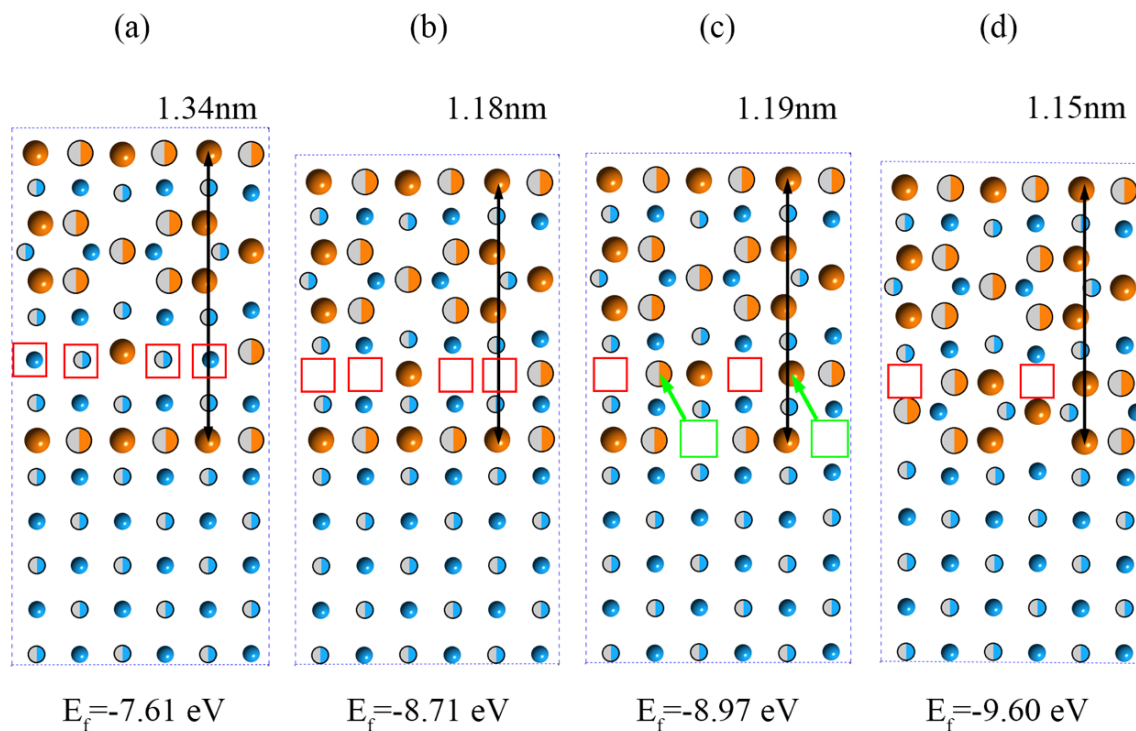


Fig. 6.19 Atomic models for the thickening process of a  $\eta^*$  precipitate. The formation energies of the four supercells are also shown at the bottom. (a) and (b) are model A and B in Fig. 6.6. Atoms with two tones are located at  $(x, y, 0.5)$  and others are at  $(x, y, 0.0)$ . Red squares indicate the energetically preferred positions of vacancies, and green arrows indicate the possible motion directions of Cu atoms from (b) to (c).

The author proposes that the thickening process of a  $\eta^*$  precipitate follows the process from (a) to (c), as described below.

- (1) At the first step of  $\eta^*$  thickening, Cu atoms replace some Al atoms in the FCC Al lattice sites and form a structure as the one shown in Fig. 6.19 (a). This process must trigger a significant compression strain in the Al matrix because the thickness of the Cu-rich part is 10% thicker than the matching Al matrix. If excess vacancies are available, they can be expected to accumulate in the surrounding Al matrix or at the vacancy positions shown in (b) (highlighted by red rectangles).
- (2) At the second step as depicted from (a) to (b), vacancies diffuse into the precipitate and replace some Al atoms (in red rectangles). This step reduces the free energy of the supercell and lowers the mismatch between the Al matrix and the precipitate. This results in a  $\eta^*$  precipitate with the third kind of defect
- (3) The last step is the relocation of Cu atoms (highlighted by green arrows) to some vacancy sites and forming a thickened  $\eta^*$  precipitate with defect type 1 (from (b) to (c)). Please

note that the relocation of Cu atoms is not only a displacement in the plane of the paper but also a displacement perpendicular to the paper.

Fig. 6.19 (d) shows an atomic model of a thick  $\eta^*$  precipitate ( $\eta_2$  more accurately) without defects. Comparing (c) with (d), we can find a  $\eta^*$  precipitate with a defect type 1 (shown in (c)) can match better with six  $(002)_{\text{Al}}$  planes ( $\sim 1.215$  nm) than a  $\eta^*$  precipitate without defects. The good matching between  $\eta^*$  with a defect and the Al matrix implies a  $\eta^*$  precipitate with a defect type 1 induces lower residual misfit strain energy, compared with a thick  $\eta^*$  precipitate without defects. The lower residual misfit energy could be a reason why  $\eta^*$  precipitates with such a thickness always have a defect (type 1) in the Al-Cu-In-Sb and Al-Cu-Ge alloys.

## 6.6 Strong similarities between $\eta^*$ and H

The H phase discussed in Chapter 5 (Section 5.5) has been proposed to form first and provide nucleation sites for  $\theta'$  type III precipitates. It shows strong similarities with the  $\eta^*$  phase. Besides being independent precipitates, both the H phase and the  $\eta^*$  phase are also found at the  $\theta'/\text{Al}$  interfaces as a segment (half unit cell along  $[100]_{\eta^*}$  or  $[100]_{\text{H}}$ ). However, the locations of their segments are different: the H phase segment located at the  $\{011\}_{\text{Al}}//\{010\}_{\theta'}$  coherent  $\theta'/\text{Al}$  interface, while the  $\eta^*$  phase segment located at the  $\{100\}_{\text{Al}}//\{100\}_{\theta'}$  semi-coherent  $\theta'/\text{Al}$  interface. Moreover, the above discussion suggests they tend to form in the condition with abundant excess vacancies. In the following, their similarities in structure will be discussed.

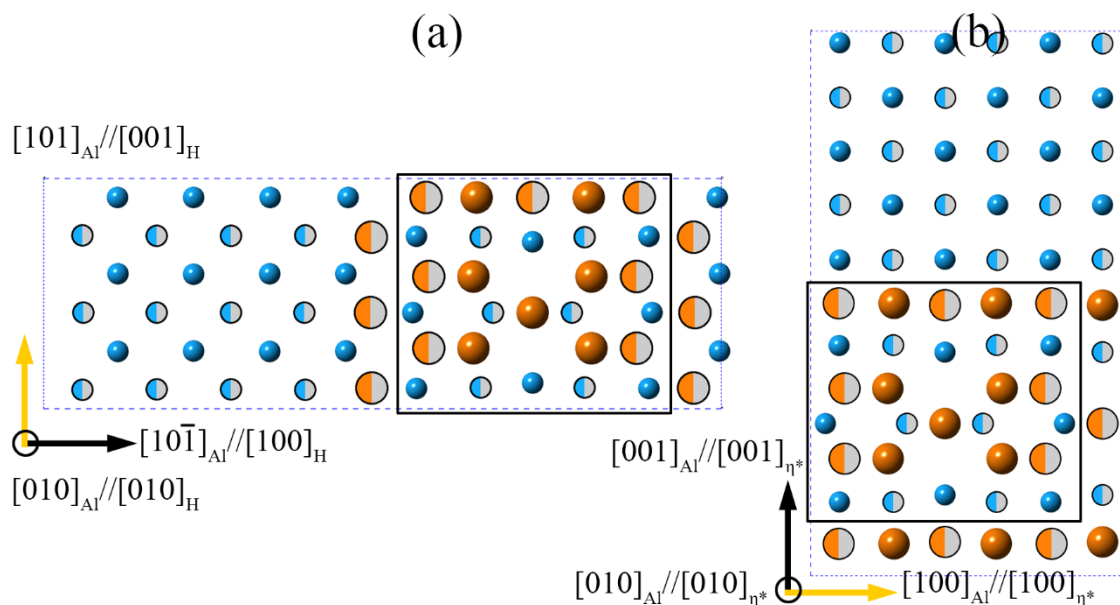


Fig. 6.20 DFT-relaxed atomic models for (a) the H phase lying on  $\{110\}_{\text{Al}}$  planes and (b) the  $\eta^*$  phase lying on  $\{100\}_{\text{Al}}$  planes. The yellow arrows indicate the lengthening directions for the two Cu-rich phases. The black rectangles highlight the common structural feature between (a) and (b). Atoms with two tones are located at  $(x, y, 0.5)$  and others are at  $(x, y, 0.0)$ .

The atomic models for  $\eta^*$  and H phases embedded in the Al matrix are shown in Fig. 6.20. The common structural feature of the two phases is highlighted by black rectangles. Please note that the common part is almost the same in three dimensions. The significant differences between the two phases are only located at their interfaces with the Al matrix. Besides, their lengthening directions are different: the H phase along  $[001]_H$ , while the  $\eta^*$  phase along  $[100]_{\eta^*}$ . Please note that  $[001]_H$  is equivalent to  $[001]_{\eta^*}$  regarding the common structure between the  $\eta^*$  phase and the H phase.

The H phase was only observed in the Al-Cu-Ge alloy but not in the Al-Cu-In-Sb alloy. The absence of the H phase on  $\{110\}_{Al}$  in the Al-Cu-In-Sb alloy is proposed to be correlated with whether GP zones and  $\theta''$  precipitates are present at the very early ageing stage. GP zones and  $\theta''$  precipitates are found at the very beginning of ageing in the Al-Cu-In-Sb alloy but are not observed in the Al-Cu-Ge alloy. The GP zones and  $\theta''$  precipitates (lying on  $\{100\}_{Al}$ ) may be nucleation templates for  $\eta^*$  precipitates on  $\{100\}_{Al}$ , therefore favouring the  $\eta^*$  phase over the H phase. How GP zones and  $\theta''$  precipitates promote the nucleation of  $\eta^*$  or  $\theta'$  is another big research topic for future work.

### 6.7 $\eta^*/H$ precipitates being the precursors of $\theta'$ precipitates

In the last two chapters, we have shown that the nucleation rate of  $\theta'$  is significantly increased in the Al-Cu-In-Sb and the Al-Cu-Ge alloys compared with the Al-Cu binary alloy. The first mechanism of the enhanced nucleation is enhancing  $\theta'$  heterogeneous nucleation on InSb or Ge particles, which has been well-discussed in the last two chapters. The second mechanism is correlated with excess vacancies released by In, Sb and Ge solutes, which will be further discussed here considering the formation of  $\eta^*/H$  precipitates.

The excess vacancies are expected to have two roles in boosting the nucleation of  $\theta'$  precipitates. First, excess vacancies can partially accommodate transformation strain and misfit strain around a  $\theta'$  precipitate, which has been discussed in the past reports [88, 89]. However, it may be very difficult to occur at the nucleation stage because condensation of vacancies in the Al matrix will increase the energy of the Al matrix. The condensation/segregation of vacancies is expected to occur only around  $\theta'$  precipitates, which may accommodate the misfit strain. In this condition, excess vacancies are only expected to facilitate the growth of  $\theta'$  but not nucleation. Please note that we only propose the segregation/condensation of vacancies near a structure with a strong misfit strain (see Fig. 6.18 and 6.19). Second, excess vacancies increase the diffusivity of Cu and make the nucleation of  $\eta^*/H$  possible. This is our new hypothesis based on the new findings in the thesis. As discussed above,  $\eta^*$  and H precipitates are favoured over  $\theta'$  precipitates regarding thermodynamic nucleation energy barrier but are

limited by diffusion kinetics. The nucleation of  $\eta^*$  and H precipitates can be expected to be much easier than  $\theta'$  precipitates if diffusivity is fast enough upon abundant vacancies. However, excess vacancies will soon annihilate and the continuing growth of  $\eta^*$  will become difficult at most sites. A very small fraction of  $\eta^*$  precipitates can continue growing and form large  $\eta^*$  precipitates (<1% of Cu-rich precipitates in experimental observations). In contrast, most of the infant  $\eta^*$  and H precipitates transform into  $\theta'$  precipitates partially or wholly and start the growth of  $\theta'$ . As shown in HAADF-STEM images (see Fig. 5.15 and 5.16), H precipitates (only 1 unit cell thick along  $[100]_H$ ) forms before  $\theta'$  type III precipitates, followed by the transformation of half of the thickness into  $\theta'$  type III precipitates. In this chapter, the transformation intermediate between the  $\eta^*$  segment (half unit cell along  $[100]_{\eta^*}$ ) and  $\theta'$  was directly imaged by HAADF-STEM at the  $\eta^*$ -decorated  $\theta'/Al$  semi-coherent interface (see Fig. 6.12). Therefore, it is safe to conclude that excess vacancies are expected to enhance  $\theta'$  nucleation by facilitating the nucleation of its precursor,  $\eta^*$  or H precipitates. The formation of  $\theta'$  precipitates can be started by transforming half unit cell of  $\eta^*$  or H precipitates (along  $[100]_{\eta^*}$  or  $[100]_H$ ) into  $\theta'$  precipitates.

## 6.7 Conclusions

A new Cu-rich phase,  $\eta^*$ , was found in both the Al-Cu-Ge alloy and the Al-Cu-In-Sb alloy. Its atomic structure is similar to that of  $\eta_2$ , a bulk equilibrium phase now only observed in Al-Cu alloys with >30at.%Cu. The  $\eta^*$  phase was found at three locations: as free-standing  $\eta^*$  precipitates in the Al matrix, embedded in large  $\theta'$  precipitates and located at the  $\theta'/Al$  semi-coherent interface. The thermodynamic nucleation energy barriers and the thermodynamic stability of different Cu-rich precipitates in the Al matrix were analyzed using DFT calculations and an Al-Cu thermodynamic database. The analysis seems to suggest that the  $\eta^*$  phase has a lower nucleation energy barrier compared with the  $\theta'$  phase at the expense of less lowering the energy of the (precipitates and the Al matrix) system. In contrast, precipitation in the form of  $\theta'$  lowers the energy of the system more, but the  $\theta'$  phase has a higher thermodynamic nucleation energy barrier than the  $\eta^*$  phase. This is consistent with our experimental observations that  $\eta^*$  precipitates tend to form first in some conditions and will transform into  $\theta'$  precipitates finally (private communication with Laure Bourgeois). Excess vacancies released by In, Sb and Ge solutes appear to be critical for the formation of  $\eta^*$  precipitates from the perspective of diffusion kinetics. Two roles of these excess vacancies are proposed based on experimental observations and DFT calculations. First, vacancy segregation/condensation at/near the  $\eta^*/Al$  interfaces are important for the lengthening and thickening of  $\eta^*$  precipitates. The vacancy segregation/condensation at the  $\eta^*/Al$  (or  $\eta^*$ -decorated  $\theta'/Al$ ) semi-coherent

interface is expected to break the stacking change of one atomic layer ( $//\{002\}_{Al}$ ) into discrete atomic movements, avoiding the difficult gliding on  $\{002\}_{Al}$ . Similarly, vacancy segregation/condensation at the coherent  $\eta^*/Al$  interface could also facilitate the thickening of  $\eta^*$  precipitates by avoiding some high energy states. The first role of excess vacancies is necessary for  $\eta^*$  formation but not sufficient to favour  $\eta^*$  over  $\theta'$ . This is because  $\theta'$  formation also requires the same stacking change at the  $\eta^*$ -decorated  $\theta'/Al$  semi-coherent interface. The second proposed role of vacancies is increasing the diffusivity of Cu, which is proposed to be the main reason favouring  $\eta^*$  over  $\theta'$ . Since the kinetic bottleneck for  $\eta^*$  formation is the time to accumulate enough Cu atoms (more Cu atoms per volume than  $\theta'$ ), the increased diffusivity of Cu upon excess vacancies can be expected to facilitate  $\eta^*$  formation. However, the thermodynamic bottleneck (thermodynamic nucleation energy barrier) of  $\theta'$  is not expected to be affected by excess vacancies significantly. This explanation can rationalize all our observations in the Al-Cu-In-Sb and Al-Cu-Ge alloys where local vacancy concentration can be increased due to In, Sb and Ge additions [26]. However further work is required to ascertain these proposed mechanisms.

The  $\eta^*$  phase displays strong similarities with the H phase described in Chapter 5. They have similar local atomic structure and chemical composition. An abundance of vacancies is proposed to be their common formation conditions. Furthermore,  $\eta^*$  and H phases are hypothesized to play the same and important role in enhancing  $\theta'$  nucleation. HAADF-STEM images showed that half unit cell of  $\eta^*$  or H precipitates (along  $[100]_{\eta^*}$  or  $[100]_H$ ) can transform into  $\theta'$  and start the formation of  $\theta'$  precipitates. Therefore,  $\eta^*$  and H phases are proposed to be the precursors of  $\theta'$  precipitates. Excess vacancies are proposed to enhance  $\theta'$  nucleation by facilitating the nucleation of its precursor,  $\eta^*$  or H precipitates. Different from the first role that InSb particles or Ge particles being the heterogeneous nucleation sites for  $\theta'$  precipitates, the second role of the microalloying additions of In, Sb and Ge is hypothesized to bring more excess vacancies in the Al matrix and enable the first nucleation of  $\eta^*$  or H precipitates.

# Chapter 7

## Conclusions and future work

### 7.1 Conclusions

In and Sb or Ge additions remarkably enhance the precipitation response in the Al-Cu alloy. Similar enhancing effects are well-known for Sn, In and Cd additions, which are correlated with either buffering excess vacancies or providing heterogeneous nucleation sites in the literature [30, 100]. However, the underlying mechanisms are still controversial. Here, the role of In and Sb or Ge additions in Al-Cu alloys were investigated in detail using high-resolution microscopy together with first-principles computer simulations, with the following conclusions.

#### 7.1.1 Two precipitation sequences correlated with excess vacancies in Al-Cu-In-Sb

The combined In and Sb additions in an Al-1.7at.%Cu alloy enhance both precipitation kinetics and peak hardness. The main precipitates are InSb particles, GP zones,  $\theta''$  and  $\theta'$ . InSb particles adopt a previously unreported cubic closed packed structure and cannot transform into the most stable zinc blende structure after 30 days ageing. Detailed microstructural characterisation reveals that InSb precipitates adopt two positions relative to the Cu-rich precipitates, which suggests two nucleation sequences. In the first sequence, InSb particles nucleate before Cu-rich precipitates, and its prerequisite is faster diffusion of In and Sb compared with Cu. The first sequence occurs in the alloy directly aged at low temperatures ( $\leq 200$  °C) after solution treatment and water quenching. In this condition, density functional theory (DFT) calculations suggest that excess vacancies are strongly bound to In and Sb atoms and form vacancy-solute clusters. The tight binding between In and Sb atoms with vacancies is likely to accelerate the diffusion of In and Sb atoms and results in InSb nanoparticles nucleating first. GP zones,  $\theta''$  and  $\theta'$  precipitates then nucleate heterogeneously from InSb particles (InSb particles located at the coherent  $\theta'/\text{Al}$  interface). In the second sequence,  $\theta'$  precipitates nucleate first and offer the semi-coherent  $\theta'/\text{Al}$  interface as heterogeneous nucleation sites for InSb particles. In this condition, excess vacancies are free and accelerate the diffusion of Cu atoms significantly, which usually occurs in the alloy aged at high temperature (250 °C). DFT calculations suggest that the binding energy between solute atoms

(In and Sb) and a vacancy increases continuously with solute number up to 3. Therefore, the active precipitation sequence can be selected by both ageing temperature and the solute-vacancy cluster size. The first nucleation sequence could be achieved in the alloy aged at 250 °C after an additional 10-day natural ageing. Similarly, the second nucleation sequence was repeated at 200 °C in the alloy that was interrupted quenched at 160 °C after solid solution treatment.

In both precipitation sequences, the role of quenched-in vacancies is critical, and the nucleation rate of  $\theta'$  is increased compared with the binary alloy counterpart. Firstly, the quenched-in vacancies will become excess vacancies relative to the equilibrium vacancies at an ageing temperature and affect the diffusivity of Cu, In and Sb solutes differently. The binding state between excess vacancies and solute atoms is the origin of the two precipitation sequences. Secondly, as will be stated in the following, the excess vacancies will change the way in which  $\theta'$  nucleates from the Al matrix, which is critical for the second precipitation sequence.

### 7.1.2 Multiple precipitation mechanisms of Cu-rich precipitates in Al-Cu-Ge

Ge additions (0.78at.%) also result in accelerated precipitation kinetics and a higher peak hardness. The main precipitates are Ge particles,  $\text{Al}_2\text{Cu}$  (not only  $\theta'$ ) precipitates at the peak aged condition. GP I zones and  $\theta''$  precipitates occur at under-aged condition only when the alloy is aged at low temperatures, e.g., 160 °C. There are at least 6 kinds of  $\text{Al}_2\text{Cu}$  precipitates; 5 kinds are the  $\theta'$  phase (type I to V) with different crystallographic orientation relationships (OR) with the matrix, another kind is the  $\Omega$  phase.  $\theta'$  precipitates of type I (lying on  $\{100\}_{\text{Al}}$ ) are the most common  $\theta'$  precipitates found in Al-Cu alloys and constitute > 80% of all Cu-rich precipitates in the peak-aged condition. < 20% of  $\theta'$  type I precipitates nucleate heterogeneously on Ge precipitates, while > 80% of  $\theta'$  type I precipitates nucleate and grow without the help of Ge precipitates (200 °C ageing). The low fraction of  $\theta'$  precipitates formed by heterogeneous nucleation on Ge particles is because the binding strength between Ge atoms and a vacancy (V) is very weak. DFT calculations suggest natural ageing cannot significantly increase the Ge-V binding strength in the Al-Cu-Ge alloy. Thus, the fraction of heterogeneous nucleation cannot be increased significantly by additional natural ageing. The other types of  $\theta'$  precipitates (particles or plates) form on  $\{110\}_{\text{Al}}$ ,  $\{111\}_{\text{Al}}$  and 10-20 degree off  $\{001\}_{\text{Al}}$ . Each  $\theta'$  types other than type I accounts for < 5% of Cu-rich precipitates (200 °C ageing). The  $\Omega$  plates lie on  $\{111\}_{\text{Al}}$  and are very rare (< 1% of Cu-rich precipitates). All precipitates of  $\theta'$  type II, type IV and type V nucleate heterogeneously on Ge particles. However, only 40% of  $\theta'$  type

III precipitates are associated with heterogeneous nucleation on Ge particles. 60% of  $\theta'$  type III precipitates are proposed to be transformed from a Cu-rich phase (named H phase). DFT calculations showed that the H phase has a lower interfacial energy and a higher driving force of nucleation than  $\theta'$  type I and type III. Therefore, the formation of the H phase is expected to form first and provide nucleation sites for  $\theta'$  type III precipitates, which is confirmed by HAADF-STEM imaging. All  $\theta'$  type III precipitates are covered by the H phase on the coherent interface. The thickness of the H phase covering  $\theta'$  type III precipitates is only half unit cell.

The nucleation mechanisms of  $\theta'$  precipitates in the Al-Cu-Ge alloy are the same as that in the Al-Cu-In-Sb alloy. One mechanism is associated with heterogeneous nucleation on InSb or Ge particles. The other one is the enhanced nucleation of  $\theta'$  precipitates from the Al matrix due to increased vacancies.

### 7.1.3 An unexpected phase ( $\eta^*$ ) preceding $\theta'$ in Al-Cu alloys with abundant vacancies

Precipitates of an unexpected Cu-rich ( $\eta^*$ ,  $\text{Al}_1\text{Cu}_1$ ) phase were also found in the Al-Cu-In-Sb and Al-Cu-Ge alloys at very low fractions (<1% of Cu-rich precipitates), which unveiled the critical role of vacancies in these alloys. The  $\eta^*$  phase was found at three locations: as independent  $\eta^*$  precipitates in the Al matrix, embedded in large  $\theta'$  precipitates and located at the  $\theta'/\text{Al}$  semi-coherent interface. The thermodynamic nucleation energy barriers and the thermodynamic stability of different Cu-rich phases in the Al matrix were examined using DFT calculations and an Al-Cu thermodynamic database. The analysis suggests that  $\eta^*$  has a lower nucleation energy barrier compared with  $\theta'$  but is ultimately less thermodynamically stable. In contrast, precipitation in the form of  $\theta'$  lowers the energy of the system more, but  $\theta'$  has a higher nucleation energy barrier than  $\eta^*$ . Excess vacancies released by In, Sb and Ge solutes are proposed to be critical for the formation of  $\eta^*$  from the perspective of phase transformation kinetics. Two roles of these excess vacancies are hypothesized based on experimental observations and DFT calculations. First, vacancy segregation/condensation at/near the  $\eta^*/\text{Al}$  interfaces can be expected to facilitate the lengthening and thickening of  $\eta^*$  precipitates by avoiding some intermediates of  $\eta^*$  with high energies or high energy barriers. However, the first role of excess vacancies is also applicable to the lengthening of  $\theta'$ , which implies there is a second role of vacancies favouring  $\eta^*$ . The second role of excess vacancies is increasing the diffusivity of Cu, which is proposed to be the main factor favouring  $\eta^*$  over  $\theta'$ . Since the bottleneck (a kinetic bottleneck) for  $\eta^*$  formation is the time to accumulate enough Cu atoms (more Cu atoms per volume in  $\eta^*$  than in  $\theta'$ ), the increased diffusivity of Cu resulting from excess vacancies can be expected to facilitate  $\eta^*$  formation. However, the bottleneck (thermodynamic nucleation energy barrier) of  $\theta'$  is not expected to be affected by excess

vacancies significantly. This explanation can rationalize all our observations in the Al-Cu-In-Sb and Al-Cu-Ge alloys where local vacancy concentration can be increased due to In, Sb and Ge additions.

The  $\eta^*$  phase displays strong similarities with the H phase. They have a similar structure and a similar formation condition (vacancy abundant). Furthermore,  $\eta^*$  and H phases are proposed to play the same and important role in enhancing  $\theta'$  nucleation. HAADF-STEM images show that half unit cell of  $\eta^*$  or H precipitates ( along  $[100]_{\eta^*}$  or  $[100]_H$ ) can transform into  $\theta'$  and start the formation of  $\theta'$  precipitates. Therefore,  $\eta^*$  and H phases are proposed to be the precursor of  $\theta'$ . Excess vacancies are proposed to enhance  $\theta'$  nucleation by facilitating the nucleation of its precursor,  $\eta^*$  or H precipitates. The second role of the microalloying additions of In, Sb and Ge in enhancing  $\theta'$  nucleation is proposed to bring more excess vacancies in the Al matrix and enable the first nucleation of  $\eta^*$  or H precipitates.

#### **7.1.4 More remarks: comparing the two kinds of microalloying additions**

This thesis comprehensively investigated the mechanisms of two solute additions in enhancing precipitation in Al-Cu alloys. Two mechanisms are recognised. The first one is providing heterogeneous nucleation sites (InSb or Ge particles) for  $\theta'$  precipitates, which has been proposed for more than 20 years [16]. This mechanism is mainly operative when the binding strength between the added solutes and a vacancy is very strong relative to the ageing temperature, e.g., in the Al-Cu-In-Sb aged at 200 °C but not at 250 °C. The second mechanism is proposed to be associated with retaining excess vacancies and boosting the formation of the predecessor of  $\theta'$ , the  $\eta^*$  or H phase. This mechanism is primarily observed when the binding strength between the microalloying solutes and a vacancy is strong enough to trap vacancies during the quenching process but weak enough to release vacancies during the ageing process. The binding energy between the microalloying solutes and a vacancy should be  $< 0$  eV in order to trap vacancies during the quenching process, and it should be larger than a threshold in order to release vacancies when aged at 200 °C. Ge additions work mainly by the second mechanism at 200 °C (binding energy  $> -0.29$  from DFT calculations), and InSb additions function through the first mechanism at 200 °C (binding energy  $< -0.29$  eV from DFT calculations ). Therefore, the threshold is expected to be  $-0.29$  eV.

## **7.2 Recommendations for future work**

The crucial roles of excess vacancies that come with solute additions on precipitation kinetics and pathways were discussed in detail in this study, but there remain many open questions.

- (1) Both InSb additions and Ge additions change the morphology of  $\theta'$  precipitates and even the atomic structure of the semi-coherent  $\theta'/\text{Al}$  interface. Therefore, In, Sb and Ge atoms are proposed to be segregated at the semi-coherent  $\theta'/\text{Al}$  interface. Here is an interesting observation: a  $\theta'$  precipitate tends to develop a square morphology when an InSb/Ge particle is located near the edge of the  $\theta'$  precipitate but on the coherent  $\theta'/\text{Al}$  interface. The open question is whether the attaching InSb/Ge particle modulates the distribution of solute atoms along the semi-coherent  $\theta'/\text{Al}$  interface. More work using other techniques, such as APT or new generation EDS detectors in a STEM, is desired to characterise the concentrations of In, Sb and Ge solutes along the semi-coherent  $\theta'/\text{Al}$  interface.
  
- (2) The diffusivity of Cu and microalloying elements in the Al matrix is significantly affected by excess vacancies. Free vacancies can enhance the diffusivity of Cu and the microalloying elements, and vacancies bound to solutes are expected to increase the diffusivity of the microalloying elements only. By how much excess vacancies can enhance the diffusivity is still unknown. The theoretical model of calculating diffusivity from DFT currently uses equilibrium vacancy concentration. Therefore, a new framework is necessary to predict the diffusivities of Cu and microalloying elements with supersaturated vacancies quantitatively.
  
- (3) The thermodynamic nucleation energy barriers of  $\theta'$  and  $\eta^*$  were compared here using a rough estimation of strain energy, due to present limitations in strain energy calculations. A calculation method of strain energy considering the anisotropy of Young's modulus [205-207] and the difference of Young's modulus in the precipitate and the matrix is important for a more accurate comparison of the thermodynamic nucleation energy barriers of  $\theta'$  and  $\eta^*$ .
  
- (4) The thermodynamic nucleation energy barrier is widely used in understanding phase selection, including for phase transitions between different states of matter. However, the results in this study primarily suggest the thermodynamic nucleation energy barrier ( $\Delta G$ ) is not enough for understanding phase selection in solid-to-solid phase transformations. A more accurate way is to compare nucleation rate,  $I = A^* \exp\left(\frac{-\Delta G}{K_b T}\right)$ , where  $A^*$  incorporates the contributions of atomic movements [190]. However, the

theoretical framework about nucleation rate is not well-established for the conditions where the diffusivities of participating elements change with processing conditions.

- (5) Vacancies in the investigated alloys cannot be directly imaged in this study. More work is needed to directly probe the distribution of vacancies in the Al matrix with new advanced techniques, such as positron annihilation lifetime spectroscopy.
- (6) This study has only focused on the chosen addition amounts of InSb and Ge. Other addition amounts are also desirable for further investigation. The investigated addition amounts of InSb and Ge are near their maximum solid solubility in the Al matrix at the solid solution temperature. A lower addition amount may give an acceptable enhancing effect on the precipitation of Cu-rich phases but is at a much lower cost.

# Publications and conference presentations

1. Yong Zhang, et al. Vacancy-tuned precipitation pathways in Al-1.7 Cu-0.025 In-0.025 Sb (at.%) alloy. *Acta Materialia* 141 (2017): 341-351.
2. Yong Zhang, et al. Structure and Function of Nano-sized InSb Precipitate Embedded in an Al Alloy. M&M meeting 2017 St. Louis, USA (student scholar).
3. Yong Zhang, et al. Complex nucleation mechanisms of  $\theta'$  precipitates in Al-Cu-Ge alloy: different ways to lower the interfacial energy penalty (in preparation).
4. Yong Zhang, et al. An unexpected Cu-rich phase ( $\eta^*$ ) induced by excess vacancies in Al-Cu-In-Sb and Al-Cu-Ge alloy (in preparation).

# References

- [1] J.E. Saal, S. Kirklin, M. Aykol, B. Meredig, C. Wolverton, Materials Design and Discovery with High-Throughput Density Functional Theory: The Open Quantum Materials Database (OQMD), *JOM* 65(11) (2013) 1501-1509.
- [2] National Science and Technology Council, Materials Genome Initiative for Global Competitiveness.  
[https://www.mgi.gov/sites/default/files/documents/materials\\_genome\\_initiative-final.pdf](https://www.mgi.gov/sites/default/files/documents/materials_genome_initiative-final.pdf)
- [3] R. Martoňák, D. Donadio, A.R. Oganov, M. Parrinello, Crystal structure transformations in SiO<sub>2</sub> from classical and ab initio metadynamics, *Nature materials* 5(8) (2006) 623-626.
- [4] R.Z. Khaliullin, H. Eshet, T.D. Kühne, J. Behler, M. Parrinello, Nucleation mechanism for the direct graphite-to-diamond phase transition, *Nature materials* 10(9) (2011) 693-697.
- [5] G.C. Sosso, J. Chen, S.J. Cox, M. Fitzner, P. Pedevilla, A. Zen, A. Michaelides, Crystal nucleation in liquids: Open questions and future challenges in molecular dynamics simulations, *Chemical reviews* 116(12) (2016) 7078-7116.
- [6] J. Duncan, A. Harjunmaa, R. Terrell, R. Drautz, G. Henkelman, J. Rogal, Collective Atomic Displacements during Complex Phase Boundary Migration in Solid-Solid Phase Transformations, *Physical review letters* 116(3) (2016) 035701.
- [7] B. Wang, H.M. Urbassek, Molecular dynamics study of the  $\alpha$ - $\gamma$  phase transition in Fe induced by shear deformation, *Acta Materialia* 61(16) (2013) 5979-5987.
- [8] K. Lejaeghere, G. Bihlmayer, T. Björkman, P. Blaha, S. Blügel, V. Blum, D. Caliste, I.E. Castelli, S.J. Clark, A. Dal Corso, Reproducibility in density functional theory calculations of solids, *Science* 351(6280) (2016) aad3000.
- [9] J. Chen, E. Costan, M. Van Huis, Q. Xu, H. Zandbergen, Atomic pillar-based nanoprecipitates strengthen AlMgSi alloys, *Science* 312(5772) (2006) 416-419.
- [10] C. Wolverton, V. Ozoliņš, Entropically favored ordering: the metallurgy of Al<sub>2</sub>Cu revisited, *Physical review letters* 86(24) (2001) 5518-5521.
- [11] P. Souvatzis, O. Eriksson, M.I. Katsnelson, S.P. Rudin, Entropy Driven Stabilization of Energetically Unstable Crystal Structures Explained from First Principles Theory, *Physical Review Letters* 100(9) (2008) 095901.
- [12] Q. Yu, L. Qi, T. Tsuru, R. Traylor, D. Rugg, J. Morris, M. Asta, D. Chrzan, A.M. Minor, Origin of dramatic oxygen solute strengthening effect in titanium, *Science* 347(6222) (2015) 635-639.
- [13] J. Nie, Y. Zhu, J. Liu, X. Fang, Periodic segregation of solute atoms in fully coherent twin boundaries, *Science* 340(6135) (2013) 957-960.
- [14] S.P. Ringer, K. Hono, I.J. Polmear, T. Sakurai, Nucleation of precipitates in aged AlCuMg(Ag) alloys with high Cu:Mg ratios, *Acta Materialia* 44(5) (1996) 1883-1898.
- [15] L. Reich, M. Murayama, K. Hono, Evolution of  $\Omega$  phase in an Al-Cu-Mg-Ag alloy—a three-dimensional atom probe study, *Acta Materialia* 46(17) (1998) 6053-6062.
- [16] S.P. Ringer, K. Hono, T. Sakurai, The effect of trace additions of Sn on precipitation in Al-Cu alloys: An atom probe field ion microscopy study, *Metallurgical and Materials Transactions A* 26(9) (1995) 2207-2217.
- [17] F.W. Gayle, M. Goodway, Precipitation hardening in the first aerospace aluminum alloy: the Wright flyer crankcase, *Science* 266(5187) (1994) 1015-1017.
- [18] A. Guinier, Structure of age-hardened aluminium-copper alloys, *Nature* 142(3595) (1938) 569.
- [19] G. Preston, Structure of age-hardened aluminium-copper alloys, *Nature* 142(3595) (1938) 570.

- [20] H.-L. Chen, Q. Chen, A. Engström, Development and applications of the TCAL aluminum alloy database, *Calphad* 62 (2018) 154-171.
- [21] E. Matsubara, J. Cohen, The GP zones in Al-Cu alloys-I, *Acta Metallurgica* 33(11) (1985) 1945-1955.
- [22] D.A. Porter, K.E. Easterling, M. Sherif, *Phase Transformations in Metals and Alloys*, (Revised Reprint), CRC press 2009.
- [23] P. Marth, H. Aaronson, G. Lorimer, T. Bartel, K. Russell, Application of heterogeneous nucleation theory to precipitate nucleation at GP zones, *Metallurgical Transactions A* 7(10) (1976) 1519-1528.
- [24] Y. Peng, F. Wang, Z. Wang, A.M. Alsayed, Z. Zhang, A.G. Yodh, Y. Han, Two-step nucleation mechanism in solid–solid phase transitions, *Nature materials* 14(1) (2015) 101-108.
- [25] A.E. Van Driessche, N. Van Gerven, P.H. Bomans, R.R. Joosten, H. Friedrich, D. Gil-Carton, N.A. Sommerdijk, M. Sleutel, Molecular nucleation mechanisms and control strategies for crystal polymorph selection, *Nature* 556(7699) (2018) 89.
- [26] S. Pogatscher, H. Antrekowitsch, M. Werinos, F. Moszner, S.S.A. Gerstl, M.F. Francis, W.A. Curtin, J.F. Löffler, P.J. Uggowitzer, Diffusion on Demand to Control Precipitation Aging: Application to Al-Mg-Si Alloys, *Physical Review Letters* 112(22) (2014) 225701.
- [27] L. Bourgeois, C. Dwyer, M. Weyland, J.-F. Nie, B.C. Muddle, Structure and energetics of the coherent interface between the  $\theta'$  precipitate phase and aluminium in Al-Cu, *Acta Materialia* 59(18) (2011) 7043-7050.
- [28] L. Bourgeois, N.V. Medhekar, A.E. Smith, M. Weyland, J.-F. Nie, C. Dwyer, Efficient Atomic-Scale Kinetics through a Complex Heterophase Interface, *Physical Review Letters* 111(4) (2013) 046102.
- [29] K. Kim, A. Roy, M.P. Gururajan, C. Wolverton, P.W. Voorhees, First-principles/Phase-field modeling of  $\theta'$  precipitation in Al-Cu alloys, *Acta Materialia* 140 (2017) 344-354.
- [30] H. Hardy, The ageing characteristics of ternary aluminium copper alloys with cadmium, indium, or tin, *Journal of the Institute of Metals* 80(9) (1952) 483-492.
- [31] H. Hardy, The ageing characteristics of binary Aluminium-Copper Alloys, *Journal of the institute of metals* 79(11) (1951) 321-369.
- [32] J. Silcock, T. Heal, H. Hardy, The structural ageing characteristics of ternary aluminium-copper alloys with cadmium, indium, or tin, *Journal of the Institute of Metals* 84(1) (1955) 23-56.
- [33] D. Kent, G.B. Schaffer, J. Drennan, Age hardening of a sintered Al-Cu-Mg-Si-(Sn) alloy, *Materials Science and Engineering: A* 405(1) (2005) 65-73.
- [34] H. Kimura, R.K. Hasiguti, Interaction of vacancies with Sn atoms and the rate of GP zone formation in an Al-Cu-Sn alloy, *Acta Metallurgica* 9(12) (1961) 1076-1078.
- [35] B. Noble, Theta-prime precipitation in aluminium-copper-cadmium alloys, *Acta Metallurgica* 16(3) (1968) 393-401.
- [36] C.W. Bartges, J.S. Lin, Effect of Sn additions on GP Zone formation in Al-Cu alloys, *Scripta Metallurgica et Materialia* 28(10) (1993) 1283-1286.
- [37] W. Desorbo, H.N. Treafis, D. Turnbull, Rate of clustering in Al-Cu alloys at low temperatures, *Acta Metallurgica* 6(6) (1958) 401-413.
- [38] J.B.M. Nuyten, Quenched structures and precipitation in Al-Cu alloys with and without trace additions of Cd, *Acta Metallurgica* 15(11) (1967) 1765-1770.
- [39] C. Wolverton, Solute–vacancy binding in aluminum, *Acta Materialia* 55(17) (2007) 5867-5872.
- [40] L. Bourgeois, C. Dwyer, M. Weyland, J.-F. Nie, B.C. Muddle, The magic thicknesses of  $\theta'$  precipitates in Sn-microalloyed Al-Cu, *Acta Materialia* 60(2) (2012) 633-644.
- [41] B.T. Sofyan, K. Raviprasad, S.P. Ringer, Effects of microalloying with Cd and Ag on the precipitation process of Al-4Cu-0.3Mg (wt%) alloy at 200 °C, *Micron* 32(8) (2001) 851-856.

- [42] A. Kiselev, F. Bachmann, P. Pedevilla, S.J. Cox, A. Michaelides, D. Gerthsen, T. Leisner, Active sites in heterogeneous ice nucleation—the example of K-rich feldspars, *Science* 355(6323) (2017) 367-371.
- [43] J.H. Martin, B.D. Yahata, J.M. Hundley, J.A. Mayer, T.A. Schaedler, T.M. Pollock, 3D printing of high-strength aluminium alloys, *Nature* 549(7672) (2017) 365-369.
- [44] S.G. Kwon, G. Krylova, P.J. Phillips, R.F. Klie, S. Chattopadhyay, T. Shibata, E.E. Bunel, Y. Liu, V.B. Prakapenka, B. Lee, Heterogeneous nucleation and shape transformation of multicomponent metallic nanostructures, *Nature materials* 14(2) (2015) 215.
- [45] L. Bourgeois, J. Nie, B. Muddle, Assisted nucleation of  $\theta'$  phase in Al-Cu-Sn: the modified crystallography of tin precipitates, *Philosophical Magazine* 85(29) (2005) 3487-3509.
- [46] T. Homma, M.P. Moody, D.W. Saxey, S.P. Ringer, Effect of Sn addition in preprecipitation stage in Al-Cu alloys: a correlative transmission electron microscopy and atom probe tomography study, *Metallurgical and Materials Transactions A* 43(7) (2012) 2192-2202.
- [47] B. Klobes, O. Balarisi, M. Liu, T.E.M. Staab, K. Maier, The effect of microalloying additions of Au on the natural ageing of Al-Cu, *Acta Materialia* 58(19) (2010) 6379-6384.
- [48] D. Mitlin, J.W. Morris, V. Radmilovic, U. Dahmen, Precipitation and ageing in Al-Si-Ge-Cu, *Metallurgical and Materials Transactions A* 32(1) (2001) 197-199.
- [49] Y. Chen, Z. Zhang, Z. Chen, A. Tsalanidis, M. Weyland, S. Findlay, L.J. Allen, J. Li, N.V. Medhekar, L. Bourgeois, The enhanced theta-prime ( $\theta'$ ) precipitation in an Al-Cu alloy with trace Au additions, *Acta Materialia* 125 (2017) 340-350.
- [50] L. Bourgeois, Z. Zhang, J. Li, N.V. Medhekar, The bulk and interfacial structures of the  $\eta$  ( $\text{Al}_2\text{Au}$ ) precipitate phase, *Acta Materialia* 105 (2016) 284-293.
- [51] E. Hornbogen, A.K. Mukhopadhyay, E.A. Starke, Precipitation hardening of Al-(Si, Ge) alloys, *Scripta Metallurgica et Materialia* 27(6) (1992) 733-738.
- [52] D. Mitlin, U. Dahmen, V. Radmilovic, J.W. Morris, Precipitation and hardening in Al-Si-Ge, *Materials Science and Engineering: A* 301(2) (2001) 231-236.
- [53] D. Mitlin, J.W. Morris, V. Radmilovic, Catalyzed precipitation in Al-Cu-Si, *Metallurgical and Materials Transactions A* 31(11) (2000) 2697-2711.
- [54] K. Raviprasad, C.R. Hutchinson, T. Sakurai, S.P. Ringer, Precipitation processes in an Al-2.5Cu-1.5Mg (wt. %) alloy microalloyed with Ag and Si, *Acta Materialia* 51(17) (2003) 5037-5050.
- [55] R.K.W. Marceau, G. Sha, R. Ferragut, A. Dupasquier, S.P. Ringer, Solute clustering in Al-Cu-Mg alloys during the early stages of elevated temperature ageing, *Acta Materialia* 58(15) (2010) 4923-4939.
- [56] Y.L. Zhao, Z.Q. Yang, Z. Zhang, G.Y. Su, X.L. Ma, Double-peak age strengthening of cold-worked 2024 aluminum alloy, *Acta Materialia* 61(5) (2013) 1624-1638.
- [57] M. Mantina, Y. Wang, R. Arroyave, L. Chen, Z. Liu, C. Wolverton, First-principles calculation of self-diffusion coefficients, *Physical review letters* 100(21) (2008) 215901.
- [58] Y. Nagai, M. Murayama, Z. Tang, T. Nonaka, K. Hono, M. Hasegawa, Role of vacancy-solute complex in the initial rapid age hardening in an Al-Cu-Mg alloy, *Acta Materialia* 49(5) (2001) 913-920.
- [59] A. Deschamps, T.J. Bastow, F. de Geuser, A.J. Hill, C.R. Hutchinson, In situ evaluation of the microstructure evolution during rapid hardening of an Al-2.5Cu-1.5Mg (wt.%) alloy, *Acta Materialia* 59(8) (2011) 2918-2927.
- [60] A. Garg, Y. Chang, J. Howe, Precipitation of the  $\Omega$  phase in an Al-4.0 Cu-0.5 Mg alloy, *Scripta Metallurgica et Materialia* 24(4) (1990) 677-680.
- [61] J.M. Rosalie, L. Bourgeois, B.C. Muddle, Precipitate assemblies formed on dislocation loops in aluminium-silver-copper alloys, *Philosophical Magazine* 89 (25), 2195-2211.
- [62] D. Wang, M. Amsler, V.I. Hegde, J.E. Saal, A. Issa, B.-C. Zhou, X. Zeng, C. Wolverton, Crystal structure, energetics, and phase stability of strengthening precipitates in Mg alloys: A first-principles study, *Acta Materialia* 158 (2018) 65-78.

- [63] S.J. Kang, Y.-W. Kim, M. Kim, J.-M. Zuo, Determination of interfacial atomic structure, misfits and energetics of  $\Omega$  phase in Al–Cu–Mg–Ag alloy, *Acta Materialia* 81 (2014) 501-511.
- [64] V. Araullo-Peters, B. Gault, F.d. Geuser, A. Deschamps, J.M. Cairney, Microstructural evolution during ageing of Al–Cu–Li–x alloys, *Acta Materialia* 66 (2014) 199-208.
- [65] B. Decreus, A. Deschamps, F. De Geuser, P. Donnadieu, C. Sigli, M. Weyland, The influence of Cu/Li ratio on precipitation in Al–Cu–Li–x alloys, *Acta Materialia* 61(6) (2013) 2207-2218.
- [66] P. Donnadieu, Y. Shao, F. De Geuser, G.A. Botton, S. Lazar, M. Cheynet, M. de Boissieu, A. Deschamps, Atomic structure of T<sub>1</sub> precipitates in Al–Li–Cu alloys revisited with HAADF-STEM imaging and small-angle X-ray scattering, *Acta Materialia* 59(2) (2011) 462-472.
- [67] C. Dwyer, M. Weyland, L.Y. Chang, B.C. Muddle, Combined electron beam imaging and ab initio modeling of T<sub>1</sub> precipitates in Al–Li–Cu alloys, *Applied Physics Letters* 98(20) (2011) 201909.
- [68] B.P. Huang, Z.Q. Zheng, Independent and combined roles of trace Mg and Ag additions in properties precipitation process and precipitation kinetics of Al–Cu–Li–(Mg)–(Ag)–Zr–Ti alloys, *Acta Materialia* 46(12) (1998) 4381-4393.
- [69] W. Cassada, G. Shiflet, E. Starke, Mechanism of Al<sub>2</sub>CuLi (T<sub>1</sub>) nucleation and growth, *Metallurgical transactions A* 22(2) (1991) 287-297.
- [70] D. Finkenstadt, D.D. Johnson, Solute/defect-mediated pathway for rapid nanoprecipitation in solid solutions:  $\gamma$  surface analysis in fcc Al–Ag, *Physical Review B* 73(2) (2006) 024101.
- [71] E. Gumbmann, W. Lefebvre, F. De Geuser, C. Sigli, A. Deschamps, The effect of minor solute additions on the precipitation path of an AlCuLi alloy, *Acta Materialia* 115 (2016) 104-114.
- [72] J.M. Rosalie, L. Bourgeois, Silver segregation to  $\theta'$ (Al<sub>2</sub>Cu)–Al interfaces in Al–Cu–Ag alloys, *Acta Materialia* 60(17) (2012) 6033-6041.
- [73] E. Gumbmann, F. De Geuser, C. Sigli, A. Deschamps, Influence of Mg, Ag and Zn minor solute additions on the precipitation kinetics and strengthening of an Al–Cu–Li alloy, *Acta Materialia* 133 (2017) 172-185.
- [74] A. Deschamps, M. Garcia, J. Chevy, B. Davo, F. De Geuser, Influence of Mg and Li content on the microstructure evolution of AlCuLi alloys during long-term ageing, *Acta Materialia* 122 (2017) 32-46.
- [75] E. Gumbmann, F. De Geuser, A. Deschamps, W. Lefebvre, F. Robaut, C. Sigli, A combinatorial approach for studying the effect of Mg concentration on precipitation in an Al–Cu–Li alloy, *Scripta Materialia* 110 (2016) 44-47.
- [76] C. Wolverton, Crystal structure and stability of complex precipitate phases in Al–Cu–Mg–(Si) and Al–Zn–Mg alloys, *Acta Materialia* 49(16) (2001) 3129-3142.
- [77] G. Sha, A. Cerezo, Early-stage precipitation in Al–Zn–Mg–Cu alloy (7050), *Acta Materialia* 52(15) (2004) 4503-4516.
- [78] R.O. Simmons, R.W. Balluffi, Measurements of Equilibrium Vacancy Concentrations in Aluminum, *Physical Review* 117(1) (1960) 52-61.
- [79] R.O. Simmons, R.W. Balluffi, Measurement of Equilibrium Concentrations of Vacancies in Copper, *Physical Review* 129(4) (1963) 1533-1544.
- [80] D.R. Beaman, R.W. Balluffi, R.O. Simmons, Measurement of Equilibrium Vacancy Concentrations in Dilute Aluminum–Silver Alloys, *Physical Review* 134(2A) (1964) A532-A542.
- [81] D. Beaman, R. Balluff, R. Simmons, Measurement of Equilibrium Vacancy Concentrations in Dilute Aluminum–Magnesium Alloys, *Physical Review* 137(3A) (1965) A917.

- [82] A. King, J. Burke, The equilibrium vacancy concentration in an Aluminium-Copper alloy, *Acta Metallurgica* 18(2) (1970) 205-210.
- [83] D. Simonovic, M.H. Sluiter, Impurity diffusion activation energies in Al from first principles, *Physical Review B* 79(5) (2009) 054304.
- [84] M. Mantina, Y. Wang, L.Q. Chen, Z.K. Liu, C. Wolverton, First principles impurity diffusion coefficients, *Acta Materialia* 57(14) (2009) 4102-4108.
- [85] S. Hirose, T. Sato, A. Kamio, H.M. Flower, Classification of the role of microalloying elements in phase decomposition of Al based alloys, *Acta Materialia* 48(8) (2000) 1797-1806.
- [86] M. Werinos, H. Antrekowitsch, T. Ebner, R. Prillhofer, W.A. Curtin, P.J. Uggowitzer, S. Pogatscher, Design strategy for controlled natural ageing in Al-Mg-Si alloys, *Acta Materialia* 118 (2016) 296-305.
- [87] M.F. Francis, W.A. Curtin, Microalloying for the controllable delay of precipitate formation in metal alloys, *Acta Materialia* 106 (2016) 117-128.
- [88] G. Dlubek, O. Brümmer, P. Hautojärvi, A positron study of precipitation phenomena in Al-Ge and Al-Si alloys, *Acta Metallurgica* 34(4) (1986) 661-667.
- [89] S. Xiao, S. Hinderberger, K. Westmacott, U. Dahmen, The effect of twinning on the shapes of cube-cube-related Ge precipitates in Al, *Philosophical Magazine A* 73(5) (1996) 1261-1278.
- [90] U. Dahmen, S.Q. Xiao, S. Paciornik, E. Johnson, A. Johansen, Magic-Size Equilibrium Shapes of Nanoscale Pb Inclusions in Al, *Physical Review Letters* 78(3) (1997) 471-474.
- [91] J.C. Hamilton, F. Léonard, E. Johnson, U. Dahmen, Pb Nanoprecipitates in Al: Magic-Shape Effects due to Elastic Strain, *Physical Review Letters* 98(23) (2007) 236102.
- [92] Q. Yu, L. Qi, T. Tsuru, R. Traylor, D. Rugg, J.W. Morris, M. Asta, D.C. Chrzan, A.M. Minor, Origin of dramatic oxygen solute strengthening effect in titanium, *Science* 347(6222) (2015) 635-639.
- [93] D. Blavette, E. Cadel, A. Fraczkiewicz, A. Menand, Three-Dimensional Atomic-Scale Imaging of Impurity Segregation to Line Defects, *Science* 286(5448) (1999) 2317-2319.
- [94] M. Kuzmina, M. Herbig, D. Ponge, S. Sandlöbes, D. Raabe, Linear complexions: Confined chemical and structural states at dislocations, *Science* 349(6252) (2015) 1080-1083.
- [95] G.P.M. Leyson, W.A. Curtin, L.G. Hector Jr, C.F. Woodward, Quantitative prediction of solute strengthening in aluminium alloys, *Nature materials* 9(9) (2010) 750.
- [96] J. Huang, M. Meyer, V. Pontikis, Is pipe diffusion in metals vacancy controlled? A molecular dynamics study of an edge dislocation in copper, *Physical Review Letters* 63(6) (1989) 628-631.
- [97] M. Legros, G. Dehm, E. Arzt, T.J. Balk, Observation of giant diffusivity along dislocation cores, *Science* 319(5870) (2008) 1646-1649.
- [98] T. Hu, K. Ma, T.D. Topping, J.M. Schoenung, E.J. Lavernia, Precipitation phenomena in an ultrafine-grained Al alloy, *Acta Materialia* 61(6) (2013) 2163-2178.
- [99] C. Liu, S.K. Malladi, Q. Xu, J. Chen, F.D. Tichelaar, X. Zhuge, H.W. Zandbergen, In-situ STEM imaging of growth and phase change of individual CuAl<sub>x</sub> precipitates in Al alloy, *Scientific reports* 7(1) (2017) 2184.
- [100] A. Biswas, D.J. Siegel, C. Wolverton, D.N. Seidman, Precipitates in Al-Cu alloys revisited: Atom-probe tomographic experiments and first-principles calculations of compositional evolution and interfacial segregation, *Acta Materialia* 59(15) (2011) 6187-6204.
- [101] A. Biswas, D.J. Siegel, D.N. Seidman, Simultaneous segregation at coherent and semicoherent heterophase interfaces, *Physical Review Letters* 105(7) (2010) 076102.
- [102] D. Shin, A. Shyam, S. Lee, Y. Yamamoto, J.A. Haynes, Solute segregation at the Al/ $\theta'$ -Al<sub>2</sub>Cu interface in Al-Cu alloys, *Acta Materialia* 141 (2017) 327-340.

- [103] J.D. Boyd, R.B. Nicholson, The coarsening behaviour of  $\theta''$  and  $\theta'$  precipitates in two Al-Cu alloys, *Acta Metallurgica* 19(12) (1971) 1379-1391.
- [104] U. Dahmen, K.H. Westmacott, Ledge structure and the mechanism of  $\theta'$  precipitate growth in Al-Cu, *physica status solidi (a)* 80(1) (1983) 249-262.
- [105] K. Ma, H. Wen, T. Hu, T.D. Topping, D. Isheim, D.N. Seidman, E.J. Lavernia, J.M. Schoenung, Mechanical behavior and strengthening mechanisms in ultrafine grain precipitation-strengthened aluminum alloy, *Acta Materialia* 62 (2014) 141-155.
- [106] Y. Chen, N. Gao, G. Sha, S.P. Ringer, M.J. Starink, Microstructural evolution, strengthening and thermal stability of an ultrafine-grained Al-Cu-Mg alloy, *Acta Materialia* 109 (2016) 202-212.
- [107] K. Ma, T. Hu, H. Yang, T. Topping, A. Yousefiani, E.J. Lavernia, J.M. Schoenung, Coupling of dislocations and precipitates: Impact on the mechanical behavior of ultrafine grained Al-Zn-Mg alloys, *Acta Materialia* 103 (2016) 153-164.
- [108] Y.H. Zhao, X.Z. Liao, S. Cheng, E. Ma, Y.T. Zhu, Simultaneously increasing the ductility and strength of nanostructured alloys, *Advanced Materials* 18(17) (2006) 2280-2283.
- [109] D. Vaughan, Grain boundary precipitation in an Al-Cu alloy, *Acta Metallurgica* 16(4) (1968) 563-577.
- [110] X. Huang, N. Hansen, N. Tsuji, Hardening by Annealing and Softening by Deformation in Nanostructured Metals, *Science* 312(5771) (2006) 249-251.
- [111] N. Kamikawa, X. Huang, N. Tsuji, N. Hansen, Strengthening mechanisms in nanostructured high-purity aluminium deformed to high strain and annealed, *Acta Materialia* 57(14) (2009) 4198-4208.
- [112] P.N.T. Unwin, G.W. Lorimer, R.B. Nicholson, The origin of the grain boundary precipitate free zone, *Acta Metallurgica* 17(11) (1969) 1363-1377.
- [113] D. Simonovic, M.H.F. Sluiter, Impurity diffusion activation energies in Al from first principles, *Physical Review B* 79(5) (2009) 054304.
- [114] M. Mantina, S.L. Shang, Y. Wang, L.Q. Chen, Z.K. Liu, 3d transition metal impurities in aluminum: A first-principles study, *Physical Review B* 80(18) (2009) 184111.
- [115] T. Marlaud, A. Deschamps, F. Bley, W. Lefebvre, B. Baroux, Influence of alloy composition and heat treatment on precipitate composition in Al-Zn-Mg-Cu alloys, *Acta Materialia* 58(1) (2010) 248-260.
- [116] J. Buha, R.N. Lumley, A.G. Crosky, K. Hono, Secondary precipitation in an Al-Mg-Si-Cu alloy, *Acta Materialia* 55(9) (2007) 3015-3024.
- [117] K.S. Kumar, S.A. Brown, J.R. Pickens, Microstructural evolution during ageing of an AlCuLiAgMgZr alloy, *Acta Materialia* 44(5) (1996) 1899-1915.
- [118] A.K. Khan, J.S. Robinson, Effect of cold compression on precipitation and conductivity of an Al-Li-Cu alloy, *Journal of Microscopy* 232(3) (2008) 534-538.
- [119] K. Oh-ishi, K. Edalati, H.S. Kim, K. Hono, Z. Horita, High-pressure torsion for enhanced atomic diffusion and promoting solid-state reactions in the aluminum-copper system, *Acta Materialia* 61(9) (2013) 3482-3489.
- [120] N. Ünlü, B.M. Gable, G.J. Shiflet, E.A. Starke, The effect of cold work on the precipitation of  $\Omega$  and  $\theta'$  in a ternary Al-Cu-Mg alloy, *Metallurgical and Materials Transactions A* 34(12) (2003) 2757-2769.
- [121] M. Murayama, Z. Horita, K. Hono, Microstructure of two-phase Al-1.7 at% Cu alloy deformed by equal-channel angular pressing, *Acta Materialia* 49(1) (2001) 21-29.
- [122] S.C. Wang, M.J. Starink, Two types of S phase precipitates in Al-Cu-Mg alloys, *Acta Materialia* 55(3) (2007) 933-941.
- [123] S. Cheng, Y.H. Zhao, Y.T. Zhu, E. Ma, Optimizing the strength and ductility of fine structured 2024 Al alloy by nano-precipitation, *Acta Materialia* 55(17) (2007) 5822-5832.

- [124] X. Sauvage, N. Enikeev, R. Valiev, Y. Nasedkina, M. Murashkin, Atomic-scale analysis of the segregation and precipitation mechanisms in a severely deformed Al-Mg alloy, *Acta Materialia* 72 (2014) 125-136.
- [125] G. Sha, K. Tugcu, X.Z. Liao, P.W. Trimby, M.Y. Murashkin, R.Z. Valiev, S.P. Ringer, Strength, grain refinement and solute nanostructures of an Al-Mg-Si alloy (AA6060) processed by high-pressure torsion, *Acta Materialia* 63 (2014) 169-179.
- [126] G. Sha, R.K.W. Marceau, X. Gao, B.C. Muddle, S.P. Ringer, Nanostructure of aluminium alloy 2024: Segregation, clustering and precipitation processes, *Acta Materialia* 59(4) (2011) 1659-1670.
- [127] S.-S. Wang, J.-T. Jiang, G.-H. Fan, A.M. Panindre, G.S. Frankel, L. Zhen, Accelerated precipitation and growth of phases in an Al-Zn-Mg-Cu alloy processed by surface abrasion, *Acta Materialia* 131 (2017) 233-245.
- [128] C. Flament, J. Ribis, J. Garnier, Y. Serruys, F. Leprêtre, A. Gentils, C. Baumier, M. Descoins, D. Mangelinck, A. Lopez, K. Colas, K. Buchanan, P. Donnadieu, A. Deschamps, Stability of  $\beta''$  nano-phases in Al-Mg-Si(-Cu) alloy under high dose ion irradiation, *Acta Materialia* 128 (2017) 64-76.
- [129] C.B. Fuller, D.N. Seidman, D.C. Dunand, Mechanical properties of Al(Sc,Zr) alloys at ambient and elevated temperatures, *Acta Materialia* 51(16) (2003) 4803-4814.
- [130] S. Jiang, H. Wang, Y. Wu, X. Liu, H. Chen, M. Yao, B. Gault, D. Ponge, D. Raabe, A. Hirata, Ultrastrong steel via minimal lattice misfit and high-density nanoprecipitation, *Nature* 544(7651) (2017) 460-464.
- [131] C.B. Fuller, J.L. Murray, D.N. Seidman, Temporal evolution of the nanostructure of Al(Sc,Zr) alloys: Part I – Chemical compositions of  $\text{Al}_3(\text{Sc}_{1-x}\text{Zr}_x)$  precipitates, *Acta Materialia* 53(20) (2005) 5401-5413.
- [132] E. Clouet, L. Laé, T. Épicier, W. Lefebvre, M. Nastar, A. Deschamps, Complex precipitation pathways in multicomponent alloys, *Nature materials* 5(6) (2006) 482-488.
- [133] T. Saito, F.J.H. Ehlers, W. Lefebvre, D. Hernandez-Maldonado, R. Bjørge, C.D. Marioara, S.J. Andersen, E.A. Mørtzell, R. Holmestad, Cu atoms suppress misfit dislocations at the  $\beta''$ /Al interface in Al-Mg-Si alloys, *Scripta Materialia* 110 (2016) 6-9.
- [134] M.W. Zandbergen, A. Cerezo, G.D.W. Smith, Study of precipitation in Al-Mg-Si Alloys by atom probe tomography II. Influence of Cu additions, *Acta Materialia* 101 (2015) 149-158.
- [135] D.J. Chakrabarti, D.E. Laughlin, Phase relations and precipitation in Al-Mg-Si alloys with Cu additions, *Progress in Materials Science* 49(3) (2004) 389-410.
- [136] D.A. Muller, Structure and bonding at the atomic scale by scanning transmission electron microscopy, *Nature Materials* 8 (2009) 263-270.
- [137] <http://www.jems-saas.ch/Home/documentation.htm>.
- [138] J.M. LeBeau, S.D. Findlay, L.J. Allen, S. Stemmer, Position averaged convergent beam electron diffraction: Theory and applications, *Ultramicroscopy* 110(2) (2010) 118-125.
- [139] D. Sholl, J.A. Steckel, *Density functional theory: a practical introduction*, John Wiley 2011.
- [140] P.-O. Löwdin, Quantum theory of many-particle systems. III. Extension of the Hartree-Fock scheme to include degenerate systems and correlation effects, *Physical review* 97(6) (1955) 1509.
- [141] E. Wigner, On the interaction of electrons in metals, *Physical Review* 46(11) (1934) 1002.
- [142] P. Hohenberg, W. Kohn, Inhomogeneous electron gas, *Physical review* 136(3B) (1964) B864.
- [143] W. Kohn, L.J. Sham, Self-consistent equations including exchange and correlation effects, *Physical review* 140(4A) (1965) A1133.
- [144] D.M. Ceperley, B. Alder, Ground state of the electron gas by a stochastic method, *Physical Review Letters* 45(7) (1980) 566.

- [145] C. Stampfl, W. Mannstadt, R. Asahi, A.J. Freeman, Electronic structure and physical properties of early transition metal mononitrides: Density-functional theory LDA, GGA, and screened-exchange LDA FLAPW calculations, *Physical Review B* 63(15) (2001) 155106.
- [146] C. Wolverton, V. Ozoliņš, First-principles aluminum database: Energetics of binary Al alloys and compounds, *Physical Review B* 73(14) (2006) 144104.
- [147] G. Kresse, D. Joubert, From ultrasoft pseudopotentials to the projector augmented-wave method, *Physical Review B* 59(3) (1999) 1758.
- [148] J.P. Perdew, K. Burke, M. Ernzerhof, Generalized Gradient Approximation Made Simple, *Physical Review Letters* 77(18) (1996) 3865-3868.
- [149] K. Lejaeghere, G. Bihlmayer, T. Björkman, P. Blaha, S. Blügel, V. Blum, D. Caliste, I.E. Castelli, S.J. Clark, A. Dal Corso, S. de Gironcoli, T. Deutsch, J.K. Dewhurst, I. Di Marco, C. Draxl, M. Dułak, O. Eriksson, J.A. Flores-Livas, K.F. Garrity, L. Genovese, P. Giannozzi, M. Giantomassi, S. Goedecker, X. Gonze, O. Grånäs, E.K.U. Gross, A. Gulans, F. Gygi, D.R. Hamann, P.J. Hasnip, N.A.W. Holzwarth, D. Iuşan, D.B. Jochym, F. Jollet, D. Jones, G. Kresse, K. Koepf, E. Küçükbenli, Y.O. Kvashnin, I.L.M. Loch, S. Lubeck, M. Marsman, N. Marzari, U. Nitzsche, L. Nordström, T. Ozaki, L. Paulatto, C.J. Pickard, W. Poelmans, M.I.J. Probert, K. Refson, M. Richter, G.-M. Rignanese, S. Saha, M. Scheffler, M. Schlipf, K. Schwarz, S. Sharma, F. Tavazza, P. Thunström, A. Tkatchenko, M. Torrent, D. Vanderbilt, M.J. van Setten, V. Van Speybroeck, J.M. Wills, J.R. Yates, G.-X. Zhang, S. Cottenier, Reproducibility in density functional theory calculations of solids, *Science* 351(6280) (2016).
- [150] M. Methfessel, A. Paxton, High-precision sampling for Brillouin-zone integration in metals, *Physical Review B* 40(6) (1989) 3616.
- [151] P.E. Blöchl, O. Jepsen, O.K. Andersen, Improved tetrahedron method for Brillouin-zone integrations, *Physical Review B* 49(23) (1994) 16223.
- [152] V. Vaithyanathan, C. Wolverton, L.Q. Chen, Multiscale modeling of  $\theta'$  precipitation in Al-Cu binary alloys, *Acta Materialia* 52(10) (2004) 2973-2987.
- [153] Y. Wang, Z.K. Liu, L.Q. Chen, C. Wolverton, First-principles calculations of  $\beta''$ -Mg<sub>5</sub>Si<sub>6</sub>/ $\alpha$ -Al interfaces, *Acta Materialia* 55(17) (2007) 5934-5947.
- [154] Y.Z. Ji, A. Issa, T.W. Heo, J.E. Saal, C. Wolverton, L.Q. Chen, Predicting  $\beta'$  precipitate morphology and evolution in Mg-RE alloys using a combination of first-principles calculations and phase-field modeling, *Acta Materialia* 76 (2014) 259-271.
- [155] A. Issa, J.E. Saal, C. Wolverton, Formation of high-strength  $\beta'$  precipitates in Mg-RE alloys: The role of the Mg/ $\beta''$  interfacial instability, *Acta Materialia* 83 (2015) 75-83.
- [156] J.L. Murray, The aluminium-copper system, *International Metals Reviews* 30(1) (1985) 211-234.
- [157] I.J. Polmear, Role of Trace Elements in Aged Aluminium-Alloys, *Materials Science Forum* (1987) 195-214.
- [158] J.F. Nie, B.C. Muddle, Strengthening of an Al-Cu-Sn alloy by deformation-resistant precipitate plates, *Acta Materialia* 56(14) (2008) 3490-3501.
- [159] M.S. Shur, Handbook series on semiconductor parameters, World Scientific 1996.
- [160] J. Donohue, Structures of the Elements John Wiley 1974.
- [161] M. Losurdo, A. Suvorova, S. Rubanov, K. Hingerl, A.S. Brown, Thermally stable coexistence of liquid and solid phases in gallium nanoparticles, *Nature materials* 15(9) (2016) 995-1002.
- [162] S. Pogatscher, E. Kozeschnik, H. Antrekowitsch, M. Werinos, S.S.A. Gerstl, J.F. Löffler, P.J. Uggowitzer, Process-controlled suppression of natural ageing in an Al-Mg-Si alloy, *Scripta Materialia* 89 (2014) 53-56.
- [163] A. Van der Ven, G. Ceder, First Principles Calculation of the Interdiffusion Coefficient in Binary Alloys, *Physical Review Letters* 94(4) (2005) 045901.

- [164] M. Werinos, H. Antrekowitsch, E. Kozeschnik, T. Ebner, F. Moszner, J.F. Löffler, P.J. Uggowitzer, S. Pogatscher, Ultrafast artificial ageing of Al-Mg-Si alloys, *Scripta Materialia* 112 (2016) 148-151.
- [165] J. Hamilton, F. Leonard, E. Johnson, U. Dahmen, Pb nanoprecipitates in Al: Magic-shape effects due to elastic strain, *Physical review letters* 98(23) (2007) 236102.
- [166] R. Tran, Z. Xu, D.W. Balachandran Radhakrishnan, W. Sun, K.A. Persson, S.P. Ong, Surface energies of elemental crystals, *Scientific Data* 3 (2016).
- [167] E. Marquis, D. Seidman, M. Asta, C. Woodward, V. Ozoliņš, Mg Segregation at Al/Al<sub>3</sub>Sc Heterophase Interfaces on an Atomic Scale: Experiments and Computations, *Physical review letters* 91(3) (2003) 036101.
- [168] B. Chen, G. Liu, R. Wang, J. Zhang, L. Jiang, J. Song, J. Sun, Effect of interfacial solute segregation on ductile fracture of Al-Cu-Sc alloys, *Acta Materialia* 61(5) (2013) 1676-1690.
- [169] H. Aaronson, J. Clark, C. Laird, Interfacial energy of dislocation and of coherent interphase boundaries, *Metal Science Journal* 2(1) (1968) 155-158.
- [170] A. Kiselev, F. Bachmann, P. Pedevilla, S.J. Cox, A. Michaelides, D. Gerthsen, T. Leisner, Active sites in heterogeneous ice nucleation—the example of K-rich feldspars, *Science* 355(6323) (2016) 367-371.
- [171] G. Hood, R. Schultz, Indium diffusion in aluminum, *Physical Review B* 4(8) (1971) 2339.
- [172] N. Peterson, S. Rothman, Impurity diffusion in aluminum, *Physical Review B* 1(8) (1970) 3264.
- [173] Y. Du, Y. Chang, B. Huang, W. Gong, Z. Jin, H. Xu, Z. Yuan, Y. Liu, Y. He, F.-Y. Xie, Diffusion coefficients of some solutes in fcc and liquid Al: critical evaluation and correlation, *Materials Science and Engineering: A* 363(1) (2003) 140-151.
- [174] J. Zhang, Y. Tang, K. Lee, M. Ouyang, Nonepitaxial growth of hybrid core-shell nanostructures with large lattice mismatches, *Science* 327(5973) (2010) 1634-1638.
- [175] J. Lee, J. Yang, S.G. Kwon, T. Hyeon, Nonclassical nucleation and growth of inorganic nanoparticles, *Nature Reviews Materials* 1 (2016) 16034.
- [176] R. Yoshimura, T.J. Konno, E. Abe, K. Hiraga, Transmission electron microscopy study of the evolution of precipitates in aged Al-Li-Cu alloys: the  $\theta'$  and T<sub>1</sub> phases, *Acta Materialia* 51(14) (2003) 4251-4266.
- [177] G.R. Hugo, B.C. Muddle, The morphology of precipitates in an Al-Ge Alloy-I. experimental observations, *Acta Metallurgica et Materialia* 38(2) (1990) 351-363.
- [178] S. Hinderberger, S.-Q. Xiao, K. Westmacott, U. Dahmen, Effect of pre-ageing on the evolution of Ge precipitates in an Al-1.8 at.% Ge alloy, *Zeitschrift für Metallkunde* 87(3) (1996) 161-169.
- [179] A.H. Committee, Alloy and Temper Designation Systems for Aluminum and Aluminum Alloys, ASM Handbook 1990.
- [180] A.H. Committee, Heat Treating of Aluminum Alloys ASM Handbook 1991.
- [181] J.E. Saal, C. Wolverton, Thermodynamic stability of Mg-based ternary long-period stacking ordered structures, *Acta Materialia* 68 (2014) 325-338.
- [182] A.R. Natarajan, A. Van der Ven, A unified description of ordering in HCP Mg-RE alloys, *Acta Materialia* 124 (2017) 620-632.
- [183] M.X. Zhang, P.M. Kelly, M. Qian, J.A. Taylor, Crystallography of grain refinement in Mg-Al based alloys, *Acta Materialia* 53(11) (2005) 3261-3270.
- [184] M.-X. Zhang, P.M. Kelly, Crystallographic features of phase transformations in solids, *Progress in Materials Science* 54(8) (2009) 1101-1170.
- [185] F. Wang, D. Qiu, Z.-L. Liu, J.A. Taylor, M.A. Easton, M.-X. Zhang, The grain refinement mechanism of cast aluminium by zirconium, *Acta Materialia* 61(15) (2013) 5636-5645.

- [186] K. Kim, B.-C. Zhou, C. Wolverton, Interfacial stability of  $\theta'$ /Al in Al-Cu alloys, *Scripta Materialia* 159 (2019) 99-103.
- [187] S. Alexander, J. McTague, Should All Crystals Be bcc? Landau Theory of Solidification and Crystal Nucleation, *Physical Review Letters* 41(10) (1978) 702-705.
- [188] S. Auer, D. Frenkel, Prediction of absolute crystal-nucleation rate in hard-sphere colloids, *Nature* 409(6823) (2001) 1020.
- [189] P.R. ten Wolde, M.J. Ruiz-Montero, D. Frenkel, Numerical Evidence for bcc Ordering at the Surface of a Critical fcc Nucleus, *Physical Review Letters* 75(14) (1995) 2714-2717.
- [190] G. Grimvall, B. Magyari-Köpe, V. Ozoliņš, K.A. Persson, Lattice instabilities in metallic elements, *Reviews of Modern Physics* 84(2) (2012) 945-986.
- [191] J. Bhattacharya, A. Van der Ven, Mechanical instabilities and structural phase transitions: The cubic to tetragonal transformation, *Acta Materialia* 56(16) (2008) 4226-4232.
- [192] A. Togo, I. Tanaka, First principles phonon calculations in materials science, *Scripta Materialia* 108 (2015) 1-5.
- [193] Z. Yu, P.R. Cantwell, Q. Gao, D. Yin, Y. Zhang, N. Zhou, G.S. Rohrer, M. Widom, J. Luo, M.P. Harmer, Segregation-induced ordered superstructures at general grain boundaries in a nickel-bismuth alloy, *Science* 358(6359) (2017) 97-101.
- [194] C. Liu, H. Chen, J.-F. Nie, Interphase boundary segregation of Zn in Mg-Sn-Zn alloys, *Scripta Materialia* 123 (2016) 5-8.
- [195] M. El-Boragy, R. Szepan, K. Schubert, Kristallstruktur von  $\text{Cu}_3\text{Al}_2^+$  (h) und  $\text{CuAl}$  (r), *Journal of the Less Common Metals* 29(2) (1972) 133-140.
- [196] C.V. Singh, D.H. Warner, Mechanisms of Guinier-Preston zone hardening in the athermal limit, *Acta Materialia* 58(17) (2010) 5797-5805.
- [197] V. Yamakov, D. Wolf, S. Phillpot, A. Mukherjee, H. Gleiter, Deformation-mechanism map for nanocrystalline metals by molecular-dynamics simulation, *Nature materials* 3(1) (2004) 43.
- [198] C. Liu, Z. Ma, P. Ma, L. Zhan, M. Huang, Multiple precipitation reactions and formation of  $\theta'$ -phase in a pre-deformed Al-Cu alloy, *Materials Science and Engineering: A* 733 (2018) 28-38.
- [199] C. Ravi, C. Wolverton, First-principles study of crystal structure and stability of Al-Mg-Si-(Cu) precipitates, *Acta Materialia* 52(14) (2004) 4213-4227.
- [200] A. Bobel, K. Kim, C. Wolverton, M. Walker, G.B. Olson, Equilibrium composition variation of Q-phase precipitates in aluminum alloys, *Acta Materialia* 138 (2017) 150-160.
- [201] K. Kelton, A.L. Greer, *Nucleation in condensed matter: applications in materials and biology*, Elsevier 2010.
- [202] Hubert I. Aaronson, Masato Enomoto, J.K. Lee, *Mechanisms of Diffusional Phase Transformations in Metals and Alloys*, CRC Press 2010.
- [203] E.A. Marquis, D.N. Seidman, M. Asta, C. Woodward, V. Ozoliņš, Mg Segregation at  $\text{Al}_3\text{Sc}$  Heterophase Interfaces on an Atomic Scale: Experiments and Computations, *Physical Review Letters* 91(3) (2003) 036101.
- [204] W.M. Stobbs, G.R. Purdy, The elastic accommodation of semicoherent  $\theta'$  in Al-4wt.%Cu alloy, *Acta Metallurgica* 26(7) (1978) 1069-1081.
- [205] J. Turley, G. Sines, The anisotropy of Young's modulus, shear modulus and Poisson's ratio in cubic materials, *Journal of Physics D: Applied Physics* 4(2) (1971) 264.
- [206] R.H. Baughman, J.M. Shacklette, A.A. Zakhidov, S. Stafström, Negative Poisson's ratios as a common feature of cubic metals, *Nature* 392 (1998) 362-365.
- [207] P.N. Nakashima, A.E. Smith, J. Etheridge, B.C. Muddle, The bonding electron density in aluminum, *Science* 331(6024) (2011) 1583-1586.
- [208] S. Hu, M. Baskes, M. Stan, L. Chen, Atomistic calculations of interfacial energies, nucleus shape and size of  $\theta'$  precipitates in Al-Cu alloys, *Acta materialia* 54(18) (2006) 4699-4707.

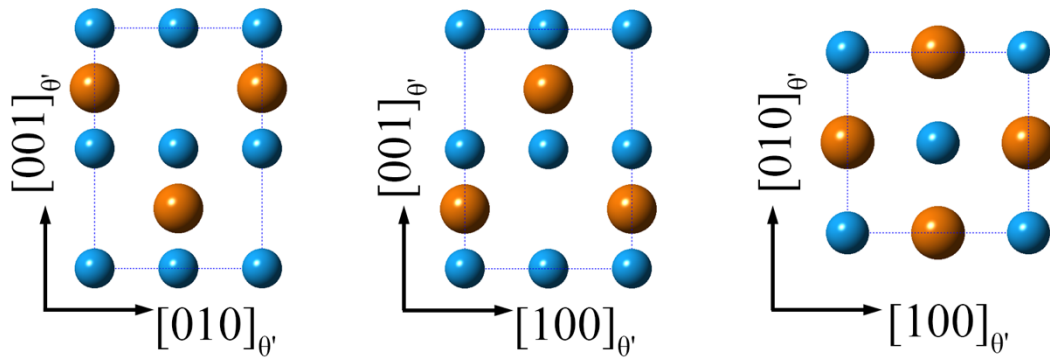
- [209] T. Gödecke, F. Sommer, Solidification behaviour of the Al<sub>2</sub>Cu phase, *Zeitschrift für Metallkunde* 87(7) (1996) 581-586.
- [210] V. Yamakov, D. Wolf, S.R. Phillpot, A.K. Mukherjee, H. Gleiter, Dislocation processes in the deformation of nanocrystalline aluminium by molecular-dynamics simulation, *Nature materials* 1(1) (2002) 45.
- [211] M. Mantina, S. Shang, Y. Wang, L. Chen, Z. Liu, 3 d transition metal impurities in aluminum: a first-principles study, *Physical Review B* 80(18) (2009) 184111.
- [212] R. Le Hazif, J.-P. Poirer, Cross-slip on {110} planes in aluminum single crystals compressed along <100> axis, *Acta Metallurgica* 23(7) (1975) 865-871.
- [213] C. Woodward, D.R. Trinkle, L.G. Hector, D.L. Olmsted, Prediction of Dislocation Cores in Aluminum from Density Functional Theory, *Physical Review Letters* 100(4) (2008) 045507.
- [214] J. Baumgartner, A. Dey, P.H. Bomans, C. Le Coadou, P. Fratzl, N.A. Sommerdijk, D. Faivre, Nucleation and growth of magnetite from solution, *Nature materials* 12(4) (2013) 310-314.
- [215] Y. Diao, T. Harada, A.S. Myerson, T.A. Hatton, B.L. Trout, The role of nanopore shape in surface-induced crystallization, *Nature materials* 10(11) (2011) 867.

# Appendix 1

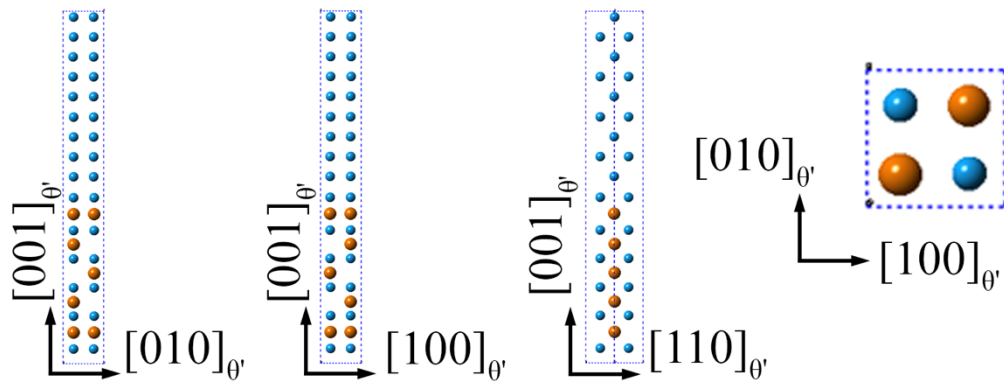
## Atomic models used in Chapter 5

Supercells for Table 5.2

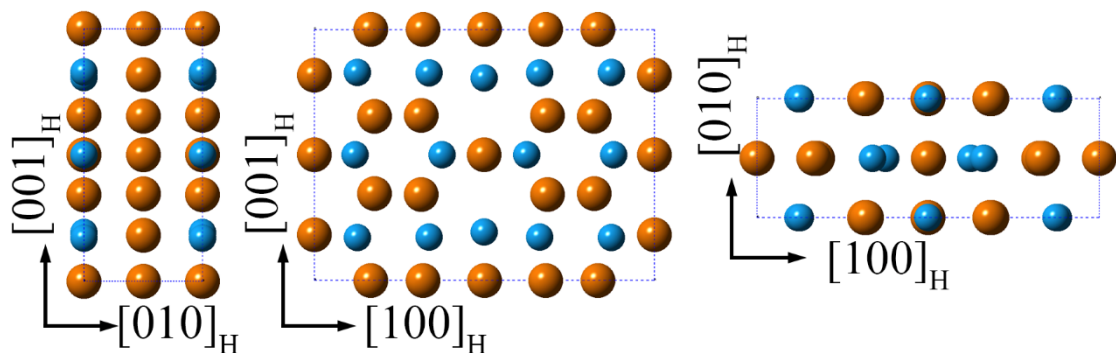
1.  $\theta'$  (after DFT relaxation)



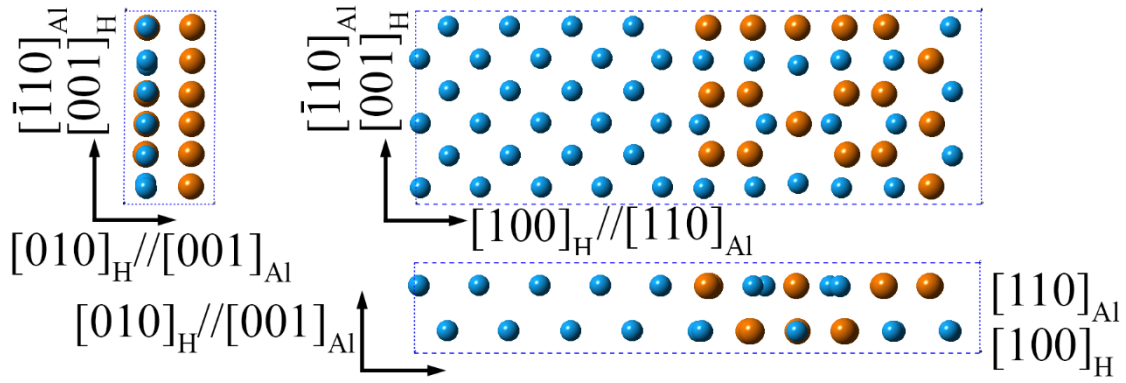
2.  $\theta'$  (embedded, after DFT relaxation)



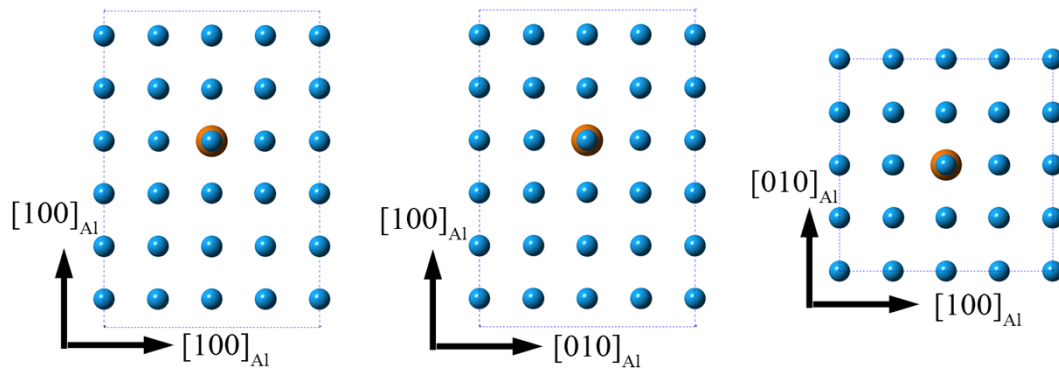
3. H (after DFT relaxation)



4. H (embedded, after DFT relaxation)

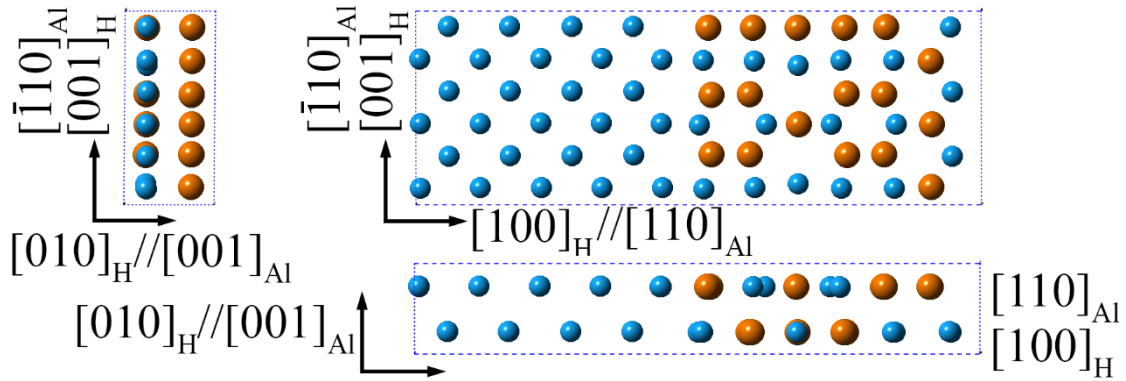


5. A Cu atom in the FCC lattice of Al with 47 Al atoms (Al-2.1at.%Cu, to approximate the Al-1.7at.%Cu solid solution).

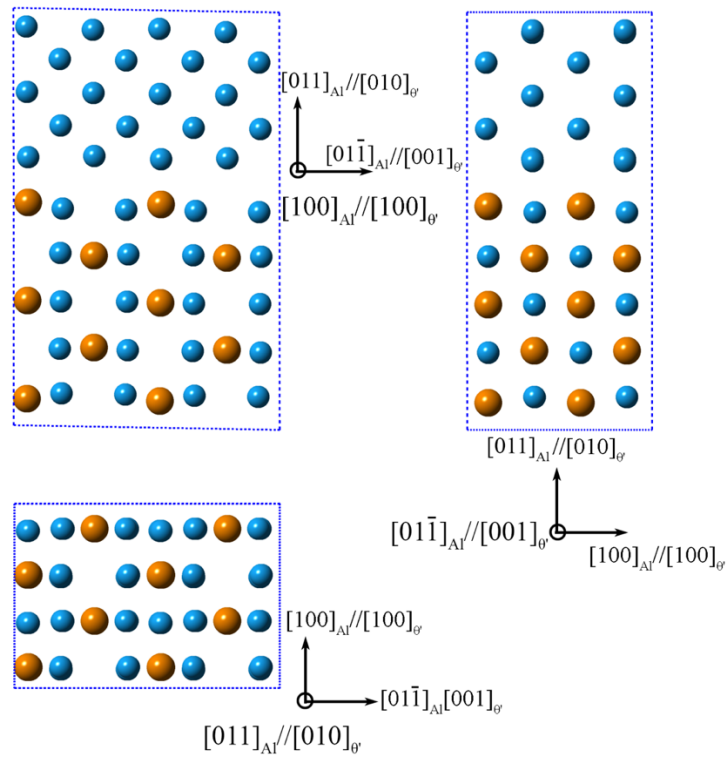


Supercells for Fig. 5.22

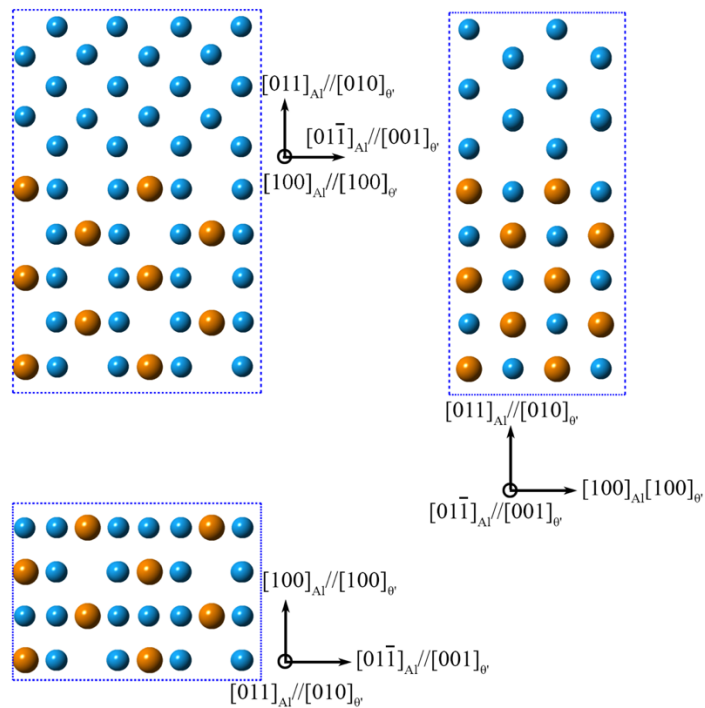
6. The H/Al coherent interface (two interfaces in the model are non-equivalent)



7. The first possible atomic model of the direct interface between the Al matrix and a  $\theta'$  type III precipitate (the same to Fig. 5.20 (a)).



8. The second possible atomic model of the direct interface between the Al matrix and a  $\theta'$  type III precipitate (the same to Fig. 5.20 (b)).

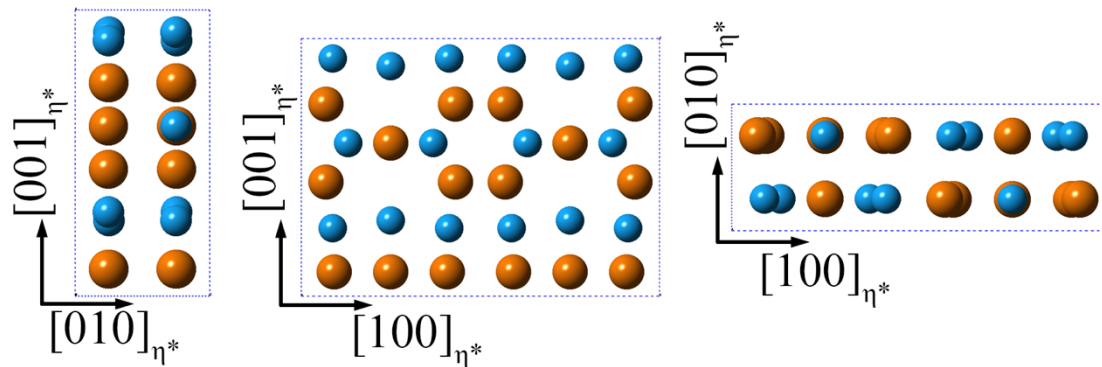


# Appendix 2

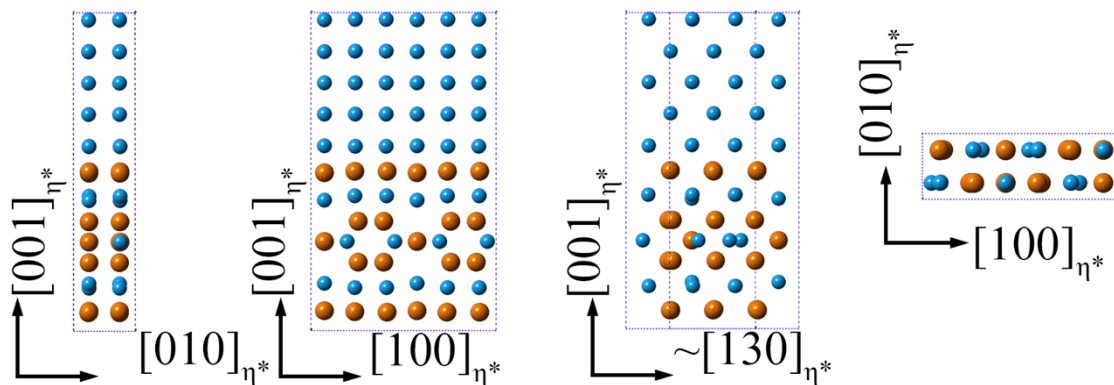
## Atomic models used in Chapter 6

Supercell cells for Table 6.2 (After DFT relaxation)

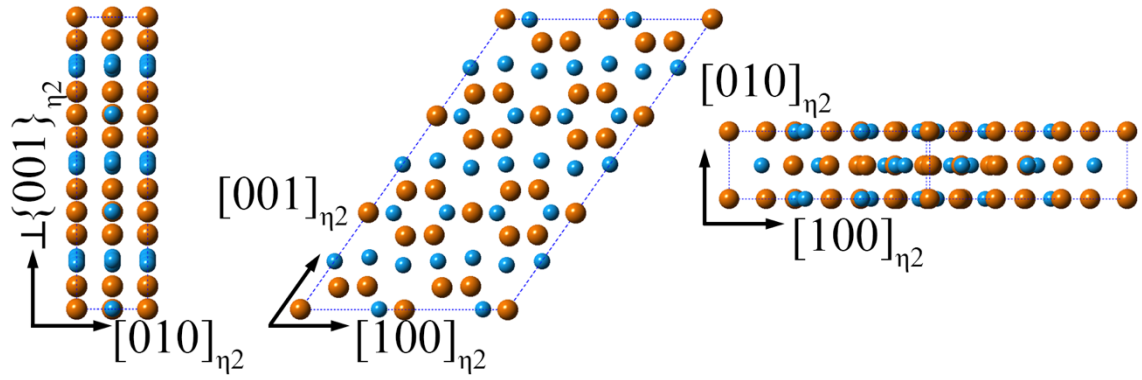
1.  $\eta^*$  (No defects)



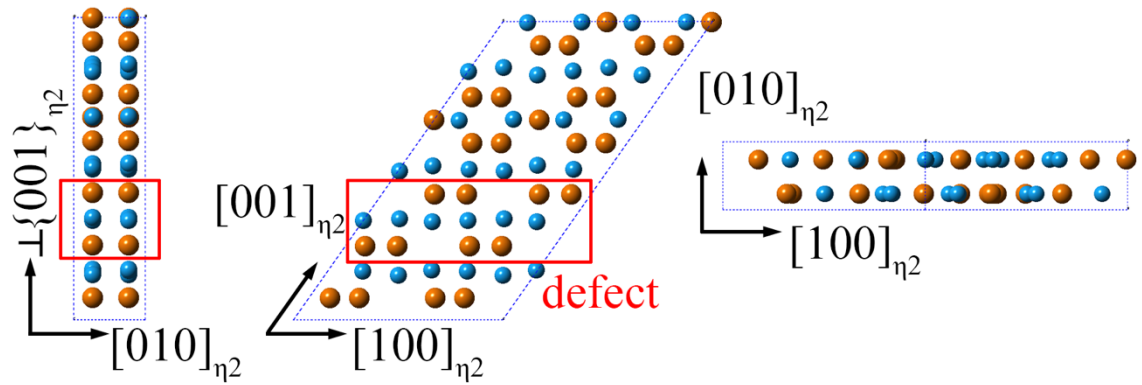
2.  $\eta^*$  (No defect, embedded) viewed along  $[100]_{Al}$ ,  $[010]_{Al}$ ,  $[110]_{Al}$  and  $[001]_{Al}$ .



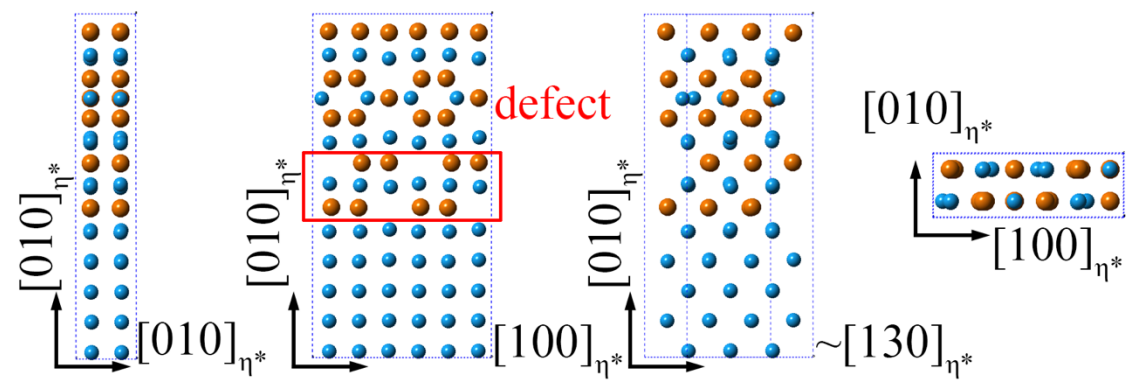
3.  $\eta_2$  (after DFT relaxation)



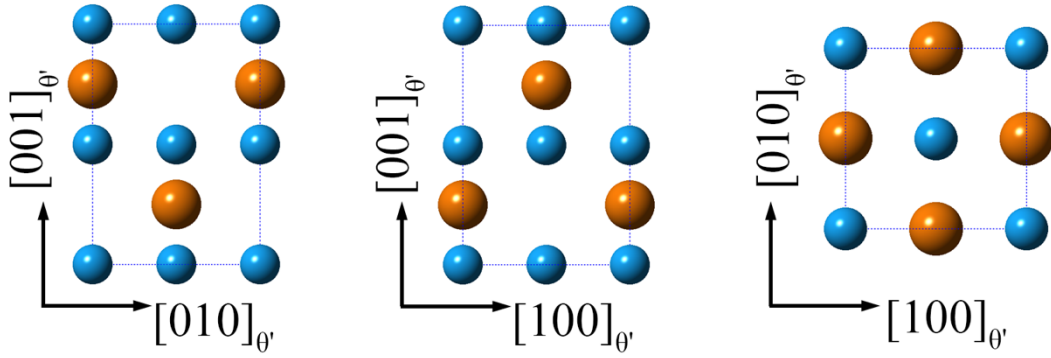
4.  $\eta^*$  (Defect inside, after DFT relaxation)



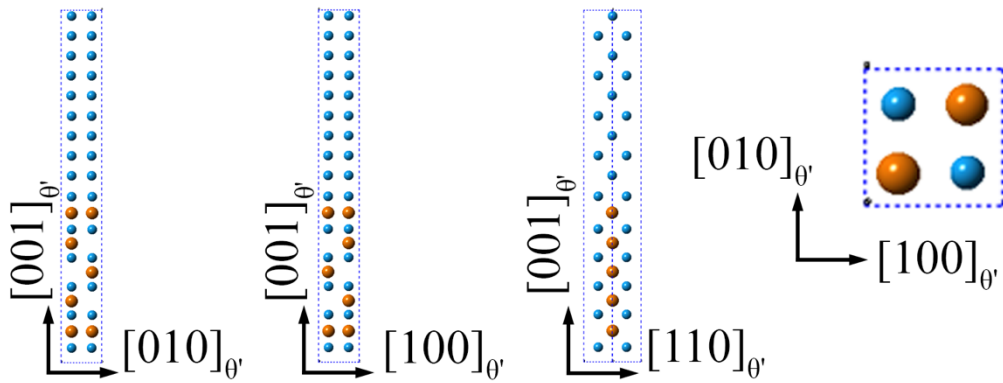
5.  $\eta^*$  with defect embedded (after relaxation) viewed along  $[100]_{Al}$ ,  $[010]_{Al}$ ,  $[110]_{Al}$  and  $[001]_{Al}$ .



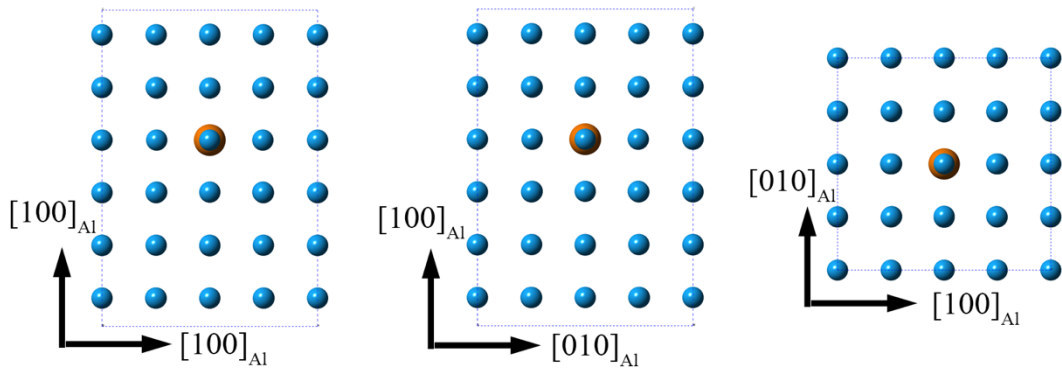
6.  $\theta'$  (after DFT relaxation)



7.  $\theta'$  (embed, after DFT relaxation) viewed along  $[100]_{Al}$ ,  $[010]_{Al}$ ,  $[110]_{Al}$  and  $[001]_{Al}$ .

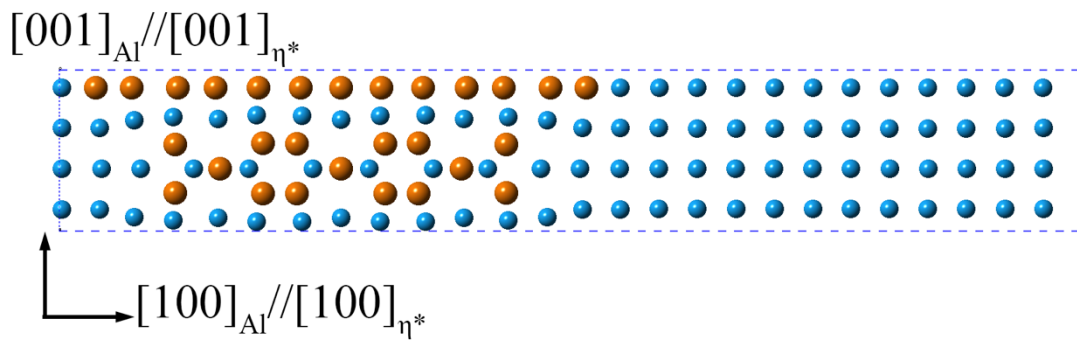


8. 1 Cu atom in the FCC lattice of Al with 47 Al atoms (Al-2.1at.%Cu, to approximate the Al-1.7at.%Cu solid solution).

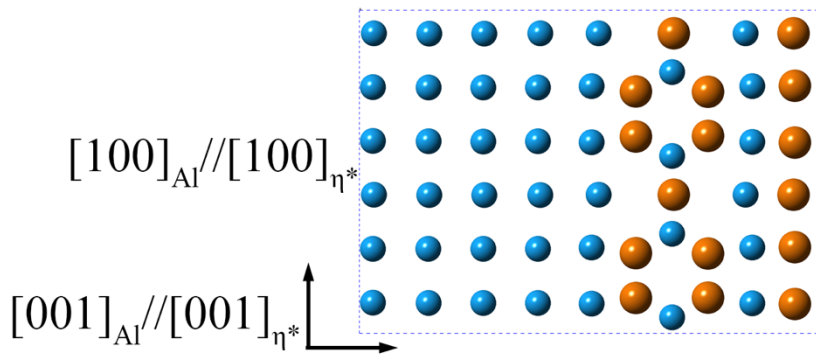


Atomic models for different interfacial structures in Fig. 6.15

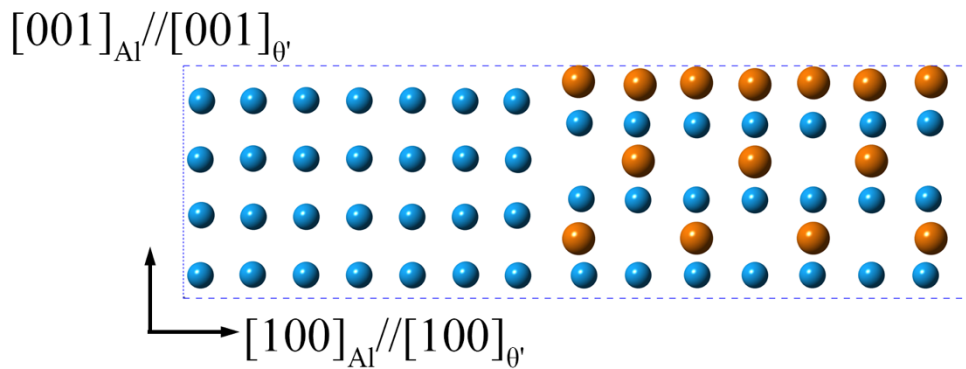
1. The  $\eta^*/Al$  semi-coherent interface



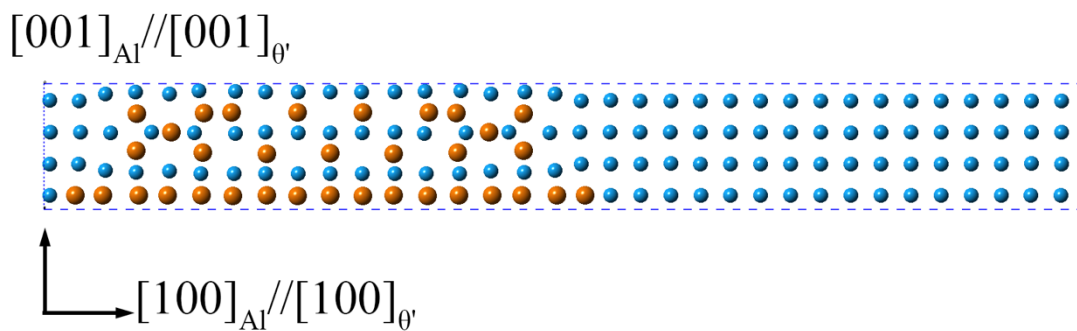
2. The  $\eta^*/\text{Al}$  coherent interface (two interfaces in the model are non-equivalent)



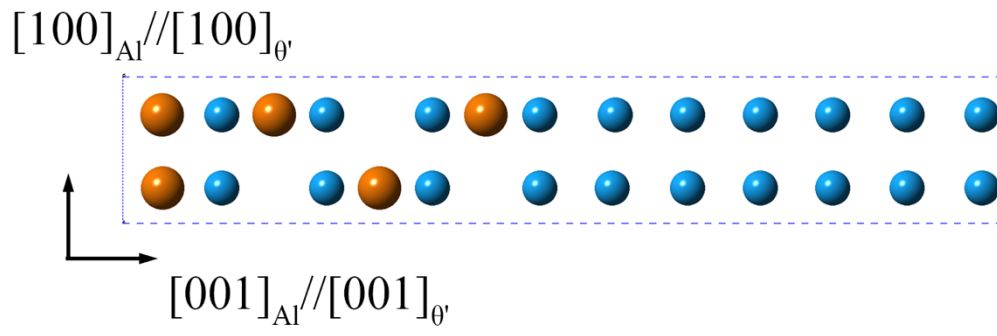
3. The  $\theta'/\text{Al}$  semi-coherent interface (rarely observed in experiments)



4. The  $\eta^*$  decorated  $\theta'/\text{Al}$  semi-coherent interface (widely observed in experiments)



5. The  $\theta'/\text{Al}$  coherent interface (two interfaces in the model are non-equivalent)



## Appendix 3

# CIF files for the newly-reported Cu-rich precipitates

1. CIF file for the H phase on  $\{110\}_{Al}$  (After DFT relaxation)

```

=====
# CRYSTAL DATA
#-----

data_VESTA_phase_1

_chemical_name_common          'POSCAR'
_cell_length_a                 11.85837
_cell_length_b                 4.11264
_cell_length_c                 8.74840
_cell_angle_alpha              90
_cell_angle_beta               90
_cell_angle_gamma              90
_space_group_name_H-M_alt      'P 1'
_space_group_IT_number         1

loop_
_space_group_symop_operation_xyz
  'x, y, z'

loop_
_atom_site_label
_atom_site_occupancy
_atom_site_fract_x
_atom_site_fract_y
_atom_site_fract_z
_atom_site_adp_type
_atom_site_B_iso_or_equiv
_atom_site_type_symbol
Al1      1.0  0.126554  0.000000  0.170176  Biso 1.000000 Al
Al2      1.0  0.336828  0.500000  0.172783  Biso 1.000000 Al
Al3      1.0  0.499992 -0.000000  0.192774  Biso 1.000000 Al

```

Al4	1.0	0.120472	0.000000	0.500000	Biso	1.000000	Al
Al5	1.0	0.375417	0.500000	0.500000	Biso	1.000000	Al
Al6	1.0	0.873432	-0.000000	0.170177	Biso	1.000000	Al
Al7	1.0	0.663164	0.500000	0.172785	Biso	1.000000	Al
Al8	1.0	0.879522	0.000000	0.500000	Biso	1.000000	Al
Al9	1.0	0.624569	0.500000	0.500000	Biso	1.000000	Al
Al10	1.0	0.126554	0.000000	0.829824	Biso	1.000000	Al
Al11	1.0	0.336828	0.500000	0.827217	Biso	1.000000	Al
Al12	1.0	0.499992	0.000000	0.807226	Biso	1.000000	Al
Al13	1.0	0.873432	0.000000	0.829823	Biso	1.000000	Al
Al14	1.0	0.663164	0.500000	0.827215	Biso	1.000000	Al
Cu1	1.0	0.000002	0.500000	0.181787	Biso	1.000000	Cu
Cu2	1.0	0.000002	0.500000	0.818213	Biso	1.000000	Cu
Cu3	1.0	0.177568	0.500000	0.346241	Biso	1.000000	Cu
Cu4	1.0	0.314428	0.000000	0.342867	Biso	1.000000	Cu
Cu5	1.0	0.499987	0.000000	0.500000	Biso	1.000000	Cu
Cu6	1.0	0.822400	0.500000	0.346238	Biso	1.000000	Cu
Cu7	1.0	0.685562	-0.000000	0.342866	Biso	1.000000	Cu
Cu8	1.0	0.000008	0.500000	0.500000	Biso	1.000000	Cu
Cu9	1.0	0.166518	0.500000	0.000000	Biso	1.000000	Cu
Cu10	1.0	0.319381	0.000000	0.000000	Biso	1.000000	Cu
Cu11	1.0	0.500001	0.500000	0.000000	Biso	1.000000	Cu
Cu12	1.0	0.177568	0.500000	0.653759	Biso	1.000000	Cu
Cu13	1.0	0.314428	-0.000000	0.657133	Biso	1.000000	Cu
Cu14	1.0	0.680605	0.000000	0.000000	Biso	1.000000	Cu
Cu15	1.0	0.833459	0.500000	0.000000	Biso	1.000000	Cu
Cu16	1.0	0.822400	0.500000	0.653762	Biso	1.000000	Cu
Cu17	1.0	0.685562	0.000000	0.657134	Biso	1.000000	Cu

2. CIF file for the  $\eta^*$  phase on  $\{100\}_{Al}$  (No defects inside, after DFT relaxation).

```

=====
#-----
# CRYSTAL DATA
#-----
data_eta
_chemical_name_common      'etalone'
_cell_length_a              12.16693
_cell_length_b              8.79366
_cell_length_c              4.13582
_cell_angle_alpha           90
_cell_angle_beta            90.00201
_cell_angle_gamma           90
_space_group_name_H-M_alt   'P 1'
_space_group_IT_number      1
loop_
_space_group_symop_operation_xyz
  'x, y, z'
loop_
_atom_site_label
_atom_site_occupancy
_atom_site_fract_x

```

	_atom_site_fract_y	_atom_site_fract_z	_atom_site_adp_type	_atom_site_B_iso_or_equiv	_atom_site_type_symbol
Al1	1.0	0.912803	0.264401	0.250249	Biso 1.000000 Al
Al2	1.0	0.087197	0.264401	0.749751	Biso 1.000000 Al
Al3	1.0	0.250015	0.294467	0.249752	Biso 1.000000 Al
Al4	1.0	0.869020	0.593757	0.250076	Biso 1.000000 Al
Al5	1.0	0.130980	0.593757	0.749924	Biso 1.000000 Al
Al6	1.0	0.749985	0.294467	0.750248	Biso 1.000000 Al
Al7	1.0	0.587312	0.264524	0.250170	Biso 1.000000 Al
Al8	1.0	0.412688	0.264524	0.749830	Biso 1.000000 Al
Al9	1.0	0.630955	0.593799	0.250121	Biso 1.000000 Al
Al10	1.0	0.369045	0.593799	0.749879	Biso 1.000000 Al
Al11	1.0	0.912758	0.922970	0.250231	Biso 1.000000 Al
Al12	1.0	0.087242	0.922970	0.749769	Biso 1.000000 Al
Al13	1.0	0.250018	0.893001	0.249755	Biso 1.000000 Al
Al14	1.0	0.749982	0.893001	0.750245	Biso 1.000000 Al
Al15	1.0	0.587355	0.922957	0.250159	Biso 1.000000 Al
Al16	1.0	0.412645	0.922957	0.749841	Biso 1.000000 Al
Cu1	1.0	0.930931	0.442825	0.750101	Biso 1.000000 Cu
Cu2	1.0	0.069069	0.442825	0.249899	Biso 1.000000 Cu
Cu3	1.0	0.249986	0.593775	0.249865	Biso 1.000000 Cu
Cu4	1.0	0.569078	0.442893	0.750091	Biso 1.000000 Cu
Cu5	1.0	0.430922	0.442893	0.249909	Biso 1.000000 Cu
Cu6	1.0	0.750014	0.593775	0.750135	Biso 1.000000 Cu
Cu7	1.0	0.907618	0.093602	0.750356	Biso 1.000000 Cu
Cu8	1.0	0.092382	0.093602	0.249644	Biso 1.000000 Cu
Cu9	1.0	0.249959	0.093840	0.749740	Biso 1.000000 Cu
Cu10	1.0	0.930892	0.744670	0.750096	Biso 1.000000 Cu
Cu11	1.0	0.069108	0.744670	0.249904	Biso 1.000000 Cu
Cu12	1.0	0.750041	0.093840	0.250260	Biso 1.000000 Cu
Cu13	1.0	0.407961	0.093670	0.249826	Biso 1.000000 Cu
Cu14	1.0	0.592039	0.093670	0.750174	Biso 1.000000 Cu
Cu15	1.0	0.569125	0.744748	0.750086	Biso 1.000000 Cu
Cu16	1.0	0.430875	0.744748	0.249914	Biso 1.000000 Cu

3. CIF file for the  $\eta^*$  phase on  $\{100\}_{Al}$  (defects inside, after DFT relaxation).

```

#=====
=====
# CRYSTAL DATA
#-----
data_VESTA_phase_1
_chemical_name_common      'eta2-stacking'
_cell_length_a              12.11475
_cell_length_b              4.09943
_cell_length_c              21.15907
_cell_angle_alpha           90.00016
_cell_angle_beta            54.98087
_cell_angle_gamma           90.00011
_space_group_name_H-M_alt   'P 1'

```

```

_space_group_IT_number      1

loop_
_space_group_symop_operation_xyz
  'x, y, z'

loop_
  _atom_site_label
  _atom_site_occupancy
  _atom_site_fract_x
  _atom_site_fract_y
  _atom_site_fract_z
  _atom_site_adp_type
  _atom_site_B_iso_or_equiv
  _atom_site_type_symbol
Al1      1.0  0.506563  0.000246  0.832879  Biso 1.000000 Al
Al2      1.0  0.999809  0.500159  0.166617  Biso 1.000000 Al
Al3      1.0  0.499836  0.000155  0.166594  Biso 1.000000 Al
Al4      1.0  0.006589  0.500215  0.832865  Biso 1.000000 Al
Al5      1.0  0.492748  0.000204  0.500307  Biso 1.000000 Al
Al6      1.0  0.992745  0.500255  0.500311  Biso 1.000000 Al
Al7      1.0  0.832440  0.000239  0.837061  Biso 1.000000 Al
Al8      1.0  0.842268  0.000113  0.154382  Biso 1.000000 Al
Al9      1.0  0.851333  0.000306  0.482684  Biso 1.000000 Al
Al10     1.0  0.332416  0.500239  0.837085  Biso 1.000000 Al
Al11     1.0  0.351321  0.500215  0.482706  Biso 1.000000 Al
Al12     1.0  0.342300  0.500145  0.154384  Biso 1.000000 Al
Al13     1.0  0.157398  0.000127  0.178766  Biso 1.000000 Al
Al14     1.0  0.166897  0.000279  0.496128  Biso 1.000000 Al
Al15     1.0  0.148045  0.000257  0.850493  Biso 1.000000 Al
Al16     1.0  0.657402  0.500119  0.178745  Biso 1.000000 Al
Al17     1.0  0.666900  0.500285  0.496109  Biso 1.000000 Al
Al18     1.0  0.648022  0.500335  0.850481  Biso 1.000000 Al
Al19     1.0  0.378620  0.000185  0.330588  Biso 1.000000 Al
Al20     1.0  0.333545  0.000295  0.661574  Biso 1.000000 Al
Al21     1.0  0.878120  0.500152  0.004592  Biso 1.000000 Al
Al22     1.0  0.833514  0.500432  0.661572  Biso 1.000000 Al
Al23     1.0  0.878630  0.500179  0.330583  Biso 1.000000 Al
Al24     1.0  0.499627  0.500295  0.666579  Biso 1.000000 Al
Al25     1.0  0.620881  0.000156  0.002616  Biso 1.000000 Al
Al26     1.0  0.621498  0.000174  0.328513  Biso 1.000000 Al
Al27     1.0  0.120838  0.500160  0.002653  Biso 1.000000 Al
Al28     1.0  0.121509  0.500196  0.328523  Biso 1.000000 Al
Al29     1.0  0.165654  0.500248  0.671630  Biso 1.000000 Al
Al30     1.0  0.999619  0.000285  0.666579  Biso 1.000000 Al
Al31     1.0  0.378088  0.000160  0.004634  Biso 1.000000 Al
Al32     1.0  0.665647  0.000371  0.671624  Biso 1.000000 Al
Cu1      1.0  0.998102  0.000214  0.330334  Biso 1.000000 Cu
Cu2      1.0  0.498088  0.500210  0.330336  Biso 1.000000 Cu
Cu3      1.0  0.001498  0.000125  0.002803  Biso 1.000000 Cu
Cu4      1.0  0.501503  0.500134  0.002801  Biso 1.000000 Cu
Cu5      1.0  0.256828  0.000170  0.252856  Biso 1.000000 Cu

```

Cu6	1.0	0.756805	0.500146	0.252845	Biso	1.000000	Cu
Cu7	1.0	0.747667	0.500345	0.580026	Biso	1.000000	Cu
Cu8	1.0	0.758713	0.500195	0.925958	Biso	1.000000	Cu
Cu9	1.0	0.742861	0.000146	0.080313	Biso	1.000000	Cu
Cu10	1.0	0.594189	0.000300	0.579981	Biso	1.000000	Cu
Cu11	1.0	0.740684	0.000188	0.407172	Biso	1.000000	Cu
Cu12	1.0	0.251617	0.500308	0.753147	Biso	1.000000	Cu
Cu13	1.0	0.242831	0.500128	0.080347	Biso	1.000000	Cu
Cu14	1.0	0.751595	0.000438	0.753138	Biso	1.000000	Cu
Cu15	1.0	0.240698	0.500209	0.407185	Biso	1.000000	Cu
Cu16	1.0	0.247660	0.000179	0.580050	Biso	1.000000	Cu
Cu17	1.0	0.405059	0.000260	0.753202	Biso	1.000000	Cu
Cu18	1.0	0.258692	0.000218	0.926015	Biso	1.000000	Cu
Cu19	1.0	0.094169	0.500280	0.579999	Biso	1.000000	Cu
Cu20	1.0	0.897993	0.000189	0.925999	Biso	1.000000	Cu
Cu21	1.0	0.893807	0.000147	0.253301	Biso	1.000000	Cu
Cu22	1.0	0.397951	0.500218	0.926034	Biso	1.000000	Cu
Cu23	1.0	0.393823	0.500161	0.253305	Biso	1.000000	Cu
Cu24	1.0	0.105717	0.000167	0.079897	Biso	1.000000	Cu
Cu25	1.0	0.101459	0.000169	0.407178	Biso	1.000000	Cu
Cu26	1.0	0.605767	0.500177	0.079855	Biso	1.000000	Cu
Cu27	1.0	0.601450	0.500136	0.407166	Biso	1.000000	Cu
Cu28	1.0	0.905049	0.500261	0.753195	Biso	1.000000	Cu

4 CIF file for the  $\eta_2$  phase (experimental result).

```

data_653749-ICSD
#?2009 by Fachinformationszentrum Karlsruhe, and the U.S. Secretary of
#Commerce on behalf of the United States. All rights reserved.
_database_code_ICSD          653749
_audit_creation_date         2008/08/01
_chemical_name_systematic    'Aluminium Copper (1/1)'
_chemical_formula_structural  'Al Cu'
_chemical_formula_sum        'Al1 Cu1'
_publ_section_title
;
Kristallstruktur von Cu3 Al2+ (h) und Cu Al (r)
;
loop_
_citation_id
_citation_journal_abbrev
_citation_year
_citation_journal_volume
_citation_page_first
_citation_page_last
_citation_journal_id_ASTM
primary 'Journal of the Less-Common Metals' 1972 29 133 140 JCOMAH
_publ_author_name
;
El-Boragy, M.;Szeapan, R.;Schubert, K.
;
_cell_length_a              12.066

```

```
_cell_length_b      4.105
_cell_length_c      6.913
_cell_angle_alpha   90.0
_cell_angle_beta    55.04
_cell_angle_gamma   90.0
_cell_volume        280.62
_cell_formula_units_Z  10
_symmetry_space_group_name_H-M  'C 1 2/m 1'
_symmetry_Int_Tables_number  12
_refine_ls_R_factor_all  0.19
loop_
_symmetry_equiv_pos_site_id
_symmetry_equiv_pos_as_xyz
  1 '-x, y, -z'
  2 '-x, -y, -z'
  3 'x, -y, z'
  4 'x, y, z'
  5 '-x+1/2, y+1/2, -z'
  6 '-x+1/2, -y+1/2, -z'
  7 'x+1/2, -y+1/2, z'
  8 'x+1/2, y+1/2, z'
loop_
_atom_type_symbol
_atom_type_oxidation_number
Al0+      0
Cu0+      0
loop_
_atom_site_label
_atom_site_type_symbol
_atom_site_symmetry_multiplicity
_atom_site_Wyckoff_symbol
_atom_site_fract_x
_atom_site_fract_y
_atom_site_fract_z
_atom_site_occupancy
_atom_site_attached_hydrogens
Al1 Al0+ 2 d 0 0.5 0.5 1 0
Al2 Al0+ 4 i 0.155 0 0.543 1 0
Al3 Al0+ 4 i 0.382 0 0.013 1 0
Cu1 Cu0+ 2 a 0 0 0 1 0
Cu2 Cu0+ 4 i 0.256 0 0.760 1 0
Cu3 Cu0+ 4 i 0.109 0 0.228 1 0

#End of data_653749-ICSD
```

## Appendix 4

# Rare $\eta^*$ -decorated semi-coherent $\theta'$ /Al interface observed in the Al-Cu-Ge alloy

Rare  $\eta^*$ -decorated semi-coherent  $\theta'$ /Al interface observed in the Al-Cu-Ge alloy aged for 1 h at 200 °C. The arrows indicate the  $\eta^*$  segments which are commonly observed in Al-Cu alloys and in the Al-Cu-In-Sb alloy. The precipitate is  $\theta'$  type I.

